Success is not final, failure is not fatal, it is the courage to continue that counts.

Winston Churchill

Study of the relationship between the EEG and BOLD signals using intracranial EEG - fMRI data simultaneously acquired in humans

Teresa Inês Gonçalves Murta

Department of Clinical and Experimental Epilepsy

Institute of Neurology

University College London

PhD

Personal Statement

I, Teresa Inês Gonçalves Murta, confirm that the work presented in this thesis is my own. Where information has been derived from other sources, I confirm that this has been indicated in the thesis.

Financial Support

This work was conducted through the support of the Foundation for Science and Technology (FCT) grant SFRH/BD/80421/2011 (Bolsa de Doutoramento (BD) individual atribuída a Teresa Inês Gonçalves Murta), and project grants PTDC/BBB-IMG/2137/2012 and LARSyS [UID/EEA/50009/2013], Portugal; Medical research centre, grant G0301067, United Kingdom; and National Institute for Health Research UCL Hospitals Biomedical Research Centre, United Kingdom.

Table of Contents

Table of Figures **8**

Table of Tables **12**

Acronyms **13**

Abstract **15**

1 Preface **17**

2 Introduction **23**

2.1 Neural basis of EEG and BOLD signals 24

2.1.1 Cerebral electrophysiological signals 24

2.1.1.1 Different spatial scales and their relationship to neuronal activity 25

2.1.1.2 Commonly observed electrophysiological activity 27

- Epileptiform activity 27
- Rhythmic and arrhythmic activity 28
- Event-related activity 29

2.1.2 Functional MRI: the BOLD signal 29

2.1.2.1 The origin of the BOLD signal 30

2.1.2.2 Neurovascular coupling mechanisms in the diseased brain 31

2.2 Electrophysiological correlates of the BOLD signal 31

2.2.1 Mapping BOLD changes related to electrophysiological activity 31

2.2.1.1 Epileptic activity 32

- Mapping BOLD changes related to scalp EEG IED 33
- Mapping BOLD changes related to scalp EEG seizures 33
- Mapping BOLD changes related to intracranial EEG IED 34

2.2.1.2 Non-epileptic spontaneous activity 35

- Mapping BOLD changes related to the occipital EEG spectral content in the α range 35
- Mapping BOLD changes related to the EEG spectral content in the δ, θ, α, β, γ ranges 36

2.2.1.3 Cognitive, sensory and motor functions 37

- Mapping BOLD changes related to ERP amplitude and latency 37
- Mapping BOLD changes related to EEG synchronisation and phase coherence 37
- Mapping BOLD changes related to the EEG spectral content in the δ, θ, α, β, γ ranges 37

2.2.1.4 Improving the interpretation of scalp EEG-informed fMRI 39

2.2.2 Characterising the local relationship between the EEG and BOLD signals 39

2.2.2.1 ECoG-BOLD coupling in humans 39

2.2.2.2 Depth EEG-, LFP-, and multiunit activity- BOLD coupling 41

2.3 EEG phase-amplitude coupling (PAC) and the BOLD signal 42
2.3.1 Functional relevance of EEG activities in different frequency ranges 43
2.3.2 Improving the understanding of the EEG-BOLD signals relationship 44
2.4 EEG IED morphology and the BOLD signal 45
2.5 Simultaneity of electrophysiological and BOLD fMRI acquisitions 45
2.5.1 Necessity or preference for simultaneous acquisitions 46
2.5.2 Data degradation mechanisms 46
2.6 Concluding remarks 48

3 Simultaneously acquired icEEG and BOLD fMRI data 51
3.1 IcEEG and MRI data acquisition 52
3.2 IcEEG and fMRI data pre-processing 54
3.3 Estimating the icEEG contacts coordinates in the CT, T1, or EPI space 55

4 Quality of icEEG data recorded during fMRI 59
4.1 Motivation 60
4.2 Methods 61
4.2.1 Gradient artefact 61
4.2.1.1 Gradient artefact correction 61
- IcEEG data filtering and segmentation 61
- Gradient template construction approaches 62
- Gradient template subtraction 63
- Gradient artefact correction SVD – based improvements 63

4.2.1.2 IcEEG data quality measures 66
4.2.1.3 Set of gradient artefact template parameters tested 66
- Sequential average 66
- Weighted average 66

4.2.1.4 Gradient artefact construction approach and optimal data quality 67
4.2.1.5 Gradient artefact template parameters, optimal data quality, and motion 67
4.2.1.6 Gradient artefact template parameters, optimal data quality, and EEG frequency band of interest 67
4.2.2 MR scanner vibration artefacts 67
4.2.2.1 Characterisation 67
4.2.2.2 Correction 68
- Internal scanner ventilation artefact 68
- Cooling compression pump artefact 68

4.3 Results 68
4.3.1 Gradient artefact 68
4.3.1.1 Gradient artefact template construction approach and optimal data quality 69
4.3.1.2 Gradient artefact template parameters, optimal data quality, and motion 69
4.3.1.3 Gradient artefact template parameters, optimal data quality, and EEG frequency band of interest 70

4.3.1.4 SVD-based gradient artefact correction improvements 70
4.3.2 MR scanner vibration artefacts 74
4.3.2.1 Characterisation 74
- Internal scanner ventilation artefact 74
- Cooling compression pump system artefact 75
4.3.2.2 Correction 75
- Internal scanner ventilation artefact 75
- Cooling compression pump artefact 76
4.4 Discussion 76
4.4.1 Gradient artefact 77
4.4.1.1 Gradient artefact template construction approach and optimal data quality 77
4.4.1.2 Gradient artefact template parameters, optimal data quality, and motion 77
4.4.1.3 Gradient artefact template parameters, optimal data quality, and EEG frequency band of interest 78
4.4.1.4 SVD-based gradient artefact correction improvements 78
4.4.1.5 IcEEG data quality measures 78
4.4.2 Vibration related artefacts 78
4.4.2.1 Internal scanner ventilation artefact 78
4.4.2.2 Cooling compression pump artefact 79
4.4.3 Future work 79
4.5 Conclusion 79
5 EEG phase-amplitude coupling and the BOLD signal 81
5.1 Motivation 82
5.2 Methods 83
5.2.1 Data pre-processing 83
5.2.1.1 Patient selection 84
5.2.1.2 Motor task paradigm 84
5.2.1.3 BOLD time course of interest 84
5.2.1.4 EEG time-frequency decomposition 84
5.2.1.5 ECoG contacts and frequency bands of interest 85
- Patient-specific contacts of interest (COI) 85
- Patient-specific frequency bands 85
5.2.2 EEG power and the BOLD signal amplitude relationship 87
5.2.2.1 EEG band power - BOLD amplitude correlation (experiment 1) 87
5.2.2.2 Influence of the EEG α and β phase in the EEG γ power - BOLD amplitude correlation curve (experiment 2) 87
5.2.3 EEG PAC and the BOLD signal amplitude relationship (experiment 3) 88
5.2.3.1 PAC strength estimation 88
- Canolty's PAC 88
- Phase-amplitude comodulogram 89

5.2.3.2 PAC strength - based BOLD predictors 89
5.2.3.3 BOLD model definition 90
5.3 Results 91
5.3.1 Data pre-processing 91
5.3.1.1 BOLD time-course of interest 91
5.3.1.2 ECoG contact pairs and frequency bands of interest (COI) 94
5.3.2 EEG power and the BOLD signal amplitude relationship 96
5.3.2.1 EEG band power - BOLD amplitude correlation (experiment 1) 96
5.3.2.2 Influence of the EEG α and β phases in the EEG γ power - BOLD amplitude correlation (experiment 2) 97
5.3.3 EEG PAC and the BOLD signal amplitude relationship (experiment 3) 98
5.3.3.1 PAC-derived BOLD predictors 98
5.3.3.2 BOLD model 98
5.4 Discussion 99
5.4.1 EEG power and the BOLD signal amplitude relationship 100
5.4.2 EEG PAC and the BOLD signal amplitude relationship 100
5.4.2.1 PAC strength - derived BOLD predictors 100
5.4.2.2 BOLD signal variance explained by EEG PAC and power 101
5.4.3 Methodological aspects 102
5.4.3.1 Electrical stimulation results and contacts of interest (COI) 102
5.4.3.2 Patient-specific frequency bands 102
5.4.4 Technical limitations 102
5.4.5 Future work 103
5.5 Conclusion 104

6 EEG sharp wave morphology and the BOLD signal 107
6.1 Motivation 108
6.2 Methods 109
6.2.1 Patient selection 109
6.2.2 IED classification 109
6.2.3 Patient-specific contacts of interest (COI) 110
6.2.4 IED parameterisation 115
6.2.5 Models of IED-related BOLD changes 117
6.2.5.1 Variance explained quantification 118
6.2.5.2 Voxels of interest 118
6.3 Results 119
6.4 Discussion 121
6.4.1 Sharp wave width neurophysiological correlates and the BOLD signal 121
6.4.2 Sharp wave amplitude neurophysiological correlates and the BOLD signal 122
6.4.3 IED spatial field extent neurophysiological correlates and the BOLD signal 123
6.4.4 Methodological aspects 123
6.4.5 Technical limitations 124

6.4.6 Relevance to EEG-fMRI studies 125
6.4.7 Relevance to Neuroscience 125
6.5 Future Work..... 125
6.6 Conclusion..... 126

7 General conclusions 127

Bibliography 131

Appendix A PAC and the BOLD signal amplitude relationship (experiment 3) supplementary methods, results, and discussion 157

Table of Figures

Figure 1-1 Common pipeline of EEG-informed fMRI in epilepsy. Functional MRI is used to map the generators of interictal activity, visually identified in the simultaneously recorded EEG. Matrix design example borrowed from Chaudhary et al. (2012b). EEG traces and fMRI maps illustrations borrowed from Vulliemoz et al. (2011). 19

Figure 2-1 Brain signals at multiple scales: from thousands of neurons to whole-brain. Illustration of recording of scalp EEG, ECoG, depth EEG and LFP signals, and three hypothetical BOLD-fMRI clusters, in different lobes. The spatial sensitivity profiles of the four electrophysiological techniques are sketched in shaded grey: mainly neocortical for scalp EEG and ECoG, local to each electrode pair for depth EEG (~1cm^3), and local to each microelectrode for LFP (~100µm^3). LFP recording is illustrated using a drawing from (Ramón y Cajal, 1899). 26

Figure 2-2 General EEG-informed fMRI integration scheme, highlighting the mechanisms underlying each signal. In a given voxel, the neuronal activity generates an ensemble of postsynaptic potentials (ePSP). The temporarily and spatially synchronised summated PSP produce the primary current sources (PCD). The head volume conductor properties transform the PCD into EEG. The ePSP generates a vasomotor feed forward signal (VFFS), via its own forward model, which is in turn transformed, via the haemodynamic forward model, into the observed BOLD signal. ePSP, PCD, VFFS, EEG, and BOLD are time-dependent. The EEG is considered to have the same time evolution as the PCD, which is considered to be a driver for the BOLD signal. This is an asymmetrical EEG and fMRI data integration approach because the EEG temporal dynamics are taken as surrogates for the VFFS. Diagram adapted from Valdes-Sosa et al. (2009). 32

Figure 3-1 Examples of icEEG signal power spectra after the gradient artefact correction. Different colours represent different icEEG contacts (located over the motor cortex). 54

Figure 3-2 Example of CT and T1 images. Blue arrow highlight icEEG contacts. Red arrow highlights a group of high intensity voxels that it is not a icEEG contact. 55

Figure 3-3 Illustration of the clustering algorithm designed by me to find the coordinates of the icEEG contacts. In this example, the final solution (i.e. coordinates of the contacts) is found after two iterations. 56

Figure 4-1 Representative icEEG time courses (Patient IH; see an illustration of the icEEG implantation scheme in **Figure 4-3**), before (blue) and after (orange) the subtraction of the gradient artefact template. Note the different scales of the y-axes. In this example, the artefact template was computed with the sequential average approach, using 51 data epochs (k=51). 64

Figure 4-2 Internal scanner ventilation artefact time-frequency characterisation in the eigenvariates space. Time-frequency amplitude profile (Morlet wavelet factor: 1800; y-axis samples: 100) of the first three eigenvariates, for the frequency range 92.7 - 93.7 Hz, obtained by a SVD of the band-pass filtered icEEG signal. 69

Figure 4-3 IcEEG implantation scheme for patients IH, on the left, and CB, on the right. 70

Figure 4-4 **A** $1\text{-}\mathrm{RIAR}$ (x-axis) as function of $1\text{-}\mathrm{RBSD}$ (y-axis) for the correction parameters that resulted in the lowest Q. Weighted average results are showed in red. Sequential average results are showed in blue. Different geometric shapes represent different contact groups (cortical grids A (GA), B (GB), C, (GC); cortical stripe F (SF); depth A (DA)). Dotted lines illustrate Q contour lines. RBSD and RIAR were obtained using the icEEG signal power in the range [2 – 200] Hz, averaged across contacts. Note: In these plots, a smaller distance between the data point and the origin implies a lower Q value and, therefore, a better data quality. **B** w and k values for which the quality ratios are showed in **A**. 71

Figure 4-5 Translations, arc of rotation (x displayed in blue, y in green, z in red, and $\mathrm{x}2 + \mathrm{y}2 + \mathrm{z}2$ in black) and motion events *, which represent fMRI volumes where the total differential motion was above 0.2 millimetres. 72

Figure 4-6 Internal scanner ventilation artefact time-frequency characterisation, in the contacts space. Power spectra for the frequency range [90 - 96] Hz are shown on the top right, and time-frequency amplitude profiles for the frequency range [92.7 - 93.7] Hz are shown on the bottom, of two representative icEEG contacts. 74

Figure 4-7 Cooling compression pump artefact correction effect. Spectra for the frequency range [90 - 120] Hz of three representative icEEG contacts. Data corrected for gradient and cooling pump related artefacts are presented in red, overlying data only corrected for gradient artefacts, presented in black. Blue boxes highlight the cooling pump artefact peaks. Green boxes highlight the ventilation artefact peaks. Yellow boxes highlight residual gradient artefact peaks. 75

Figure 4-8 Internal scanner ventilation artefact correction effect. Power spectra for the frequency range [90 - 96] Hz (top right), and time-frequency amplitude profiles for the frequency range [92.7 - 93.7] Hz (bottom), of two representative icEEG contacts, after gradient and internal ventilation artefact corrections. 76

Figure 5-1 Design matrices of all the BOLD signal models considered. The regressor of interest, i.e. the regressor that was orthogonalised with respect to the combination of the others, is highlighted in dark grey. 91

Figure 5-2 Finger tapping related BOLD increases (t-contrast, p<0.001, uncorrected). 92

Figure 5-3 Patient-specific α and β bands of interest. Fractal and harmonic spectra for the ipsilateral finger tapping periods, computed using a coarse-graining spectral analysis (CGSA) (Yamamoto and Hughson, 1991), as described in He et al. (2010). 94

Figure 5-4 Contact pairs of interest. **A** ECoG contacts (black), and finger tapping BOLD increases (red). **B** Spectral differences for contralateral and ipsilateral finger tapping periods. **C** Pre-surgical electrical stimulation results. Contacts showing peaks of apparent artefactual origins (harmonic high-amplitude peaks (prominent residual gradient artefacts), or a 50 Hz

(electrical component) high-amplitude peak) were not analysed, and are displayed as a dotted cross. 95

Figure 5-5 EEG band power – BOLD amplitude correlation. Pearson's linear correlation coefficients between the power of multiple EEG frequency components and the amplitude of the contralateral finger tapping - related BOLD time course. The grey tone identifies the distance between the ECoG contact pair (middle distance between the two contacts) and the maximum t-value of the cluster of significant contralateral finger tapping - related BOLD changes. 96

Figure 5-6 Influence of the EEG α and β phases in the EEG γ power - BOLD amplitude correlation. Pearson's linear correlation coefficients between the power of multiple EEG frequency components and the amplitude of the finger tapping - related BOLD time course, when the γ power was segmented according to the α phase (on the left) or the β phase (on the right). The curve colour identifies the phase bin according to which the γ power was segmented. 97

Figure 5-7 { α, γ } and { β, γ } frequency pairs of interest. Phase-amplitude comodulogram plots (z-scored PAC strength values) for the patient-specific α and β bands, obtained with the Canolty metric ($p < 0.05$; corrected for multiple comparisons using Bonferroni criterion). 98

Figure 5-8 BOLD signal changes GLM results. t-values for the $PAC_{\beta\gamma}$, P_{α}, P_{β}, and P_{γ} effects. Different shapes represent different patients. Filled shapes represent t-values with $p < 0.05$. 99

Figure 5-9 Cross-correlation matrices. Pairwise Pearson's linear correlation coefficients for all EEG-derived regressors and BOLD time course of interest. No values are shown for $PAC_{\alpha\gamma}$ for patient LT and CB because no significant PAC effect was found for the α band of these patients. 99

Figure 6-1 Representative EEG time courses (patient HD) showing sharp waves of different amplitudes and widths (blue arrows point at events visually marked at COI: DA 3 – 4). 110

Figure 6-2 Average IED for each set of events of interest (SCOI). 111

Figure 6-3 A - **D** Sharp wave morphology-based features: **A** amplitude, **B** width, **C** rising phase slope, **D** energy, overlaid on an example of a single-trial IED estimate. **E** - **F** Single-trial IED estimates examples. The original IED is displayed in black, the average IED is displayed in grey, and the estimated IED is displayed in blue. 116

Figure 6-4 Representative example (patient BS, events of interest set: S_2, see..... 119

Figure 6-5 Variance explained (VE) results. Experiments level analysis: **A** Average VE values, by modulatory feature; for the set of voxels comprised in pBOLD, and **D** in nBOLD. Group level analysis: **B** Average VE and respective standard deviation values, by modulatory feature; for the set of voxels comprised in pBOLD, and **D** in nBOLD. Undefined values correspond to cases where no voxel had a large enough *t-value* to survive the threshold used ($p < 0.05$, uncorrected). 120

Figure A-1 Phase-amplitude comodulogram plots obtained using three different PAC strength estimation metrics, for each patient-specific COI_{β}. The plots obtained with Canolty's and Tort's

metrics are thresholded at $p < 0.05$ and corrected for multiple comparisons using the Bonferroni criterion..... 160

Figure A-2 BOLD signal changes GLM results. t-values for the $PAC_{\beta\gamma}$, P_{α}, P_{β}, and P_{γ} effects. Different colours represent different PAC strength metrics. Different shapes represent different patients. Filled shapes represent t-values with $p < 0.05$..... 161

Figure A-3 BOLD signal changes GLM results. t-values for the $PAC_{\beta\gamma}$, P_{α}, P_{β}, and P_{γ} effects. Different colours represent different epoch durations for the estimation of the PAC strength. Different shapes represent different patients. Filled shapes represent t-values with $p < 0.05$. 161

Table of Tables

Table 3-I Description of the icEEG-fMRI data acquisitions: icEEG recording parameters, scanner-related factors, and experimental protocols. 53

Table 4-I Correction parameters, w and k, that led to the optimal data quality, and respective Q values, by EEG frequency band of interest. W stands for weighed and S for sequential average approach. Concerning the sequential average approach; the lowest Q values are highlighted in grey and the lowest k values are highlighted in light blue, for each contact group. 73

Table 5-I IcEEG implantation characterisation: types of electrodes, number of contacts per electrode, and implantation scheme. The ECoG contact pairs analysed (over the motor cortex) are highlighted with numbered black squares. FLE: Frontal lobe epilepsy, R: right, L: left, A: anterior, M: medial, P: posterior, I: inferior, and S: superior. 93

Table 6-I Description of $\boldsymbol{S}_{COI}$ and sharp wave feature estimates for BOLD modelling. FW: focal plus more widespread, F: focal. 111

Table 6-II IcEEG implantation characterisation: type of electrodes, number of contacts per electrode, and implantation scheme. TLE: Frontal lobe epilepsy, FLE: Frontal lobe epilepsy, R: right, L: left, A: anterior, M: medial, P: posterior, I: inferior, and S: superior. Intra-contact distances: 10 millimetres for grids, strips, and most depths; 5mm for high-density grids and medial contact pairs in some depths. The approximated location of each COI is highlighted with a green arrow (depth), or square (ECoG). 112

Acronyms

BOLD	Blood-oxygen-level-dependent
CBF	Cerebral blood flow
CBV	Cerebral blood volume
$CMRO_2$	Cerebral metabolic rate of oxygen
COI	Contact pair of interest
DAN	Dorsal Attention Network
DMN	Default Mode Network
ECoG	Electrocorticography
EEG	Electroencephalography, Electroencephalogram
EPSP	Excitatory post-synaptic potential
ERD	Event-related desynchronisation
ERP	Event-related potential
ERS	Event-related synchronisation
fMRI	Functional magnetic resonance imaging
FWHM	Full-width at half-maximum
GLM	General linear model
HF	High-frequency
HRF	Haemodynamic response function
IC	Independent component
ICA	Independent component analysis
icEEG	Intracranial electroencephalography
IED	Interictal epileptiform discharge
IPSP	Inhibitory post-synaptic potential
LF	Low-frequency
LFP	Local filed potential
MUA	Multi-unit activity
PAC	Phase-amplitude coupling
PAC	Phase-amplitude coupling
PC	Principal component
PCA	Principal component analysis
PCD	Primary current sources
PSP	Post-synaptic potential
RSN	Resting State Network
SEEG	Stereotactic EEG
SOZ	Seizure onset zone
SPM	Statistical Parametric Mapping
SUA	Single-unit activity
SVD	Singular value decomposition

Abstract

The principal aim of this work was to further characterise the relationship between the electrophysiological and BOLD fMRI signals at the local level, exploiting the unique opportunity to analyse intracranial EEG (icEEG) and fMRI data recorded simultaneously in humans, during a finger tapping task and at rest. The MR-environment (gradient switch and mechanical vibration) related artefacts corrupting the icEEG data were the first problem tackled; they were characterised and removed using techniques developed by me. The two parts that followed aimed to shed further light on the neurophysiological basis of the BOLD effect. Firstly, the influence of the phase of the low frequency EEG activities (< 30 Hz) on capability of an EEG power - based model to predict the amplitude of finger tapping related BOLD changes was investigated; the strength of the coupling between the phase of β and the amplitude of γ (>70 Hz) (phase-amplitude coupling: $PAC_{\beta\gamma}$) was found to explain variance in addition to a combination of α, β, and γ band powers, suggesting that $PAC_{\beta\gamma}$ strength and power fluctuations result from complementary neuronal processes. Secondly, five interictal epileptiform discharge (IED) morphology and field extent related features were tested in their individual capability to predict the amplitude of the co-localised BOLD signal; these were the amplitude and rising phase slope, thought to reflect the degree of neuronal activity synchrony; width and energy, thought to reflect the duration of the excitatory post-synaptic potentials; and spatial field extent, thought to reflect the spatial extent of the surrounding, synchronised sources of neuronal activity. Among these features, the IED width was the only one found to explain BOLD signal variance in addition to the IED onsets, suggesting that the amplitude of the BOLD signal is comparatively better predicted by the duration of the underlying field potential, than by the degree of neuronal activity synchrony.

1

Preface

In the last century, human brain activity has been recorded most commonly as electrical potentials on the scalp (scalp electroencephalography - EEG), neocortex surface (electrocorticography - ECoG), or deep inside the brain (depth EEG). Since the early 1990s, using blood-oxygen-level-dependent (BOLD) functional magnetic resonance imaging (fMRI) to record changes in the local blood oxygenation has become an increasingly important tool, largely due to its non-invasive whole-brain coverage and relatively high spatial resolution. These indirect measurements of neuronal activity have been used to study a wide range of processes and phenomena, ranging from sensory or cognitive functions, to sleep or rest stages (which sometimes include spontaneous epileptic discharges). Combining electrophysiological and BOLD fMRI signals emerged as a natural consequence of the complementarity of their temporal and spatial resolutions, and the potential capability of fMRI to locate scalp EEG generators, while bypassing the scalp EEG inverse problem. Simultaneously recorded scalp EEG and BOLD fMRI data have been used to locate brain regions involved in the generation and propagation of epileptic seizures (Chaudhary et al., 2012a; Murta et al., 2012) and interictal epileptiform discharges (IED) (Caballero-Gaudes et al., 2013). The accurate delineation of these regions is the main purpose of the pre-surgical evaluation performed in patients with drug-resistant epilepsies because the best treatment available is to surgically disrupt them. Most studies combining EEG and fMRI data are asymmetric data integration strategies that use the EEG to capture characteristic temporal patterns (e.g.: epileptic spikes, seizure activity, sleep stages, ongoing brain rhythms, etc.) and the fMRI to locate the generator(s) of such activity (**Figure 1-1**). These strategies are often called EEG-informed fMRI.

Despite extensive investigations and discussions over recent years, we are still not completely aware of the aspects of neuronal processing which are most closely related to the BOLD signal, or about their generality across brain regions and between normal and pathological activities (Ekstrom, 2010; Logothetis, 2010, 2008; Magri et al., 2012). For instance, both BOLD increases and decreases have been linked to the occurrence of epileptic discharges (Pittau et al., 2013), but BOLD decreases have been thought to reflect neuronal activity decreases (Shmuel et al., 2006), which seem incompatible with the occurrence of epileptic discharges. The neural basis of EEG and BOLD signals are briefly described in the first section of Chapter 2, § 2.1, which help us to understand what is currently known about the electrophysiological correlates of the BOLD signal, extensively described in the second section of Chapter 2, § 2.2.

This project was designed to further characterise the local electrophysiological correlates of the BOLD signal, taking advantage of the unique opportunity to analyse intracranial EEG (icEEG) and BOLD fMRI data recorded simultaneously in humans. As a consequence of better understanding the BOLD signal neuronal correlates, the sensitivity of future EEG-informed fMRI data integration strategies may be improved, and, perhaps, more importantly, their interpretation facilitated. Even the most complex theoretically-based EEG-fMRI data integration approaches rely on assumptions about the local electrophysiological correlates of the BOLD signal, usually

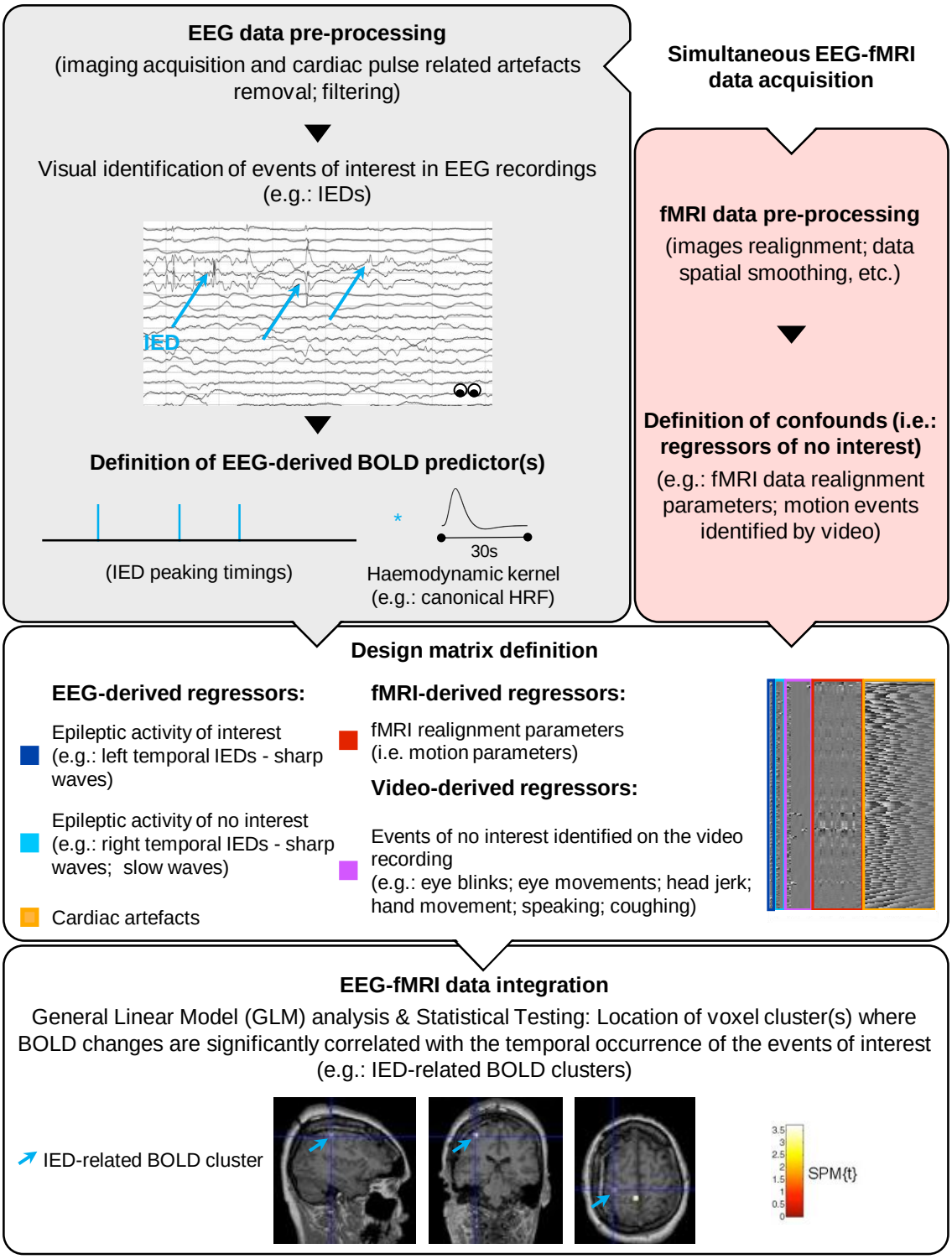

Figure 1-1 Common pipeline of EEG-informed fMRI in epilepsy. Functional MRI is used to map the generators of interictal activity, visually identified in the simultaneously recorded EEG. Matrix design example borrowed from Chaudhary et al. (2012b). EEG traces and fMRI maps illustrations borrowed from Vulliemoz et al. (2011).

embedded in mathematical models that describe the relationships between the two signals and the underlying neuronal activity. For example, Babajani et al. (2005) and Valdes-Sosa et al. (2009) proposed theoretically-based EEG-fMRI data integration models that relied on Logothetis et al. (2001)'s findings suggesting that local field potentials (LFP) were better predictors of BOLD

fluctuations than single- or multi-unit activities (SUA or MUA) (LFP and (S)MUA measured with microelectrodes implanted in the visual cortex of macaques). Knowing which particular EEG-derived feature(s) (e.g.: ongoing activity power, phase-synchrony, phase-amplitude coupling strength; event-by-event morphological and field extent characteristics) correlate better with the simultaneous and co-localised BOLD signal will probably lead to key insights into the neuronal substrate of the BOLD signal, and therefore help us to interpret the commonly observed BOLD fMRI maps.

Activities of multiple frequency ranges, characteristically associated with sensory, motor, and cognitive events, are commonly observed on electrophysiological recordings (Engel et al., 2001; Jacobs and Kahana, 2010; Varela et al., 2001). Interestingly, these activities appear to hierarchically interact with each other, as the “basic units” of a complex system that seems to regulate how information is processed in the brain, across multiple spatial and temporal scales (Buzsaki et al., 2012; Canolty and Knight, 2010; Hyafil et al., 2015; Lakatos et al., 2005; Palva et al., 2005; Roopun et al., 2008). The interaction between the phase of the low (<30 Hz; LF) and the amplitude of high frequency activities (>30 Hz; HF), often simply called phase-amplitude coupling (PAC), has attracted great interest due to its potential functional role (Axmacher et al., 2010; Buzsáki et al., 2012; Cohen et al., 2009a, 2009b; Kramer et al., 2008; Lakatos et al., 2008; Tort et al., 2009). In brief, the strength of PAC fluctuates in a task-dependent manner, both within and across regions; it goes from no influence to strong influence, and back within a few tenths of a second; it can assume different patterns and be modulated in time differently, within different brain structures (Tort et al., 2008); it is proportional to the intensity of training and level of performance (Dürschmid et al., 2014; Tort et al., 2009). A short literature review on the functional relevance of the LF activities phase and, in particular, on the PAC strength, is presented in the third section of Chapter 2, § 2.3. It is currently known that BOLD changes are better predicted by a combination of power of multiple LF and HF activities rather than by the power of the HF activity alone. However, the electrophysiology-based BOLD signal models previously explored did not account for the temporal dynamics of the phase of the LF activities, nor for its coupling to the amplitude of the HF activity. Taking advantage of the unique opportunity to analyse icEEG and BOLD fMRI data simultaneously recorded in humans performing a finger tapping task, we investigated whether fluctuations in the PAC strength explained variance of the BOLD signal amplitude in addition to fluctuations in the power of the EEG signal at multiple LF and HF bands, at the local level, as described in Chapter 5.

While the aforementioned study aimed to investigate the influence of an important EEG-derived feature (the phase of the LF activities) in the currently accepted best electrophysiology-based model of the BOLD signal, the following study aimed to shed further light on the neuronal basis of the BOLD signal, using the knowledge we already have on the relationship between a group of EEG-derived features and the underlying neuronal activity. For this, five IED morphology and spatial field extent related features - amplitude, rising phase slope, width, energy (area under the curve), and spatial field extent (number of icEEG contacts over which the IED was simultaneously observed) – were estimated, event-by-event, and compared, in terms of

capability to explain variance of the amplitude of the simultaneous and co-localised BOLD signal, which was not explained by the IED onsets alone, in the surroundings of the most active icEEG contact (likely to be in the immediate vicinity of the neuronal generator), as described in Chapter 6. A literature review of studies with similar aims is presented in the fourth section of Chapter 2, § 2.4.

The two aforementioned studies were designed to exploit the unique opportunity to analyse icEEG and BOLD fMRI data simultaneously acquired in humans (acquisition and pre-processing details described in Chapter 3), recently available after solving a number of challenging technical aspects (Boucousis et al., 2012; Carmichael et al., 2012, 2010). The simultaneity of the acquisition of the two signals is essential to investigate ongoing phenomena and events variability; however, it poses some difficulties, as discussed in the fifth section of Chapter 2, § 2.5. Due to this simultaneity, a number of artefacts corrupt both EEG and MRI data. Of particular relevance to us is the quality of the icEEG data because the accuracy of the estimation of the EEG-derived features of interest (phase and amplitude of multiple frequency EEG components; IED event-by-event morphological and spatial field extent characteristics) may be compromised. Therefore, this project started with an exploratory investigation towards improving the icEEG data quality, as described in Chapter 4.

The general conclusions of this work and potential methodological improvements are discussed in Chapter 7.

2

Introduction[1]

[1] The first three sections of this chapter were adapted from Murta, T., Leite, M., Carmichael, D.W., Figueiredo, P., Lemieux, L., 2015. Electrophysiological correlates of the BOLD signal for EEG-informed fMRI. Hum. Brain Mapp. 36, 391–414.

This chapter starts with a brief description of the neurophysiological origins of the EEG and BOLD signals, in § 2.1, to clarify their complementarity. The second section of this chapter, § 2.2, comprises a review of studies that aimed to improve the neurophysiological interpretation of the commonly observed BOLD fMRI maps, by investigating how the electrophysiological and the BOLD signals relate to each other, in multiple scenarios: epilepsy; non-epileptic spontaneous activity; and cognitive, sensory and motor functions. The reviewed studies were grouped as those using fMRI to map haemodynamic changes associated with a particular electrophysiological phenomenon, discussed in § 2.2.1; and those focused on characterising the local relationship between the electrophysiological and haemodynamic signals, often through systematic comparisons of electrophysiology-derived metrics in terms of their capability to predict BOLD signal fluctuations, discussed in § 2.2.2. The third section of this chapter, § 2.3, comprises a review of the studies supporting the functional relevance of the phase of the low frequency EEG activities and, in particular, of the interaction between the phase of the low and the amplitude of the high frequency EEG activities (PAC), the ongoing EEG phenomenon that was later compared with the also ongoing EEG power for multiple frequency bands, in terms of capability to predict the amplitude of the BOLD signal. The forth section of this chapter, § 2.4, comprises a review of the studies that have investigated the relationship between the morphology of IED (amplitude and duration), events commonly observed on EEG, and the amplitude of the BOLD signal. Finally, in the fifth section of this chapter, § 2.5, we discuss the importance of the simultaneity of the EEG and fMRI data acquisition, essential to investigate ongoing phenomena and events variability, and therefore essential to this project, together with the difficulties associated with it. This chapter is focused on human studies, the most relevant for this project, apart from the subsection on the relationship between neuronal spiking rates and the BOLD signal (§ 2.2.2), and a few studies in animals discussed in § 2.4.

2.1 Neural basis of EEG and BOLD signals

In this section, we describe the key aspects of the current understanding of the neurophysiological origin of EEG and BOLD fMRI signals. Cerebral electrophysiological signals (LFP, icEEG, scalp EEG) can be recorded at multiple spatial scales (**Figure 2-1**). Despite reflecting the underlying neuronal activity differently, these signals related to each other, to a reasonable extent, as discussed in § 2.1.1.1. Most EEG-informed fMRI studies rely on one of the set of electrophysiological phenomena: ongoing (during cognitive, sensory, motor functions, or at rest), event-related, or epileptic activity. These electrophysiological phenomena are briefly described in § 2.1.1.2. The origin of the BOLD effect, together with how its underlying mechanisms may be affected by disease, is discussed in § 2.1.2.

2.1.1 Cerebral electrophysiological signals

Brain function relies on a causal chain of events originated at the level of synapses, the basic elements for communication between neurons. Active neurons generate time-varying electric currents, which result from ions crossing their cellular membranes. There are two main forms of neuronal activation: the slow changes in membrane potential due to synaptic activation, which

are mediated by several neurotransmitter systems - these are the post-synaptic potentials (PSP; excitatory and inhibitory: EPSP and IPSP); and the fast neuronal membrane depolarisations, which result from action potentials (Lopes da Silva, 2010). The electrical currents arising during synaptic activation can sum to generate electrical potentials that can be measured at different spatial scales (**Figure 2-1**) (Kajikawa and Schroeder, 2011; Riera et al., 2005).

Most multimodal studies mapping BOLD changes related to particular electrophysiological phenomena use scalp EEG, whereas those focused on characterising the local relationship between the two signals often use LFP, ECoG, or depth EEG (invasive) recordings.

2.1.1.1 Different spatial scales and their relationship to neuronal activity

LFP are recorded with low-impedance microelectrodes placed in the extracellular medium, sufficiently far from individual cells to prevent any particular neuron from dominating the signal, and reflect the activity of several tens of thousands of nerve cells (Fermaglich, 1982). Action potentials (SUA or MUA, depending on the number of cells involved) are obtained by high-pass filtering the extracellular recordings, or by placing the microelectrodes within (or close to) the cell membrane. LFP, SUA, and MUA are rarely recorded in humans due to the required invasiveness.

Due to the particular geometry and hierarchical organisation of neuronal ensembles in some brain structures (e.g.: cortical pyramidal cells arranged parallel to each other, with apical dendrites on one side and soma on the other), PSP can sum into an effective current source. Due to the head tissue conductor properties, this current source can be large enough to be remotely recorded (Niedermeyer and Lopes da Silva, 1999). Scalp EEG primarily reflects the slow EPSP and IPSP of cortical populations (Creutzfeldt et al., 1966a, 1966b; Klee et al., 1965), with some contribution from mechanisms not directly coupled to synaptic activity (e.g.: voltage-dependent membrane oscillations and spike after-potentials) (Buzsaki and Chrobak, 1995; Creutzfeldt et al., 1966a, 1966b; Kandel and Buzsaki, 1997; Kocsis et al., 1999). IcEEG can be recorded in humans with severe drug-resist epilepsy undergoing a clinical pre-surgical evaluation for the curative resective surgery, using macroelectrode arrays (grids or strips) placed over the cortical surface (ECoG), or within the brain (depth EEG; or stereotactic EEG: SEEG). Despite being described as LFP measurements occasionally (Baumgartner et al., 2011; Conner et al., 2011), icEEG[2] measurements represent significantly larger integration volumes than those recorded with microelectrodes (Fermaglich, 1982). As consequence of the uncertainty in the location of the epileptic activity generators, icEEG electrodes are often placed over regions that turn out to be apparently free of pathology, which provides an opportunity to study normal brain activity (Conner et al., 2011; Hermes et al., 2012; Khursheed et al., 2011). Clinical icEEG electrodes combined with microelectrodes are not yet in common use, but are a promising research tool (Fried et al., 1999; Hochberg et al., 2006; Schevon et al., 2012; Waziri et al., 2009).

.

[2] The term “icEEG” is used when the statement refers to either “ECoG”, “depth EEG” or “SEEG”.

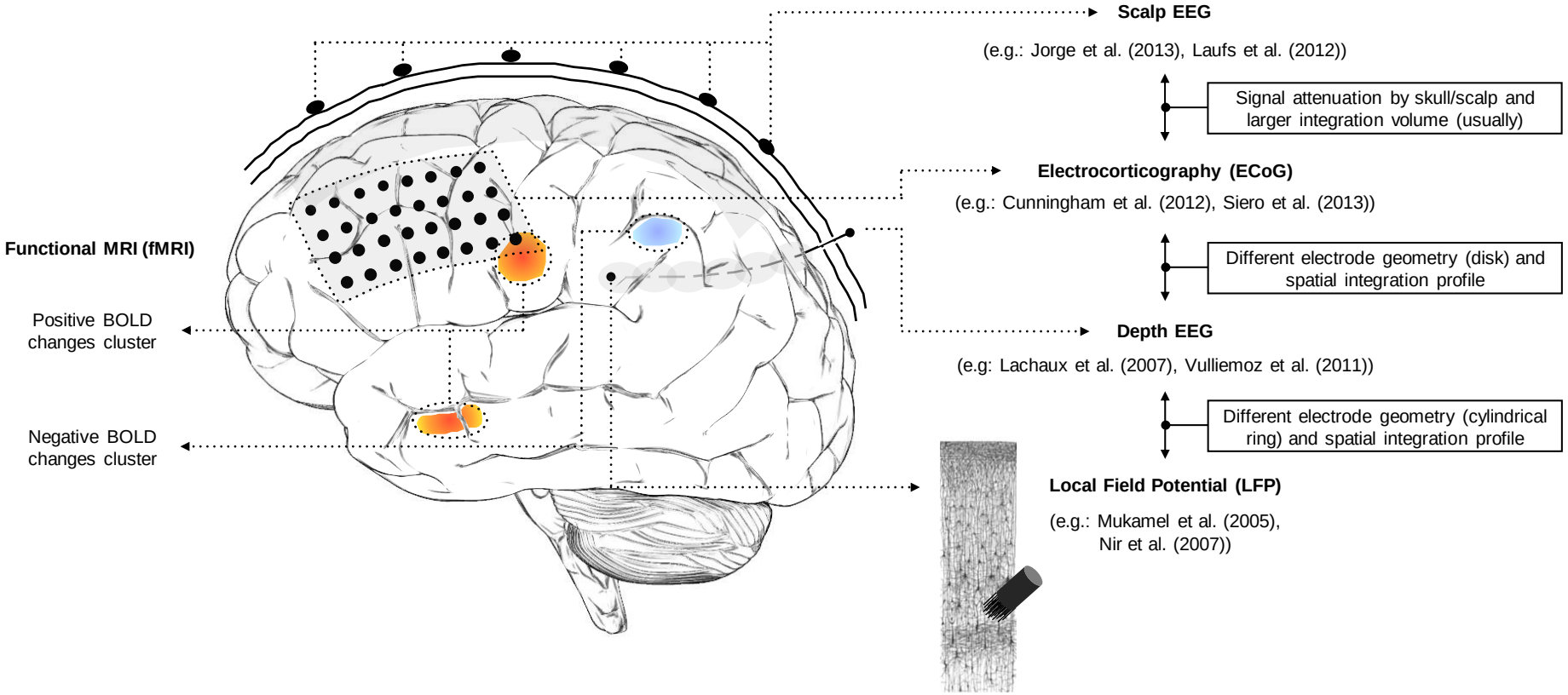

Figure 2-1 Brain signals at multiple scales: from thousands of neurons to whole-brain. Illustration of recording of scalp EEG, ECoG, depth EEG and LFP signals, and three hypothetical BOLD-fMRI clusters, in different lobes. The spatial sensitivity profiles of the four electrophysiological techniques are sketched in shaded grey: mainly neocortical for scalp EEG and ECoG, local to each electrode pair for depth EEG (~1cm^3), and local to each microelectrode for LFP (~100µm^3). LFP recording is illustrated using a drawing from (Ramón y Cajal, 1899).

The geometry and size of electrodes determines the sensitivity profile of each type of recording. In general, icEEG has greater regional sensitivity and specificity than scalp EEG (approximately 1cm^3 for depth EEG) (Church et al., 1985). In case of deep generators, scalp EEG and ECoG are more affected by volume-related averaging effects than depth EEG. Both ECoG and depth EEG have limited spatial sampling because there is a limited number of electrodes that can be used, due to the risks associated with the implantation procedure (Engel, 2013). Despite the high regional specificity, LFP, depth EEG, and ECoG recordings consist of “mean field signals” that result from the collective behaviour of aggregates of neurons; therefore, there is always some ambiguity on the nature of their origin (Buzsaki et al., 2012).

At a larger scale, a particular distribution of electrical potentials recorded on the scalp can be explained by the activity of infinite different configurations of intracranial current sources (Fender, 1987). These current sources are not simple point-like charge accumulations; they have dipolar configurations (Bishop, 1949; Brazier, 1949), which are not simple dipoles, but dipole layers that are convoluted (Bishop, 1949; Gloor, 1985; Vaughn, 1974, 1969). The particular geometry and orientation of these current sources with regard to the electrode contacts are crucial determinants of the potential distribution within the brain or at the scalp (Gloor, 1985; Vaughn, 1974, 1969). Reconstructing the current sources originating the scalp EEG measurements, i.e., solving the scalp EEG inverse problem, is a well-known ill-posed problem with no unique solution. Solving it requires prior assumptions on the number, geometry, and/or location of the current sources, thereby introducing a fundamental uncertainty on the origin of the measured signals (Ferree et al., 2001). Different inverse models are based on different *a* priori assumptions (for a review see Michel et al. (2004)), and can be categorised as: overdetermined (dipolar) models (e.g.: (Gulrajani et al., 1984; Homma et al., 1990; Kavanagh et al., 1978; Scherg and Von Cramon, 1986; Stok, 1987)), based on the assumption that a small and known number of current sources can adequately model the measurements at the surface; or underdetermined (distributed) source models (e.g.: Pascual-Marqui et al. (1994); Grave de Peralta Menendez et al. (2001)), which reconstruct the brain electric activity in each point of a 3D grid of solution points and do not need an a priori assumption on the number of current sources.

2.1.1.2 Commonly observed electrophysiological activity

FMRI has been used to locate brain regions generating different electrophysiological phenomena, which are briefly explained in the following subsections.

- **Epileptiform activity**

The electrophysiological signal of patients with epilepsy often encompasses characteristic activity during seizures, also called ictal events, and between seizures, the so-called interictal epileptiform discharges (IED).

In focal epilepsies, the electrophysiological signal at the seizure onset often consists of fast and low-amplitude activity that may spread and become slower and higher in amplitude, and which reflects excessive and hyper-synchronous neuronal activity (Blume et al., 2001). Nevertheless,

the power-frequency profile of scalp EEG recordings during seizures is highly variable across patients.

IED are high-amplitude fast EEG transients that can last less than 70 milliseconds, and be called interictal spikes, or between 70 and 120 milliseconds, and be called sharp waves. Both spikes and sharp waves are often followed by a slow wave that can last several hundred of milliseconds (De Curtis and Avanzini, 2001). Interictal spikes tend to occur periodically (Chatrian et al., 1964) and often in brief paroxysms, which either remain localised in space or establish a secondary propagation to other parts of the cortex. Interictal spikes reflect the synchronous and excessive discharge of a cortical neuronal ensemble and are associated with a burst discharge, which is characterised by a rapid sequence of fast action potentials at 200 - 500 Hz, superimposed on a slow depolarising potential (De Curtis and Avanzini, 2001).

- **Rhythmic and arrhythmic activity**

The power spectrum of LFP, icEEG, and scalp EEG signals follows a power law distribution, i.e., it can be broadly represented by a straight line on a logarithmic scale ($\mathrm{P}(\log(\mathrm{f})) \propto \mathrm{f}^{-\mathrm{c}}$, usually with $0 < \mathrm{c} < 4$), which characterises the brain arrhythmic activity. Under specific conditions, peaks superimposed to this straight line are observed at particular frequencies. These peaks characterise the brain rhythmic or oscillatory activity (Bullock et al., 2003; Buzsaki and Draguhn, 2004; He et al., 2010).

The brain rhythmic activity, commonly categorised as δ (0.5 – 4 Hz), θ (4 – 8 Hz), α (8 – 12 Hz), β (12 – 30 Hz), and γ (> 30 Hz) (Lopes da Silva, 2011), seems to be an important element linking neuronal activity and behaviour (Engel et al., 2001; Hasselmo et al., 2002; Somers and Kopell, 1993; Steriade, 2001; Traub et al., 1999; Whittington and Traub, 2003). Despite differences in brain's sizes of several orders of magnitude, its temporal characteristics are phylogenetically preserved in the mammalian brain. Such preservation throughout evolution has been suggested as evidence that brain rhythmic activity has a specific functional role (see Buzsaki et al. (2013) for further details).

The terms rhythm and oscillation are sometimes applied incorrectly to electrophysiological signals. An increase of the electrophysiological activity within a particular frequency band does not imply the presence of a true rhythm (oscillation) (Lopes da Silva, 2013). Rather, a relatively narrow peak, within the frequency band of interest, must be identifiable in the power spectrum. The rhythm is defined by the central frequency, bandwidth, and power of this peak. To investigate whether a certain peak denotes a rhythm, we can use a period specific average approach, as proposed by Bullock et al. (2003), for example. According to these authors, a rhythm is defined by a narrow peak with frequency modulation of <5 % of the centre frequency, a strength of 2.5 to 10 times the expectation from chance of the background noise, and showing a fine structure by being local and brief (on the order of 10 cycles).

Brain rhythmic activity arises from competition (via inhibition) and cooperation (via excitation) within local micro-networks (between individual, or small groups of neurons), or within broad macro-networks (between large ensembles of neurons) that can exhibit different synchronisation

states, which result in oscillations at different frequencies (Pfurtscheller and Lopes da Silva, 1999; Riera et al., 2006). The synchronisation of these neuronal networks seems to enable the brain to functionally integrate computations at multiple spatial and temporal scales (Bushara et al., 2003; Buzsaki et al., 2003). Lower frequencies (8 – 12 Hz) are often associated with the recruitment of neurons from larger cortical areas, while higher frequencies (> 12 Hz) are often spatially more restricted and with a functional organisation that resembles a mosaic of cortical neuronal assemblies exhibiting relatively synchronous oscillations at multiple dominant frequencies (Pfurtscheller and Lopes da Silva, 1999).

Although the brain arrhythmic activity constitutes a significant part of electrophysiological signals, less is known about it when compared to the rhythmic activity (Bullock et al., 2003, 1995; Freeman and Zhai, 2009). Interestingly, it has been suggested that synchronisation between neuronal ensembles may be reached not only in a rhythmic mode but also in an arrhythmic one (Eckhorn, 1994; Thivierge and Cisek, 2008).

- **Event-related activity**

A cognitive, sensory, or motor stimulus can generate a time- and phase- locked event-related potential (ERP), or a time- but not phase- locked alteration of the ongoing activity (Pfurtscheller and Lopes da Silva, 1999). An ERP can be seen as a series of transient post-synaptic responses of principal pyramidal neurons, triggered by a specific stimulus (Lopes da Silva, 1991). Assuming that the evoked activity has a fixed time delay to the stimulus, and treating the ongoing activity as additive noise, ERP are typically extracted by averaging across trials. However, inter-trial variability is emerging as an important aspect when studying brain function (Debener et al., 2005; Sadaghiani and Kleinschmidt, 2013). For example, Fox et al. (2006) and Becker et al. (2011) found that a significant fraction of the variability of the event-related BOLD responses across trials was explained by fluctuations in the ongoing task-unrelated activity. Event-related changes in the ongoing electrophysiological signal power, within particular frequency bands, and in relation to a baseline, can only be identified by a time-frequency decomposition of individual responses. A decrease (or increase) in the synchrony of the underlying neuronal populations due to the stimulus presentation may lead to a decrease (or increase) in the ongoing power for a particular frequency band; these phenomena are called event-related desynchronisation (ERD) (or event-related synchronisation (ERS)) (Pfurtscheller and Lopes da Silva, 1999), respectively. ERD/ERS can be seen as reflections of changes in one or more parameters that regulate neuronal networks oscillations (Lopes da Silva, 1991).

2.1.2 Functional MRI: the BOLD signal

Functional MRI (fMRI) comprises a number of MRI techniques capable of mapping changes in signal intensity related to changes in brain activity. For cognitive and clinical fMRI studies at the conventional field strengths (1.5 and 3 T), the BOLD effect, usually recorded with gradient-echo EPI scanning sequences, is the most used contrast mechanism.

2.1.2.1 The origin of the BOLD signal

In the current standard model of the BOLD effect, an increase in neuronal activity induces a regional increase in cerebral blood flow (CBF), auto-regulated by local mechanisms, which ultimately provides more oxygen and glucose to the tissues. If the CBF increase is enough to compensate the concurrent cerebral metabolic rate of oxygen ($CMRO_2$) increase (Fox and Raichle, 1986; Fox et al., 1988), the local concentration of deoxyhaemoglobin declines and the BOLD signal intensity increases (Kwong et al., 1992; Ogawa et al., 1990). Accompanying the increase in CBF, there is an increase in the cerebral blood volume (CBV), which was characterised by Grubb et al. (1974) as $cCBV(cCBF) = cCBF^{\alpha}$, where cCBV and cCBF are the CBV and CBF normalised to their baseline values, and $\alpha<1$. This relationship also appears in the current standard model of the BOLD effect, usually with the assumption that the fractional change in the venous CBV corresponds to the fractional change in the total CBV because most of the deoxyhaemoglobin is comprised within the venules and veins (Buxton, 2012). However, the BOLD effect is also dependent on volume exchange effects that are not directly related to changes in the level of blood oxygenation (e.g.: arterial CBV changes that displace extravascular tissue). These effects grow with the field strength (Buxton, 2012; Uludag et al., 2009).

Therefore, the BOLD effect is a complex function of changes in CBF, $CMRO_2$, and CBV. An important effort has been to disentangle how changes in CBF, believed to be the primary source of the BOLD effect, relate to changes in $CMRO_2$. It is currently accepted that there are a “hemodynamic response” and a “metabolic response”; two independent features driven in parallel, possibly by different aspects of the neuronal activity (Buxton, 2012). On the one hand, $CMRO_2$ increases during the recovery from neuronal signalling (information transfer from the external environment to neurons, and vice-versa). For example, $CMRO_2$ increases to meet the metabolic demand created by the restoration of ion gradients and to recycle neurotransmitters (Attwell and Laughlin, 2001; Buxton, 2012). $CMRO_2$ can reflect the overall energy cost of neuronal activity. On the other hand, there is good evidence that CBF increases may not be initiated by signals reflecting an energy deficit, but instead be driven by fast glutamate-mediated signalling processes locally, or by amine- and acetylcholine- mediated neural systems more globally (Attwell and Iadecola, 2002). CBF seems therefore to be driven in a feed-forward way by aspects of neuronal signalling (Uludag et al., 2004). This mechanism is likely to be mediated by astrocytes, acting as intermediaries between neuronal activity and blood flow, pericytes and neuronal signalling molecules (e.g.: nitric oxide), that act on the blood vessel diameter (Andreone et al., 2015; Attwell and Iadecola, 2002; Buxton, 2012; Hamel, 2006; Iadecola and Nedergaard, 2007; Koehler et al., 2009). A more detailed and complete understanding of which neuronal activity aspects strongly modulate the vascular (CBF, CBV) and metabolic ($CMRO_2$) responses (i.e. of the neurovascular coupling mechanisms) will help to better describe the complex mechanisms that relate the neuronal activity with the BOLD signal; see Attwell et al. (2010); Cauli (2004); Devor et al. (2007); Lauritzen (2005); Riera and Sumiyoshi (2010).

2.1.2.2 Neurovascular coupling mechanisms in the diseased brain

Disease may affect the neurovascular coupling mechanisms, with potentially important implications for the sensitivity and interpretation of EEG-informed fMRI studies. It has been shown that the occurrence of seizures may lead to the deterioration of the cerebral glycolytic metabolic state (Folbergrova et al., 1981); and that normal physiological CBF changes may be insufficient to satisfy the metabolic demand expected during ictal and interictal discharges (Schwartz, 2007). Moreover, some mediators of these mechanisms are known to be involved in epileptogenesis (Salek-Haddadi et al., 2003). For example, extracellular K+ rises significantly following ictal and interictal bursting (Jensen and Yaari, 1997), and has an effect on CBF fluctuations (Dreier et al., 1995) and arteriolar diameter (Kuschinsky et al., 1972); astrocytes are an important mediator in the genesis of epileptic activity (Grisar et al., 1999), as well as in the neurovascular coupling mechanisms (Ekstrom, 2010).

2.2 Electrophysiological correlates of the BOLD signal

In this section, we describe the methods and principal findings of EEG-informed fMRI studies using the temporal dynamics of a number of EEG-derived features to predict the BOLD response and thereby improves its neurophysiological interpretation. EEG-informed fMRI studies are asymmetric data integration approaches, often also called EEG-correlated fMRI or simply EEG-fMRI. The studies reviewed here are divided into those using fMRI to map BOLD changes associated with particular electrophysiological phenomena ("EEG-fMRI mapping"), in §2.2.1, and those aiming to characterise the local relationship between the electrophysiological and BOLD signals ("local EEG-fMRI coupling"), through systematic comparisons of EEG-derived metrics with BOLD fluctuations, in § 2.2.2. The studies described in § 2.2.1 are grouped according to the type of activity: epileptic; non-epileptic spontaneous activity; and cognitive, sensory and motor functions; and those described in § 2.2.2 are grouped according to the spatial scale of the electrophysiological recordings: neuronal spiking activity and LFP; and icEEG. Most of the studies reviewed here were based on simultaneously acquired data.

2.2.1 Mapping BOLD changes related to electrophysiological activity

An EEG-derived BOLD predictor is usually computed as the convolution of a mathematical representation of an electrophysiological phenomenon of interest with a haemodynamic kernel, often the canonical haemodynamic response function (HRF) (Logothetis, 2003) (**Figure 2-2**).

It is also common to use a General Linear Model (GLM) to relate the two signals (Worsley and Friston, 1995). In this case, statistical inferences on the estimated GLM parameters are made to find the voxels at which BOLD changes are significantly correlated with the EEG-derived BOLD predictor (**Figure 1-1**). The EEG phenomena can be categorised as either isolated events with variable morphologies (e.g.: epileptic spikes or sharp waves, epileptic seizures, ERP amplitude and/or latency, EEG band power change time-locked to a stimulus or task); or continuously variable (e.g.: spontaneous fluctuations in the power of the α band during awake rest, or task performance related fluctuations in the power of the γ range).

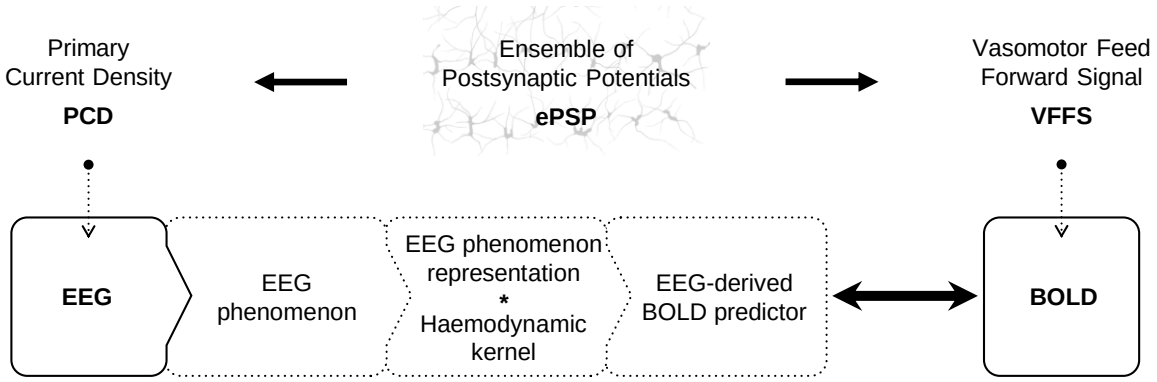

Figure 2-2 General EEG-informed fMRI integration scheme, highlighting the mechanisms underlying each signal. In a given voxel, the neuronal activity generates an ensemble of postsynaptic potentials (ePSP). The temporarily and spatially synchronised summated PSP produce the primary current sources (PCD). The head volume conductor properties transform the PCD into EEG. The ePSP generates a vasomotor feed forward signal (VFFS), via its own forward model, which is in turn transformed, via the haemodynamic forward model, into the observed BOLD signal. ePSP, PCD, VFFS, EEG, and BOLD are time-dependent. The EEG is considered to have the same time evolution as the PCD, which is considered to be a driver for the BOLD signal. This is an asymmetrical EEG and fMRI data integration approach because the EEG temporal dynamics are taken as surrogates for the VFFS. Diagram adapted from Valdes-Sosa et al. (2009).

The studies reviewed here are grouped according to the type of brain activity being addressed: epileptic activity, in § 2.2.1.1; non-epileptic spontaneous activity, in § 2.2.1.2 ; and cognitive, sensory and motor functions, in § 2.2.1.3.

2.2.1.1 Epileptic activity

EEG-informed fMRI was first implemented in the field of epilepsy (Ives et al., 1993) due to the clinical interest in spatially mapping the generators of IED. In this context, the simultaneity of data acquisition is necessary[3] because IED are unpredictable and can only be identified or characterised on the EEG recording (Ives et al., 1993). FMRI held promise to bypass the limitations imposed by the EEG inverse problem, particularly challenging for deep and extensive epileptic activity generators (Chaudhary et al., 2012a; Jacobs et al., 2008; Salek-Haddadi et al., 2006; R. Thornton et al., 2010; Thornton et al., 2011; Zijlmans et al., 2007).

Most EEG-informed fMRI studies in epilepsy start with the identification of the clinically relevant events on the EEG signal, either visually, by an electroencephalographer (An et al., 2013; Flanagan et al., 2014; Moeller et al., 2013; Pittau et al., 2013), or using an automated signal analysis technique (Formaggio et al., 2011; Liston et al., 2006; Marques et al., 2009). Investigations of BOLD fluctuations related to ictal activity (Chaudhary et al., 2012a; LeVan et al., 2010b; Murta et al., 2012; Thornton et al., 2010; Tyvaert et al., 2009; Vaudano et al., 2012) are fewer than those related to interictal activity, mainly due to methodological and practical concerns (e.g.: patient safety, relative paucity of events, seizure-related motion) (Chaudhary et

[3] In contrast to fMRI of epileptic seizures, which can, in some patients, be performed without simultaneous EEG, if one uses pre-seizure clinical manifestations to inform the fMRI model.

al., 2013). Ictal and interictal activities are probably generated by different neuronal populations, and different cellular and network mechanisms (De Curtis and Avanzini, 2001); therefore, their BOLD correlates may well have different neurophysiological meanings.

- **Mapping BOLD changes related to scalp EEG IED**

In the GLM framework, IED are commonly represented as (zero-duration, unitary) stick functions at the time of their maximum amplitude (Aghakhani et al., 2015; Pittau et al., 2013; R. Thornton et al., 2010), or at a series of regularly spaced intervals on either side of the IED peaking time (Bagshaw et al., 2005; Jacobs et al., 2009), the latter allowing for some variation in the haemodynamic latency. IED with different electro-clinical characteristics have been modelled as distinct effects, reflecting the modelling assumption of distinct sources (Jacobs et al., 2009; Vulliemoz et al., 2010). More complex representations have also been investigated (Formaggio et al., 2011; Leite et al., 2013; Vulliemoz et al., 2010). For example, Vulliemoz et al. (2010) used EEG Source Imaging (ESI) to locate and estimate the current density time course of different IED sources. After convolving these time courses with the canonical HRF, which resulted in different continuous ESI (cESI) regressors, and estimating a whole brain GLM where these regressors were the effects of interest, they found that cESI regressors explained BOLD variance in addition the standard IED regressors (stick functions), in clinically expected regions. In another example, Formaggio et al. (2011), used an independent component analysis (ICA) on EEG data to find potential IED generators, which were back-projected to the EEG contacts space to obtain the IED-related EEG signals (IED-EEG). The EEG contact exhibiting the highest correlation with the IED-EEG time course was selected, and its maximum power values within 3.7 seconds epochs were used to define the IED-representative regressor, which revealed BOLD changes in clinically expected regions.

- **Mapping BOLD changes related to scalp EEG seizures**

In the GLM framework, ictal events are often represented as (unitary) boxcar functions with the duration of the clinical event (Iannetti et al., 2002; Marrosu et al., 2009; Morocz et al., 2003; Salek-Haddadi et al., 2009, 2002; Tyvaert et al., 2008). Arguing that such an approach does not account for ictal dynamics (Niedermeyer and Lopes da Silva, 1999), more complex models have been proposed (Donaire et al., 2009; Thornton et al., 2010; Tyvaert et al., 2009). For example, Donaire et al. (2009) divided the pre-ictal, ictal, and post-ictal periods into a sequence of 10 seconds boxcar functions; Tyvaert et al. (2009) used sequential full-width at half-maximum (FWHM) 2 seconds γ functions peaking around the ictal EEG onset as regressors of interest, in independent GLM; and Thornton et al. (2010b) partitioned each seizure into up to three phases - early ictal (first EEG changes), clinical onset, and late ictal (onset of high amplitude low frequency), and used a boxcar function to represent each phase, in a unique GLM. The three groups found a good agreement between the location of the earliest positive BOLD changes and the clinically inferred seizure onset zone (SOZ; defined by icEEG), which is not surprising because the ictal activity is likely to start at the SOZ. A different example, Leite et al. (2013), compared a number of EEG-derived metrics representing different electro-haemodynamic coupling functions (previously applied in the context of a visual task (Rosa et al. (2010)),

associated with interictal and ictal activity, in a patient with a hypothalamic hamartoma. The group found that the frequency-weighted metrics yielded to a higher number of voxels exhibiting statistically significant BOLD changes, when compared to power-weighted metrics or to the standard boxcar function, in agreement with the heuristic proposed by Kilner et al. (2005).

In summary, different representations of interictal and ictal activities have been related to BOLD changes in regions known to be involved in the origin or propagation of epileptic activity. More sophisticated representations have led to better results (Leite et al., 2013; Vulliemoz et al., 2010), but no study has convincingly identified an optimal approach. In part, this can be related with the way in which the success of these studies is appraised. The “gold standard” to locate the origin of epileptic activity is the visual inspection of scalp EEG and icEEG recordings, which has limitations. For instance, electro-clinical information derived from scalp EEG has limited sensitivity, and that derived from icEEG has limited spatial sampling. Comparing the BOLD maps with the resected area after assessing the surgical outcome in terms of seizure reduction is therefore a promising approach (Thornton et al., 2010; van Houdt et al., 2013). Nonetheless, it has two limitations: seizure disruption or cessation may result from disruption of only part of the seizure generation network, which makes the assessment of spatial concordance complex; and the patterns revealed by fMRI may represent a combination of both the source and propagation regions. Distinguishing the latter has been attempted using Diffusion Tensor Imaging DTI (Hamandi et al., 2008), ESI (Vulliemoz et al., 2010), and Dynamic Causal Modelling (DCM) (Murta et al., 2012), for example, with some success. Further work in this area is crucial for the clinical interpretability of BOLD maps in epilepsy.

- **Mapping BOLD changes related to intracranial EEG IED**

Vulliemoz et al. (2011), Cunningham et al. (2012), and more recently Aghakhani et al. (2015), mapped IED-related BOLD changes using simultaneously recorded icEEG and fMRI data; these studies found IED-related BOLD changes in regions not only close to but also remote from the most active icEEG contacts (likely to be in the immediate vicinity of the epileptic activity generators). Vulliemoz et al. (2011) investigated two patients whose scalp EEG-fMRI recordings (performed prior to the icEEG implantation) did not show IED. In one case, regions that could not be sampled by icEEG were found to exhibit significant IED-related BOLD changes, in agreement with previous MEG investigations. In this case, the persistence of seizures after the resective surgery suggested that these regions were likely to have key roles within the epileptic network. Cunningham et al. (2012), who investigated two patients, found IED-related BOLD changes at locations in broad agreement with non-invasive findings; in one patient, some remote BOLD clusters matched regions of hyper-perfusion revealed by ictal SPECT. Aghakhani et al. (2015) reported high spatial concordance between IED-related BOLD changes and the most active icEEG contacts in the mesial temporal region (6/7 patients). These three studies showed that simultaneous icEEG-fMRI data acquisitions at 1.5 T and 3 T are feasible in humans, under certain conditions, offering not only the measurement of BOLD responses over the whole brain but also the unsurpassed regional specificity and sensitivity of icEEG.

2.2.1.2 Non-epileptic spontaneous activity

Selecting one or some meaningful electrophysiological phenomena is the first challenge of an EEG-informed fMRI study (**Figure 2-2**). Most EEG-informed fMRI studies regarding non-epileptic forms of spontaneous activity investigated the spatial distribution of positive and negative correlations between the amplitude of the BOLD signal and the power of one or more EEG frequency bands (Laufs et al., 2003a; Martinez-Montes et al., 2004).

Visual inspection, contact position, or blind signal separation algorithms, are examples of strategies that have been used to isolate potentially interesting electrophysiological phenomena. For example, Goldman et al. (2002), who were particularly interested on the posterior dominant α rhythm (in contrast to other rhythms in the same frequency range), computed the α rhythm power time course by averaging the time courses of the occipital contact pairs. Instead of using visual inspection and/or contact location criteria, Makeig et al. 2002 used a spatial ICA to un-mix the EEG recordings into statistically independent components (IC), assuming that EEG recordings represent a linear mixture of neuronal activities originated from independent sources. Scheeringa et al. (2008), who were particularly interested in the frontal θ rhythm, performed a temporal ICA on band-pass filtered (2 - 9 Hz) scalp EEG data and selected the IC that showed a mid-frontal mixing-weights topography to compute the time course of the θ rhythm power.

- **Mapping BOLD changes related to the occipital EEG spectral content in the α range**

From the early days of EEG-informed fMRI, there has been a considerable interest to locate the regions exhibiting statistically significant correlations between the occipital ongoing scalp EEG α power changes and the BOLD signal amplitude (De Munck et al., 2007; Difrancesco et al., 2008; Goldman et al., 2002; Goncalves et al., 2006; Laufs et al., 2003a, 2003b; Moosmann et al., 2003). Negative correlations were found in the occipital (De Munck et al., 2007; Difrancesco et al., 2008; Goldman et al., 2002; Goncalves et al., 2006; Moosmann et al., 2003), temporal (Goldman et al., 2002), parietal (De Munck et al., 2009; Goncalves et al., 2006; Laufs et al., 2003a, 2003b), and frontal (Goldman et al., 2002; Goncalves et al., 2006; Laufs et al., 2003a, 2003b) cortices. Positive, locally restricted correlations were found in the thalamus (De Munck et al., 2007; Difrancesco et al., 2008; Goldman et al., 2002; Goncalves et al., 2006). These correlation patterns were found to be more significant when only occipital contacts were selected (De Munck et al., 2009; Goncalves et al., 2006; Laufs et al., 2003a). Using a less conventional method (multi-way Partial Least-Squares analysis), Martinez-Montes et al. (2004) decompose both EEG (independent variable) and fMRI data (dependent variable) uniquely, as a sum of "atoms". In this method, each EEG “atom” is the outer product of spatial, spectral, and temporal signatures, and each fMRI “atom” is the product of spatial and temporal signatures. While Martinez-Montes et al. (2004) found positive, locally restricted correlations in thalamus, Laufs et al. (2003a, b) did not. Moosmann et al. (2003) argued that these correlations could be of artificial origin due to cardiac pulse effects in the nearby ventricles. If not spurious, these correlations may be related with the findings of previous invasive studies in animals; the thalamus has a key

role in the generation and modulation of the cortical α rhythm, and its activity is importantly connected with the neocortical rhythmic activity (Lopes da Silva et al., 1973).

More recently, Jann et al. (2009) investigated the relationship between the α rhythm global field synchronisation (GFS) (a measure of the zero-phase lag synchronisation between electrode contacts) (Koenig et al., 2005, 2001) and the amplitude of BOLD changes at rest, with closed eyes. For the lower α (8.5 - 10.5 Hz) GFS, the group found positive correlations in the anterior and posterior cingulate cortices, and in the orbitofrontal and parieto-temporal regions; and negative correlations in the superior frontal gyrus, insula, supramarginal gyrus, and supplementary motor areas. Interestingly, the latter regions had been previously identified as a brain network, the Default Mode Network (DMN) (Raichle and Mintun, 2006; Raichle et al., 2001). The DMN function has been the subject of numerous investigations, the main finding being that its activity is greater at rest than during reduced consciousness or extroverted perception and action (Mazoyer et al., 2001). The DMN is an example of a Resting State Network (RSN). In general, RSN are synchronised fluctuating networks that involve cortical and subcortical areas, which can be obtained by spatial ICA of the resting state BOLD time courses across the whole brain (Beckmann and Smith, 2004). These independent varying patterns of BOLD signal coherence arise from the resting brain, involve cortical areas, and show similar spatial configurations to the functional-anatomical networks usually recruited by particular cognitive processes. Therefore, the RSN may represent the “default state” of the functional-anatomical networks (De Luca et al., 2006). Jann et al. (2009) also found a positive correlation between the upper α (10.5 - 12.5 Hz) GFS and the amplitude of BOLD changes in the Dorsal Attention Network RSN (posterior portion of the cingulate gyrus, bilateral dorsolateral prefrontal cortex, and areas in the parietal lobe).

- **Mapping BOLD changes related to the EEG spectral content in the δ, θ, α, β, γ ranges**

Aiming to investigate a broader EEG frequency content, Laufs et al. (2003b) included power in the occipital θ (4 - 7 Hz), α, and β (17 - 23 Hz) bands, in a single GLM of BOLD changes; while no significant correlations were found for the θ band, positive correlations were found in the DMN (Raichle et al., 2001) for the β band. A few years later, Mantini et al. (2007) investigated the correlation between the amplitude of BOLD changes within six RSN and the δ, θ (4 - 8 Hz), α (8 - 13 Hz), β (13 - 30 Hz), and γ (30 - 50 Hz) band powers, averaged across the scalp; they found that each RSN was characterised by a specific combination of EEG frequency bands. More recently, De Munck et al. (2009) used EEG power fluctuations in the δ, θ, α, β, and γ bands as different regressors in a single GLM, and concluded that these regressors were correlated. Arguing that the brain does not generally display pure frequency components within distinct bands but rather a coalescence of different frequency components, Mantini et al. (2007) and De Munck et al. (2009) concluded that all frequency bands should be modelled, and their interactions must be accounted for, irrespectively of the band of interest.

In summary, the occipital α band power was negatively correlated with widespread occipital, parietal, temporal, and frontal BOLD changes, and, perhaps, positively correlated with a further

remote (far from scalp contacts) brain region, the thalamus. Probably due to practical and historical reasons, the most explored EEG-derived feature has been the α band power. However, other EEG frequency ranges were found to be potentially as interesting as the α range. The importance of all frequency ranges is further discussed in § 2.2.2.

2.2.1.3 Cognitive, sensory and motor functions

We review here studies mapping BOLD changes related with multiple EEG phenomena, conspicuous during cognitive, sensory, or motor functions: ERP morphological characteristics, EEG synchronisation and phase coherence, and EEG power fluctuations within multiple frequency ranges.

- **Mapping BOLD changes related to ERP amplitude and latency**

Several studies using scalp EEG and fMRI data simultaneously acquired have investigated single-trial correlations between the amplitude and/or latency of ERP and the amplitude of the BOLD signal (Benar et al., 2007; Debener et al., 2005; Eichele et al., 2005; Fuglo et al., 2012; Mulert et al., 2008). For example, Mulert et al. (2008) investigated the spatial distribution of statistically significant correlations between fluctuations in the amplitude of the N1 potential (AofN1), measured during a forced choice reaction task, under low- and high- effort conditions, and the amplitude of the BOLD signal. By contrasting AofN1-related BOLD changes under high-effort and passive listening, the group found positive correlations in the anterior cingulate cortex. Mulert et al. (2008) showed that single-trial correlations could be particularly helpful to separate different aspects of the BOLD signal based on their specific correlation to different ERP features (e.g.: N1 potential fluctuations related to the high-effort condition).

- **Mapping BOLD changes related to EEG synchronisation and phase coherence**

Single-trial scalp EEG synchronisation and phase coherence have also been investigated as potential predictors of the BOLD signal amplitude (Kottlow et al., 2012; Mizuhara et al., 2005). For example, the first study analysing the BOLD correlates of common-phase signals during visual binding in humans, Kottlow et al. (2012), searched for γ (40 - 42 Hz) global field synchronisation (GFS) - related BOLD changes, during film viewing. The film consisted of face parts changing their positions, which, during some periods, rearranged themselves, yielding to a visually recognisable face (FACE). A unitary boxcar regressor (FACE) and a scaled boxcar regressor (modulated by the GFS values) (GFS-FACE) were convolved with a double-γ HRF. The GFS-FACE regressor was orthogonalised with respect to the FACE regressor, in order to be able to test for the presence of GFS-dependent modulations of the BOLD signal. The group found positive GFS-BOLD correlations in the bilateral middle fusiform gyrus and left precuneus, important regions for visual binding and face perception.

- **Mapping BOLD changes related to the EEG spectral content in the δ, θ, α, β, γ ranges**

The BOLD correlates of the power within the classical EEG frequency bands have also been investigated during tasks (Michels et al., 2010; Mulert et al., 2010; Scheeringa et al., 2011a, 2011b). For example, Michels et al. (2010) investigated the relationship between the amplitude

of the BOLD signal and the power of θ (5 - 7 Hz), α (low-α: 8 - 10 Hz; high-α:10 - 12 Hz), β (low-β: 13 - 20 Hz; high-β 20 - 30 Hz), and γ (30 - 40 Hz) bands, during the retention phase of a working memory task in humans. All frequency bands were included in a single GLM. The group found only positive correlations for high-β (20 - 30 Hz) in dorsolateral prefrontal cortex (DLPFC), and inferior frontal gyrus (IFG); and for γ in IFG, and medial prefrontal cortex (MPFC). The group also found only negative correlations for θ in MPFC, posterior parietal cortex (PPC), cingulate cortex (CC); and for high-α (10 - 12 Hz) in parieto-occipital regions. For low-α (8 - 10 Hz), and low-β (13 - 20 Hz), both positive and negative correlations were found, in diverse locations. They concluded that the power of both low and high frequency bands correlates with the amplitude of the BOLD signal, in diverse locations; and that these correlations tend to be negative for the lower frequencies (<7 Hz) and positive for the higher ones (>20 Hz). While investigating γ (40 Hz) amplitude – related BOLD changes during an auditory task, Mulert et al. (2010) found positive correlations in the auditory cortex, thalamus, and anterior cingulate cortex. Furthermore, Scheeringa et al. (2011a), who investigated the relationship between the power of multiple frequency ranges and the amplitude of occipital BOLD changes in healthy subjects performing a visual attention task, found positive single-trial correlations for the high-γ (60 - 80 Hz) range, and negative single-trial correlations for α (10 Hz) and β (18 - 28 Hz) ranges. Interestingly, Scheeringa et al. (2011b) compared the amplitude of the BOLD signal for visual stimuli given at the peak or trough of the α cycle, and found a stronger positive BOLD response for stimuli given at the peak, which suggests that the phase of the α rhythm at which the stimulus is given has an impact on the simultaneous BOLD response.

To this point, we reviewed studies mapping the BOLD correlates of multiple EEG-derived features, over the entire brain. Notwithstanding the relevance of these studies, one might be interested in the more general questions “Which aspects of the electrophysiological signal best correlate with the amplitude of the BOLD signal?”, “Are these aspects common across regions and brain states?”. Aiming to address the first question, at least, in part, Rosa et al. (2010) compared several heuristic EEG-derived metrics in the form of moments of the EEG spectrum (in the range 1 - 40 Hz) in terms of their individual capability to explain occipital BOLD fluctuations recorded in healthy subjects performing a visual task; they found that the amplitude of task-related BOLD changes was best explained by the root mean squared frequency function, proposed by Kilner et al. (2005), $q_{RMSF}(t) = \sqrt{\sum_{f_{min}}^{f_{max}} f^2 P(f,t)}$, which revealed more significant voxels and higher statistical significance levels.

In summary, the electro-haemodynamic coupling function during both non-epileptic spontaneous activity (§ 2.2.1.2) and cognitive, sensory, and motor functions is likely to be a complex combination of the power and frequency of the electrophysiological signal. The studies reviewed to this point are somewhat unsatisfactory due to the intrinsic limitations of scalp EEG, and the difficulty of defining what a better fit with the BOLD signal is. When using scalp EEG, it is hard to know the location of the neural activity specifically responsible for, or associated with, the EEG and BOLD signals. We return to the question “What aspects of the electrophysiological

signal best correlate with the amplitude of the co-localised BOLD signal?", in subsection § 2.2.2, where studies using invasive electrophysiological recordings are reviewed.

2.2.1.4 Improving the interpretation of scalp EEG-informed fMRI

In scalp EEG-informed fMRI studies, the uncertainty in the nature of the neuronal activity being mapped is a severe limitation for the physiological interpretation of the related BOLD changes. For example, it is often hard to know if the fMRI technique is mapping the primary generator of the EEG activity or if it is instead mapping brain regions whose activity is a systematic consequence of the primary generator's activity (e.g.: propagated epileptic activity[4]), which is time-locked and correlated to the first. In part, such uncertainty results from the fact that scalp EEG is mostly sensitive to neocortical activity, when compared to that of deep generators. Using simultaneous icEEG-fMRI data and having icEEG contacts covering not only the primary generator but also, at least part of, the propagation network, can help to distinguish the two types of activity. Moreover, using electrophysiological features that reflect well-known aspects of the underlying neuronal activity helps to physiologically interpret the related BOLD maps. Finding these more informative electrophysiological features can best be done using comparatively more local measures of electrophysiological activity (MUA, LFP, depth EEG, ECoG) and further investigating the co-localised BOLD changes.

2.2.2 Characterising the local relationship between the EEG and BOLD signals

In this subsection, we review studies aiming to identify the best electrophysiology-based predictors of the BOLD signal, helpful to further understand the neuronal origin of the latter. Most of these studies consist of defining alternative electrophysiology-derived quantities, and comparing the significance of their individual correlations with the amplitude of co-localised BOLD changes. The reviewed studies are grouped according to the spatial scale of the electrophysiological recordings: the ECoG-BOLD coupling in humans is discussed in § 2.2.2.1; and the depth EEG-, LFP-, and multiunit activity- BOLD coupling in both humans and non-humans is discussed in § 2.2.2.2.

2.2.2.1 ECoG-BOLD coupling in humans

To the best of our knowledge, no study has used icEEG and BOLD fMRI data simultaneously recorded in humans performing a task or at rest (non-epileptic spontaneous activity); therefore, here, we review studies using ECoG and fMRI data sequentially recorded in humans performing the same task. Most of these studies investigated the relationship between the power of the ECoG signal and the amplitude of the co-localised BOLD response. For example, Khursheed et al. (2011) used ECoG and fMRI data sequentially recorded in subjects performing the same working memory task to compare the mean ECoG power standardised difference spectra

[4] The possibility of the converse of propagation (or downstream) effects, namely preparatory (or upstream) effects, is also acknowledged. For example, it is conceivable that changes in the pattern of activity in regions outside the generator itself are needed for the generator to reach the state required to generate a particular type of activity.

(between delay period and background; 50 periods average) between the electrode contacts close to, and far from, the task-related BOLD changes (Statistical Parametric Mapping (SPM) maps obtained with a boxcar-task regressor). The group found that the amplitude of BOLD changes was positively correlated with γ (30 - 200 Hz) band power and negatively correlated with θ (4 - 8 Hz) band power, during the working memory delay periods. Another example, Conner et al. (2011), investigated the correlation between ECoG and fMRI data sequentially recorded in subjects performing the same visually cued noun and verb generation task. The ECoG activity within each frequency band was linearly regressed with the BOLD changes mean t-value, found within regions located around each electrode contact. The group found positive correlations for γ (60 - 120 Hz) and negative correlations for β (13 - 30 Hz) bands, with γ and β activities independently explaining different components of the BOLD signal. While studying the spatial relationship between finger movement-induced BOLD amplitude and ECoG power changes, Hermes et al. (2012) found that increases in the power of γ (65 - 95 Hz) were co-localised with increases in the amplitude of BOLD changes, and that decreases in the power of the lower frequency bands (α (5 - 13 Hz), low-β (13 - 24 Hz), and high-β (24 - 30 Hz) subject-specific frequency bands) were co-localised with weaker increases in the amplitude of BOLD changes. The group also found that the lower frequency power changes did not significantly explain additional BOLD signal variance when compared to the γ power changes alone, in the primary sensorimotor areas, despite explaining most of the BOLD signal variance in the non-primary hand areas. Another example, Kunii et al. (2013), investigated the correlation between ECoG high-γ (60 - 120 Hz) power and BOLD fluctuations around electrode contacts exhibiting ECoG high-γ power increases due to a word interpretation task, and found that the amplitude of BOLD changes was strongly correlated with long-lasting high-γ power increases in frontal language areas, but weakly correlated with short-duration high-γ power increases in temporal language areas. While investigating how ECoG high-γ (65 - 95 Hz) power related to task-expected and measured BOLD changes in the sensorimotor cortex, during a motor task with increasing movement rates, Siero et al. (2013) found that although the task-derived linear models failed to predict the measured BOLD changes, the co-localised measured ECoG power and the amplitude of BOLD changes were highly correlated, and concluded that a large portion of the BOLD nonlinearity with respect to behaviour (movement rate) was well predicted by electrophysiological measurements. While arguing that ECoG responses in visual cortex can be separated into two visually driven components: a specific temporal response that follows each stimulus contrast reversal that is narrow-band, and an increase in the response variance that is broadband, Winawer et al. (2013) found that the BOLD response in the visual areas (V1, V2, and V3) was better predicted by ECoG broadband (30 - 100 Hz) changes than by the stimulus-locked ECoG narrowband changes, which suggests that the BOLD response reflects arrhythmic rather than rhythmic ECoG activity. According to the group, this finding does not imply that a stimulus-locked response does not have an effect on the BOLD response, nor that such effect is always immeasurable (it may be possible to isolate the BOLD response driven by the stimulus using adequate manipulation); nor that rhythmic narrowband electrophysiological changes not

locked to the stimulus (e.g.: β rhythm in the motor cortex, or α rhythm in the visual cortex) are poor predictors of the co-localised BOLD response.

2.2.2.2 Depth EEG-, LFP-, and multiunit activity- BOLD coupling

Due to the invasiveness of the electrophysiological recordings and related technical difficulties, most of the studies reviewed in this subsection were performed in animals; Mukamel et al. (2005) and Lachaux et al. (2007) are the exceptions. Mukamel et al. (2005) exposed two different groups of subjects to the same stimulus paradigm to be able to investigate the relationship between BOLD changes (acquired in heathy subjects) and MUA and LFP activities (recorded in patients with epilepsy). The group found equally good positive correlations between BOLD changes and LFP and spiking rate activities. While investigating the relationship between depth EEG and BOLD changes sequentially recorded in subjects performing the same semantic decision task, Lachaux et al. (2007) found a close spatial correspondence between the recording sites showing power increases in the γ range (>40 Hz) and the brain regions showing positive task-related BOLD changes. A few years earlier, Logothetis et al. (2001) had compared electrophysiological (recorded with microelectrodes) and BOLD data simultaneously recorded in the primary visual cortex of anaesthetised monkeys performing a visual task, and found a strong correlation between the amplitude of the BOLD signal and the co-localised LFP (10 - 130 Hz) activity, as well as a robust, but slightly weaker correlation between the amplitude of the BOLD signal and the co-localised MUA (300 – 3000 Hz) activity. Across recordings sites, LFP accounted for significantly larger amounts of BOLD variance (Logothetis and Wandell, 2004). Earlier studies in the rat cerebellum had suggested that regional increases in CBF could be strongly correlated with LFP, but also present in the absence of spiking activity (manipulated with drugs) (Mathiesen et al., 2000, 1998). While some studies suggested that BOLD changes did not dependent on the rate of neuronal spiking (Bartolo et al., 2011; Gsell et al., 2006; Hewson-Stoate et al., 2005; Huttunen et al., 2008; Kayser et al., 2004; Lippert et al., 2010; Martin et al., 2006; Masamoto et al., 2008; Niessing et al., 2005; Ureshi et al., 2004; Yen et al., 2011), others involving electrical stimulation of the forepaw in rats (Smith et al., 2002), or visual tasks in other animals (Kim et al., 2004; Nir et al., 2007), found that the amplitude of the BOLD signal depended on the co-localised rate of neuronal spiking. Recent studies suggested that the relationship between BOLD changes and MUA activity varies from site to site and stimulus and stimulus (Lippert et al., 2010; Maier et al., 2008). However, there is some agreement in the sense that the BOLD signal is primarily predicted by the LFP activity (Goense and Logothetis, 2008). Since the correlation between LFP and MUA seems to be dependent on the regional input, and on what neuronal circuit is being stimulated (Mitzdorf, 1985), the BOLD signal may actually reflect both LFP and MUA, depending on the conditions (Ekstrom, 2010).

Since different LFP frequency bands correlate with different behavioural states (Basar, 1980; Lindsley and Wicke, 1974; Steriade and Hobson, 1976), and seem to reflect activity of different neuronal processing pathways (Belitski et al., 2008), exploring the relationship between different LFP frequency bands and simultaneous BOLD changes may lead to a better understanding of the nature of the BOLD signal. Logothetis et al. (2001), Kayser et al. (2004), Niessing et al.

(2005), Nir et al. (2007), Goense and Logothetis (2008), Murayama et al. (2010), and Ojemann et al. (2010) found that local BOLD changes were positively correlated with the LFP power in the γ (>30 Hz) range. Whether the BOLD signal independently relates to each LFP frequency band or to a particular relationship across bands, needs to be further investigated (Kilner et al., 2005; Magri et al., 2012). While investigating the electro-hemodynamic coupling function in the early visual cortex of anesthetised monkeys during spontaneous activity (darkness, eyes closed, no direct visual stimulation), Magri et al. (2012) found that LFP power fluctuations in the α and β (18 - 30 Hz) ranges explained additional variance of the BOLD signal when compared to fluctuations in the γ (40 - 100 Hz) range. In particular, the group found that an increase in the α power was correlated with a decrease in the amplitude of the BOLD signal, while an increase in γ power was correlated with an increase in the amplitude of the BOLD signal, when no change in the total power was observed, in agreement with the heuristic proposed by Kilner et al. (2005).

2.3 EEG phase-amplitude coupling (PAC) and the BOLD signal

Electrophysiological activities in particular frequency ranges, characteristically associated with sensory, motor, and cognitive functions, have been observed since the discovery of scalp EEG (Engel et al., 2001; Jacobs and Kahana, 2010; Varela et al., 2001). These activities can be either broadband or narrowband (Hermes et al., 2015), in which case they can be rhythmic. Part of the studies relating fluctuations in the power of the EEG signal with sensory, motor, or cognitive functions did not evaluate the rhythmicity of the EEG activity (see “Rhythmic and arrhythmic activity” in § 2.1.1.2). Therefore, to be entirely correct, we use the expression “EEG activity in a particular frequency range”, rather than “EEG rhythmic activity”, to refer to EEG activity restricted to a particular frequency band, notwithstanding that many studies have been focused on truly rhythmic activity.

Both in studies mapping BOLD changes related to EEG activity (§ 2.2.1), or aiming to characterise the local relationship between the EEG and BOLD signals (§ 2.2.2), the power of the ongoing EEG activity has been used as a predictor of the amplitude of the BOLD signal extensively. It was found that fluctuations in the EEG power in different frequency ranges explain independent, as well as common, components of the variance of the amplitude of the BOLD signal (Magri et al., 2012; Scheeringa et al., 2011a); it is currently accepted that a combination of low (LF) and high frequency (HF) band powers explains the amplitude of the BOLD signal better than the HF band power alone. However, the amplitude of the BOLD signal has not been related to ongoing interactions between the phase and amplitude (or power) of these multiple EEG frequency bands.

In the following subsections, we review studies supporting the functional role of the phase of LF EEG activities and, in particular, of the coupling between the phase of LF and the amplitude of HF EEG activities, and discuss how they may be relevant for the study of the relationship between the EEG spectral content and the amplitude of the BOLD signal.

2.3.1 Functional relevance of EEG activities in different frequency ranges

EEG activities in different frequency ranges are often associated with different spatial scales (different cell population sizes) (Canolty and Knight, 2010; Ohl et al., 2001; VanRullen and Koch, 2003); in particular, the correlation between the neuronal activity at two different points in space is often larger for LF than for HF activities (Dickson et al., 2000), suggesting that LF modulate neuronal activity over larger spatial regions in longer temporal windows, while HF modulate neuronal activity over smaller spatial regions in shorter temporal windows (von Stein and Sarnthein, 2000). Interestingly, these electrophysiological activities of different frequency ranges appear to hierarchically interact with each other, as the "basic units" of a complex system that regulates the processing of information in the brain, across multiple spatial and temporal scales (Buzsaki et al., 2012; Canolty and Knight, 2010; Hyafil et al., 2015; Lakatos et al., 2005; Palva et al., 2005; Roopun et al., 2008). Three types of cross-frequency interaction have been reported: (1) cross-frequency phase synchronisation or phase-phase coupling (Belluscio et al., 2012), (2) cross-frequency amplitude envelope correlation or amplitude-amplitude coupling (Tokariev et al., 2015), and (3) LF phase - HF amplitude coupling ($PAC_{LF\ HF}$). The latter has attracted a great interest due to the potential functional role of its strength (Axmacher et al., 2010; Buzsáki et al., 2012; Cohen et al., 2009a, 2009b; Kramer et al., 2008; Lakatos et al., 2008; Tort et al., 2009). For instance, Tort et al. (2008) found that the amplitude of multiple LFP γ (>30 Hz) components was dynamically modulated (in a task-dependent manner) by the phase of the simultaneous θ activity, both within and across the rats' hippocampus and striatum, and, particularly, during the decision-making epochs of an active navigation and decision-making task. The authors found that not only does PAC strength go from no coupling to strong coupling, and back within a few tenths of a second, but also that there are different patterns of coupling and temporal modulation within different brain structures. Later, the same group found that higher levels of $PAC_{\theta\gamma}$ were maintained throughout overtraining sessions of a task where rats learned to associate items with their spatial context, and that the $PAC_{\theta\gamma}$ strength increase associated with the learning process was strongly correlated with the performance improvement, in the CA3 region of the hippocampus (Tort et al. 2009). More recently, Dürschmid et al. (2014) used ECoG data from six patients (humans) that learn three different finger movement coordination tasks to investigate how the strength PAC relates to motor performance, and found that the $PAC_{\theta\gamma}$ (θ: 4 - 8 Hz, γ: 80 - 180 Hz) strength in the pre-motor and motor areas was positively correlated with performance level. These studies suggest that PAC reflects strong task- and/or state- related modulations, as well as behavioural and/or performance measures, suggesting that PAC has a functional role.

PAC has been observed in animals (Lakatos et al., 2005; Tort et al., 2009, 2008; van Wingerden et al., 2014; Wulff et al., 2009) and humans (Axmacher et al., 2010; He et al., 2010; Hermes et al., 2013; Miller et al., 2012; Sato et al., 2014; Voytek et al., 2010; Yanagisawa et al., 2012). Several studies have documented modulations of the amplitude of γ by the phase of β (de Hemptinne et al., 2013; Miller et al., 2012), sleep spindle (12 – 15 Hz) (Peyrache et al., 2011), α (Cohen et al., 2009a; Palva et al., 2005; Yanagisawa et al., 2012), θ (Canolty et al., 2006;

Colgin et al., 2009; Demiralp et al., 2007; Friese et al., 2013; Griesmayr et al., 2010; Mormann et al., 2005; Tort et al., 2008, 2010; Wulff et al., 2009), δ (Lakatos et al., 2005; Szczepanski et al., 2014), slow (<1.5 Hz) (Isomura et al., 2006), and ultraslow (<0.1 Hz) (Leopold et al., 2003) activities. Most studies have investigated PAC at a particular area (Axmacher et al., 2010; He et al., 2010; Hermes et al., 2013; Miller et al., 2012, 2010; Voytek et al., 2010; Yanagisawa et al., 2012), but there is also evidence for cross-areas PAC (Fitzgerald et al., 2013; Malekmohammadi et al., 2014; Maris et al., 2011; Sirota et al., 2008; Tort et al., 2008; van der Meij et al., 2012).

In humans, task-dependent fluctuations of PAC strength have been found in various cognitive frameworks, ranging from working memory load (Axmacher et al., 2010), episodic memory retrieval (Köster et al., 2014), visual motion discrimination (Händel and Haarmeier, 2009), visual search (Miller et al., 2010), visual-motor control (Soto and Jerbi, 2012), visual-target detection (Fiebelkorn et al., 2013), face processing (Sato et al., 2014), verb generation (Hermes et al., 2013), motor task execution (Miller et al., 2012; Yanagisawa et al., 2012), to motor task performance (Dürschmid et al., 2014). Eyes-closed, eyes-open resting condition dependent fluctuations of PAC strength have also been found. For example, Osipova et al. (2008) found stronger MEG $PAC_{\alpha\gamma}$ (α: 8 - 13 Hz, γ: 30 - 70 Hz) in the occipital areas during the eyes-closed period. Of particular relevance to us are the observations by Miller et al. (2012) and Yanagisawa et al. (2012) of movement preparation, execution, and inhibition - related $PAC_{\alpha\gamma}$ and $PAC_{\beta\gamma}$ strength fluctuations.

Several methods for PAC detection and quantification have been proposed (Canolty et al., 2006; Cohen, 2008; Lakatos et al., 2005; Özkurt and Schnitzler, 2011; Tort et al., 2008); however, there is no commonly accepted gold standard. Tort et al. (2010) evaluated the performance of seven empirical PAC detection and/or quantification methods, using both simulated and real data, and concluded that Canolty et al. (2006)'s and Tort et al. (2008)'s were the most suitable to quantify the strength of PAC. More recently, Özkurt and Schnitzler (2011) defined PAC analytically, rather than empirically, and proposed a new method to estimate its strength.

2.3.2 Improving the understanding of the EEG-BOLD signals relationship

Although it is currently accepted that the amplitude of local BOLD changes is better explained by a combination of the power of multiple LF and HF EEG activities, rather than by the power of HF alone, our understanding of the relationship between the two signals remains incomplete (Murta et al., 2015; Valdes-Sosa et al., 2009). Due to the important role that the phase of the LF activities and, in particular, the strength of PAC, seem to have in how information is processed in the brain, should we be ignoring them and focusing on the power of the EEG signal alone, when investigating the electro-hemodynamic coupling function? To the best of our knowledge, Miller et al. (2012) is the only study relating BOLD changes amplitude with PAC strength fluctuations. The group used ECoG and BOLD fMRI data sequentially recorded in two patients performing the same finger-tapping task to investigate the spatial overlap between finger-tapping related BOLD changes and ECoG power (ratio between power during movement and at rest) and PAC strength. The authors found that the spatial overlap between BOLD changes at the

pre- and post- central gyri and the ECoG measures was the greatest for the β band power; good for the γ broadband power (yet more spatially restricted than for the β band power), and the lowest for the PAC strength. However, they did not investigate the temporal correlation between the PAC strength and the BOLD signal amplitude.

2.4 EEG IED morphology and the BOLD signal

Interictal epileptiform discharges (IED) are high-amplitude, fast electrophysiological transients constituted by a spike or a sharp wave, often followed by a slow wave (De Curtis and Avanzini, 2001). For simplicity, the first part of the IED is here called sharp wave. Although commonly associated with an epileptic state, sharp waves have also been observed in the healthy hippocampus (Buzsáki et al., 1983; Skaggs et al., 2007; Suzuki and Smith, 1987); such universality makes them a potentially informative device for the study of neurophysiological correlates of the BOLD signal.

While several scalp EEG - informed fMRI studies investigated single-trial correlations between the amplitude and/or latency of ERP and the amplitude of the BOLD signal (see “Mapping BOLD changes related to ERP amplitude and latency” in § 2.2.1.3), only two studies in humans investigated how the amplitude of scalp EEG sharp waves is related with the amplitude of the BOLD fMRI signal (Benar et al., 2002; LeVan et al., 2010a), with mixed results. More recently, the relationship between the amplitude and duration of LFP sharp waves and the amplitude of changes in CBF, simultaneously recorded using laser-Doppler flowmetry, was investigated in rats (Geneslaw et al., 2011; Vanzetta et al., 2010); a positive correlation between the amplitude (and width (Geneslaw et al., 2011)) of sharp waves and CBF was found. Since the sharp wave morphology is thought to reflect interesting aspects of the underlying neuronal activity (e.g.: sharp wave amplitude and rising phase slope are thought to reflect the degree of neuronal synchrony (Einevoll et al., 2013); sharp wave width and energy (area under the curve) are thought to reflect the duration of the field potential, which, in turn, reflects the geometry are relative positions of the sources in relation to the recording sensors (Gold et al., 2006), the study of its relationship with the amplitude of simultaneous, co-localised BOLD changes is likely to help to further understand the local neurophysiological correlates of the haemodynamic signal.

2.5 Simultaneity of electrophysiological and BOLD fMRI acquisitions

As supported by most studies reviewed in § 2.2, the simultaneity of the acquisition of the two signals can be very informative when studying their relationship. Due to the nature of the phenomena of interest (ongoing EEG phase and amplitude fluctuations in multiple frequency ranges, event-by-event sharp wave morphological and field extent features), the simultaneity of the acquisition of the two signals was necessary for this work. However, this is not always the case. In this section, we discuss the necessity or preference for simultaneous acquisitions, rather than sequential, in § 2.5.1, and their technical difficulties and limitations, in § 2.5.2.

2.5.1 Necessity or preference for simultaneous acquisitions

If the events of interest are considered to be reproducible across sessions, single-modality recordings performed non-simultaneously (i.e. in different sessions) can be subsequently combined (e.g.: co-registered in space, compared in terms of signal features, etc.). However, simultaneous sessions are essential in the following situations: unique, unpredictable, or uncontrolled events (e.g.: epileptic activity, healthy wakeful resting); events that can only be identified or characterised on one of the modalities; individual event parameterisation (e.g.: epileptic activity); and in the presence of inter-event / inter-session variability (e.g.: habituation effects, plasticity, or uncontrolled variations in response to stimulation paradigms while performing a task) (Villringer et al., 2010). In non-simultaneous acquisitions, the EEG recording conditions will always, to some degree, differ from those during fMRI scanning (inter-session effects), even when the signals are recorded under the same external stimulus. Therefore, strictly speaking, only data simultaneously acquired are guaranteed to relate to the same neuronal phenomenon. Nevertheless, the potential benefits of simultaneous recordings must be weighed against their technical difficulties: higher costs (e.g.: non-paramagnetic and RF-shielded EEG recording equipment for MR compatibility); instrumental interactions leading to data quality degradation (e.g.: MR-environment related artefacts affecting the EEG; fMRI signal dropout, image distortion, and non-physiological fMRI signal changes in the electrode contacts vicinity; see the following subsection for further details on these effects) (Krakow et al., 2000; Mullinger et al., 2008); and additional safety concerns (Lemieux et al., 1997). Depending on the phenomena of interest and nature of the scientific question at hand, non-simultaneous observations can be preferable (Conner et al., 2011; Hermes et al., 2012; Khursheed et al., 2011), or even necessary (such as the validation of non-invasive source localisation methods in epilepsy (Grouiller et al., 2011; Thornton et al., 2010)).

2.5.2 Data degradation mechanisms

The major physical effect underlying EEG data degradation in the magnetic resonance imaging (MRI) environment is described by the Faraday's induction law. This law states that an electromotive force is induced in a conducting circuit (in this case, formed by the EEG wires, electrodes, patient, and EEG amplification system) when the magnetic flux through a surface, bounded by the circuit, changes in time. Such changes in flux can be produced by the application of time-varying magnetic fields or by the movement of the conducting circuit in a static magnetic field due to, for example, the subject's head movements or system vibrations.

Time-varying magnetic field gradients, used for the MR signal spatial encoding, produce large changes in the magnetic flux over short periods of time, creating voltages at the amplifier inputs that appear as artefacts; these artefacts are problematic because they are up to three orders of magnitude larger than the EEG signal (Allen et al., 2000). Such artefacts represent the most significant effect corrupting the EEG signal simultaneously acquired with fMRI (Mullinger and Bowtell, 2011). Given the repetitive nature of the gradient switching sequence, these artefacts have a strong deterministic component, not expected to be correlated with the

electrophysiological activity of interest, and based on which they can be removed (Allen et al., 2000). However, changes in the conductive circuits geometry or position in relation to the magnetic field, due to subject's head movements or system vibrations, combined with the gradients temporal variation, can lead to random fluctuations in the induced voltages, which represent a real challenge for the artefact correction (Ritter et al., 2010).

The second most significant effect corrupting EEG data is the heartbeat (or pulse) artefact, which results from the quasi-periodic motion and blood flow (Hall effect) linked to the cardiac cycle (Ives et al., 1993; Mullinger and Bowtell, 2011). Since its temporal and spatial characteristics are similar across repeated cardiac cycles, a commonly used correction method involves the computation of an artefact template by averaging the waveform at each contact, across multiple cardiac cycles (Allen et al., 1998). The amplitude and spatial variability of this artefact increase with the strength of the static magnetic field, making its correction more difficult at higher fields (Debener et al., 2008; Neuner et al., 2013).

Acquisition strategies such as limiting the area inside the conductive circuit, twisting the wires, and mechanically restricting head movements (e.g.: vacuum cushion) were found to limit the impact of both the gradient- and heartbeat- related artefacts (Mullinger and Bowtell, 2011). Even after artefacts correction, the EEG signal may remain corrupted, especially when there is head movements during the acquisition. For this reason, the identification and/or quantification of the EEG phenomenon may be compromised. For instance, inappropriate heartbeat artefact correction may lead to spurious δ and/or θ activity, while inappropriate gradient artefact correction may lead to spurious α, β, and/or γ activity.

The EEG signal can be corrupted by other MR-environment related artefacts, which are not imaging acquisition or physiology related. For instance, an artefact originated by the vibration of the MRI scanner, caused by its internal ventilation system (a fan) was reported by Nierhaus et al. (2013). A different artefact, more complex in terms of spectral signature, also originated by the vibration of the MRI scanner, however caused by the cooling compression (Helium) pump system, has also been reported (Nierhaus et al., 2013; Rothlübbers et al., 2015). Both artefacts were found to corrupt EEG signals recorded by devices placed in physical contact with the MRI scanner, even when no image was being acquired (Nierhaus et al., 2013); therefore, both systems should be turned off to avoid them, which is, however, not always possible. Rothlübbers et al. (2015) proposed a post-processing approach to remove that caused by the cooling compression pump system.

When compared to EEG data degradation, fMRI data degradation caused by the presence of the EEG recording system (conducting wires and electrodes) is a relatively minor effect (Luo and Glover, 2012; Mullinger and Bowtell, 2011). FMRI data degradation results from: (1) magnetic susceptibility effects, which lead to signal dropout and geometric distortion, and (2) the perturbation of the radio-frequency fields, which may cause local signal changes and a global reduction in the SNR. The impact of these effects on fMRI data quality depends on the strength of the magnetic field, the number of, and the distance between, electrode contacts (Mullinger et al., 2008).

2.6 Concluding remarks

In the first section of this chapter, we described the main aspects of the current understanding of the neurophysiological origin of the electrophysiological (LFP, MUA, depth EEG, ECoG, scalp EEG) and BOLD fMRI signals, essential to understand the relationship between the two types of signal.

In the second section of this chapter, we reviewed both studies using fMRI to map haemodynamic changes related to particular EEG phenomena, across the entire brain; and aiming to characterise the relationship between the EEG and BOLD signals, recorded at the same location, to establish the current understanding of the relationship between these signals. In brief, studies using LFP, icEEG, or scalp EEG recordings during cognitive, sensory and motor functions have systematically revealed significant correlations between the power of the EEG signal and the amplitude of the BOLD fMRI signal at the same location, or at regions expected to be activated by the task in use. In particular, the power of the EEG signal in the HF range (>30 Hz) was found to be positively correlated with the amplitude of the BOLD signal, while the power of the EEG signal in the LF ranges (θ, α, and β) was found to be negatively correlated with it. A particularly important study on spontaneous brain activity in the visual cortex of anesthetised macaques, Magri et al. (2012), found an identical profile of correlations, suggesting that the relationship between the two signals is identical for task and non-epileptic rest conditions. It was also found that EEG power fluctuations in the α, β, and γ bands explain independent, as well as common, components of the variance of the BOLD signal amplitude (Magri et al., 2012; Scheeringa et al., 2011a). Therefore, it is almost certain that the entire EEG spectral content should be considered and modelled when investigating the relationship between the two signals. Many studies have also investigated the relationship between MUA, LFP, and BOLD. While some found that both MUA and LFP were equally good correlates of the BOLD signal amplitude (Mukamel et al., 2005; Nir et al., 2007), others found that LFP accounted for significantly larger amounts of its variance (Logothetis and Wandell, 2004). It is currently accepted that the BOLD signal reflects both LFP and MUA, to different degrees, depending on the conditions (Ekstrom, 2010). Of particular relevance to us is the study by Whittingstall and Logothetis (2009), who found that the scalp EEG γ band power was a good predictor of MUA only when its increases were time-locked to a certain scalp EEG δ phase, suggesting that a particular interaction between the phase and the amplitude of the two frequency bands may predict MUA better, and may therefore be related to the BOLD signal differently.

In the third section of this chapter, we reviewed studies supporting the functional role of the phase of LF EEG activities and, in particular, of the strength of $PAC_{LF\ HF}$. Given that the latter reflects strong task- and/or state- related modulations, as well as behavioural and/or performance measures, should we be ignoring it while investigating the electro-hemodynamic coupling function? Should we keep ignoring the phase, or phase-amplitude interactions, and keep focusing on the power of the EEG signal alone? Aiming to address these questions, and knowing that local BOLD changes are better explained by a combination of the power of multiple LF and HF activities rather than by the power of HF activities alone, we started by investigating

if the phase of the LF activities had an impact on the EEG power - BOLD amplitude correlation profile, previously found by invasive studies in animals and sequential studies in humans, followed by whether fluctuations in the PAC strength explained variance of the BOLD signal amplitude that was not explained by a combination of α, β, and γ band powers, at a local level, using icEEG-fMRI data simultaneously recorded in humans performing a finger tapping task, as described in Chapter 5. To the best of our knowledge, this is the first work relating PAC strength estimates from human icEEG data with simultaneous, co-localised BOLD changes over time.

In the fourth section of this chapter, we reviewed studies on the relationship between the morphology of epileptic sharp waves and the amplitude of hemodynamic (CBF, BOLD) signals. In brief, while scalp EEG - BOLD fMRI studies in humans found mixed results, LFP - CFB studies in rats found that both sharp wave amplitude and duration were good predictors of the amplitude of the simultaneous, co-localised CBF changes. Acknowledging that sharp wave morphological features reflect interesting aspects of the underlying neuronal activity, we used icEEG and BOLD fMRI data simultaneously recorded in humans at rest to further investigate the relationship between these features, together with the sharp wave spatial field extent, thought to reflect the spatial extent of the surrounding, synchronised sources of neuronal activity, and the amplitude of the simultaneous, co-localised BOLD changes, aiming to improve the current knowledge on the neurophysiological correlates of the BOLD signal, as described in Chapter 6.

Simultaneously recorded icEEG and BOLD fMRI data were previously used to study IED-related BOLD changes (Cunningham et al., 2012; Vulliemoz et al., 2011), and estimate IED-related patient- and location- specific hemodynamic responses (Beers et al., 2015). The possibility of correlating icEEG measurements (invasive, local) with BOLD changes simultaneously acquired in humans (Boucousis et al., 2012; Carmichael et al., 2010) was an excellent opportunity for us to further explore the relationship between the two signals. A detailed description of the data used in this work is presented in Chapter 3. When compared to the scalp EEG signal, the icEEG signal is a considerably more sensitive reflection of the local underlying neuronal activity (see § 2.1.1); the number of sharp waves recorded with icEEG is higher and the estimation of their morphological features is potentially more accurate, for instance. Moreover, the deep neuronal activity previously measured with fMRI but inaccessible with scalp EEG, can now be recorded by both techniques; sharp waves can now be measured in the immediate vicinity of its generators, and therefore be co-localised with the related BOLD fMRI changes, for instance. In this work, we took advantage of these valuable aspects of the simultaneously recorded icEEG - BOLD fMRI data to confirm the validity of the EEG power - BOLD amplitude correlation profile previously found in both invasive studies in animals and non-simultaneous studies in humans (Chapter 5, § 5.2.2); to further investigate the relationship between the two signals by taking into account electrophysiological phenomena that were not previously explored (PAC strength) in terms of their capability to predict the amplitude of the simultaneous, co-localised BOLD signal (Chapter 5, § 5.2.3); and to further clarify the neuronal correlates of the BOLD response by investigating the relationship between the morphology and spatial field extent of sharp waves and the amplitude of the simultaneous, co-localised BOLD signal.

Due to the nature of the phenomena of interest (ongoing EEG phase and amplitude fluctuations in multiple frequency ranges; event-by-event morphological and field extent characteristics), the simultaneity of the icEEG and BOLD data acquisition was necessary. However, such simultaneity leads to data degradation (§ 2.5.2). Of particular relevance to us was the degradation of the icEEG signal by MR-environment artefacts because the quality of this signal may affect the accuracy the quantification of the phenomena of interest and therefore all the following investigations (Chapters 5 and 6). For that reason, this work started with an exploratory investigation towards improving the quality of the icEEG signal, as described in Chapter 4.

3

Simultaneously acquired icEEG and BOLD fMRI data

This chapter describes the acquisition and pre-processing of the icEEG and MRI data analysed in this work, in § 3.1 and § 3.2, respectively, and an algorithm designed to estimate the coordinates of the icEEG electrode contacts in the computed tomography, T1, or echo-planar imaging image spaces, in § 3.3.

3.1 IcEEG and MRI data acquisition

The data was acquired[5] with the written informed consent of patients, as part of a project approved by the Joint UCL/UCLH Committees on the Ethics of Human 107 Research.

The icEEG and fMRI data were simultaneously recorded in patients with severe drug-resistant epilepsy, who underwent invasive electrophysiological monitoring as part of their pre-surgical evaluation. The icEEG implantation strategies (electrodes type and location) were determined by the clinical history of each patient, and varied from patient to patient. The details of the data acquisitions performed by our group to date are presented in **Table 3-I**.

The MRI data was acquired on a 1.5 T scanner (TIM Avanto, Siemens, Erlangen, Germany), with a quadrature head transmit–receive radio frequency (RF) coil using low specific absorption rate sequences (<0.1 W/kg head average), simultaneously with icEEG data, in accordance with our acquisition protocol (Carmichael et al. 2012).

The fMRI scan consisted of a gradient-echo echo-planar imaging (EPI) sequence with the following parameters: repetition time (TR) / echo time (TE) / flip angle=3000ms/40ms/90°, 64×64 acquisition matrix, 38×2.5mm slices with 0.5mm gap. In addition, a fast low angle shot (FLASH) T1 weighted structural scan was acquired with the following parameters: TR/TE/flip angle=15ms/4.49ms/25°, resolution 1.0×1.2×1.2mm, field of view (FoV) 260×211×170mm, 256×176×142 image acquisition matrix with the readout direction lying in the sagittal plane; scan duration: 6 min 15 sec.

IcEEG data were acquired with an MR-compatible system (Brain Products, Gilching, Germany) and respective software (Brain Recorder, Brain Products, Gilching, Germany), at a 5 kHz sampling rate. The icEEG recording system was synchronised with the 20 kHz gradient MR scanner clock.

The computed tomography (CT) data was acquired with a Siemens, SOMATOM Definition AS+ scanner, with a 0.43×0.43×1mm resolution and a 512×512×169 image matrix, shortly after the implantation of the icEEG electrodes and prior to the icEEG-fMRI acquisition, as part of the patients' clinical management.

[5] People involved in icEEG-fMRI data acquisition were D.W. Carmichael, S. Vulliemoz, M. Pugnaghi, R. Thornton, U.J. Chaudhary, R. Rodionov, M. Centeno, S. Perani, N. Sharma.

Table 3-I Description of the icEEG-fMRI data acquisitions: icEEG recording parameters, scanner-related factors, and experimental protocols.

Patient ID	Operator	Amplitude Resolution (µV)	Low Cut Off (Hz)	High Cut Off (Hz)	Sync Box	Internal MR Scanner Ventilation System	Cooling Compression Pump Artefact	Data Type Session Duration (min) (different sessions are separated by ;)						Comments
								Rest outside MR room	Rest inside MR scanner, without fMRI acquisition	Rest with fMRI acquisition	Finger tapping with fMRI acquisition	Foot tapping with fMRI acquisition	Verbal fluency with fMRI acquisition	
LT	SV	10	0.1	250	On	On	On	10	-	10; 10	5	-	-	Left- and right-hand finger tapping only.
CR								7; 10	-	10; 10	-	-	-	-
MB	RT			1000				10	-	10; 10	-	-	-	-
NA					Off			-	-	-	-	-	-	Not useful data. Impossible to correct for MR related artefacts.
GC	UC	0.5		250	On			36	-	10; 10	-	-	5	-
JM								16	-	5; 10; 10	-	-	5	Two sessions (5 and 10 min) are with eyes closed.
BS								18	-	10; 10	-	5	-	Left- and right-foot toe movement intercalated with rest.
JR								19	-	10	5	-	5	Patient slept during acquisitions.
MR								15	1	8; 10	5	-	5	Left- and right-hand finger tapping intercalated with rest.
HD								5; 10; 15	-	10	5	-	5	Left- and right-hand finger tapping intercalated with rest.
				1000				-	-	10	-	-	-	
KB				250				66	-	10	5	-	5	Left- and right-hand finger tapping only.
IH						Off	Off	5	-	10	5	-	10	Left- and right-hand finger tapping only.
SH								14; 18	-	10; 10	-	-	-	-
CB							On	48	-	10; 10	5	-	-	Left- and right-hand finger tapping only.
JN							Off	12	-	10;10	-	-	-	-
MP								11	-	10;10	-	-	5	-

3.2 IcEEG and fMRI data pre-processing

FMRI data was realigned and spatially smoothed (using an isotropic 5mm FWHM Gaussian kernel) using the SPM12 toolbox (www.fil.ion.ucl.ac.uk/spm/software/spm12/). Prior to smoothing, physiological noise was removed from the fMRI data using FIACH (Functional Image Artefact Correction Heuristic) (Tierney et al., 2015).

The gradient artefact was removed from the icEEG data using an average template subtraction approach (Allen et al., 2000). Two other MR-environment, but not image acquisition, related artefacts, caused by mechanical vibrations of the MR scanner linked to the internal ventilation and cooling compression pump systems, were also removed from these data (see Chapter 4 for all the details). The corrected icEEG data were down-sampled to 500 Hz, and their temporal and spectral signatures were visually inspected; icEEG contacts showing clear artefacts (peaks at 50 Hz, or residual gradient artefacts) were not further analysed.

A previous study from our group, Carmichael et al. (2012), found that the amplitude of the heartbeat-related artefact in our icEEG recordings is much smaller (approximately 95%) than the amplitude of a typical IED. From the visual inspection of **Figure 3-1**, we confirm that there is no clear peak in the power spectrum of the icEEG signal, corrected for the gradient artefact, in the frequency range [1 – 1.7] Hz, which is the average heartbeat rate range for adults at rest, according to the National Institute of Health. Hence, the heartbeat-related artefact correction was unnecessary.

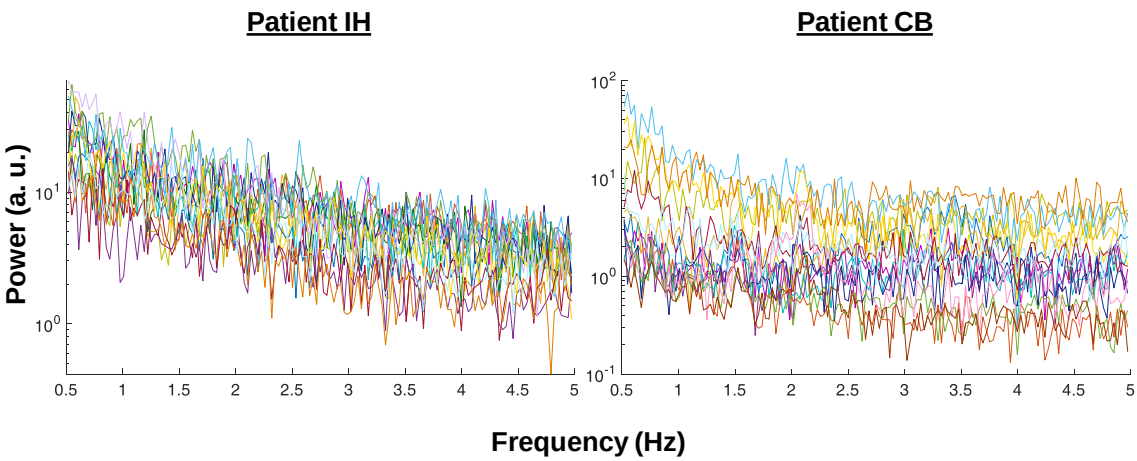

Figure 3-1 Examples of icEEG signal power spectra after the gradient artefact correction. Different colours represent different icEEG contacts (located over the motor cortex).

IcEEG quantification within the scope of the studies described in Chapters 5 and 6 was performed on bipolar time courses, obtained for every pair of adjacent contacts, by subtraction of the voltage of the more posterior contact from that of the more anterior one, in cases of ECoG electrodes, and of the more lateral contact from that of the more medial one, in cases of depth EEG electrodes.

3.3 Estimating the icEEG contacts coordinates in the CT, T1, or EPI space

The estimation of the icEEG contacts coordinates was done in two steps: the creation of the patient-specific contacts mask; and the clustering of the voxels representing the contacts, together with the computation of the centres of mass of these clusters.

The visual inspection of **Figure 3-2** shows that the icEEG contacts can be detected in the CT image (where they appear as approximately spherical groups of the highest intensity voxels), by thresholding its intensity; but not in the T1 weighted structural image (where they appear as the lowest intensity voxels and are hardly distinguishable from the CSF or head-surrounding space voxels). Hence, the CT image was used to create the contacts mask, which was later co-registered in the T1 and/or EPI spaces, when necessary.

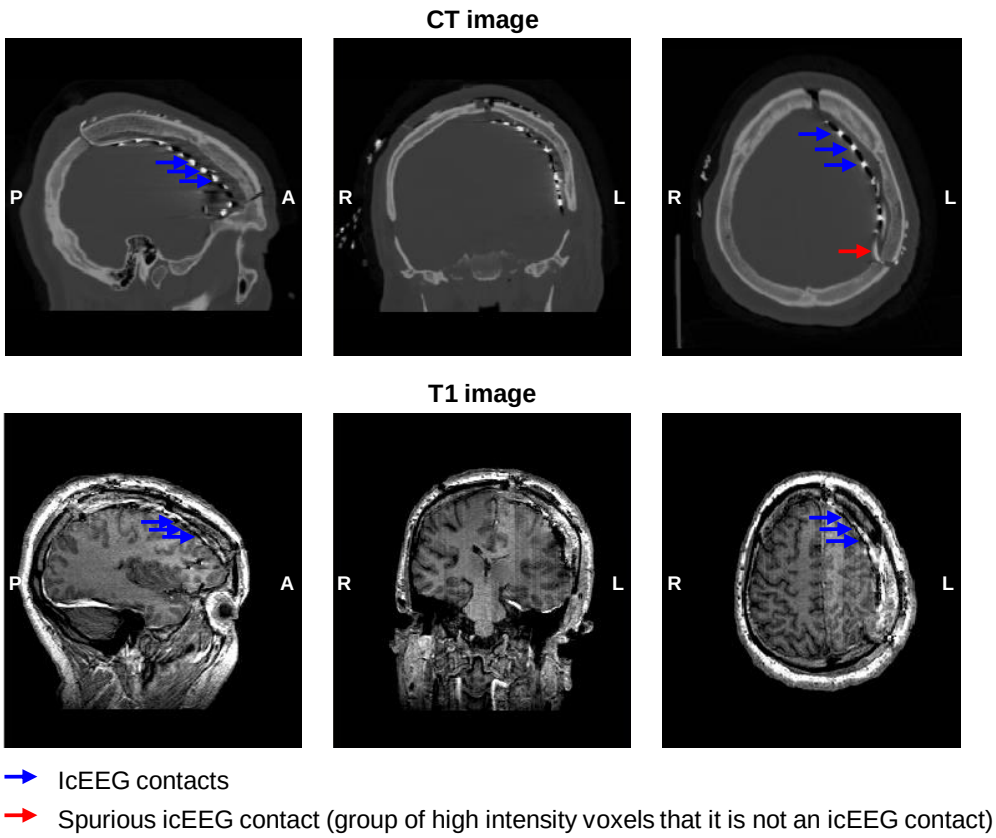

Figure 3-2 Example of CT and T1 images. Blue arrow highlight icEEG contacts. Red arrow highlights a group of high intensity voxels that it is not a icEEG contact.

The contacts mask was created by thresholding the intensity of an up-sampled version (0.5 millimetres axial slice thickness) of the original CT (1 millimetre axial slice thickness), in order to isolate the voxels with the highest intensities (contact-voxels) from those with the lowest intensities (head tissues, CSF, and head-surrounding space). The intensity of the contact-voxels was kept the same, and that of the remaining voxels was set to zero. The threshold value was chosen by trial-and-error, so that all contacts were represented by a group of voxels that was large enough to be detected even after the eventual co-registrations. Note that the intensity of

the contact-voxels in the CT image can differ from patient to patient, probably due to differences in the implantation scheme (type and number of contacts, geometry).

The next step was to cluster the contact-voxels and find the coordinates of the centres of mass (CM) of these clusters. Since the exact number of contacts is not known a priori[6], and a prior of their spatial distribution is not available, classical clustering algorithms (such as k-means and mixture of Gaussians, for example) are not useful. Therefore, I had to design a clustering algorithm, which does not require any prior information regarding the number of contacts or their positions, and is suitable for either strip/grid or depth electrodes. This clustering algorithm consists of the following steps (see **Figure 3-3** for an illustration):

(1) Computing the distances between each and every other contact-voxel (N contact-voxels; thus, N-1 distances for each contact-voxel, i.e. N*(N-1) total). Sorting these distances, for each contact-voxel, to find its nearest neighbours, which we defined to be the contact-voxels that are at most 4 mm [7] (or 3 mm, for some depth contacts) apart from it. Forming clusters composed of each contact-voxel and its nearest neighbours.

(2) Finding the coordinates of the CM of every cluster and aggregating the CM with equal coordinates, therefore reducing the dimension of the problem. Note that the group of contact-voxels illustrated in **Figure 3-3** at the top right corner of the grey square, for example, results in 4 clusters, one per contact-voxel, which have, however, the same exact CM; therefore, these 4 CM are truly a unique CM. The resulting CM become the new contact-voxels.

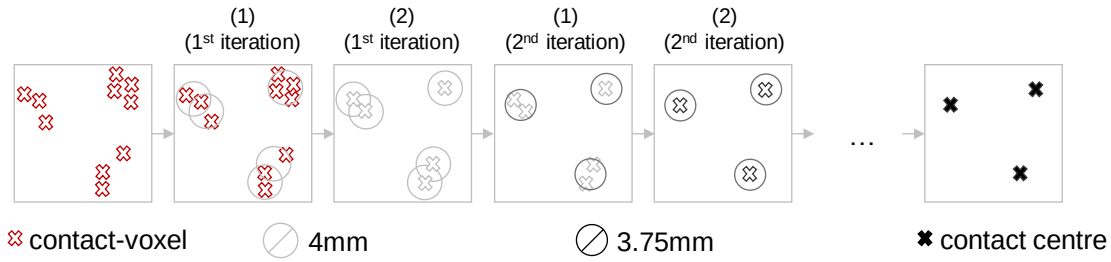

Figure 3-3 Illustration of the clustering algorithm designed by me to find the coordinates of the icEEG contacts. In this example, the final solution (i.e. coordinates of the contacts) is found after two iterations[8].

[6] Note that we know how many icEEG contacts were implanted in each patient, but it may be impossible to preserve all of them after the first steps; some may not survive the thresholding / co-registration steps, or be spurious (see red arrow in **Figure 3-2**).
[7] The distance between two consecutive contacts is 5 or 10 mm, depending on the type and position of the electrode. By trial-and-error, we found that 4 mm was a good distance to start with in the cases where the original distance between 2 consecutive contacts was 10 mm, while 3 mm was a good distance to start with in the cases where the distance between 2 consecutive contacts was 5 mm.
[8] Despite finding the final solution after two iterations, the algorithm will run until the size of the clusters matches the size of the voxel of the image, i.e., the position of the centre of the contacts will not change in the following iterations but the radius of the clusters will keep decreasing.

(3) Repeating the previous steps, decreasing, each time, the diameter of the cluster in 0.25 mm. Iteratively, this will lead to a unique set of coordinates {x,y,z} per contact, which represents its centre.

Once the coordinates of every contact were known, the contacts were plotted in a 3D representation, and visually labelled using the patient' implantation scheme (see **Table 5-I** and **Table 6-II**) and clinical notes as reference.

For this work, the contacts mask was, first, co-registered in the T1 space, and, then, in the EPI space, and the clustering step was done in the EPI space. For a collaborative project (related to functional connectivity analyses in icEEG and BOLD data), the contacts mask was only co-registered in the T1 space, and the clustering step was done in the T1 space. The co-registrations were done using the SPM12 toolbox (www.fil.ion.ucl.ac.uk/spm/software/spm12/), and the nearest neighbour criterion to resample (write) the images.

4

Quality of icEEG data recorded during fMRI

This project was focused on simultaneously recorded icEEG and fMRI data, essential to investigate ongoing icEEG phase and amplitude fluctuations, or event-by-event sharp wave morphological and spatial field extent variations, which were the EEG features of interest of the two studies described in Chapters 5 and 6. As discussed in § 2.5, the icEEG signal simultaneously recorded with fMRI is corrupted by artefacts caused by the switching of the gradient and, in some cases, by mechanical vibrations of the MR scanner (internal scanner ventilation and/or cooling compression pump systems; see § 2.5.2). Since the quality of the icEEG signal may affect the accuracy of the estimation of the EEG features of interest, this work started with the characterisation of the artefacts corrupting the icEEG data, as well as some exploratory investigations towards improving the quality of these data.

4.1 Motivation

Most EEG-informed fMRI studies in epilepsy have been using scalp EEG data qualitatively in the sense that they use experienced EEG reviewers to visually identify the epileptic events in the EEG recordings. Usually, one of the two most popular EEG analysis software (Brain Vision Analyzer (Brain Products, Munich, Germany) (Allen et al., 2000); EEGLab toolbox (Niazy et al., 2005)) is used to remove the gradient artefact from the scalp EEG data. Both software offer gradient artefact correction approaches that rely on the construction of an average gradient artefact template, based on the assumption that the physiological signal is not correlated with the artefact. However, the precise way in which the artefact template is constructed varies from software to software and involves the choice of a number of parameters.

We implemented two different (simplified) versions of the gradient artefact correction approaches proposed by Allen et al. (2000) and Freyer et al. (2009), to understand how the quality of the icEEG signal was dependent on the model and parameters used to construct the artefact template. Then, we compared these approaches in terms of their capability to remove the gradient artefact, while minimising the deterioration of data, as described in § 4.2.1.4. These gradient artefact correction approaches rely on the assumption that the physiological activity is not correlated with the deterministic component of the gradient artefact, which results from the repetitive nature of the switching of the magnetic field gradients (Allen et al., 2000). However, gradients switching combined with head movements or system vibrations (which cause changes in the conductive circuits geometry or position in relation to the magnetic field), can lead to fluctuations in the induced voltages and therefore to fluctuations in the temporal shape of the artefact (Ritter et al., 2010). Minimising the impact of these fluctuations during acquisition is the best way to improve the quality of the EEG data, which can be done by reducing the total areas formed by electrode leads between each contact and the recording reference, for example (Jorge et al., 2015). However, after data acquisition, their impact can be further reduced by carefully choosing the parameters used to construct the gradient artefact template. Here, we investigated the relationship between these parameters and the degree of motion (measured by the fMRI realignment parameters), as described in § 4.2.1.5, as well as the EEG frequency band of interest, as described in § 4.2.1.6.

The icEEG data corrected for the gradient artefact was inspected for any other MR-environment related artefacts, excluding those attributable to image acquisition or physiology; several spectral signatures of unknown origin were found, leading us to perform additional, non-standard synthetic EEG data acquisitions, as described in § 4.2.2.1. The icEEG data corrected for the gradient artefact was found to be corrupted by two artefacts caused by mechanical vibrations of the EEG recording system when in physical contact with the MR scanner: the internal scanner ventilation and the cooling compression pump artefacts, also found by Nierhaus et al. (2013) and Rothlübbers et al. (2015). The ideal approach is to turn off the sources of these artefacts during data acquisition (Nierhaus et al., 2013); however, this is not always possible, especially at a clinical environment. To the best of our knowledge, the EEG analysis software available does not offer tools to remove these artefacts. Therefore, we[9] developed an approach to remove the internal scanner ventilation artefact, and used that developed by Rothlübbers et al. (2015) to remove the cooling compression pump artefact, as described in § 4.2.2.2.

4.2 Methods

The first part of this section is dedicated to the gradient artefact, and the second part to the MR scanner mechanical vibration artefacts, the internal scanner ventilation and the cooling compression pump artefacts.

4.2.1 Gradient artefact

The approaches described here were implemented by me in Matlab (MathWorks®). The quality of the icEEG data corrected for the gradient artefact was quantified through two power based ratios that reflect the gradient artefact reduction and physiological signal deterioration (Freyer et al., 2009), as described in § 4.2.1.2. Both quality ratios take into account the power of icEEG data recorded in a non-MR environment, corrected for the gradient artefact, despite uncorrupted. Therefore, the two gradient artefact correction approaches discussed here were applied to both corrupted icEEG data, $\vec{e}_{MR}$, recorded inside the MR scanner while simultaneously acquiring fMRI, and uncorrupted icEEG data, $\vec{e}_{non-MR}$, recorded in the video-telemetry room a few minutes before the fMRI acquisition.

4.2.1.1 Gradient artefact correction

- **IcEEG data filtering and segmentation**

First, $\vec{e}_{MR}$ and $\vec{e}_{non-MR}$ were high-pass filtered (Matlab function *butter*; 2nd order Butterworth filter, 1 Hz cut-off). Second, two notch filters (Matlab function *iirnotch*; stop-bands of 49 - 51 Hz and 148 - 152 Hz) were applied to $\vec{e}_{non-MR}$ to make the spectral signatures of $\vec{e}_{non-MR}$ and $\vec{e}_{MR}$, as similar as possible (note that data recorded outside the MR scanner room is affected by the electrical artefact, but data recorded inside that room is not). $\vec{e}_{MR}$ and $\vec{e}_{non-MR}$ were segmented

[9] The methodology was developed by me and Marco Leite.

into consecutive 3 seconds epochs, u, time-locked to the start of every fMRI volume (TR = 3 seconds), which were rearranged in the following data matrices:

$$U_{MR} = [u_{MR_{i,j}}]_{i=1,\dots,n;j=1,\dots,t} \tag{4-1}$$

$$U_{non-MR} = [u_{non-MR_{i,j}}]_{i=1,\dots,n;j=1,\dots,t} \tag{4-2}$$

where n is the total number of epochs (fMRI volumes) and t is the number of sampling points within each epoch ($t = TR \times sampling\ rate$).

- **Gradient template construction approaches**

Based on the artefact temporal regularity (§ 2.5.2), two different templates were constructed. One consists of an average of k consecutive epochs (Allen et al., 2000), and the other on a weighted average of k epochs, selected based on a similarity metric (Freyer et al., 2009).

Sequential average

For a particular epoch m, the template $\vec{a}_m$ was computed:

$$\vec{a}_m = \frac{\sum_{i=m-\frac{k-1}{2}}^{m+\frac{k-1}{2}} \vec{u}_i}{k} \tag{4-3}$$

where k is the number of averaged epochs.

Weighted average

$k \times k$ "difference epochs", $\vec{d}_{l,m}$, were computed as:

$$\vec{d}_{l,m} = \vec{u}_{MR_{l,j=1,\dots,t}} - \vec{u}_{MR_{m,j=1,\dots,t}} \tag{4-4}$$

where $l = 1, \dots, k$ and $m = 1, \dots, k$.

After inspecting the spectral profile of icEEG data corrupted by the gradient artefact to find the predominant frequency range of the gradient artefact, which was found to be 150 - 250 Hz (EPI sequence dependent (Freyer et al., 2009)), the power spectral density (PSD) in the range 150 - 250 Hz was computed, for each $\vec{d}_{l,m}$. Consequently, each PSD value (one per $\{l, m\}$ epochs pair) represents a measure of the similarity between the artefacts affecting epochs l and m. By sorting the PSD values in ascending order, a sequence of progressively less similar epochs, $\left[D_{MR_m}\right]_{i=1,\dots,k;j=1,\dots,t}$, was obtained. For any epoch m, the template $\vec{a}_{MR_m}$ was computed:

$$\vec{a}_{MR_m} = \frac{\sum_{i=1}^{k} w^i \left[D_{MR_m}\right]_{i,j=1,\dots,t}}{\sum_{i=1}^{k} w^i} \tag{4-5}$$

where k is the number of averaged epochs, and w is the weighing factor. PSD values were only computed for the data corrupted by the gradient artefact, $\vec{u}_{MR}$. However, the resulting order of

progressively less similar epochs was also used to obtain the matrix $\left[\, D_{non-MR_m}\right]_{i=1,\dots,k;j=1,\dots,t}$. For a particular epoch m, the template $\vec{a}_{non-MR_m}$ was computed:

$$\vec{a}_{non-MR_m} = \frac{\sum_{i=1}^{k} w^i \left[\, D_{non-MR_m}\right]_{i;j=1,\dots,t}}{\sum_{i=1}^{k} w^i} \tag{4-6}$$

- **Gradient template subtraction**

Data correction proceeded by subtracting the templates according to:

$$\vec{c}_{MR_{m,j=1,\dots,t}} = \vec{u}_{MR_{m,j=1,\dots,t}} - \vec{a}_{MR_{m,j=1,\dots,t}} \mid m = 1, \dots, n \tag{4-7}$$

$$\vec{c}_{non-MR_{m,j=1,\dots,t}} = \vec{u}_{non-MR_{m,j=1,\dots,t}} - \vec{a}_{non-MR_{m,j=1,\dots,t}} \mid m = 1, \dots, n \tag{4-8}$$

Finally, the two matrices of corrected data, $C_{MR} = [c_{MR_{i,j}}]_{i=1,\dots,n;j=1,\dots,t}$ and $C_{non-MR} = [c_{non-MR_{i,j}}]_{i=1,\dots,n;j=1,\dots,t}$, are obtained.

Four representative icEEG data time courses, before and after the gradient artefact correction, are shown in **Figure 4-1** . The repetitive pattern seen in **Figure 4-1** is characterised by a period of ~3/38 seconds, which corresponds approximately to the time interval between the acquisition of two consecutive axial slices (each fMRI volume comprises 38 slices). However, the gradient artefact template was built from 3 seconds data epochs (entire fMRI volumes were averaged) rather than 3/38 seconds data epochs because the time interval between the acquisition of two consecutive slices was not consistent over time;the time interval between the acquisition of the last slice of a particular volume and the acquisition of the first slice of the volume that followed was longer than that between the acquisition of two consecutive slices within each fMRI volume.

- **Gradient artefact correction SVD – based improvements**

As suggested in Freyer et al. (2009), two additional steps designed to remove potential residual gradient artefacts were also implemented.

Broadband SVD-based correction of residual gradient artefacts

After removing the mean of each row of C, the global data matrix $C = [C_{MR} \quad C_{non-MR}]$ was factorised as $C = U_{svd}\Sigma_{svd}[V_{svd}]^T$ using the singular value decomposition (SVD) algorithm implemented in Matlab (function *svd*). From this factorisation result U_{svd}, Σ_{svd}, and V_{svd}, organised in terms of explained variance, i.e., $\Sigma_{svd_{11}}$ is the highest eigenvalue, and $\Sigma_{svd_{n,n}}$ is the lowest. To remove potential residual artefacts time-locked to all fMRI volumes, the projection of the 1st eigenvariate was subtracted from the corrected data matrix C:

$$C' = C - U_{svd_{i=1,\dots,n;1}}\Sigma_{svd_{11}}\left[V_{svd_{i=1,\dots t;1}}\right]^T \tag{4-9}$$

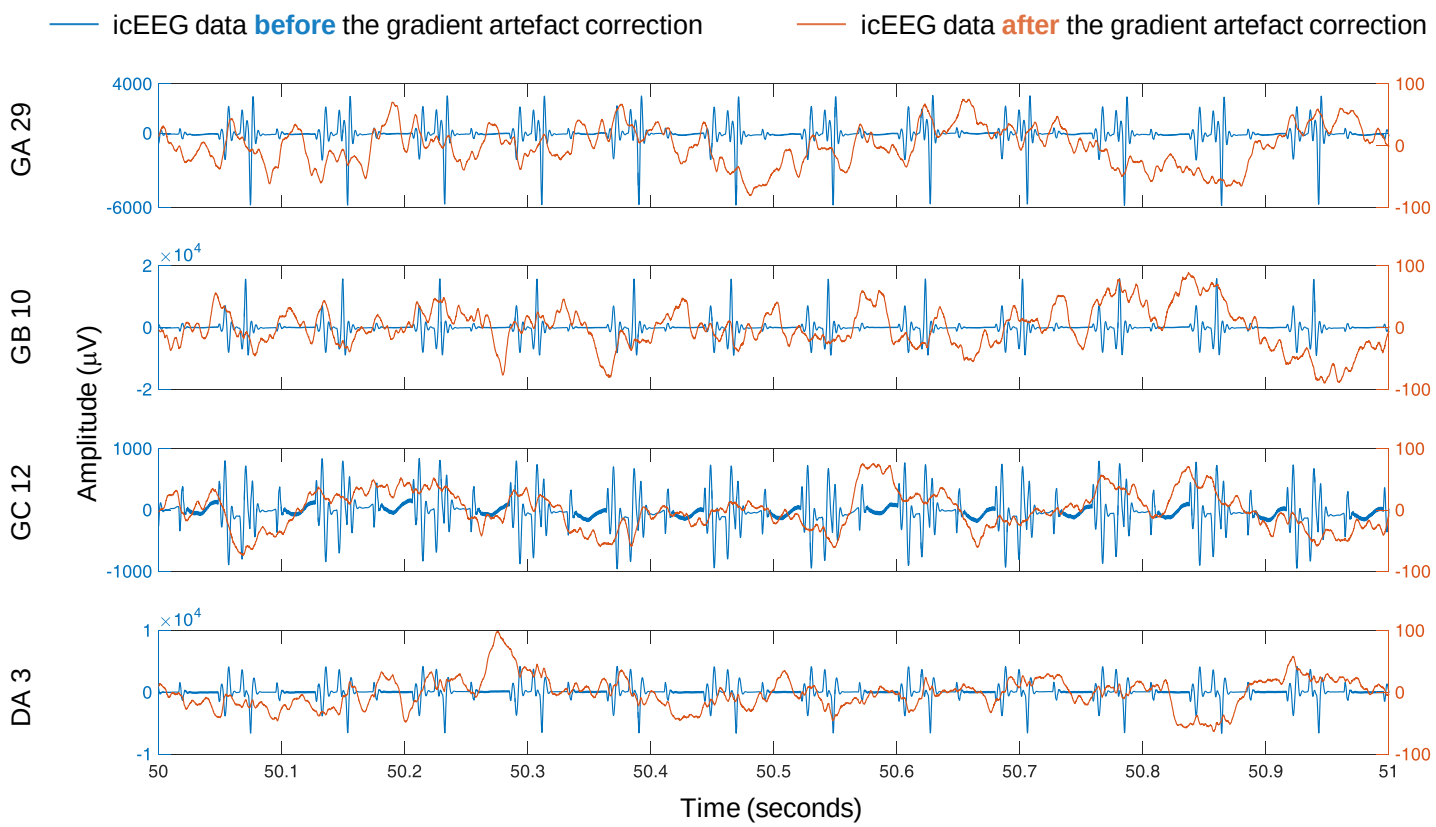

Figure 4-1 Representative icEEG time courses (Patient IH; see an illustration of the icEEG implantation scheme in **Figure 4-3**), before (blue) and after (orange) the subtraction of the gradient artefact template. Note the different scales of the y-axes. In this example, the artefact template was computed with the sequential average approach, using 51 data epochs (k=51).

High-frequency band SVD-based correction of residual artefacts

C' was band-pass filtered (Matlab function *butter*; 2nd order Butterworth filter, cut-off at 150 and 250 Hz), yielding the data matrix C'^{HF}. A SVD of C'^{HF} was then performed. Considering ${U_{svd}}^{HF}$, ${\Sigma_{svd}}^{HF}$, and ${V_{svd}}^{HF}$ organised in terms of explained variance, the eigenvariates of C' were computed as:

$$P^{HF} = {\Sigma_{svd}}^{HF}\left[{V_{svd}}^{HF}\right]^T \tag{4-10}$$

P^{HF} was partitioned into $P_{MR}^{HF} = P_{i=1,\dots,n;j=1,\dots,t}^{HF}$ and $P_{non-MR}^{HF} = P_{i=1,\dots,n;j=t+1,\dots,2t}^{HF}$. An indicator of the amount of contamination, by residual high-frequency artefacts, of the ith eigenvariate can then be computed as:

$$r_i = \frac{q_{i_{MR}}}{q_{i_{non-MR}}} | i = 1, \dots, n \tag{4-11}$$

where

$$q_{i_{MR}} = \sqrt{\frac{1}{t}\sum_{j=1}^{t}\left({\vec{\mathrm{P}}_{i,j}}^{HF}\right)^2} \, | i = 1, \dots, n \tag{4-12}$$

$$q_{i_{non-MR}} = \sqrt{\frac{1}{t}\sum_{j=t+1}^{2t}\left({\vec{P}_{i,j}}^{HF}\right)^2} \, | i = 1, \dots, n \tag{4-13}$$

A new matrix ${\Sigma'_{svd}}^{HF}$ was obtained by replacing ${\Sigma_{svd}}_{i,i}^{HF}$ by 0 when $r_i > 2$, up to a maximum of five times. The use of the condition $r_i > 2$ was suggested by Freyer et al. (2009), who argued that it represents a good compromise between the gradient artefact removal and the physiological signal deterioration. Since SVD was applied to fMRI-locked data epochs, removing eigenvariates mainly removes signal variance time-locked to the gradient artefact onset. However, as for all artefact correction approaches, some degradation of the signal of interest (physiological activity) will ensue. Note that this approach adapts to the possibly variable number of eigenvariates (from one up to five maximum) appearing to represent residual artefacts (those for which $r_i > 2$), while avoiding excessive data degradation (limiting the number of eigenvariates that can be removed to five).

The corrected data matrix $\mathrm{C}''^{\mathrm{HF}}$ was obtained:

$$C''^{HF}_{MR} = {U_{svd}}^{HF}{\Sigma'_{svd}}^{HF}\left[{V_{svd}}^{HF}\right]^T \tag{4-14}$$

4.2.1.2 IcEEG data quality measures

The quality of the icEEG data corrected for the gradient artefact was quantified through two spectral content based ratios proposed by Freyer et al. (2009): the Biosignal Deterioration (R_{BSD}) and the Imaging Artefact Reduction (R_{IAR}), computed as:

$$R_{BSD} = \frac{S_{C_{non-MR}}}{S_{U_{non-MR}}} \tag{4-15}$$

$$R_{IAR} = \frac{S_{C_{MR}}}{S_{U_{non-MR}}} \tag{4-16}$$

where $S_{C_{non-MR}}$, $S_{U_{non-MR}}$, and $S_{C_{MR}}$ are, respectively, the representative spectra of C_{non-MR}, U_{non-MR}, and C_{MR}, obtained by averaging the Fourier transforms (Matlab function *fft*) of every row of C_{non-MR}, U_{non-MR}, and C_{MR}, for the frequency bands: 2 – 4 Hz, 4.5 – 8 Hz, 8.5 – 12 Hz, 12.5 – 30 Hz, 30.5 – 80 Hz, 80.5 - 150 Hz, 150 – 200 Hz, and 2 – 200 Hz, depending on the frequency band for which we aimed to optimise the correction.

In an ideal artefact correction, R_{BSD} would be equal to 1 because the uncorrupted data (U_{non-MR}, C_{non-MR}) are expected to have similar spectral contents, regardless of being corrected or not, and R_{IAR} would also be equal to 1 because the corrected data (C_{MR}, C_{non-MR}) are expected to have similar spectral contents, regardless of being corrupted or not by the artefact.

Considering the physiological signal deterioration and the gradient artefact reduction as equality important for the quality of the data, the quality factor was computed as:

$$Q = \sqrt{|1 - R_{BSD}|^2 + |1 - R_{IAR}|^2} \tag{4-17}$$

Q is a global indicator of the performance of the gradient artefact correction. Note that a high performance is associated with a low Q value, which should be as close to zero as possible.

4.2.1.3 Set of gradient artefact template parameters tested

Both sequential and weighted average templates were used to find the w and k (see equations (4-3) and (4-5)) that resulted in the lowest Q. w and k were varied as follows:

- **Sequential average**

k = 11, 21, 31, 41, 51, and 61, since k = 31 is the default setting for the two most popular implementation of the sequential averaged approach (Brain Vision Analyzer and EEGLab toolbox).

- **Weighted average**

k = 11, 21, 31, 41, … , K (step of 10, where K is the total number of fMRI volumes acquired), and w = 0.3, 0.4., 0.5, …, 1(step of 0.1), resulting in a total of K × 8 $\{w,k\}$ combinations.

4.2.1.4 Gradient artefact construction approach and optimal data quality

To compare the performance of the two template construction approaches (sequential and weighted average), and to investigate how it varied across patients; (i) the fMRI sessions of a particular patient, contact type and spatial position, icEEG data from two patients (IH and CB), with three independent fMRI sessions each, were corrected, and (ii) the best data quality (i.e. the lowest Q value) found with the set of k and w parameters tested was compared across patients, fMRI sessions, and contacts group.

4.2.1.5 Gradient artefact template parameters, optimal data quality, and motion

First, the optimal data quality (the lowest Q value) was compared to the temporal evolution of the translations and rotations obtained from the fMRI data spatial realignment (in relation to the 1st fMRI volume, as implemented in SPM12). This was performed across sessions and electrode contact groups. Second, the Pearson correlation coefficients between the total differential motion (the differential motion norm) and the optimal Q, w, and k regressors were computed (Matlab function *corr*), to understand if Q was correlated with motion, as well as if w and k were able to adjust and account for the effect of motion on data quality. For this purpose, the quality ratios (R_{IAR}, R_{BSD}) were computed volume-by-volume instead of for the whole fMRI session, which allowed us to obtain the optimal Q, w, and k values (the lowest possible Q and the respective w and k) volume-by-volume, and therefore the optimal Q, w, and k regressors with the temporal resolution of the fMRI signal.

4.2.1.6 Gradient artefact template parameters, optimal data quality, and EEG frequency band of interest

Due to our particular interest in EEG frequency content related features, the dependence of k and w on the EEG spectral content of interest was also investigated. Since k and w reflect the number and relative weight of data epochs used to construct the artefact template, a link between them and the EEG frequency content of interest might be expected; for example, the optimal data quality might be achieved with a relatively lower k when the higher, rather than lower, frequency content is of interest. For this investigations, the quality ratios R_{BSD} and R_{IAR} were computed using the average power within each classical EEG frequency band (δ: 2 - 4 Hz; θ: 4.5 – 8 Hz; α: 8.5 – 12 Hz; β: 12.5 – 30 Hz; low-γ: 30.5 – 80 Hz; middle-γ: 80.5 – 150 Hz; high-γ: 150 - 200 Hz), instead of using the average power in the EEG broadband [2 - 200] Hz, as it was done in § 4.2.1.4 and § 4.2.1.5.

4.2.2 MR scanner vibration artefacts

4.2.2.1 Characterisation

A visual inspection of the spectral content of icEEG data corrected for the gradient artefact revealed spectral signatures of unknown origin. To investigate their origin, we performed additional, non-standard synthetic EEG data acquisitions that consisted of alternating, in turns,

several environmental variables: turning on and off the internal scanner ventilation system, i.e., the fan inside the scanner that increases the airflow to keep the patient comfortable, the scanner cooling compression Helium pump system, the room light, recording inside and outside the scanner room, with and without simultaneous image acquisition.

4.2.2.2 Correction

- **Internal scanner ventilation artefact**

Based on the artefact temporal and spatial characteristics (see § 4.3.2), the following correction approach was implemented[10] in Matlab:

(1) since the artefact spectral signature was limited to a narrow frequency band, the icEEG signal already corrected for the gradient artefact was band-pass filtered in the narrowest frequency band comprising all the ventilation artefact frequency components (1 Hz bandwidth, around 93.2 Hz);

(2) since the ventilation artefact time-frequency amplitude profile was similar across contacts, the band-pass filtered signal was decomposed using a SVD in the contacts dimension;

(3) since the 1st and 2nd eigenvariates (i.e. those explaining more variance) displayed a similar time-frequency amplitude profile and the 3rd was apparently ventilation artefact free (see **Figure 4-2**), the ventilation artefact time course estimate was obtained by multiplying the 1st and 2nd eigenvariates by the respective singular values.

(4) the ventilation artefact time course estimate was subtracted from the icEEG signal time course already corrected for the gradient artefact.

- **Cooling compression pump artefact**

The approach proposed by Rothlübbers et al. (2015) was used to remove the cooling compression pump artefact from the icEEG data previously corrected for both gradient and ventilation artefacts. The proposed approach consists of an average template subtraction that relies on the temporal regularity of the cooling compression pump artefact. A total of 21 data epochs are sequentially averaged to construct the artefact template, which is then filtered, to ensure that only artefact characteristic frequencies are left in the template, and no physiological signal is removed. This approach is similar to that used for the gradient artefact correction, with the additional step regarding the filtering of artefact template in the frequency domain.

4.3 Results

4.3.1 Gradient artefact

The results described in § 4.3.1.1, § 4.3.1.2 and § 4.3.1.3 are related to C data (not C' nor C''); we explain why in § 4.3.1.3.

[10] The methodology was developed by Marco Leite and I; a related poster was presented at ESMRMB 2012, in Lisbon.

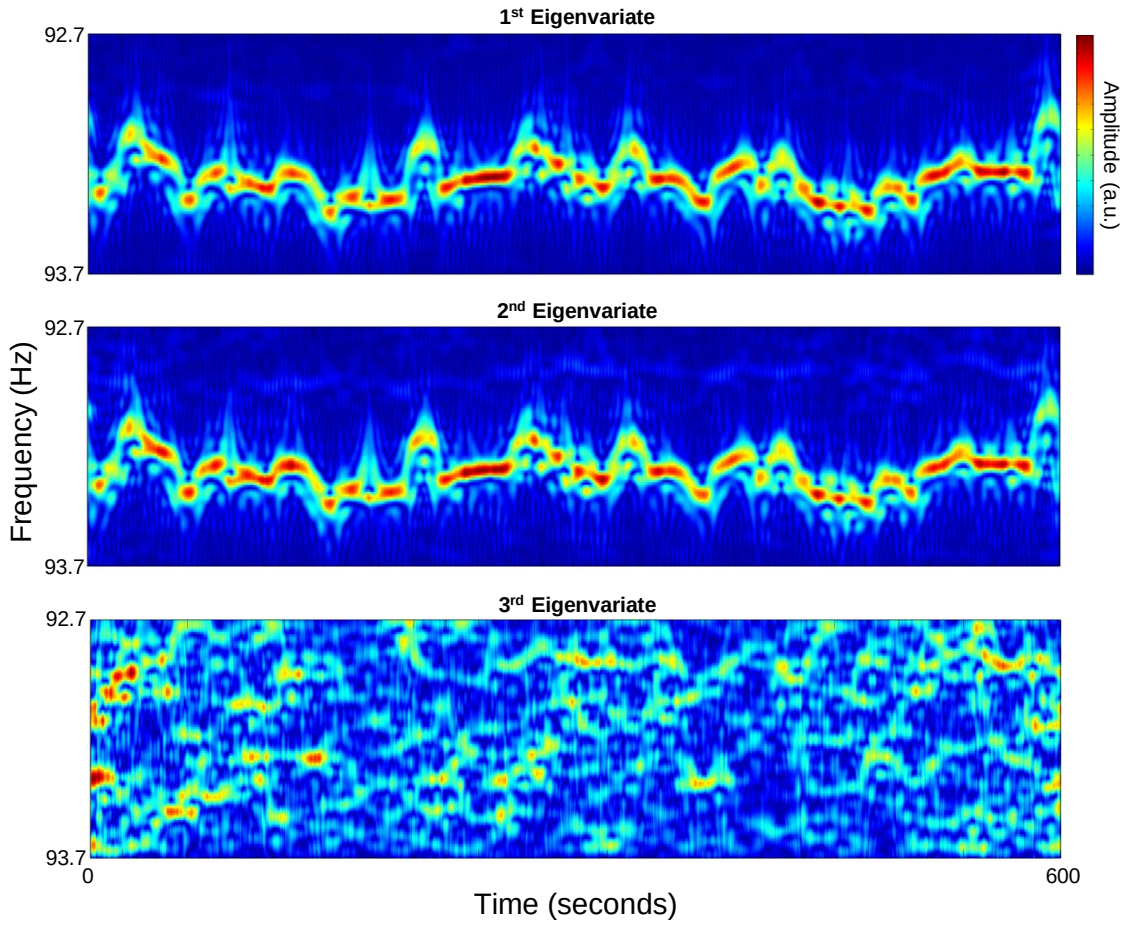

Figure 4-2 Internal scanner ventilation artefact time-frequency characterisation in the eigenvariates space. Time-frequency amplitude profile (Morlet wavelet factor: 1800; y-axis samples: 100) of the first three eigenvariates, for the frequency range 92.7 - 93.7 Hz, obtained by a SVD of the band-pass filtered icEEG signal.

4.3.1.1 Gradient artefact template construction approach and optimal data quality

Schematic representations of each icEEG implantation are shown in **Figure 4-3**. Even though the optimal Q (**Figure 4-4 A**), k, and w (**Figure 4-4 B**) values varied across patients, fMRI sessions, and contact group, the lowest Q values were systematically obtained for the cortical grid A and depth A, across patient IH's sessions, and for the cortical grids A and B, across patient CB's sessions (**Figure 4-4 A**). Considering each contact group at a time, the weighted average approach led to the lowest Q value (**Figure 4-4 A**), in general.

4.3.1.2 Gradient artefact template parameters, optimal data quality, and motion

The optimal Q values obtained for patient IH are lower than those obtained for patient CB (**Figure 4-4 A**), across sessions and contact groups (note that the x and y axis scales are different across patients). Therefore, the quality of patient IH's data corrected for the gradient artefact is comparatively better. However, the differential translations and rotations (difference between 2 consecutive fMRI volumes) are larger for patient IH's sessions 1 and 3, where several fMRI volumes are linked to a total differential motion above 0.2 millimetres (**Figure 4-5**).

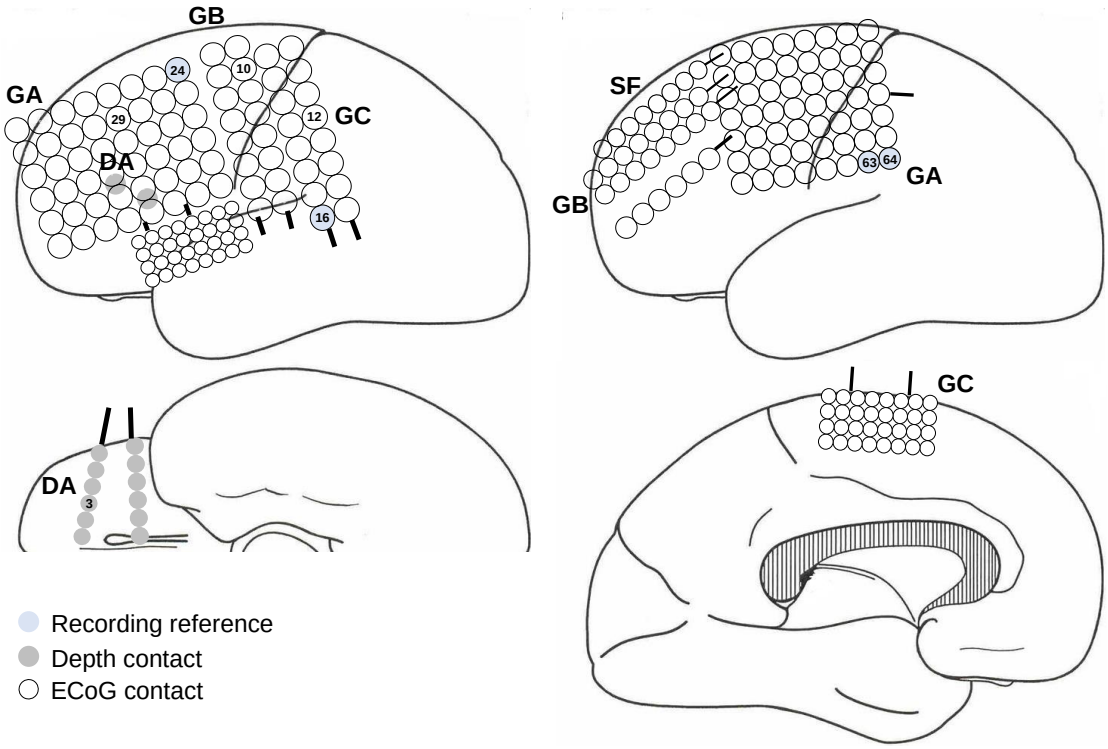

Figure 4-3 IcEEG implantation scheme for patients IH, on the left, and CB, on the right.

Despite showing significant fluctuations over time, the optimal w, k, and Q regressors were not significantly correlated with the total differential motion regressor (results not shown).

4.3.1.3 Gradient artefact template parameters, optimal data quality, and EEG frequency band of interest

The optimal w, k, and Q values by EEG frequency band are shown in **Table 4-I**. Concerning the sliding average approach; no clear pattern was found between the optimal k or Q values and the EEG frequency band used to compute the quality ratios. Concerning patient CB, for instance; the optimal data quality was achieved for the higher frequencies in session 1, but for the lower frequencies in session 2. Nonetheless, for a particular contact group, the lowest k values across frequency bands (highlighted in light blue in **Table 4-I**) are, to some degree, consistent, across fMRI sessions, especially for patient CB.

4.3.1.4 SVD-based gradient artefact correction improvements

In general, the broadband SVD-based step did not lead to a lower Q value (results not shown). However, the high-frequency band SVD-based step, applied to the data after the broadband SVD-based step (C'), lead to a lower Q value (results not shown), suggesting that the second SVD-based step could improve the quality of the high-frequency content of the icEEG data. However, we decided to stop the gradient artefact correction at the average template subtraction step (i.e. before the two SVD-based steps) because the first SVD-based step did not improve the quality of the data, and the second SVD-based step was applied to C' rather than to C. Therefore, the results previously described are related to C data (not C' nor C'').

A

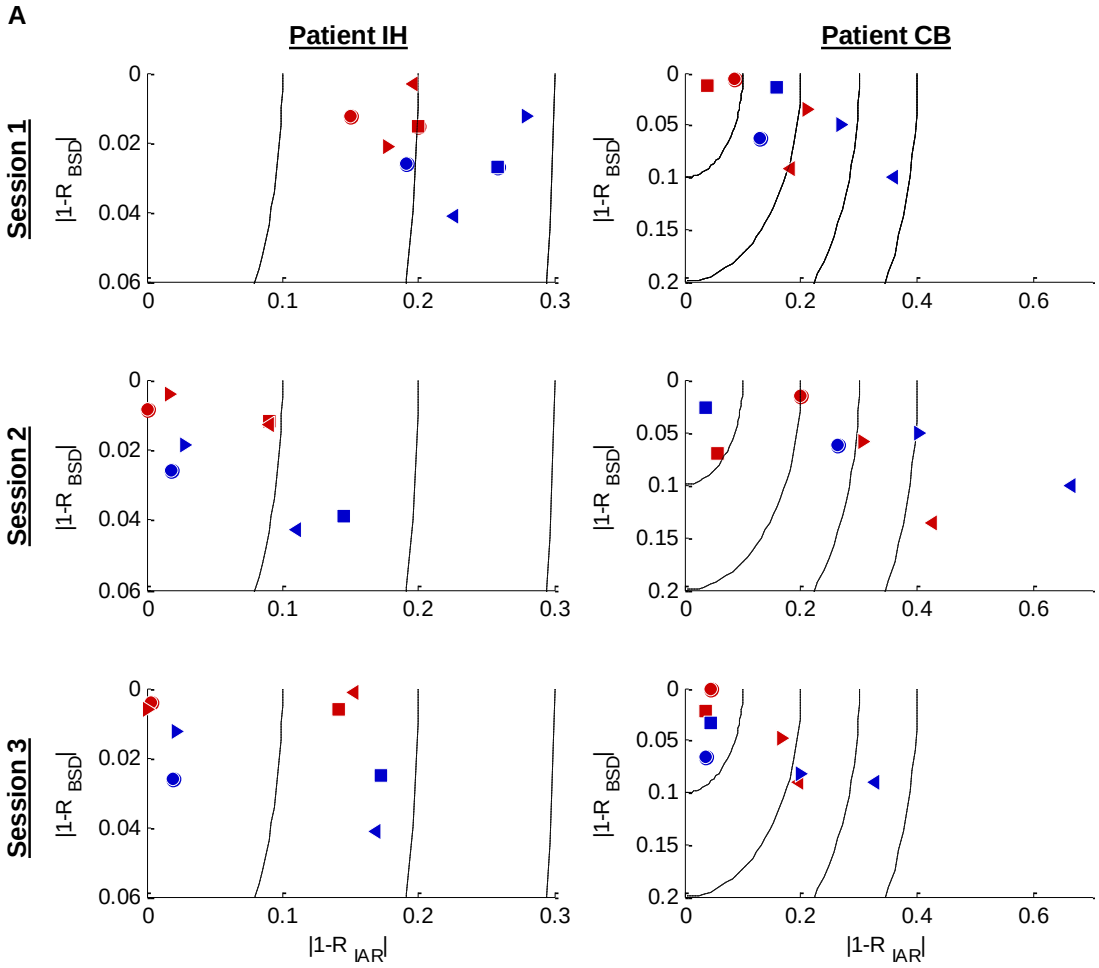

B

Session	Average Approach	Correction parameter	Contact group: GA ●	DA ▸	GB ■	GC ◂	GA ●	GB ■	GC ◂	SF ▸
1	Weighted	w k	0.9 21	0.9 21	0.9 21	1 31	0.8 11	1 121	0.6 11	0.7 11
	Sequential	k	51	51	41	61	61	61	11	31
2	Weighted	w k	1 81	1 11	1 11	1 101	0.7 11	1 51	0.5 11	0.7 11
	Sequential	k	61	31	41	61	61	11	11	31
3	Weighted	w k	1 41	0.9 21	0.9 21	1 121	0.6 61	0.9 21	0.6 11	0.7 101
	Sequential	k	51	61	41	61	61	21	11	11

Figure 4-4 A $|1 - R_{IAR}|$ (x-axis) as function of $|1 - R_{BSD}|$ (y-axis) for the correction parameters that resulted in the lowest Q. Weighted average results are showed in red. Sequential average results are showed in blue. Different geometric shapes represent different contact groups (cortical grids A (GA), B (GB), C, (GC); cortical stripe F (SF); depth A (DA)). Dotted lines illustrate Q contour lines. R_{BSD} and R_{IAR} were obtained using the icEEG signal power in the range [2 – 200] Hz, averaged across contacts. Note: In these plots, a smaller distance between the data point and the origin implies a lower Q value and, therefore, a better data quality. **B** w and k values for which the quality ratios are showed in **A**.

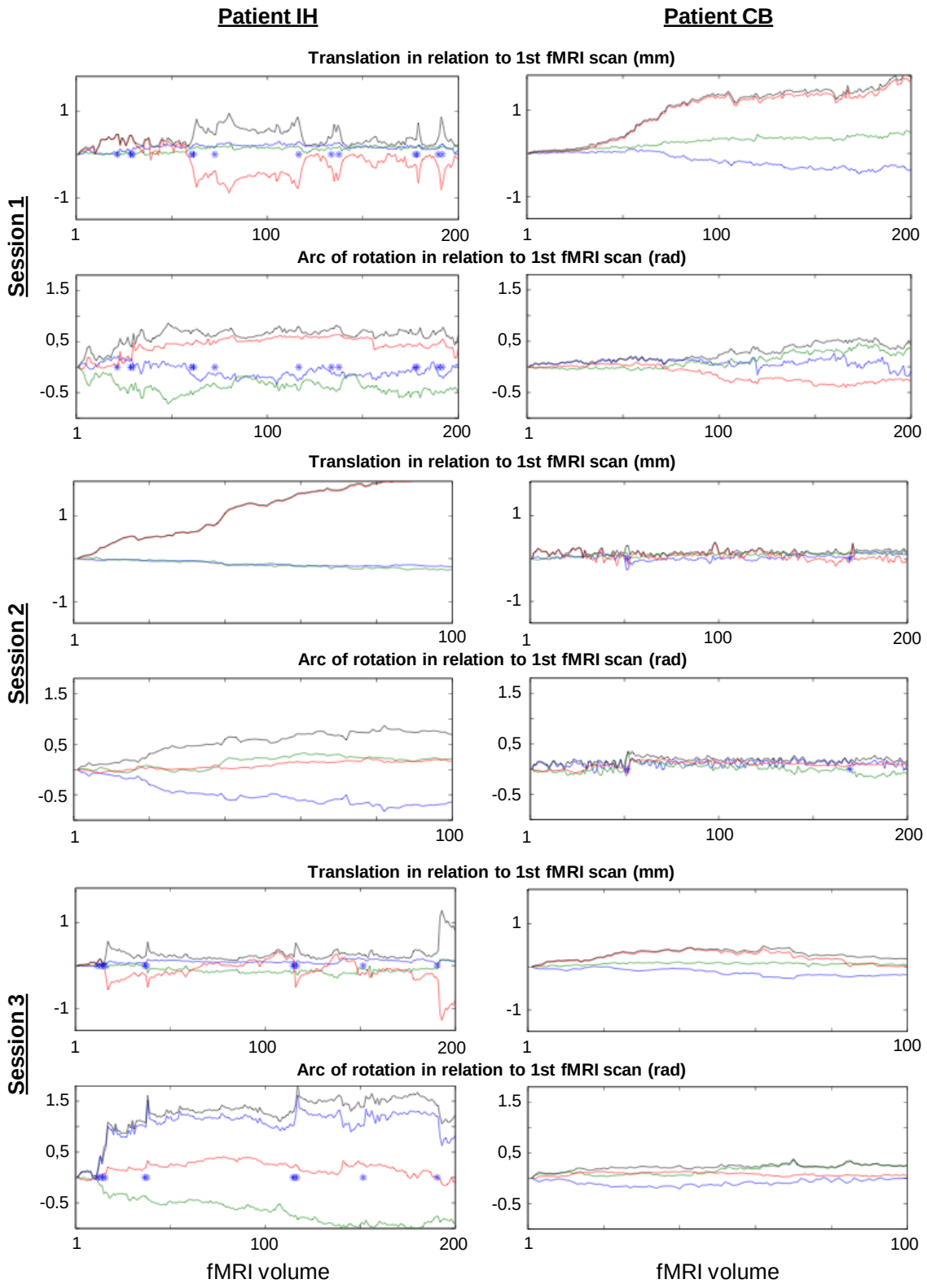

Figure 4-5 Translations, arc of rotation (x displayed in blue, y in green, z in red, and $\sqrt{x^2+y^2+z^2}$ in black) and motion events *, which represent fMRI volumes where the total differential motion was above 0.2 millimetres.

Table 4-I Correction parameters, w and k, that led to the optimal data quality, and respective Q values, by EEG frequency band of interest. W stands for weighed and S for sequential average approach. Concerning the sequential average approach; the lowest Q values are highlighted in grey and the lowest k values are highlighted in light blue, for each contact group.

Patient	Contact Group	Frequency Range								Correction Parameters	Averaging aproach
		2-4Hz	4.5-8Hz	8.5-12Hz	12.5-30Hz	30.5-80Hz	80.5-150Hz	150-200Hz	2-200Hz		
		fMRI session 1									
IH	GA	0.22	0.37	0.33	0.15	0.04	0.01	0.00	0.15	Q	W
		0.8	1	0.9	0.9	0.9	1	0.9	0.9	w	
		21	11	41	61	201	31	21	21	k	
		0.28	0.41	0.35	0.37	0.06	0.05	0.16	0.19	Q	S
		51	51	31	31	51	51	11	51	k	
	GB	0.31	0.59	0.26	0.17	0.11	0.05	0.01	0.20	Q	W
		0.9	1	0.9	1	0.9	0.9	0.9	0.9	w	
		11	21	61	31	21	21	21	21	k	
		0.41	0.64	0.29	0.20	0.25	0.11	0.19	0.26	Q	S
		21	21	41	41	41	51	41	51	k	
	GC	0.26	0.59	0.17	0.17	0.13	0.05	0.00	0.20	Q	W
		0.8	1	1	1	0.9	0.9	0.8	0.9	w	
		11	71	61	41	21	21	81	21	k	
		0.32	0.61	0.19	0.61	0.19	0.18	0.15	0.23	Q	S
		41	41	51	51	41	51	41	41	k	
	DA	0.19	0.48	0.43	0.24	0.08	0.01	0.03	0.18	Q	W
		1	1	1	1	1	1	1	1	w	
		31	41	41	31	11	51	61	31	k	
		0.29	0.55	0.48	0.28	0.25	0.12	0.22	0.28	Q	S
		61	61	61	61	51	61	51	61	k	
		fMRI session 2									
	GA	0.09	0.02	0.01	0.01	0.03	0.01	0.01	0.01	Q	W
		1	0.9	1	1	1	1	1	1	w	
		101	21	31	51	101	101	31	81	k	
		0.10	0.04	0.03	0.02	0.05	0.09	0.05	0.03	Q	S
		61	51	61	61	61	61	41	61	k	
	GB	0.06	0.37	0.04	0.12	0.08	0.00	0.01	0.09	Q	W
		0.7	1	0.9	0.9	0.9	1	0.8	1	w	
		11	11	21	21	21	41	11	11	k	
		0.15	0.43	0.08	0.14	0.11	0.03	0.14	0.15	Q	S
		41	61	41	21	41	51	31	31	k	
	GC	0.02	0.38	0.03	0.12	0.09	0.01	0.01	0.09	Q	W
		0.7	1	1	1	0.9	1	0.9	1	w	
		91	31	31	21	31	91	11	11	k	
		0.08	0.39	0.05	0.13	0.10	0.03	0.10	0.12	Q	S
		51	61	51	51	41	61	41	41	k	
	DA	0.10	0.04	0.03	0.00	0.00	0.07	0.02	0.02	Q	W
		0.4	1	1	1	1	1	1	1	w	
		41	41	41	91	81	101	101	101	k	
		0.09	0.08	0.07	0.02	0.03	0.10	0.08	0.03	Q	S
		51	61	61	61	61	61	61	61	k	

Patient	Contact Group	Frequency Range								Correction Parameters	Averaging aproach
		2-4Hz	4.5-8Hz	8.5-12Hz	12.5-30Hz	30.5-80Hz	80.5-150Hz	150-200Hz	2-200Hz		
		fMRI session 1									
CB	GA	0.13	0.05	0.18	0.15	0.04	0.06	0.10	0.15	Q	W
		1	1	1	1	0.8	1	0.4	0.9	w	
		191	191	191	21	11	51	11	21	k	
		0.19	0.08	0.22	0.17	0.09	0.08	0.17	0.19	Q	S
		61	61	61	61	61	61	61	51	k	
	GB	0.30	0.07	0.13	0.11	0.23	0.01	0.03	0.20	Q	W
		1	1	1	1	1	1	1	0.9	w	
		201	201	31	201	201	161	51	21	k	
		0.31	0.09	0.13	0.15	0.31	0.21	0.02	0.26	Q	S
		41	61	21	61	61	61	31	51	k	
	GC	0.07	0.02	0.43	0.23	0.06	0.57	0.98	0.20	Q	W
		0.8	0.9	0.6	0.7	0.8	0.4	0.4	0.6	w	
		11	41	11	11	21	11	11	11	k	
		0.22	0.20	0.54	0.31	0.14	0.87	1.69	0.37	Q	S
		11	21	21	11	11	11	11	11	k	
	SF	0.05	0.19	0.90	0.33	0.04	0.01	0.03	0.18	Q	W
		0.9	0.8	1	0.7	0.8	1	1	1	w	
		11	51	201	91	151	11	11	31	k	
		0.10	0.20	0.91	0.35	0.09	0.10	0.19	0.28	Q	S
		61	61	61	11	31	21	11	61	k	
		fMRI session 2									
	GA	0.36	0.20	0.40	0.20	0.03	0.01	0.09	0.01	Q	W
		1	1	1	0.9	0.8	0.7	1	1	w	
		181	21	181	21	91	11	51	81	k	
		0.42	0.23	0.45	0.23	0.09	0.16	0.19	0.03	Q	S
		61	61	61	61	61	61	61	61	k	
	GB	0.06	0.02	0.20	0.31	0.13	0.04	0.08	0.09	Q	W
		1	1	1	0.8	1	1	1	1	w	
		201	141	31	41	201	201	41	11	k	
		0.07	0.01	0.23	0.23	0.22	0.10	0.21	0.15	Q	S
		41	31	11	11	61	61	11	31	k	
	GC	0.14	0.04	0.55	0.98	0.15	0.78	1.18	0.45	Q	W
		0.7	0.9	0.7	0.4	0.7	0.4	0.3	0.5	w	
		31	31	11	11	21	11	51	11	k	
		0.32	0.15	0.69	0.98	0.29	1.22	2.14	0.67	Q	S
		61	31	61	11	11	11	11	11	k	
	SF	0.25	0.18	0.99	0.40	0.09	0.03	0.01	0.02	Q	W
		0.8	0.8	0.6	0.7	0.8	0.8	0.8	1	w	
		11	31	11	31	31	51	21	101	k	
		0.32	0.22	0.02	0.45	0.16	0.21	0.39	0.03	Q	S
		41	11	31	11	31	11	11	61	k	

4.3.2 MR scanner vibration artefacts

4.3.2.1 Characterisation

A visual inspection of the spectral content of icEEG data corrected for the gradient artefact revealed a peak around 93.2 Hz (**Figure 4-6**; top right plots), with a bandwidth of approximately 1 Hz, and multiple narrower peaks around 100 Hz, spaced by 1 Hz (**Figure 4-7**). These spectral signatures of unknown origin were found systematically across contacts and patients.

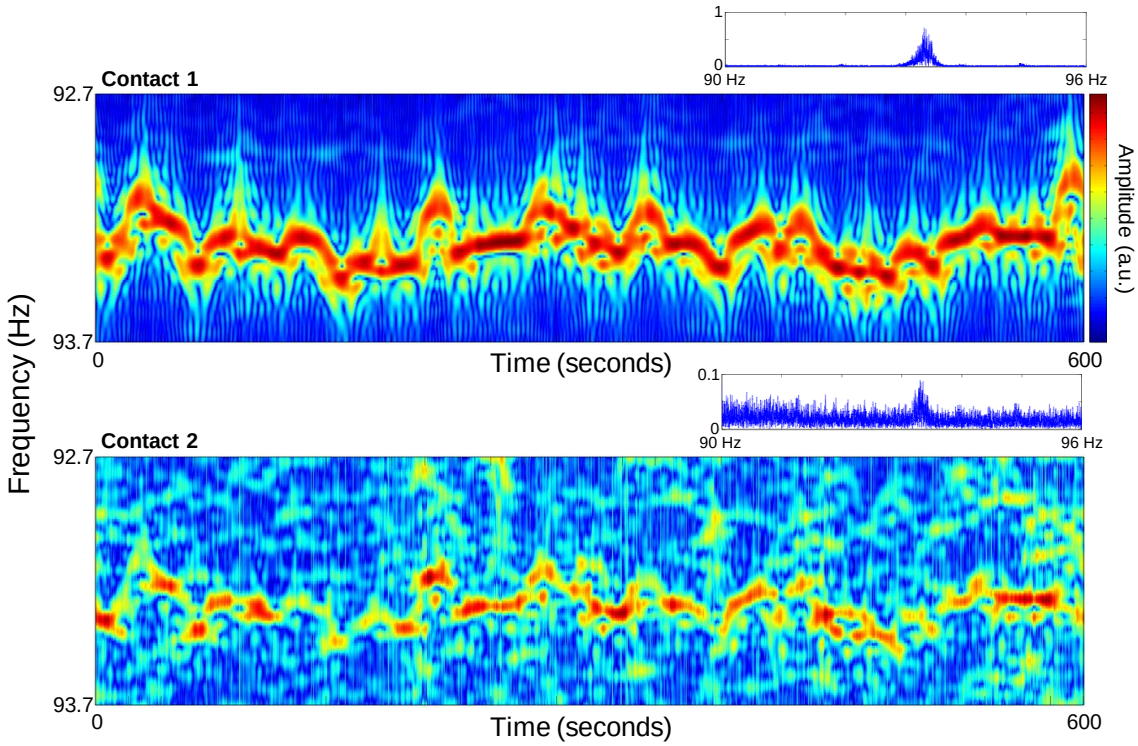

Figure 4-6 Internal scanner ventilation artefact time-frequency characterisation, in the contacts space. Power spectra for the frequency range [90 - 96] Hz are shown on the top right, and time-frequency amplitude profiles for the frequency range [92.7 - 93.7] Hz are shown on the bottom, of two representative icEEG contacts.

A visual comparison of the spectral content of the synthetic EEG signal acquired under different environmental conditions led us to conclude that the aforementioned spectral signatures were caused by the internal scanner ventilation and cooling compression pump systems. Furthermore, these spectral signatures were observed when the EEG recording system was in physical contact with the MR scanner; they are likely to be caused by mechanical vibrations of the whole MR scanner, caused by the system's moving parts (Nierhaus et al., 2013).

- **Internal scanner ventilation artefact**

By investigating the time-frequency amplitude profile of the internal scanner ventilation artefact, across contacts and patients, we found that this artefact was present in all contacts; was frequency band limited (92.7 - 93.7 Hz); and had time-frequency amplitude profiles similar in their temporal shape, but different in their amplitude, across contacts (**Figure 4-6**).

- **Cooling compression pump system artefact**

The artefact caused by the cooling compression pump system had a more complex spectral signature, consisting of several narrow peaks around 100 Hz, spaced by 1 Hz, which indicated periodicity, to some degree (**Figure 4-7**). These artefacts were present in most contacts, but with variable amplitudes.

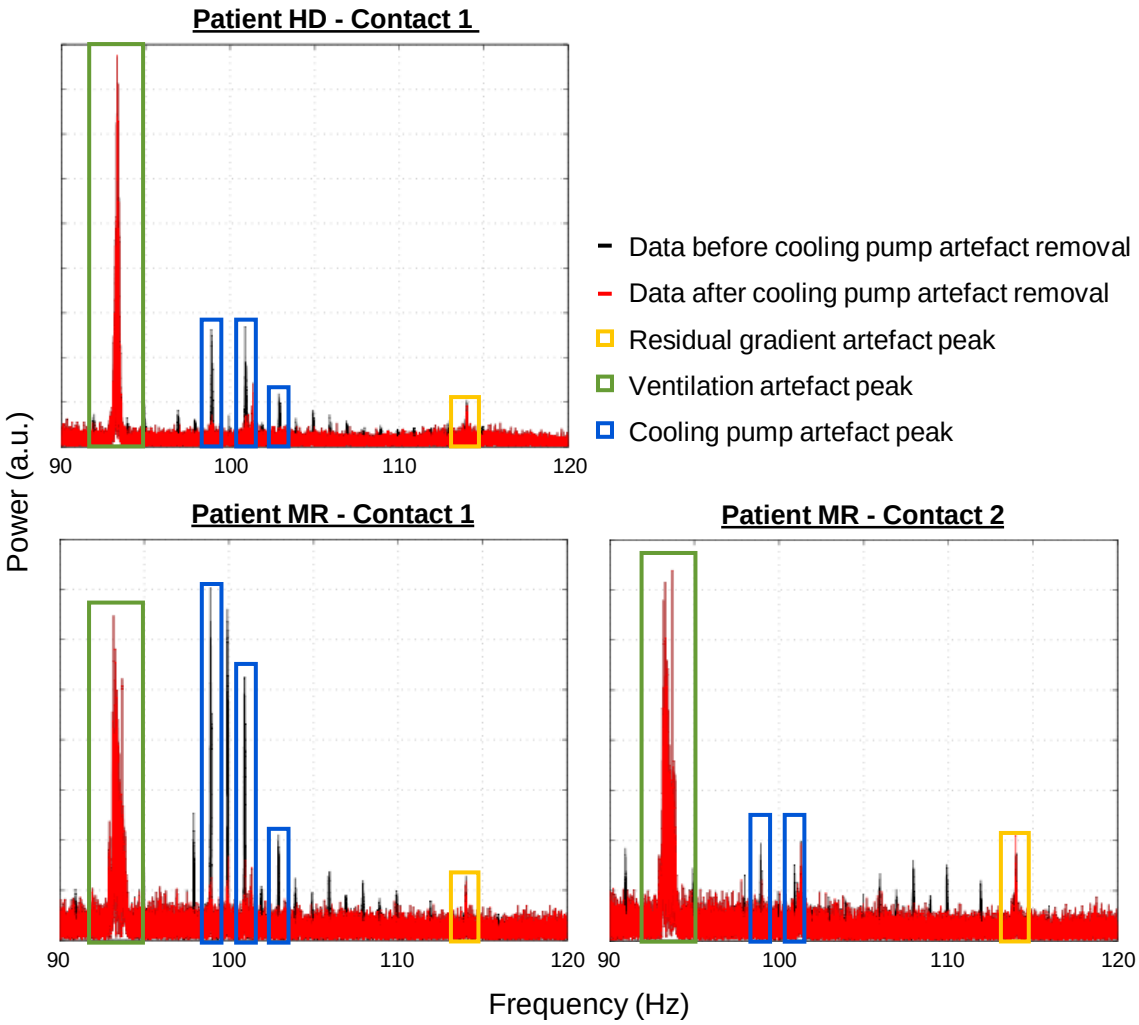

Figure 4-7 Cooling compression pump artefact correction effect. Spectra for the frequency range [90 - 120] Hz of three representative icEEG contacts. Data corrected for gradient and cooling pump related artefacts are presented in red, overlying data only corrected for gradient artefacts, presented in black. Blue boxes highlight the cooling pump artefact peaks. Green boxes highlight the ventilation artefact peaks. Yellow boxes highlight residual gradient artefact peaks.

4.3.2.2 Correction

- **Internal scanner ventilation artefact**

The subtraction of the internal ventilation artefact template from icEEG data corrected for the gradient artefact led to a visually clear reduction in the power of the ventilation artefact related peak at 93.2 Hz, without a dramatic depression in the icEEG signal power between 92.7 and 93.7 Hz (compare **Figure 4-6** with **Figure 4-8**; top right plots).

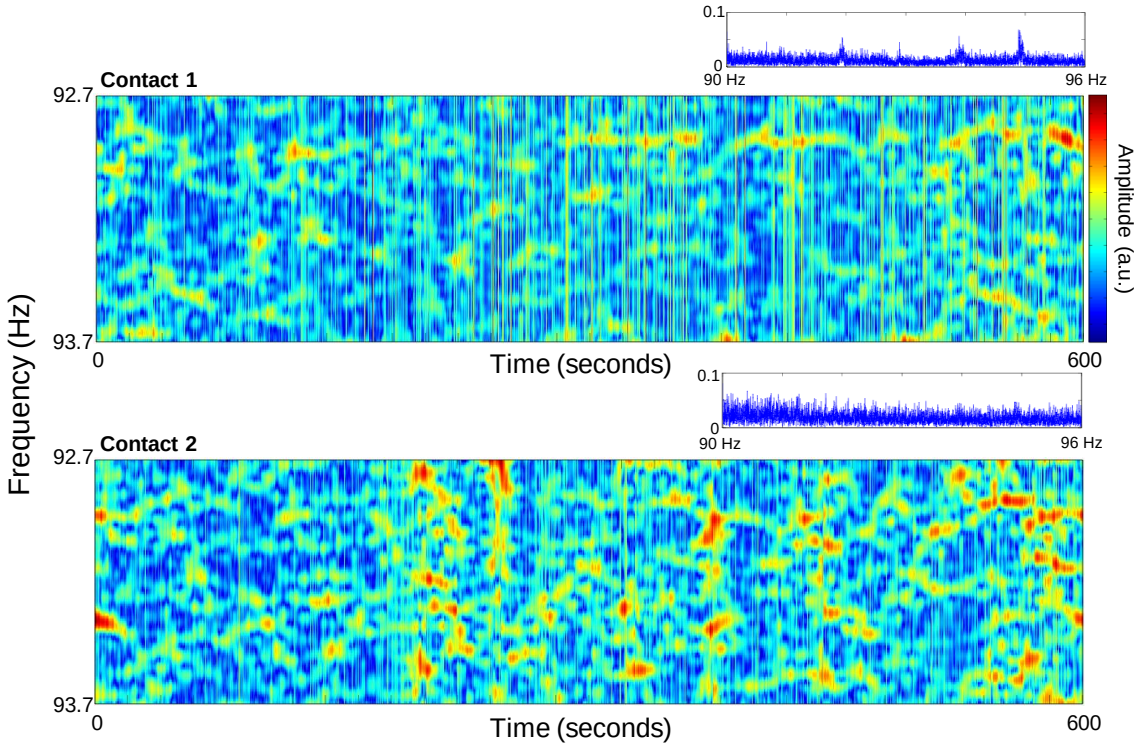

Figure 4-8 Internal scanner ventilation artefact correction effect. Power spectra for the frequency range [90 - 96] Hz (top right), and time-frequency amplitude profiles for the frequency range [92.7 - 93.7] Hz (bottom), of two representative icEEG contacts, after gradient and internal ventilation artefact corrections.

- **Cooling compression pump artefact**

The visual inspection of the power spectra of the icEEG signal corrected for the cooling compression pump artefact showed a marked reduction of the artefact spectral signature power, without a dramatic depression in the icEEG signal power for the artefact characteristic frequencies (**Figure 4-7**).

4.4 Discussion

The investigations on how the optimal gradient artefact correction parameters and icEEG signal quality were related with the icEEG contact location, presence or amplitude of motion, and EEG frequency band of interest, led us to find that the performance of the gradient artefact correction was mostly dependent on the contact location.

The evaluation of the spectral contact of the icEEG data corrected for the gradient artefact led us to realise that these data was also corrupted by the internal scanner ventilation and cooling compression pump artefacts. Using an approach developed by us[11] to remove the first, and an approach proposed in literature to remove the second, we were able to successfully remove these artefacts from our data, with minimal loss of physiological information.

[11] The methodology was developed by me and Marco Leite.

4.4.1 Gradient artefact

4.4.1.1 Gradient artefact template construction approach and optimal data quality

The results regarding the performance of the sequential and weighted averaging approaches suggest that the optimal data quality (i.e. the lowest Q value possible to achieve with the set of k and w parameters tested) depends on the icEEG contact location, rather than on the electrode type (grid, stripe, or depth). Contacts placed at different locations are likely to be part of conducting circuits with different geometries and/or orientations in relation to the magnetic field; therefore, different contacts may be differently affected by the magnetic induction effects. Furthermore, the amplitude of the EEG signal fluctuations induced by motion (circuits position changes due to motion) is proportional to the area of these circuits and their spatial relationship to the motion induced magnetic field changes. Since different contacts form different conducting circuits, the impact of the motion on the accuracy of the estimate of the gradient artefact template may vary from contact to contact. This may explain the different data quality values achieved and the variability in optimal parameters. Our findings are in line with Yan et al. (2009), who investigated these effects in a model of scalp EEG artefacts in MRI and also found significant temporal and spatial (i.e. across contacts) variations of the gradient artefact waveform. In summary, it may be worth to use different template parameters (w, k) for different contacts; in particular, it may be worth to estimate and use the best possible k for each contact, rather than a constant k for all the contacts (31 by default, in two of the most popular EEG analysis software packages). Nevertheless, more data, acquired with a carefully designed setup, together with proper statistical evaluations, would be necessary to conclude something stronger about these effects.

4.4.1.2 Gradient artefact template parameters, optimal data quality, and motion

The presence or magnitude of motion, as reflected by the fMRI realignment parameters, did not seem to have an effect on the optimal data quality, nor in the optimal template parameters (k, w). The poor capability of the fMRI realignment parameters to model motion could explain this observation, mainly because the temporal resolution of these fMRI based (3 seconds) parameters is rather small when compared to the temporal resolution of the potential motion events and icEEG data. Alternatively, the effect of motion on the optimal data quality may be minor in cases like ours, where the total differential motion is < 1.5 millimetres.

Despite clear differences between the optimal data quality values for the two patients, similar values were found across the sessions of each patient. This observation could be explained by the presence of a phenomenon corrupting (at least) one of the references, in one of the patients, but not in the other; or by differences in the spatial distribution of contacts between patients that led to variations in the gradient artefact waveform, which in turn led to different optimal k, w and Q values (see § 4.4.1.1).

4.4.1.3 Gradient artefact template parameters, optimal data quality, and EEG frequency band of interest

Concerning the sliding average approach; for a fixed data quality value, a decrease in the value of k with an increase in the frequency band of interest would have been expected because fewer data epochs could have to be averaged to achieve a similarly accurate artefact template. However, no clear pattern was found between the optimal k or Q values and the EEG frequency band used to compute the quality ratios. Interestingly, the effect of the contact location on the icEEG data quality seemed to also be present here: the lowest k values across frequency bands were, to some degree, consistent across fMRI sessions, for a particular contact group, especially for patient CB.

4.4.1.4 SVD-based gradient artefact correction improvements

While the broadband SVD-based step did not improve the data quality, the high-frequency band SVD-based step did seem to have improved it. However, to evaluate the high-frequency band SVD-based step fairly, we would have to apply it before the broadband SVD-based step.

4.4.1.5 IcEEG data quality measures

The quality ratios R_{BSD} and R_{IAR} used to quantify the quality of the icEEG data after the gradient artefact correction were proposed by Freyer et al. (2009), who used an interleaved image acquisition technique where periods of fMRI acquisition are interleaved with periods of the same duration but, during which, no image is acquired. In our case, the MR and $non - MR$ data periods were not interleaved. In fact, the $non - MR$ data periods were recorded outside the MR scanner, in a different room. Due to these differences in the environments, some differences in the spectral content of both signals, not related to the correction step itself, are likely to be present and to be a limitation of our investigations.

Notwithstanding that R_{BSD} and R_{IAR} seemed useful and informative in our exploratory investigations, a more complete evaluation of data quality would involve assessing the effect of the gradient artefact correction on the number of IED visually identified with confidence by clinical specialists, or on the temporal shape of a particular evoked-potential, for example.

4.4.2 Vibration related artefacts

4.4.2.1 Internal scanner ventilation artefact

After the internal ventilation artefact correction, no clear peak or dramatic depression were observable between the 92.7 and 93.7 Hz of the icEEG power spectra, suggesting a successful artefact removal with minimal loss of information. Therefore, the proposed approach was able to successfully remove a band-limited artefact with a time-varying frequency content, but coherent across contacts. This approach eliminated 2 degrees of freedom in the contacts dimension (1st and 2nd eigenvariates), which is reasonable in terms of information loss.

Furthermore, the initial step of band-pass filtering the icEEG data ensured that the data loss was limited to the artefact-specific frequency band.

4.4.2.2 Cooling compression pump artefact

Rothlubbers et al. (2013)'s approach was able to significantly reduce the power of the multiple cooling pump artefact related peaks in the icEEG data spectrum, without leading to visible depressions, which suggests a successful artefact removal with minimal information loss.

4.4.3 Future work

A more systematic and complete evaluation of the gradient artefact correction could be done in the future; for instance, we could evaluate the impact of this correction on the number of IED visually recognised by multiple EEG analysis experts, assuming that a better correction would lead to higher consistency across experts. We could also evaluate the effect of the choices made during this correction (for example, using the weighted approach and the optimal combination of k and w instead of the sequential approach with a fixed k), on Chapter 5 and 6 findings regarding the relationship between the EEG and BOLD fMRI signals. Nonetheless, their impact is expected to be moderate because no parameters combination led to a dramatic increase in the quality of the icEEG data.

4.5 Conclusion

The gradient artefact correction investigations revealed that the optimal data quality and respective correction parameters varied across patients, fMRI sessions of a particular patient, contact group, and icEEG frequency band of interest. More importantly, while optimal data quality and correction parameters were strongly dependant on the contact location, they were not affected by the presence nor amplitude of motion (reflected by the fMRI realignment parameters).

Given that different combinations of parameters resulted in different data quality ratios following no clear rules, we decided to proceed by correcting the icEEG data with the most commonly used averaging approach, the sequential one, using k=51, therefore favouring the representation of the neuronal signal (the increase of k reduces the contribution of the neuronal signal to the artefact template) (Mullinger et al., 2011).

Turning off the internal ventilation and cooling pump systems is now a standard procedure in our data acquisitions (most recent icEEG data are free of these artefacts; **Table 3-I**). Nonetheless, both approaches here used are useful to improve the quality of previously acquired data.

5

EEG phase-amplitude coupling and the BOLD signal[12]

[12] This chapter was adapted from Murta, T., Chaudhary, U. J., Tierney, T., Dias, A., Leite, M., Carmichael, D.W., Figueiredo, P., Lemieux, L., Phase-amplitude coupling and the BOLD signal: A simultaneous intracranial EEG (icEEG) - fMRI study in humans performing a fingertapping task. Neuroimage (under major revision)

This chapter is focused on the investigations performed to study the influence of the phase of the low frequency (LF) EEG activities on the amplitude of the high frequency (HF) EEG activities, and if that influence should be taken into account when modelling the BOLD signal. The availability of icEEG and BOLD fMRI data simultaneously recorded in humans performing a finger tapping task was a unique opportunity to further investigate the neurophysiological correlates of the BOLD signal. First, we investigated the local relationship between the EEG power and the BOLD signal amplitude, taking or not into account the phase of a particular LF EEG activity, and, second, whether single-trial fluctuations in the strength of the α phase - γ amplitude coupling ($PAC_{\alpha\gamma}$) and β phase - γ amplitude coupling ($PAC_{\beta\gamma}$) explained variance of the finger tapping related BOLD changes, in addition to a linear combination of fluctuations in the power of α, β, and γ EEG bands. The methods are presented in § 5.2, the results in § 5.3, the discussion in § 5.4, and the conclusion in § 5.5.

5.1 Motivation

Since the discovery of EEG, a range of activities in multiple frequency bands, characteristically associated with sensory, motor, and cognitive events, has been observed on its recordings (Engel et al., 2001; Jacobs and Kahana, 2010; Varela et al., 2001). These activities appear to hierarchically interact with each other, through complex mechanisms that seem to regulate how information is processed in the brain, across multiple spatial and temporal scales (Buzsaki et al., 2012; Canolty and Knight, 2010; Hyafil et al., 2015; Lakatos et al., 2005; Palva et al., 2005; Roopun et al., 2008). Among these, the interaction between the phase of the LF activities and the amplitude of HF activities has attracted great attention because its strength fluctuates in a task-dependent manner, both within and across regions; it goes from no influence to strong influence, and back within a few tenths of a second; it can assume different patterns and be modulated in time differently, within different brain structures (Tort et al., 2008); and is proportional to the intensity of training and level of performance (Dürschmid et al., 2014; Tort et al., 2009). These findings suggest that PAC reflects strong task- and/or state- related modulations, as well as behavioural and/or performance measures, suggesting that it has a functional role (Axmacher et al., 2010; Buzsáki et al., 2012; Cohen et al., 2009a, 2009b; Kramer et al., 2008; Lakatos et al., 2008; Tort et al., 2009). In the human motor cortex, EEG activity above 40 Hz is increased during movement, whereas α (8 – 14 Hz) and β (14 – 30 Hz) band activities tend to be decreased during its execution relative to periods of rest (Crone et al., 1998; Miller et al., 2012). Fluctuations in $PAC_{\alpha\gamma}$ and $PAC_{\beta\gamma}$ have also been linked to movement execution and pre- and/or post- movement rest (Miller et al., 2012; Yanagisawa et al., 2012).

With regard to fMRI, it has been found that EEG power fluctuations in the α, β, and γ bands explain independent, as well as common, components of the BOLD signal variance (Magri et al., 2012; Scheeringa et al., 2011a). Many studies have also investigated the relationship between MUA and the BOLD signal (see § 2.2.2.2). While some found that both MUA and LFP were equally good correlates of the BOLD signal (Mukamel et al., 2005; Nir et al., 2007), others found that LFP accounted for significantly larger amounts of its variance (Logothetis and

Wandell, 2004). It is currently accepted that the BOLD signal reflects both LFP and MUA, to different degrees, depending on the conditions (Ekstrom, 2010). The observation by Whittingstall and Logothetis (2009) that the γ band power was a good predictor of MUA only when its increases were time-locked to a certain δ phase is of particular relevance to us; it suggests that a particular interaction between the phase and the amplitude of the two activities may predict MUA better, and may therefore be related to the BOLD signal.

To summarise: (1) fluctuations in α, β, and γ band power, and in $PAC_{\alpha\gamma}$ and $PAC_{\beta\gamma}$ strength, reflect the brain state; (2) fluctuations in the power of multiple frequency bands predict BOLD changes better than fluctuations in the power of the γ band alone; (3) LFP and MUA predict BOLD changes differently, depending on the conditions; and (4) PAC fluctuations predict MUA better than LFP γ power fluctuations alone.

In line with previous studies using ECoG and BOLD data sequentially acquired in humans or LFP and BOLD data simultaneously acquired in animals (see § 2.2.2), we started by investigating the correlation between the power of multiple EEG frequency components and the amplitude of the BOLD signal, as described in § 5.2.2.1 (experiment 1). Since the phase of the LF activities seems to play an important role on how information is processed in the brain, it may also have an influence on how the EEG power is able to predict the BOLD signal. Based on this hypothesis, we investigated the influence of the phase of α and β EEG activities in the correlation between the power of γ EEG activities and the amplitude of the BOLD signal, as described in § 5.2.2.2 (experiment 2). To the best of our knowledge, this influence has not been previously investigated. Finally, we investigated whether fluctuations in the PAC strength explain BOLD signal variance in addition to a linear combination of power fluctuations in α, β, and γ bands, as described in § 5.2.3 (experiment 3). To the best of our knowledge, this is the first study temporally relating PAC estimates from human ECoG with simultaneously recorded co-localised BOLD changes. Taking advantage of icEEG and BOLD fMRI data simultaneously recorded in humans performing a finger tapping task, these investigations allowed us to shed further light on the relationship between the EEG signal spectral content and the BOLD signal amplitude.

Regarding the quantification of the PAC strength, we chose to use the metric proposed by Canolty et al. (2006); one of the two most suitable among a set of seven metrics compared in Tort et al. (2010). Since consistent findings across metrics were expected (de Hemptinne et al., 2013), and to ensure that a robust phenomenon was being investigated, the metrics proposed by Tort et al. (2008) and Özkurt and Schnitzler (2011) were also implemented; the respective methodological details and results are presented as supplementary material in Appendix A.

5.2 Methods

5.2.1 Data pre-processing

This section comprises the description of the patient selection criteria, in § 5.2.1.1, the finger tapping task performed, in § 5.2.1.2, the computation of the BOLD signal time course, in § 5.2.1.3, the computation of the EEG phase and amplitude time courses, in § 5.2.1.4, and the

selection of the patient-specific ECoG contacts and frequency bands of interest, in § 5.2.1.5. While the first four pre-processing steps were common to all experiments, the last pre-processing step was common to only experiments 2 and 3.

5.2.1.1 Patient selection

Based on the anatomical coverage of the icEEG implantation scheme, seven patients were selected for these investigations (patients LT, BS, MR, HD, KB, IH, and CB; see **Table 3-I**); they were precisely those who had part of, or the whole, motor cortex covered by subdural ECoG grids.

5.2.1.2 Motor task paradigm

The icEEG-fMRI session of interest consisted of a 5 minutes finger tapping task. Six patients alternatively tapped their left- and right- fingers, in blocks of 30 seconds each. In two cases, the finger tapping blocks were interleaved with 30 seconds blocks of rest. The seventh patient performed the same task, with rest, using his feet.

5.2.1.3 BOLD time course of interest

A square wave function corresponding to the periods of contralateral (in relation to the icEEG contacts) finger tapping was convolved with the canonical HRF and used as regressor of interest in a whole-brain GLM analysis of the pre-processed fMRI data (see § 3.2 for details on the fMRI data pre-processing). The following confounding effects were also included in this model, as regressors of no interest: 24 movement related confounds (6 realignment parameters, and their Volterra expansion (Friston et al., 1996)), and 6 fMRI physiological noise related confounds, including high-frequency components (Tierney et al., 2015). A square-wave function representing periods of ipsilateral finger tapping was convolved with the canonical HRF and also included as confound, in the cases where finger tapping was interleaved with rest. All GLM were estimated using the SPM12 toolbox (http://www.fil.ion.ucl.ac.uk/spm/software/spm12/).

A positive t-contrast for the regressor of interest was used to locate the BOLD changes positively correlated with the contralateral finger tapping. The corresponding statistical parametric maps were thresholded at $p < 0.001$, uncorrected, and the resulting cluster with a minimum extent of 10 voxels, located in the motor cortex, was used as the region of interest (ROI) for the following analyses. The BOLD signal time course of interest was obtained by averaging the time courses within the ROI, and high-pass filtering the resulting time course using a Butterworth filter of order 4 and cut-off at 128 seconds (Matlab function *butter*), to remove the slow drift.

5.2.1.4 EEG time-frequency decomposition

As a necessary step for the computation of all EEG-derived features investigated in this chapter, the EEG signals were band-pass filtered and Hilbert transformed.

The EEG time courses (following correction for the gradient and scanner vibration related artefacts) were band-pass filtered using a 2-way-least squares Finite Impulse Response filter

(EEGlab toolbox (http://sccn.ucsd.edu/eeglab/) function *eegfilt*), chosen because it limits phase distortion to a minimum (the input data was processed in both the forward and reverse directions). For the α and β bands, the central frequencies of the filters were 8, 9, 10, …, 30 Hz (sampled at every 1Hz), and their bandwidths were set to 1 Hz, to ensure a precise estimation of the instantaneous phase (Aru et al., 2014; Berman et al., 2012). For the γ band, the central frequencies were 70, 74, 78 …, 182 Hz (sampled at every 4 Hz), and their bandwidths were set to 60 Hz, twice the fastest β component, i.e. 30 Hz, to preserve the modulation that the instantaneous phase of β could have in the amplitude of γ (Aru et al., 2014; Berman et al., 2012).

Each band-passed EEG time course was then transformed in the complex signal $x(t) = A(t)e^{i\varphi(t)}$, using the Hilbert transform (Matlab function *Hilbert*), where A is the amplitude and φ is the instantaneous phase of $x(t)$.

5.2.1.5 ECoG contacts and frequency bands of interest

We used the classical α (8 - 14 Hz) and β (14 - 30 Hz) bands (Lopes da Silva, 2011) to identify the ECoG contact pairs that showed the largest task-related α, β, and γ power fluctuations (Miller et al., 2012); these were the contact pairs of interest (COI), for the experiments 2 and 3. Nevertheless, we used patient-specific α and β bands, narrower than the classical bands, centred at patient-specific frequencies (Aru et al., 2014), and mainly containing rhythmic activity, in the following steps of these experiments.

- **Patient-specific contacts of interest (COI)**

For each patient and ECoG contact pair located over the motor cortex (see **Table 5-I** for a schematic illustration of these contacts), we computed the power spectra (using the Matlab function *fft*) over the two finger tapping periods: ipsilateral finger tapping, $S_{ipsi}(f)$, and contralateral finger tapping, $S_{contr}(f)$. Then, for each frequency band of interest, $fb = [f1, f2]$, we computed the difference between the areas under the two power spectra, ΔS_{fb} , as:

$$\Delta S_{fb} = \left(\sum_{f=f1}^{f2} S_{contr}(f) - \sum_{f=f1}^{f2} S_{ipsi}(f) \right) \Delta f \qquad (5\text{-}1)$$

where Δf is the sampling frequency. The patient-specific COI were defined as those showing the largest ΔS_{α}, ΔS_{β}, and ΔS_{γ}, and were labelled COI_{α}, COI_{β}, and COI_{γ}, respectively. Here, α and β were defined as the classical [8 – 14] Hz and [14 – 30] Hz frequency bands (Lopes da Silva, 2011), and γ as [70 – 182] Hz.

- **Patient-specific frequency bands**

For each patient, we performed a coarse-graining spectral analysis (CGSA) (Yamamoto and Hughson, 1991) to isolate the fractal and harmonic components of the power spectra (He et al., 2010) of both COI_{α} and COI_{β}. CGSA was applied to the blocks of ipsilateral finger tapping to take advantage of the stronger α and β rhythmic activities.

Let us consider the fractal (arrhythmic) time series $x(t+t_0)$, where t_0 is the origin of time. According to the self-affinity property of a fractal time series (Yamamoto and Hughson, 1991), $x(ht+t_0)-x(t_0)$ and $h^H\big(x(t+t_0)-x(t_0)\big)$, where H is the Hurst exponent ($0<H<1$), have the same distribution function. Furthermore, the cross-power spectrum of the coarse-grained times series $x_h(t,t_0)=x(ht+t_0)$, $S_{xx_h}(f)$, and the auto-power spectrum of the original fractal time series $x(t,t_0)=x(t+t_0)$, $S_{xx}(f)$, have the same distribution function. $S_{xx_h}(f)$ and $S_{xx}(f)$ are the Fourier transforms of the cross-correlation $C_{xx_h}(\tau)=\langle x(t)x_h(t+\tau)\rangle$ and auto-correlation functions $C_{xx}(\tau)=\langle x(t)x(t+\tau)\rangle$, respectively, where $\langle\,\rangle$ stands for the ensemble average (Yamamoto and Hughson, 1991). By contract, if x is a simple harmonic motion with a frequency of ω, x_h is also a simple harmonic motion with a frequency of $h\omega$; when $h\neq 1$, $S_{xx_h}(f)$ is equivalent to the Fourier transform of the cross-correlation function between two orthogonal sinusoids and it converges to 0. Consequently, if x is a mixture of harmonic and fractal components (as EEG time courses are known to be), $\left|S_{xx_h}(f)\right|/h^H$ is equivalent to the auto-power spectrum of the fractal components, and the difference between $|S_{xx}(f)|$ and $\left|S_{xx_h}(f)\right|/h^H$ is the auto-power spectrum of the harmonic components (He et al., 2010).

In practice, first, the EEG time course was segmented into 5 seconds non-overlapping epochs, which were multiplied by a Hanning window of the same length (obtained with the Matlab function *hann*; as suggested by He et al., 2010), demeaned, and called $x(i)$. Second, $x(t)$, $x_2(t)$, and $x_{1/2}(t)$, were computed as:

$$x(t)=x(i)(i=1,2,3,\dots,N/2) \tag{5-2}$$

$$x_2(t)=x(i)(i=2,4,6,\dots,N) \tag{5-3}$$

$$x_{1/2}(t)=x(i)(i=1,1,2,2,3,3,\dots,N/4) \tag{5-4}$$

where N is the number of data samples within each 5 second epoch. $x_2(t)$, and $x_{1/2}(t)$ are the coarse-grained time courses (here, $h=2$ (5-3) and $h=1/2$ (5-4) as in He et al., 2010). Third, the auto-power spectrum of $x(t)$, S_{xx}, the cross-power spectrum of $x(t)$ and $x_2(t)$, S_{xx_2}, and the cross-power spectrum of $x(t)$ and $x_{1/2}(t)$, $S_{xx_{1/2}}$, were obtained using Matlab functions *xcorr* and *fft*. Finally, the raw, the fractal, and the harmonic power spectra were computed as:

$$S(f)_{raw}=\frac{1}{M}\sum_{m=1}^{M}|S_{xx}(f)| \tag{5-5}$$

$$S(f)_{fractal}=\sqrt{\frac{1}{M}\sum_{m=1}^{M}\frac{\left|S_{xx_2}(f)\right|}{2^H}\cdot\frac{1}{M}\sum_{m=1}^{M}\frac{\left|S_{xx_{\frac{1}{2}}}(f)\right|}{\left(\frac{1}{2}\right)^H}} \tag{5-6}$$

$$S(f)_{harmonic}=S(f)_{raw}-S(f)_{fractal} \tag{5-7}$$

where M is the total number of epochs. The estimation of the Hurst exponent H was avoided by choosing $h = 2$ and $h = 1/2$ in (5-6) (He et al., 2010).

For each patient, the centre of the α band was chosen to be the frequency showing the maximum power in the band [8 - 14] Hz of the COI_{α} harmonic power spectrum, and its width to be 2 Hz; and the centre of the β band was chosen to be the frequency showing the maximum power in the band [14 – 30] Hz of the COI_{β} harmonic power spectrum, and its width to be 6 Hz (Aru et al., 2014). The γ band was kept as [70 - 182] Hz because no obvious peak was found in this frequency band of the COI_{γ} harmonic power spectrum.

5.2.2 EEG power and the BOLD signal amplitude relationship

5.2.2.1 EEG band power - BOLD amplitude correlation (experiment 1)

We investigated the sign and strength of the correlation between the power (over the whole time course) of multiple EEG frequency components, derived from the ECoG contact pairs located over the motor cortex, and the amplitude of the simultaneous finger tapping related BOLD changes.

For each patient and contact pair, 52 EEG power band – based regressors were built (see § 5.2.1.4 for details on the central frequencies and bandwidths). Each EEG power band - based regressor was obtained by: (1) squaring the time course of the amplitude - $A^2(t)$; (2) convolving the resulting regressor with the canonical HRF; (3) segmenting it into consecutive 3 seconds (the temporal resolution of the BOLD signal) epochs; and (4) averaging each epoch's power. The time course of the BOLD signal was obtained as described in § 5.2.1.3. The sign and strength of the correlation between each EEG power band regressor and the BOLD time course of interest was computed with the Matlab function *corr*, an implementation of the Pearson's linear correlation.

Using the approach described in § 3.3, we found the ECoG contact coordinates, and investigated how the EEG power - BOLD amplitude correlation curves varied spatially, i.e., across the contact pairs located over the motor cortex of each patient.

5.2.2.2 Influence of the EEG α and β phase in the EEG γ power - BOLD amplitude correlation curve (experiment 2)

We investigated the influence of the phase of the patient-specific α and β components (central frequencies of the patient-specific α and β bands; see § 5.2.1.5 for details on the identification of the patient-specific α and β bands) on the correlation between the power of the EEG γ components and the amplitude of the simultaneous finger tapping related BOLD changes. The phase and amplitude time courses were computed for COI_{α} or COI_{β} (§ 5.2.1.5 for details on the identification of COI_{α} and COI_{β}), depending on whether the phase of α or β was of interest.

Let us call the complex LF EEG time course, x_{LF}, and the complex HF EEG, x_{HF}, time course such that:

$$x_{LF}(t) = A_{LF}(t)e^{i\varphi_{LF}(t)} \tag{5-8}$$

$$x_{HF}(t) = A_{HF}(t)e^{i\varphi_{HF}(t)} \tag{5-9}$$

First, the samples of $\varphi_{LF}(t)$ were labelled according to which phase interval they belonged to; four equally sized phase intervals ([7π/4, π/4 [, [π/4, 3π/4 [, [3π/4, 5π/4 [, [5π/4, 7π/4 [) were considered. Second, the samples of $A_{HF}(t)$ were given the same label as their concurrent samples of $\varphi_{LF}(t)$. Third, the samples of $A_{HF}(t)$ equally labelled were averaged over consecutive 3 seconds epochs (the temporal resolution of the BOLD signal time course), which resulted in four new amplitude time courses, one for each phase interval. These four new amplitude time courses were squared and convolved with the canonical HRF, which resulted in four new EEG γ power-based BOLD predictors. The new EEG γ power-based BOLD predictors (four for each frequency pair $\{LF, HF\}$) were correlated with the BOLD time course of interest; yielding four new correlation curves, per COI. See § 5.2.1.4 for details on the set of HF tested, and § 5.2.1.5 for details on the set of LF tested.

5.2.3 EEG PAC and the BOLD signal amplitude relationship (experiment 3)

We investigated whether fluctuations in the $PAC_{\alpha\gamma}$ or $PAC_{\beta\gamma}$ strength explained variance of the amplitude of the BOLD signal that was not explained by a combination of α, β, and γ band powers.

The PAC strength quantification metric proposed by Canolty et al. (2006) is described in § 5.2.3.1; the computation of the PAC strength regressors of interest, $PAC_{\alpha\gamma}$ and $PAC_{\beta\gamma}$, is described in § 5.2.3.2, and the models of the BOLD signal tested are described in § 5.2.3.3.

5.2.3.1 PAC strength estimation

Let us define the composite signal $x_{composite}(t)$ that combines the phase of a particular LF EEG component, $\varphi_{LF}(t)$, with the amplitude of a particular HF EEG component, $A_{HF}(t)$, such that:

$$x_{composite}(t) = A_{HF}(t)e^{i\varphi_{LF}(t)} \tag{5-10}$$

- **Canolty's PAC**

The PAC strength estimates were obtained using the Matlab code available online as supplementary material of Canolty et al. (2006). This metric is based on the symmetry of $x_{composite}(t)$ in the complex plane, in a particular data epoch and contact.

The raw strength of the coupling between $A_{HF}(t)$ and $\varphi_{LF}(t)$, in a particular epoch comprising T data samples, was computed as:

$$rPAC_{Canolty} = \left|\frac{1}{T}\sum_{t=1}^{T} x_{composite}(t)\right| = \left|\frac{1}{T}\sum_{t=1}^{T} A_{HF}(t)e^{i\varphi_{LF}(t)}\right| \quad (5\text{-}11)$$

Assuming an uniform distribution for $\varphi_{LF}(t)$, if $A_{HF}(t)$ is not coupled to $\varphi_{LF}(t)$ then it will be on average the same for all $\varphi_{LF}(t)$ and $x_{composite}(t)$ in the complex plane will be characterised by a circular, symmetric around zero distribution, in which case $rPAC_{Canolty}$ will be approximately zero. However, if $A_{HF}(t)$ is coupled to $\varphi_{LF}(t)$ then $A_{HF}(t)$ will be larger for a particular value of $\varphi_{LF}(t)$ (the preferred phase) and the plot of $x_{composite}(t)$ in the complex plane will show an asymmetric around zero distribution, in which case $rPAC_{Canolty}$ will translate the strength of the coupling.

The z-scored strength of the coupling between $A_{HF}(t)$ and $\varphi_{LF}(t)$ was computed as the difference between $rPAC_{Canolty}$ and the mean of a distribution of surrogates of $x_{composite}$, obtained by jittering $A_{HF}(t)$ and $\varphi_{LF}(t)$ by 200 random time lags, divided by the standard deviation of the same distribution of surrogates (Canolty et al., 2006). The mean and standard deviation of the distribution of surrogates were obtained using the Matlab function *normfit*.

- **Phase-amplitude comodulogram**

The metric described above is used to compute the strength of the coupling between the phase and the amplitude of two particular LF and HF EEG components, respectively. This metric can be applied to multiple frequency pairs (in parallel). The resulting PAC strength values (z-axis) can then be plotted as a function of the LF activity giving the phase (x-axis) and the HF activity giving the amplitude (y-axis), which is called the "phase-amplitude comodulogram". Although computationally expensive, these plots are useful for searching for the $\{LF, HF\}$ frequency pairs that show stronger PAC strengths, when we do not want to make a priori assumptions about the frequency components involved.

Here, the phase-amplitude comodulogram plots were computed using the complete COI_{α} and COI_{β} EEG signal time courses (5 minutes). These plots were later used to improve the SNR of the PAC estimates, when building the PAC strength - based regressors, as described in the following subsection.

5.2.3.2 PAC strength - based BOLD predictors

Two PAC strength- and three power- based regressors were built for BOLD modelling: $PAC_{\alpha\gamma}$, based on the α phase - γ amplitude coupling computed at COI_{α}; $PAC_{\beta\gamma}$, based on the β phase - γ amplitude coupling computed at COI_{β}; P_{α}, based on the α band power computed at COI_{α}; P_{β}, based on the β band power computed at COI_{β}; P_{γ}, based on the γ band power computed at COI_{γ}.

The computation of each PAC strength - based regressor involved: (1) the segmentation of COI_{α} and COI_{β} amplitude and phase time courses into 15 seconds overlapping epochs (5 TR), centred

at the simultaneous BOLD signal epoch, (2) the computation of a PAC strength estimate for each epoch; and (3) the concatenation of the resulting PAC strength estimates. These 3 steps resulted in a PAC strength regressor with the temporal resolution of the finger-tapping BOLD time course, 3 seconds. Tort et al. (2010) argued that 200 cycles of the LF of interest (that giving the phase) were enough to provide a reliable PAC strength estimate (in their particular experimental settings). We choose to use 15 seconds epochs, i.e., 120 cycles for the lower α component of interest (8 Hz), and 450 cycles for the higher β one (30 Hz); this was a good compromise between the accuracy of the PAC strength estimate (likely to increase with the number of cycles averaged) and the temporal smoothing (a consequence of the overlap of the 15 seconds epochs). Nonetheless, as a supplementary analysis, we investigated the influence of the epoch duration for the PAC strength estimation in the conclusions of the investigations that followed, as described in Appendix A - A1.2.

To improve the SNR of the PAC estimates, the PAC strength values for every possible low- and high- frequency combination (i.e. the phase-amplitude comodulogram plots), within the relevant patient-specific α and β bands, were computed, and the PAC strength values for the frequency pairs showing a significant effect ($p < 0.05$, Bonferroni corrected for the dimensions of the PAC strength frequency space) were averaged. This was done for the α phase - γ amplitude coupling and for the β phase - γ amplitude coupling. The desired two PAC strength regressors of interest, for each patient, were then obtained by convolving the average PAC strength time courses with the canonical HRF.

The power (P) regressors were obtained by: (1) averaging the power time courses over the corresponding patient-specific frequency bands and COI; (2) convolving the average power time courses with the canonical HRF, and (3) down-sampling the resulting regressor to a 3 seconds (TR) time resolution by averaging the power within each 3 seconds epoch.

5.2.3.3 BOLD model definition

We used the GLM framework to estimate the variance of the amplitude of the co-localised finger tapping related BOLD changes explained by each individual EEG-derived effect ($PAC_{\alpha\gamma}$, $PAC_{\beta\gamma}$, P_α, P_β, and P_γ) in turn, and that was not explained by a combination of the other regressors (e.g.: $PAC_{\alpha\gamma}$ vs [P_α P_β P_γ]).

Eight independent models were built; four for each PAC strength - based regressor of interest ($PAC_{\alpha\gamma}$ and $PAC_{\beta\gamma}$). Each model included a PAC - based regressor ($PAC_{\alpha\gamma}$ or $PAC_{\beta\gamma}$); three EEG power-based regressors (P_α, P_β, and P_γ); and 30 confounding effects (C) (24 movement-related confounds (6 realignment parameters, and their Volterra expansion (Friston et al., 1996)), and 6 fMRI physiolofical noise related confounds, which included high-frequency signal fluctuations (Tierney et al., 2015). These models were labelled: $MPAC_{\alpha\gamma}$, $MP_{\alpha,\alpha\gamma}$, $MP_{\beta,\alpha\gamma}$, $MP_{\gamma,\alpha\gamma}$ and $MPAC_{\beta\gamma}$, $MP_{\alpha,\beta\gamma}$, $MP_{\beta,\beta\gamma}$, $MP_{\gamma,\beta\gamma}$, and their design matrices are illustrated in **Figure 5-1**. In $MPAC_{\alpha\gamma}$, $PAC_{\alpha\gamma}$ was ortogonalised with respect to the [P_α P_β P_γ]; in $MP_{\alpha,\alpha\gamma}$, P_α was ortogonalised with respect to the [$PAC_{\alpha\gamma}$ P_β P_γ], and so forth. Therefore, the eight models have the same exact number of regressors, and each set of four models (one set for $PAC_{\alpha\gamma}$, other for $PAC_{\beta\gamma}$) explains exactly

the same variance of the BOLD signal (the difference being the way this explained variance is distributed among the regressors).

All models were estimated using the Matlab function *glmfit*.

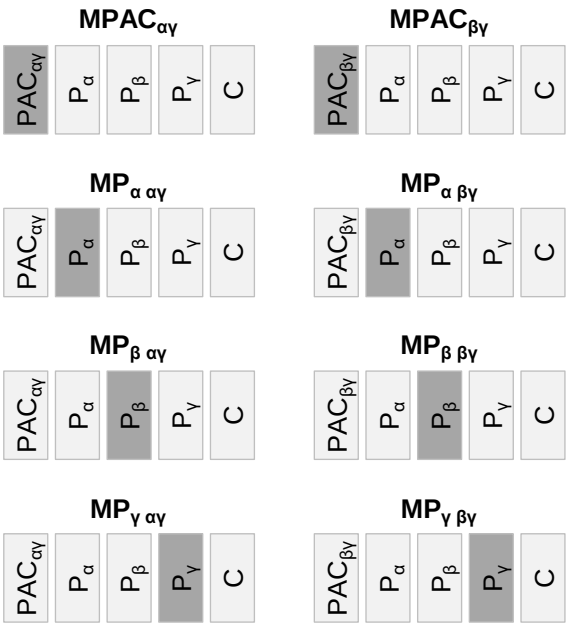

Figure 5-1 Design matrices of all the BOLD signal models considered. The regressor of interest, i.e. the regressor that was orthogonalised with respect to the combination of the others, is highlighted in dark grey.

5.3 Results

5.3.1 Data pre-processing

5.3.1.1 BOLD time-course of interest

At least one cluster of statistically significant finger tapping - related BOLD changes was found in the primary motor cortex of 3/7 patients (**Figure 5-2**), allowing us to define an appropriate ROI for the subsequent investigations. In these three patients, the task consisted of interleaved right- and left- finger tapping, without rest. The data from the other four patients were not further analysed. The icEEG implantation is illustrated in **Table 5-I**, where the black squares show the ECoG contact pairs over the motor cortex (note that we used a bipolar montage). The relative location of the significant cluster and ECoG contacts analysed is illustrated in **Figure 5-4 A.**

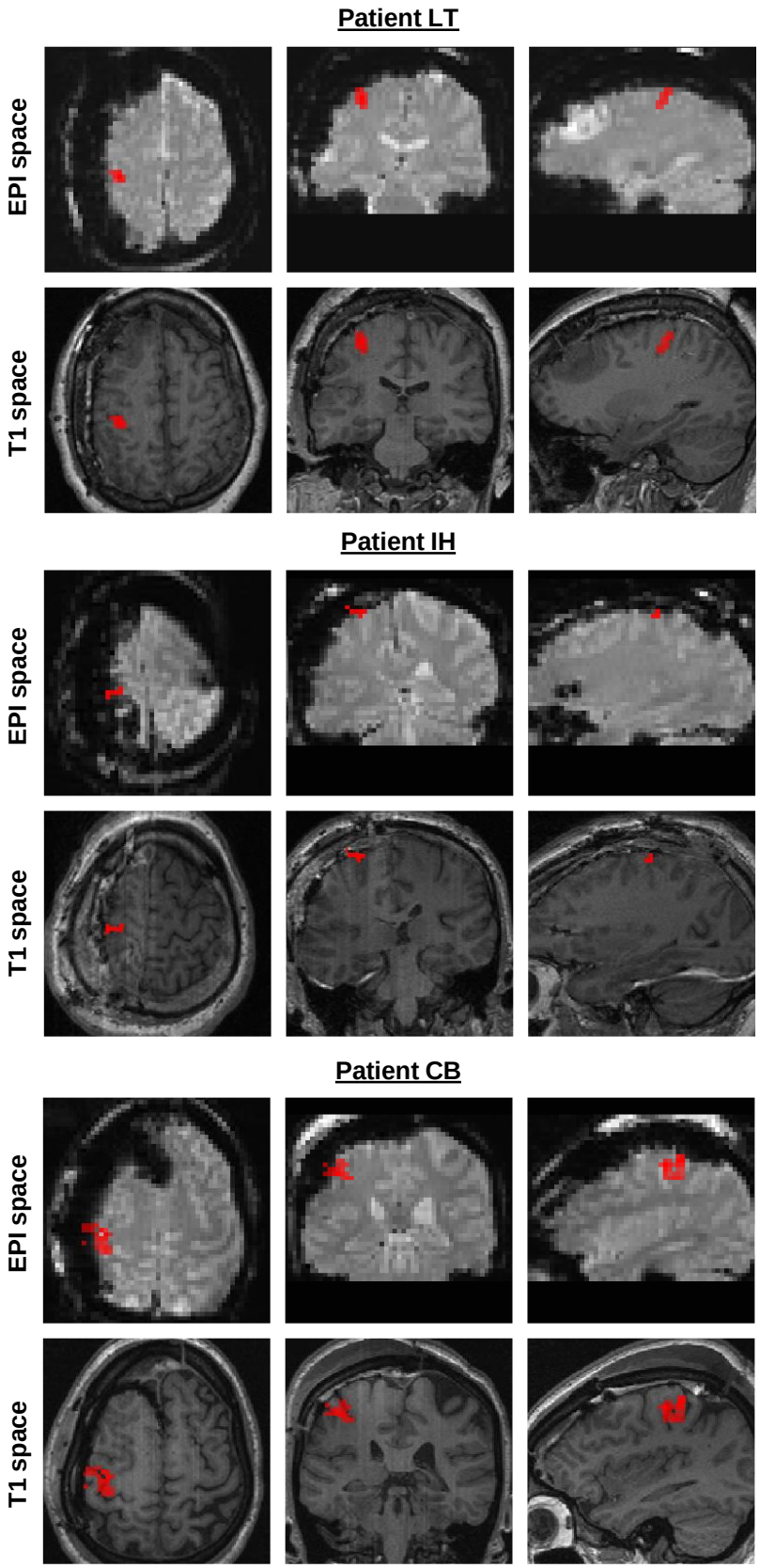

Figure 5-2 Finger tapping related BOLD increases (t-contrast, $p<0.001$, uncorrected).

Table 5-I IcEEG implantation characterisation: types of electrodes, number of contacts per electrode, and implantation scheme. The ECoG contact pairs analysed (over the motor cortex) are highlighted with numbered black squares. FLE: Frontal lobe epilepsy, R: right, L: left, A: anterior, M: medial, P: posterior, I: inferior, and S: superior.

		Implantation scheme
Patient ID	LT	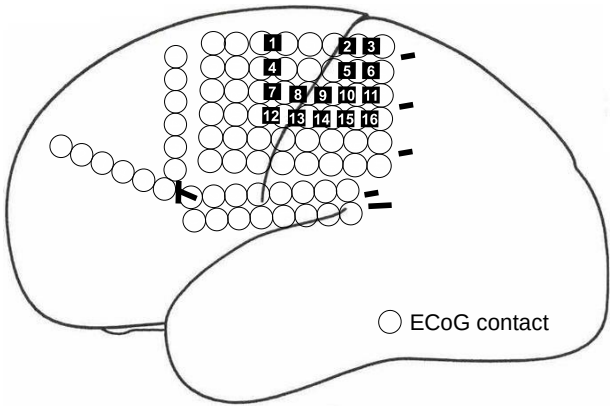
Type of epilepsy	FLE	
Anatomical location of electrodes	- L pre/postcentral gyrus - L supramarginal gyrus - I (IFG) and M (MFG) frontal gyri	
Type of electrodes	two 6-contact strips, one 8x8 contact grid, one 2x8 contact grid	
Patient ID	IH	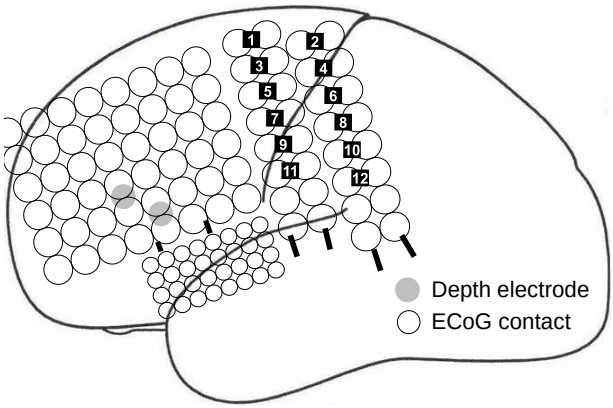
Type of epilepsy	FLE	
Anatomical location of electrodes	- L frontal lobe (laterally and inferiorly) - L M (MFG) and I (IFG) frontal gyri - L temporal lobe	
Type of electrodes	one 6x8 contact grid, two 2x8 contact grids, one 4x8 high-density contact grid, two 6-contact strips, two 6-contact depths	
Patient ID	CB	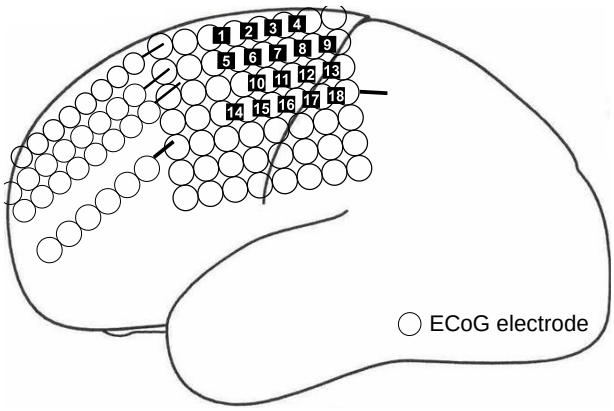
Type of epilepsy	FLE	
Anatomical location of electrodes	- L frontal and parietal convexity - L frontal pole - L S frontal gyrus (SFG) - L I frontal gyrus - L mesial frontal surface	
Type of electrodes	one 8x8 contact grid, one 2x8 contact grid, one 8-contact strip, one 6-contact strip, one high-density 4x8 contact grid	

5.3.1.2 ECoG contact pairs and frequency bands of interest (COI)

The COI, identified for each patient and LF band of interest, are highlighted with white circles in the implanted ECoG contacts scheme shown in **Figure 5-4 B**, and white rectangles in **Figure 5-4 A**. The magnitude of the difference between the area under the spectrum for the contralateral (in relation to the ECoG electrodes) and ipsilateral finger tapping periods varied considerably across the motor cortex of each patient, for all frequency bands of interest, as shown by the colour scale in **Figure 5-4 B**. The sign of these differences was positive for the γ band, and negative for the α and β bands.

The fractal and harmonic power spectra, obtained for the COI_{α} and COI_{β} of each patient, and the respective α, β, and γ power peaks, marked with a black arrow, are shown in **Figure 5-3**.

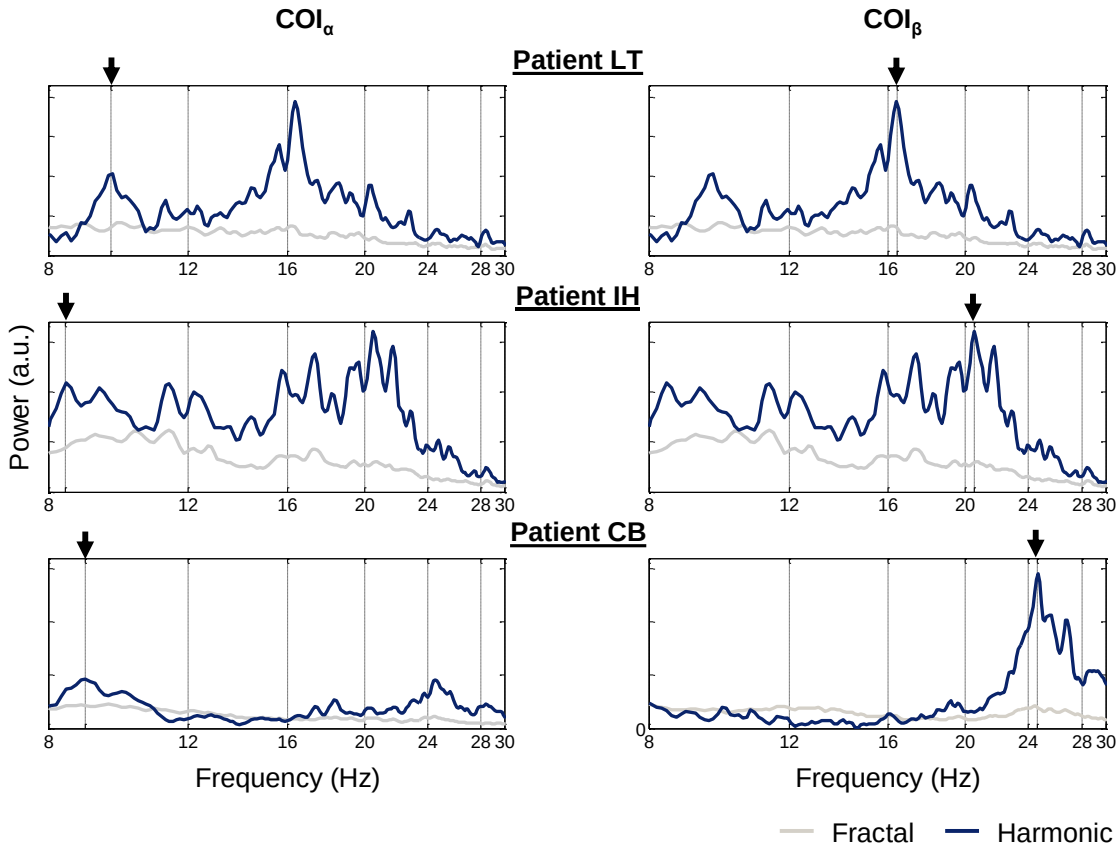

Figure 5-3 Patient-specific α and β bands of interest. Fractal and harmonic spectra for the ipsilateral finger tapping periods, computed using a coarse-graining spectral analysis (CGSA) (Yamamoto and Hughson, 1991), as described in He et al. (2010).

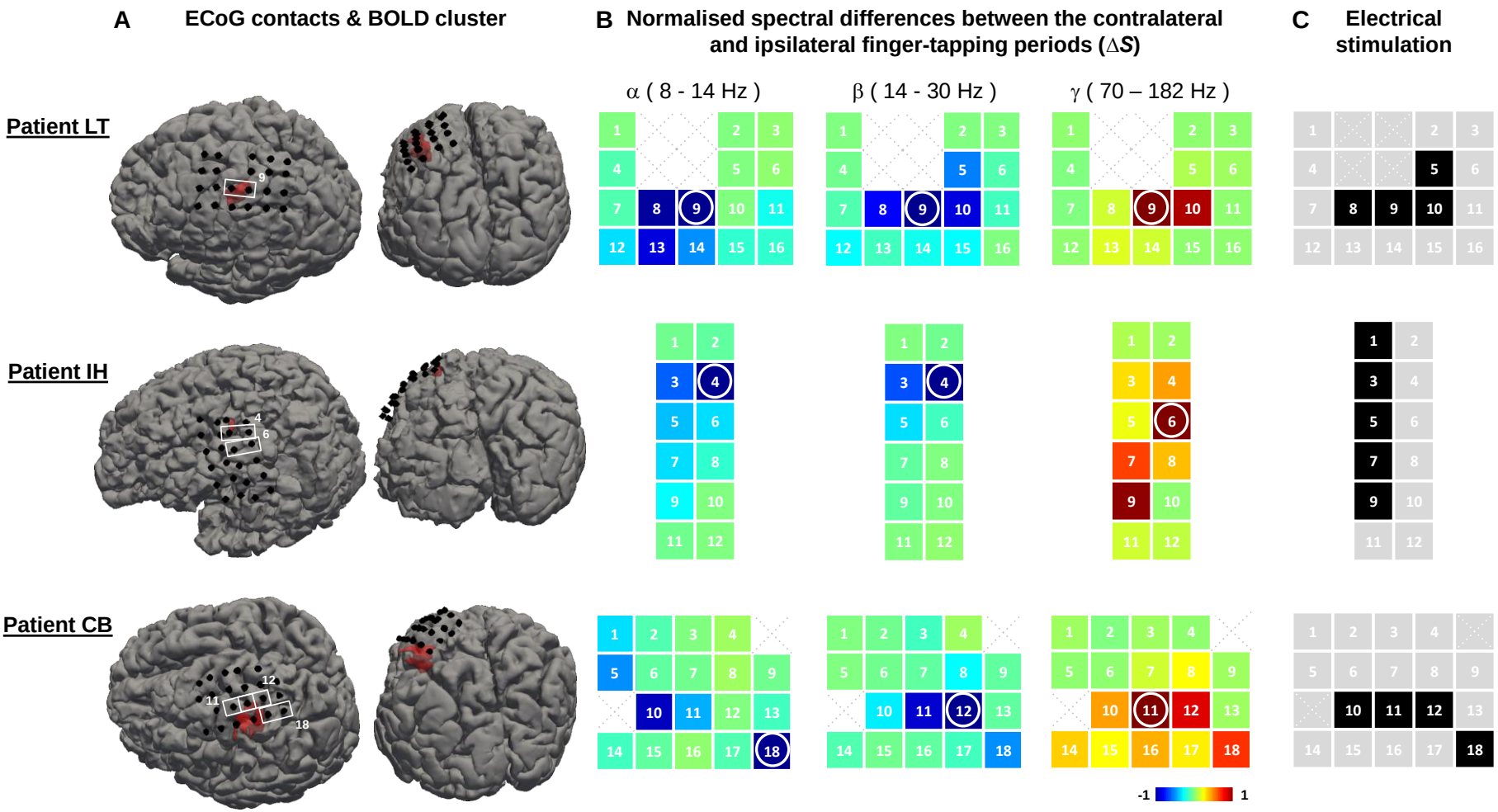

Figure 5-4 Contact pairs of interest. **A** ECoG contacts (black), and finger tapping BOLD increases (red). **B** Spectral differences for contralateral and ipsilateral finger tapping periods. **C** Pre-surgical electrical stimulation results. Contacts showing peaks of apparent artefactual origins (harmonic high-amplitude peaks (prominent residual gradient artefacts), or a 50 Hz (electrical component) high-amplitude peak) were not analysed, and are displayed as a dotted cross.

5.3.2 EEG power and the BOLD signal amplitude relationship

5.3.2.1 EEG band power - BOLD amplitude correlation (experiment 1)

In general, the power of the HF (> 70 Hz) EEG components was positively correlated with the amplitude of the BOLD signal, and the power of the LF (< 30 Hz) EEG components was negatively correlated with it (**Figure 5-5**). The ECoG contact pairs located at a distance < 10 millimetres from the voxel showing the maximum t-value for the contralateral finger tapping boxcar regressor (black curves in **Figure 5-5**) were generally among the three showing the largest (positive and negative) correlation coefficients (**Figure 5-5**).

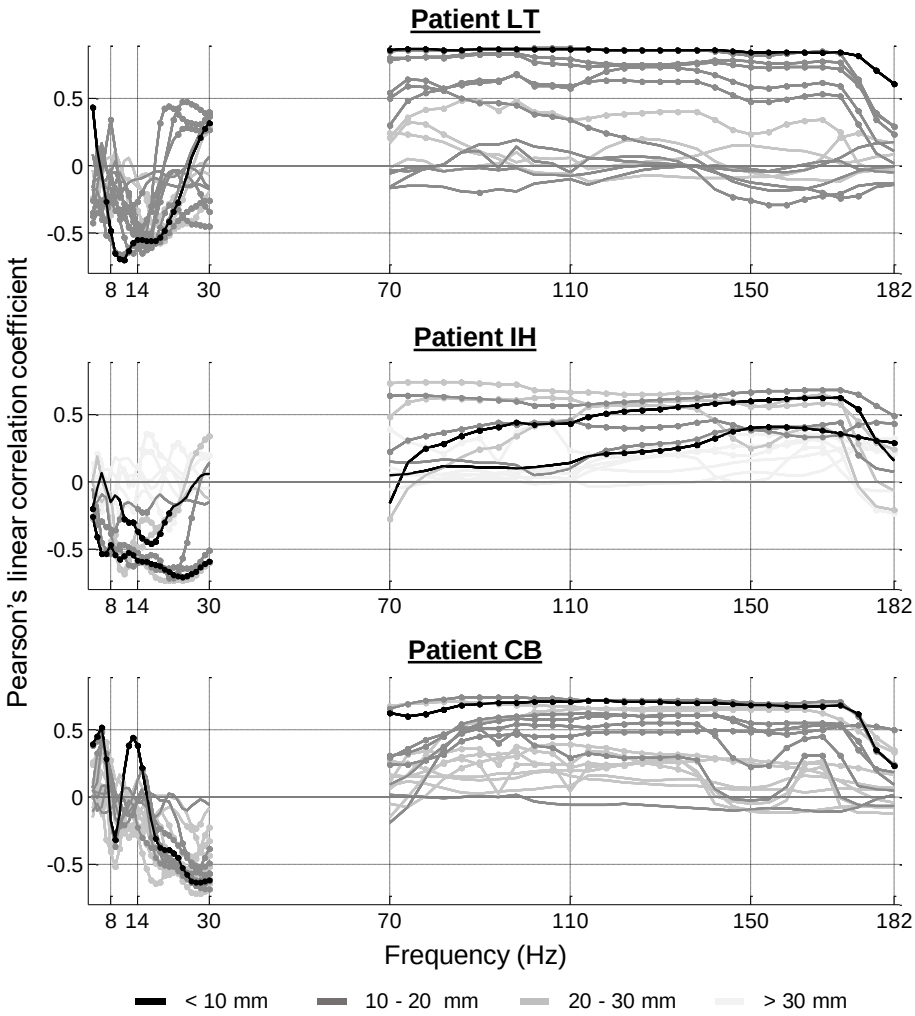

Figure 5-5 EEG band power – BOLD amplitude correlation. Pearson's linear correlation coefficients between the power of multiple EEG frequency components and the amplitude of the contralateral finger tapping - related BOLD time course. The grey tone identifies the distance between the ECoG contact pair (middle distance between the two contacts) and the maximum t-value of the cluster of significant contralateral finger tapping - related BOLD changes.

5.3.2.2 Influence of the EEG α and β phases in the EEG γ power - BOLD amplitude correlation (experiment 2)

The EEG band power - BOLD amplitude correlation curves obtained when the amplitude of the γ components was segmented according to the phase of the α component (amplitude and phase time courses derived from COI_{α}), and from the β component (amplitude and phase time courses derived from COI_{β}), are shown in **Figure 5-6**, on the left and right, respectively; these correlation curves (coloured differently in **Figure 5-6**) are visually distinguishable across the four phase bins, and, in particular, from the correlation curve obtained when the whole time course of the amplitude of the γ components was used (black curve in **Figure 5-6**). Note that [π/4 3π/4 [and [5π/4 7π/4 [are not necessarily the peak and trough of the LF activity because a bipolar montage was used.

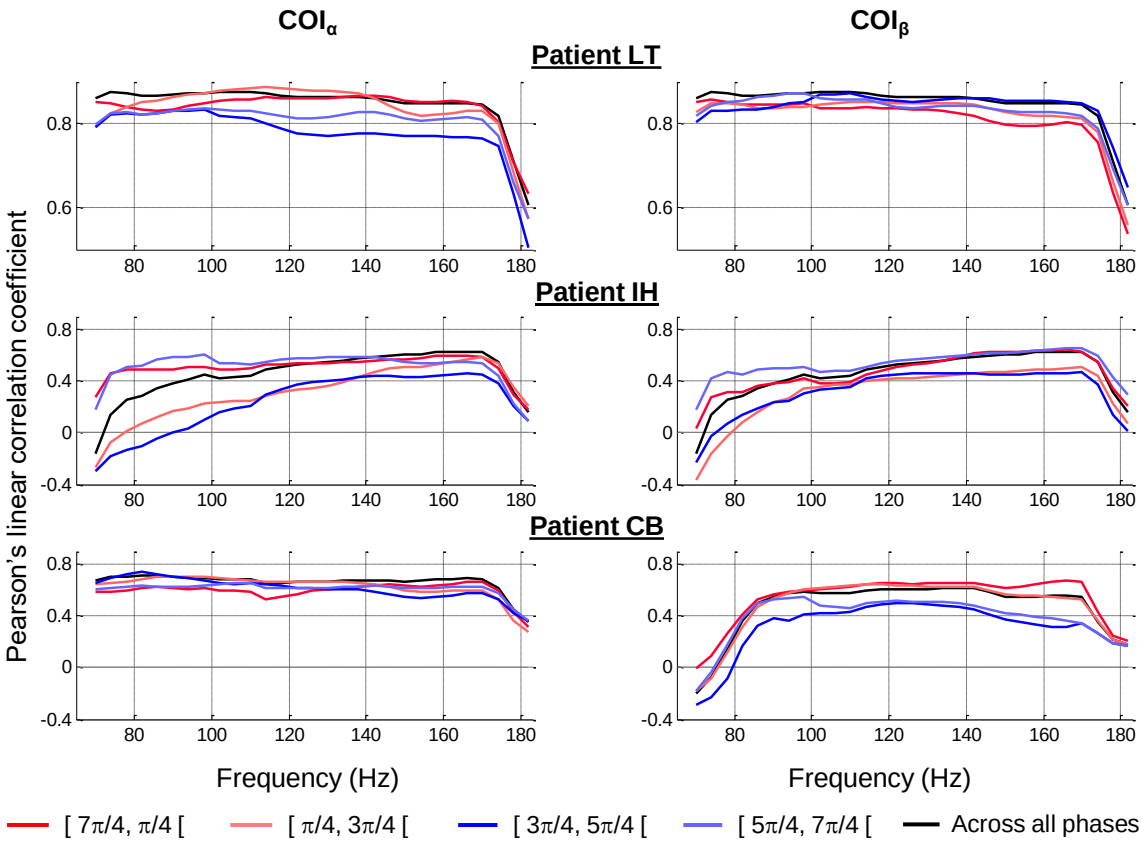

Figure 5-6 Influence of the EEG α and β phases in the EEG γ power - BOLD amplitude correlation. Pearson's linear correlation coefficients between the power of multiple EEG frequency components and the amplitude of the finger tapping - related BOLD time course, when the γ power was segmented according to the α phase (on the left) or the β phase (on the right). The curve colour identifies the phase bin according to which the γ power was segmented.

5.3.3 EEG PAC and the BOLD signal amplitude relationship (experiment 3)

5.3.3.1 PAC-derived BOLD predictors

The z-scored PAC strength values for the frequency pairs with a significant PAC effect (p<0.05, Bonferroni correction) are shown in **Figure 5-7**. No significant PAC effect was found for the α band of patients LT and CB; thus, no $PAC_{\alpha\gamma}$ regressors were defined for these patients and only the $PAC_{\beta\gamma}$ regressors were used for the subsequent analyses.

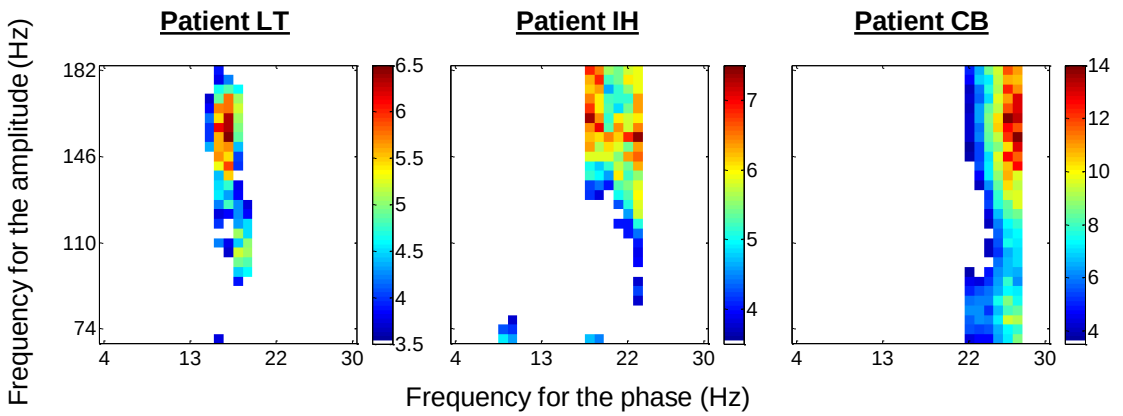

Figure 5-7 { α, γ } and { β, γ } frequency pairs of interest. Phase-amplitude comodulogram plots (z-scored PAC strength values) for the patient-specific α and β bands, obtained with the Canolty metric (p < 0.05; corrected for multiple comparisons using Bonferroni criterion).

The phase-amplitude comodulogram plots were qualitatively similar across the three PAC strength metrics implemented (see Appendix A - A2.1.1).

5.3.3.2 BOLD model

The t-values obtained for the $PAC_{\beta\gamma}$, P_{α}, P_{β}, and P_{γ} effects, after estimating the models $MPAC_{\beta\gamma}$, $MP_{\alpha,\beta\gamma}$, $MP_{\beta,\beta\gamma}$, $MP_{\gamma,\beta\gamma}$, respectively, are shown in **Figure 5-8**. The following regressors explained a significant amount of additional variance of the amplitude of the BOLD signal: $PAC_{\beta\gamma}$ in 2/3 patients, and P_{α} in 1/3 patients, and P_{γ} in 2/3 patients. Furthermore, $PAC_{\alpha\gamma}$, $PAC_{\beta\gamma}$, P_{α} , and P_{β} were negatively, and P_{γ} was positively, correlated with the amplitude of the BOLD signal, in 3/3 patients (**Figure 5-9**).

Regarding patient IH's four models including the $PAC_{\alpha\gamma}$ regressor ($MPAC_{\alpha\gamma}$, $MP_{\alpha,\alpha\gamma}$, $MP_{\beta,\alpha\gamma}$, $MP_{\gamma,\alpha\gamma}$), P_{γ} was the only effect that explained additional variance (results not shown).

The significance of the t-values for the $PAC_{\beta\gamma}$, P_{α}, P_{β}, and P_{γ} effects depends on PAC strength metric and on the duration of the epoch of data used to estimate the strength of PAC (Appendix A - A2.1.2, and A2.2, respectively); however the trend $PAC_{\beta\gamma}$ explains variance in addition to P_{α}, P_{β}, and P_{γ}, while P_{β} does not in addition to $PAC_{\beta\gamma}$, P_{α}, and P_{γ}, is present across metrics and epoch durations.

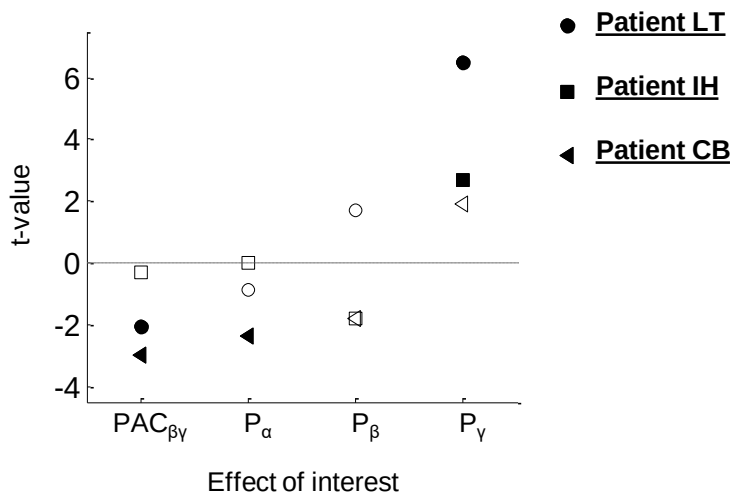

Figure 5-8 BOLD signal changes GLM results. t-values for the $PAC_{\beta\gamma}$, P_α, P_β, and P_γ effects. Different shapes represent different patients. Filled shapes represent t-values with $p < 0.05$.

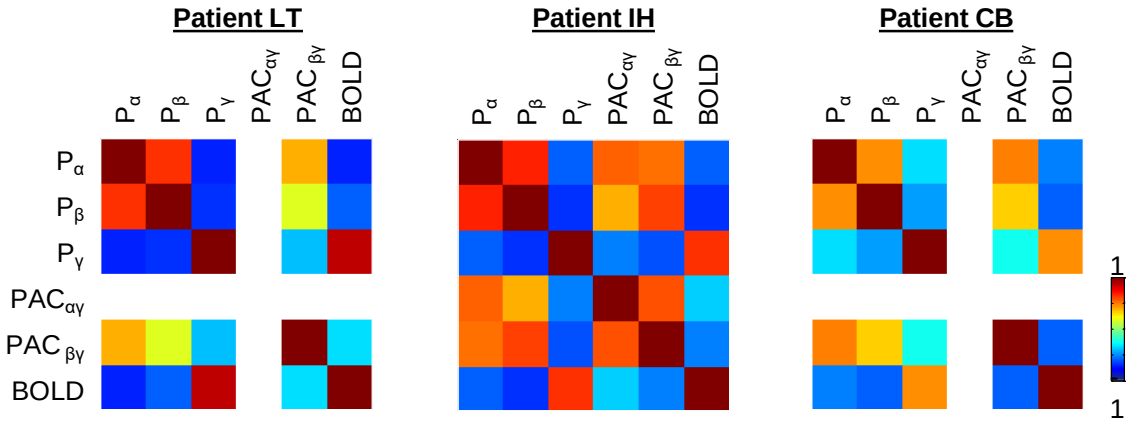

Figure 5-9 Cross-correlation matrices. Pairwise Pearson's linear correlation coefficients for all EEG-derived regressors and BOLD time course of interest. No values are shown for $PAC_{\alpha\gamma}$ for patient LT and CB because no significant PAC effect was found for the α band of these patients.

5.4 Discussion

We investigated the correlation between the power of multiple EEG frequency components and the amplitude of the simultaneous finger tapping - related BOLD changes; the influence of the phase of the α and β components on this correlation; and whether fluctuations in the $PAC_{\alpha\gamma}$ or $PAC_{\beta\gamma}$ strength explained variance of the amplitude of the BOLD signal that was not explained by a combination of α, β, and γ band powers. In line with previous studies using LFP and fMRI data simultaneously recorded in animals, or ECoG and fMRI data sequentially recorded in humans, we found positive correlation coefficients for the HF (> 70 Hz) EEG activities, and negative correlation coefficients for the LF (4 – 30 Hz) EEG activities, and the $PAC_{\beta\gamma}$ (and $PAC_{\alpha\gamma}$) strength. We also found that the phase of α and β activities seems to have an influence on how the power of the γ components correlate with the amplitude of the BOLD signal, and, more importantly, that the $PAC_{\beta\gamma}$ strength explains variance of amplitude of the BOLD signal that is not explained by a linear combination of α, β, and γ band powers.

5.4.1 EEG power and the BOLD signal amplitude relationship

In line with previous studies using ECoG and fMRI data sequentially acquired in humans during sensory-motor (Hermes et al., 2012; Siero et al., 2013) or cognitive (Conner et al., 2011; Khursheed et al., 2011; Kunii et al., 2013) functions, we found positive correlations between the BOLD signal amplitude and the power of the HF EEG activities, and negative correlations for the power of the LF EEG activities. The ECoG contact pairs located to up to 10 millimetres apart from the voxel that showed the maximum t-value for the finger tapping boxcar regressor were among the group of three contact pairs that showed the largest (positive and negative) correlation coefficients, in general. Perhaps due to spatial displacement between the EEG activity and the BOLD response, a possible consequence of fMRI data distortion in the surroundings of the metallic contacts, this was not observed for Patient IH.

We found that the phase of α and β EEG activity has an influence on the correlation between the power of the γ EEG activities and the amplitude of the BOLD response, which suggests that the LF phase may be worth considering when investigating the electro-haemodynamic coupling function.

5.4.2 EEG PAC and the BOLD signal amplitude relationship

To the best of our knowledge, this is the first study correlating ongoing fluctuations in the PAC strength with ongoing fluctuations in the amplitude of the simultaneous BOLD signal. The closest previous study is the work by Miller et al. (2012), who used ECoG and BOLD fMRI data sequentially recorded in two patients performing the same finger tapping task. They investigated the spatial overlap between the statistically significant movement related BOLD changes (found with a whole brain GLM analysis, using a boxcar regressor) and the movement related EEG power and PAC strength changes. The movement related EEG power and PAC strength changes were computed as the ratio between the power / PAC strength during movement and at rest, as well as the absolute PAC strength at rest; they were computed for every contact over the motor cortex, each resulting in a unique value per contact. Miller et al. (2012) found that the spatial overlap between the BOLD changes at the pre- and post- central gyri and the ECoG measures changes was the greatest for the β band power; good for the γ broadband power (yet more spatially restricted than for the β band power), and the lowest for the PAC strength measures.

5.4.2.1 PAC strength - derived BOLD predictors

In line with previous studies reporting that PAC is augmented during rest preceding and/or following movement, and decreased during movement execution (Miller et al., 2012; Yanagisawa et al., 2012), we found that both $PAC_{\alpha\gamma}$ and $PAC_{\beta\gamma}$ strengths were negatively correlated with the amplitude of the finger tapping related BOLD changes. Yanagisawa et al. (2012) used ECoG to investigate movement-related PAC in the human sensorimotor cortex, and found that the α (10 – 14 Hz) phase was strongly coupled to the high-γ (80 – 150 Hz) amplitude in the waiting period (> 2 seconds before execution), at the contacts with movement-selective

high-γ amplitude during movement execution; but attenuated at the time of movement execution, suggesting that γ was "released" from the phase of α, to build a motor representation with phase-independent activity. Similarly, Miller et al. (2012) found a strong coupling between the β phase and the γ broadband spectral changes (Manning et al., 2009; Miller, 2010), especially in peri-central motor areas, present during rest, but selectively diminished during movement, along with the amplitude of the β activity.

5.4.2.2 BOLD signal variance explained by EEG PAC and power

We found that the $PAC_{\beta\gamma}$ strength explained a significant amount of additional variance of the amplitude of the finger tapping related BOLD changes, in relation to α, β, and γ band powers, in general. The PAC strength has been found to be entrained to behavioural events, dynamically and independently modulated in multiple task-relevant areas (Tort et al., 2008), and strongly correlated to the level of performance in a learning task (Tort et al., 2009). The PAC phenomenon combines information regarding both LF and HF electrophysiological activities, and it has been hypothesised to be an efficient mechanism to integrate fast, spike-based computation and communication with slower, external and internal state events, guiding perception, cognition, and action (Canolty and Knight, 2010). The phase of the LF activities (δ, θ, α, or β), in turn, has been shown to play an important role in the amplification of sensory inputs (Fries et al., 2002; Lakatos et al., 2007, 2005; Womelsdorf et al., 2006), attention (Fries, 2001; Lakatos et al., 2008), and behavioural responses (Jones et al., 2002; Lakatos et al., 2008; Praamstra et al., 2006; Schroeder and Lakatos, 2009; Womelsdorf et al., 2006), and it has been hypothesised to modulate cortical excitability (Fries, 2005; Lakatos et al., 2013; John E Lisman and Jensen, 2013; Pachitariu et al., 2015; Reig et al., 2015). At a small-scale level, the neuronal response to a particular stimulus seems to be dependent on its timing relative to the phase of the ongoing LF activity (Lakatos et al., 2013). At a large-scale level, the effective gain of long-range communication across brain areas seems to be modulated by the phase of the ongoing LF activity (Voytek et al., 2015). Therefore, PAC strength and LF band power fluctuations may have different neurophysiological origins (e.g.: they may result from the activity of different populations of neurons or from different behaviours of the same population). Different origins might be associated with different metabolic demands, which would explain the independent variance of the amplitude of the BOLD signal explained by the $PAC_{\beta\gamma}$ strength and the β band power. Interestingly, if the β activity is, in some way, equivalent to the θ activity, our hypothesis is compatible with "the θ - γ neural code" theory (Lisman and Jensen, 2013), according to which different ensembles of cells are active at different γ cycles within the θ cycle.

While, in general, $PAC_{\beta\gamma}$ explained a significant amount of BOLD signal variance in addition to a combination of α, β, and γ band powers; the β band power did not in addition to a combination of $PAC_{\beta\gamma}$ strength, α, and γ band powers. Magri et al. (2012) used LFP and BOLD data simultaneously recorded in the visual cortices of anesthetised monkeys during spontaneous activity to investigate the statistical dependency between the two signals; these authors found that while the γ (40 - 100 Hz) power was the most informative about the amplitude of the BOLD

signal, both α and β band powers carried additional information, largely complementary to that carried by the γ band power. Since Magri et al. (2012) did not take into account the strength of $PAC_{\beta\gamma}$, we can hypothesise that the variance explained by the β band power in addition to the γ band power, found by Magri et al. (2012), is better explained by the strength of $PAC_{\beta\gamma}$, in our data.

To conclude, our findings suggest that including both PAC strength and power based regressors, or even the PAC strength regressor instead of the respective LF power regressor, is likely to increase the sensitivity of the BOLD signal model, in circumstances where significant PAC strength fluctuations are observed.

5.4.3 Methodological aspects

5.4.3.1 Electrical stimulation results and contacts of interest (COI)

During the pre-surgical evaluation, the clinicians performed an electrical stimulation study to map the motor function of each patient, i.e., to determine which ECoG contacts covered functional motor areas; the results of this study are shown in **Figure 5-4 C**. By comparing **Figure 5-4 B** and **Figure 5-4 C**, we confirm that the largest differences between the areas under the contralateral and ipsilateral spectra (ΔS_α, ΔS_β, and ΔS_γ) were found at, or nearby, the motor function related ECoG contact pairs identified by electrical stimulation. The good spatial concordance between the electrical stimulation findings and the largest ΔS_α, ΔS_β, and ΔS_γ corroborate our initial assumption that these differences were a good criterion to select finger tapping related EEG time courses.

5.4.3.2 Patient-specific frequency bands

The γ band of interest was kept as [70 – 182] Hz because no obvious peak was found in this frequency range for the COI_γ harmonic power spectrum. Interestingly, recent studies showed that the EEG arrhythmic (broadband) activity in the γ band is a better predictor of the BOLD signal amplitude than the rhythmic activity in the same frequency band (Nguyen et al., 2015; Winawer et al., 2013). These studies suggest that restricting our analysis to a narrower γ band, even if it would comprise mainly rhythmic activity, would reduce the significance of the correlation eventually found between the γ band power and the amplitude of the BOLD signal.

5.4.4 Technical limitations

Part of the electrophysiological data from patient KB' (in particular, two electrodes placed within the motor cortex[13]) was not possible to correct for the gradient artefact due to saturation during the recording; therefore, it had to be discarded. While, finger tapping related EEG power changes in the γ band ($\Delta S_\gamma > 0$; see § 5.2.1.5) were found in all the other patients (LT, BS, MR, HD, IH, and CB), suggesting that they had performed the task, to some degree; statistically

[13] Only depth EEG was recorded for patients BS and KB.

significant finger tapping related BOLD changes were only found in half of them (LT, IH, and CB). These observations suggest that the task design was not powerful enough to lead to significant BOLD changes (note that while LT, IH and CB performed five blocks of contralateral finger tapping, patients BS, MR, and HD, performed a maximum of three, due to the intercalation with rest), and/or there was an apparent absence of BOLD changes despite the presence of neuronal activity, may be due to partial volume effects in fMRI measurements, a consequence of the limited spatial resolution of the fMRI acquisition, and/or fMRI signal dropout and diminished SNR in the surroundings of the icEEG contacts, a consequence of magnetic susceptibility and shielding effects caused by the presence of these metallic contacts.

The temporal resolution of fMRI data (3 seconds) is another a limitation of this work. A higher temporal sampling rate would increase the number of fMRI data points per condition (contralateral, ipsilateral finger tapping, rest), which is likely to facilitate the detection of finger tapping related BOLD changes. It would also allow us to exploit better the temporal richness of the EEG signal; however, to a limit, given the inherent slow dynamics of the BOLD signal. Improving the quality of the EEG data simultaneously recorded with fMRI, by minimising the temporal variability of any residual MR-related artefacts, while maximising the cut-off frequency of the hardware low-pass filter used, would allow us to explore higher EEG frequency ranges and maybe improve the accuracy of the EEG-derived features.

5.4.5 Future work

Diseased-related differences in the PAC strength have also been reported (Allen et al., 2011; de Hemptinne et al., 2013). For example, deHemptinne et al. (2013) found stronger PAC $_{\beta\ \text{broadband-}\gamma}$ (β: 13 – 30 Hz; broadband-γ: 50 – 300 Hz) at the primary motor cortex (M1) arm area of patient with Parkinson disease (PD), when compared with patients with primary craniocervical dystonia but normal arm function or patients with epilepsy, both during rest and movement periods; strong cross-structure PAC (sub-thalamic nucleus (STN) β phase - M1 wide-γ amplitude) in PD patients; and strong STN PAC $_{\beta\ \text{narrowband--}\gamma}$ (narrowband-γ: 250 – 350 Hz) in half of the PD patients, using icEEG data (ECoG electrodes implanted over M1; deep brain stimulation electrodes implanted at the STD) recorded during an arm movement task. Of particular relevance to us are the studies investigating PAC in the context of epilepsy (Alvarado-Rojas et al., 2011; Colic et al., 2013; Guirgis et al., 2013; Ibrahim et al., 2014; Vanhatalo et al., 2004; Weiss et al., 2013). For example, Colic et al. (2013) used icEEG data to investigate PAC during seizure-like events (SLE) in MeCP2-deficient mouse models of the Rett syndrome (a neurodevelopmental condition often associated with seizures), and found a stronger PAC $_{\text{LF broadband-}\gamma}$ (LF: 6 – 10 Hz; broadband-γ: 200 – 600 Hz) during SLE, in females, but not in males, which they argue might be related with the fact that the Rett syndrome affects primarily females. A study in humans, Vanhatalo et al. (2004), found that the phase of infra-slow oscillations (0.02 - 0.2 Hz) was robustly correlated with the amplitude of faster EEG oscillations (1 – 100 Hz), and the occurrence of interictal events and K complexes (EEG waveform occurring during stage 2 of NREM sleep), on scalp EEG during sleep. Another study in humans, Guirgis et al. (2013),

found strong $PAC_{\delta\gamma}$ strength (δ: 0.5 – 4 Hz; γ: 30 – 450 Hz, variable across patients) at the seizure onset and termination, regardless of the dynamics present within the seizure episode itself, using ECoG data recorded from three patients with temporal lobe epilepsy. Both Vanhatalo et al. (2004) and Guirgis et al. (2013) were focused on the temporal dynamics of PAC, but interesting observations regarding the spatial relationship between the existence of PAC and the origin of epileptic activity have also been reported. For example, Weiss et al. (2013) found that sustained, repetitive transient increases in γ (80 – 150 Hz) amplitude were coupled to lower frequency (1 – 25 Hz) phases, and correlated with strong MUA across the ictal "core" (territories fully recruited into the seizure, following passage of the ictal wavefront characterised by intense neuronal bursting), but not across the ictal "penumbra" (territories on the periphery of the ictal core, demonstrating low level, desynchronized firing, that can be recruited intermittently into the ictal core), using microelectrode arrays placed over the cortical surface of four patients (ten seizures). Furthermore, they found that the strength of this coupling consistently predicted the timing or failure of ictal invasion, while revealing a surprisingly small and slowly spreading ictal "core", surrounded by a far larger "penumbral territory". Another interesting example is Ibrahim et al. (2014), who found that $PAC_{LF\gamma}$ (LF: 6 – 14 Hz; γ: >80 Hz) was stronger in the SOZ than in the early propagation zone during the ictal period, but no significant PAC effect (no region or frequency combinations showed significant PAC) during the interictal periods, using ECoG data recorded from 17 patients undergoing epilepsy surgery. A different study aiming to predict ictal events, Alvarado-Rojas et al. (2011), found that the preferred phases of the majority of ECoG contacts placed over the epileptogenic areas converged to a patient-specific value (i.e. the preferred-phase spatial consistency increased) at least 10 minutes before the ictal event. The low and high frequency activities contributing with the phase and amplitude were also patient-specific.

In summary, the PAC strength may not only be related with the execution and performance of heathy brain functions; it may also be related with the temporal and spatial dynamics of pathological activity. Therefore, it would be interesting to investigate how the strength of PAC derived from an icEEG contact placed at the SOZ relates with the amplitude of the co-localised BOLD signal, as well as whether it explains variance in addition to either a linear combination of EEG power at multiple frequency bands or a frequency-weighted power metric (Kilner et al., 2005; Leite et al., 2013; Rosa et al., 2010).

5.5 Conclusion

Using ECoG and fMRI simultaneously recorded in humans, we found that the amplitude of the BOLD signal was negatively correlated with both PAC strength and power of the lower α and β EEG frequencies, and positively correlated with the power of the higher γ EEG frequencies. These findings were consistent with previous studies using LFP and fMRI simultaneous recorded in animals, and ECoG and fMRI data sequentially recorded in humans. More importantly, we found that the PAC strength explained additional variance of the BOLD signal in relation to α, β, and γ band powers, which not only suggests that we may increase the sensitivity

of EEG-informed fMRI studies by taking the PAC strength into account, but also that the power of LF activities and the strength of PAC may have different neurophysiological origins, and may therefore have different functional roles worth to keep investigating.

6

EEG sharp wave morphology and the BOLD signal[14]

[14] This chapter was adapted from Murta, T., Li H., Tierney, T., Chaudhary, U. J., Walker, M.C., Carmichael, D.W., Figueiredo, P., Lemieux, L., Phase-amplitude coupling and the BOLD signal: A study of the electro-haemodynamic coupling using simultaneously acquired intracranial EEG and fMRI data in humans. Neuroimage (under major revision)

The study described here aimed to shed further light on the neuronal basis of the BOLD signal, using the knowledge we have on the relationship between five sharp wave (the fast wave of an interictal epileptiform discharge (IED)) morphology and spatial field extent related features and the underlying neuronal activity. To achieve this, these EEG-derived features were compared in terms of their individual capability to predict the amplitude of the simultaneous and co-localised BOLD signal, as described in § 6.2. Here, we investigate the BOLD response related to epileptiform discharges, rather than to a normal physiological state (finger tapping), as in the previous chapter. This chapter starts with a brief description of previous findings and methodological aspects (closely related to icEEG data) that motivated this study.

6.1 Motivation

The morphology of the sharp wave is likely to reflect interesting aspects of the neuronal activity underlying its generation; the sharp wave amplitude and slope of the rising phase are thought to reflect the degree of neuronal synchrony (Einevoll et al., 2013); the sharp wave width and energy (area under the curve) are thought to reflect the duration of the underlying field potential (Gold et al., 2006); and the sharp wave spatial field extent is thought to reflect the spatial extent of the surrounding, synchronised sources of neuronal activity (Einevoll et al., 2013). Few studies have considered the sharp wave morphology as potentially informative for the prediction of the BOLD signal amplitude. Two studies in humans investigating the significance of the correlation between the amplitude of scalp EEG sharp waves and the amplitude of BOLD changes (Benar et al., 2002; LeVan et al., 2010a) found mixed results. Two studies in rats found a significant, positive correlation between the amplitude (and width (Geneslaw et al., 2011)) of LFP sharp waves and the amplitude of CBF changes (recorded using laser-Doppler flowmetry) (Geneslaw et al., 2011; Vanzetta et al., 2010).

In terms of morphology, spatiotemporal localisation, and field distribution, sharp wave features are more accurately estimated using icEEG than scalp EEG. However, the comparatively greater amount and complexity of information related to sharp waves (or any other type of epileptic activity) recorded on icEEG, poses a challenge to the modelling of the simultaneous BOLD changes. For example, in our icEEG data, sharp waves are observed at rates ranging from 0.17 to 1.7 event per second (see

; note that our fMRI sessions last for 600 seconds each). For very regular and frequent events, the conventional way of modelling all events as identical can result in an essentially flat BOLD predictor; a very inefficient fMRI “experimental design” that potentially limits the sensitivity of the study (Dale, 1999; Friston et al., 1999). Modelling strategies that introduce some variability based on event-by-event feature measurements may actually increase the efficiency of the model, and also exploit the variability of both signals better.

Taking advantage of the unique opportunity to analyse icEEG and BOLD data simultaneously recorded in humans, we compared five sharp wave features (amplitude, slope of the rising phase, width, energy, and spatial field extent) in terms of their individual capability to explain variance of the BOLD signal amplitude that was not explained by the sharp wave onset times.

We used the GLM framework to model the linear relationship between each feature, quantified event-by-event, from the most active icEEG contact pair, and the amplitude of the BOLD signal, within the immediate surroundings of this contact pair (likely to be in the immediate vicinity of the sharp wave generators). To the best of our knowledge, this is the first study using invasively recorded sharp waves and simultaneous, co-localised BOLD fMRI data to investigate which aspects of the sharp wave best explain the variance of the amplitude of the BOLD signal.

6.2 Methods

6.2.1 Patient selection

We analysed icEEG and fMRI data simultaneously recorded from the six patients (6/15) with ILAE classification (Wieser et al., 2008) of 1 (free of seizures between 14 and 49 months after the surgery, depending on the patient), i.e., those for whom the confidence regarding the location of the epileptic focus was the highest. The patients were asked to lie still with eyes closed during data acquisition. One (patient JR, HD, and IH) or two (patient MB, BS, and CB) 10-minute sessions of 200 fMRI volumes were acquired and analysed.

6.2.2 IED classification

IED events (**Figure 6-1**) were identified visually by an experienced EEG reviewer, and their onset time (maximum peak of the sharp wave) were marked in relation to the start of the icEEG recording. IED were then classified and grouped, according to their spatiotemporal localisation and field distribution. Each IED class was labelled as either: *focal*, if simultaneously observed in 2 - 4 contiguous contacts; *regional*, if simultaneously observed in 5 - 10 contiguous contacts that could span up to two gyri; *widespread*, if involving more than 10 contiguous contacts; or *non-contiguous*, if having a focal or regional field but also propagating to non-contiguous contacts. Additionally, the position of each manually placed IED marker was adjusted to the position of the peak value using an automated process applied on the 24 milliseconds - wide window centred at the manual mark, because the accurate IED parameterisation is reliant on the precise marking of the IED peak. Visual inspection of the realignment results confirmed the validity of this approach.

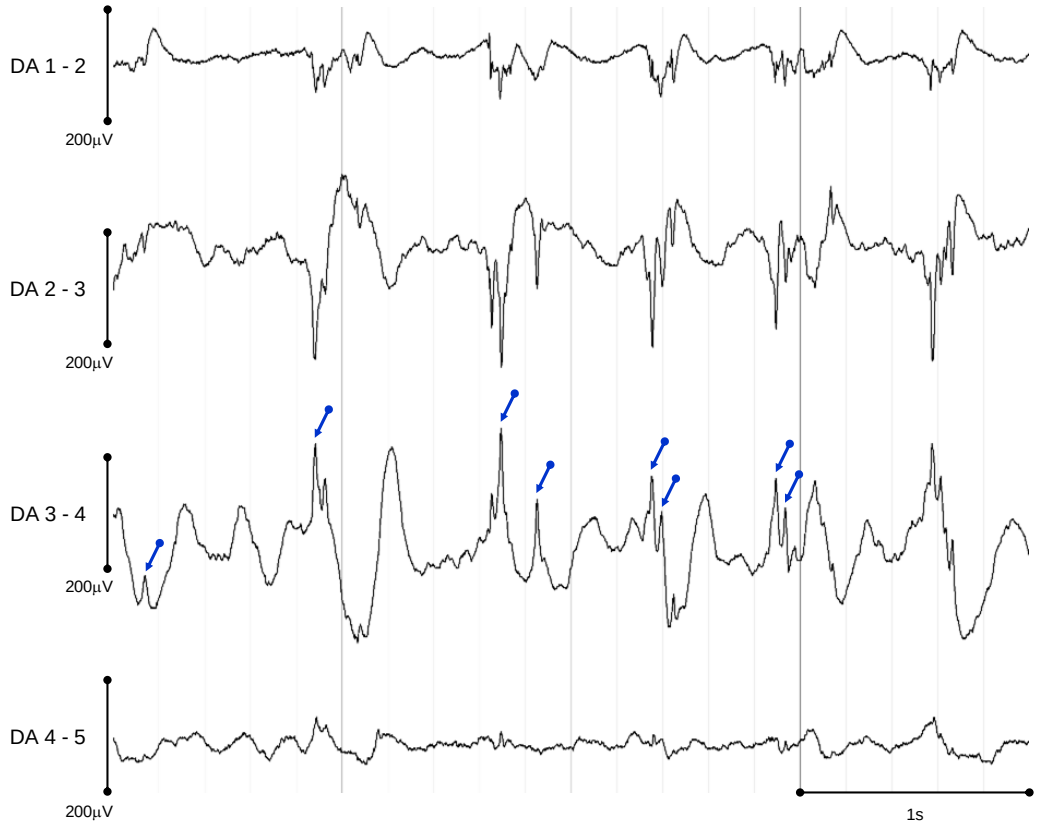

Figure 6-1 Representative EEG time courses (patient HD) showing sharp waves of different amplitudes and widths (blue arrows point at events visually marked at COI: DA 3 – 4).

6.2.3 Patient-specific contacts of interest (COI)

For each focal IED class and contact pair, the IED were averaged, and the contact pair showing the largest average focal IED was chosen as the contact pair of interest (COI) (see **Table 6-II** for details on the anatomical location of each COI). Since the BOLD changes in the immediate surroundings of a particular COI are expected to reflect all neuronal activity captured by the COI, all IED classes that shared the COI were grouped in a unique set of events of interest, called the $\boldsymbol{S}_{COI}$. For example, let the contact pair # 1 be the COI; **A** the focal IED class observed at contact pairs # 1 and 2; and **B** the regional IED class observed at contact pairs # 1, 2, 12 and 13, such that **A** and **B** constitute all IED classes that involve contact pair # 1. In this case, events in **A** and **B** are taken to form the set of events of interest: $S = \{\mathbf{A} \cup \mathbf{B}\}$. Through this process, IED were grouped in 10 $\boldsymbol{S}_{COI}$, across all patients (see **Table 6-I** for details on IED classes and numbers forming each $\boldsymbol{S}_{COI}$; see **Figure 6-2** for the average IED for each $\boldsymbol{S}_{COI}$).

Table 6-I Description of S_{COI} and sharp wave feature estimates for BOLD modelling. FW: focal plus more widespread, F: focal.

Patient ID	MB	BS			JR		HD		IH	CB
Number of fMRI sessions	2	2			1		1		1	2
Number of focal IED classes per patient	1	3			2		2		1	1
Set of events of interest ID	S_1	S_2	S_3	S_4	S_5	S_6	S_7	S_8	S_9	S_{10}
Classes of IED included in the BOLD model	FW	F	FW	FW	FW	FW	FW	F	FW	F
Number of IED visually marked at the COI	1630	209	470	253	397	613	993	194	887	191
Sharp wave feature estimates (mean ± standard deviation)										
Amplitude (μV)	71.15 ± 91.14	368.60 ± 395.52	78.62 ± 62.34	139.43 ± 241.95	101.38 ± 72.52	19.40 ± 28.51	47.11 ± 40.67	78.73 ± 66.86	41.18 ± 26.64	66.19 ± 53.36
Slope (μV / s)	4.67 ± 6.96	12.68 ± 18.04	6.45 ± 5.38	4.94 ± 8.75	7.85 ± 6.09	2.48 ± 3.77	3.77 ± 3.22	6.15 ± 5.68	3.46 ± 2.25	5.83 ± 4.96
Width (ms)	23.19 ± 6.83	40.89 ± 10.95	19.47 ± 4.08	48.68 ± 21.24	10.46 ± 2.10	8.91 ± 4.03	9.88 ± 2.90	10.81 ± 2.57	11.29 ± 4.49	21.30 ± 6.33
Energy (μV s)	1.78 ± 2.27	16.00 ± 16.51	1.48 ± 1.33	7.78 ± 12.97	2.06 ± 1.48	0.31 ± 0.49	1.01 ± 1.01	1.71 ± 1.58	1.03 ± 0.66	1.40 ±1.27
Spatial field extent (a.u.)	7.06 ± 1.61	14.85 ± 2.88	13.24 ± 2.47	14.18 ± 2.18	10.93 ± 2.76	9.45 ± 2.42	10.27 ± 1.70	9.63 ± 2.00	7.38 ± 1.61	17.32 ± 3.59

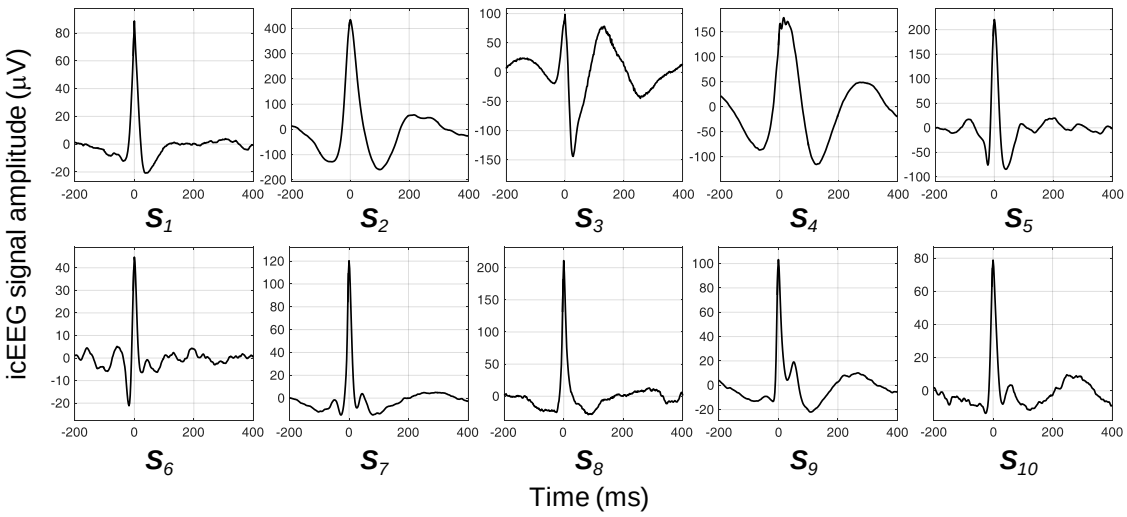

Figure 6-2 Average IED for each set of events of interest (S_{COI}).

Table 6-II IcEEG implantation characterisation: type of electrodes, number of contacts per electrode, and implantation scheme. TLE: Frontal lobe epilepsy, FLE: Frontal lobe epilepsy, R: right, L: left, A: anterior, M: medial, P: posterior, I: inferior, and S: superior. Intra-contact distances: 10 millimetres for grids, strips, and most depths; 5mm for high-density grids and medial contact pairs in some depths. The approximated location of each COI is highlighted with a green arrow (depth), or square (ECoG).

Patient ID	Type of epilepsy	Anatomical location of electrodes	Irritative Zone	Type of electrodes	Implantation scheme	COI type	COI anatomical location of	Intra-COI contacts distance (mm)	Set of events of interest
MB	TLE	- R (RA) and L (LA) amygdalae - R hippocampus L anterior (LAH) and posterior (LPH) hippocampus	R and L temporal lobes	five 6-contact depths	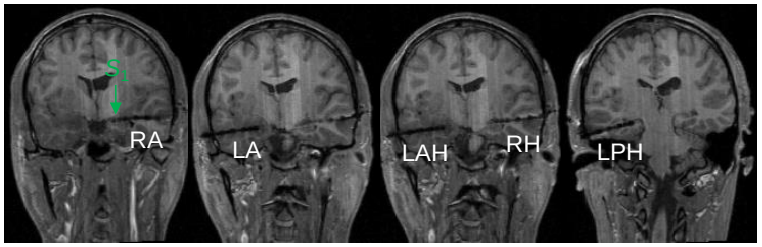	Depth	RA	5	S_1
BS	FLE	- R A (RAI) and P (RPI) insula - R A (RASMA) and P (RPSMA) supplementary sensorimotor areas - R A (RAC), M (RMC) and P (RPC) cingulum	R ASMA and R PSMA	two 6-contact depths, three 8-contact depths, two 10-contact depths	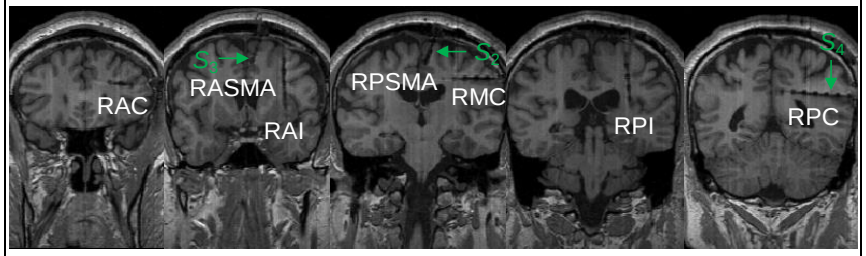	Depth	RPSMA	10	S_2
							RASMA	5	S_3
			R I parietal and M frontal gyrus				RPC	10	S_4

Patient ID	Type of epilepsy	Anatomical location of electrodes	Irritative Zone	Type of electrodes	Implantation illustration	COI type	COI anatomical location of	Intra-COI contacts distance (mm)	Set of events of interest
JR	FLE	- L superior (LSFG), middle (LMFG) and inferior frontal gyri - L precentral gyrus - L central sulcus and part of postcentral sulcus - L superior frontal sulcus - L postcentral regions	LSFG and LMFG	one 8x8 contact grid, two 4-contact depths, one 2x8 contact grid	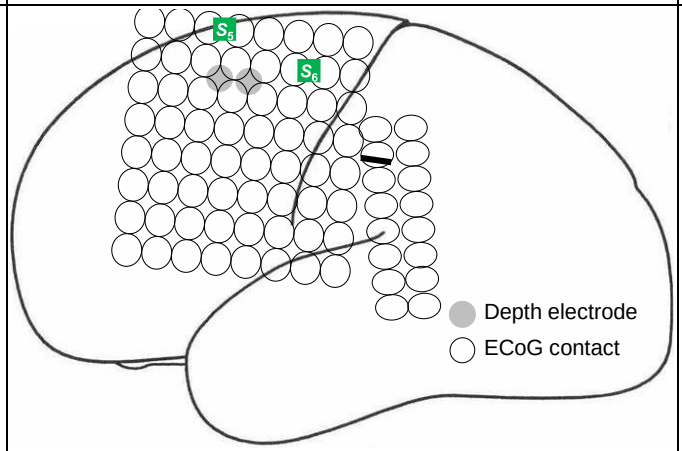	ECoG	LSFG and LMFG	10	S_5
							LSFG and LMFG	10	S_6
HD	FLE	- L frontal lobe (laterally and inferiorly) - LMFG and L I (LIFG) frontal gyri - L frontal pole	LIFG and LMFG	one 8x8 contact grid, one 2x8 contact grid, two 6-contact depths, two 6-contact strips	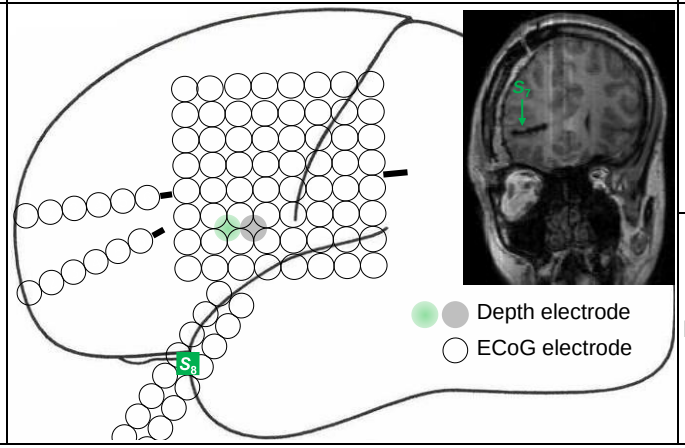	Depth	LIFG and LMFG	10	S_7
			L lateral orbitofrontal			ECoG	L lateral orbitofrontal	10	S_8

Patient ID	Type of epilepsy	Anatomical location of electrodes	Irritative Zone	Type of electrodes	Implantation illustration	COI type	COI anatomical location of	Intra-COI contacts distance (mm)	Set of events of interest
IH	FLE	- L frontal lobe (laterally and inferiorly) - L M (MFG) and I (IFG) frontal gyri - L temporal lobe	L IFG and MFG	one 6x8 contact grid, two 2x8 contact grids, ones 4x8 high-density contact grid, two 6-contact strips, two 6-contact depths	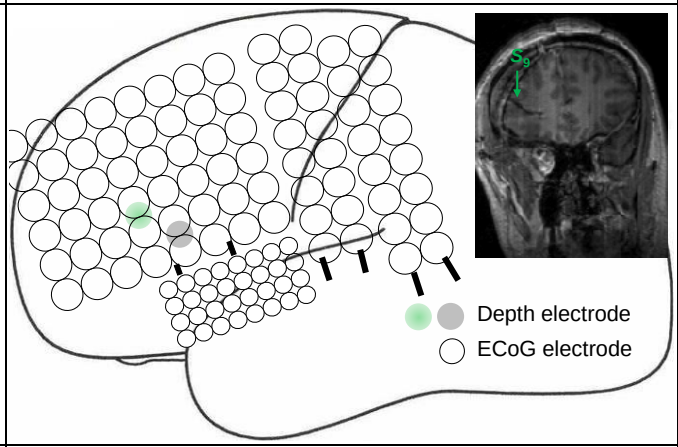	Depth	LIFG and LMFG	10	S_9
CB	FLE	- L frontal and parietal convexity - L frontal pole - L S frontal gyrus (LSFG) - L I frontal gyrus - L mesial frontal surface	LSFG (lateral and medial)	ones 8x8 contact grid, one 2x8 contact grid, one 8-contact strip, one 6-contact strip, one high-density 4x8 contact grid	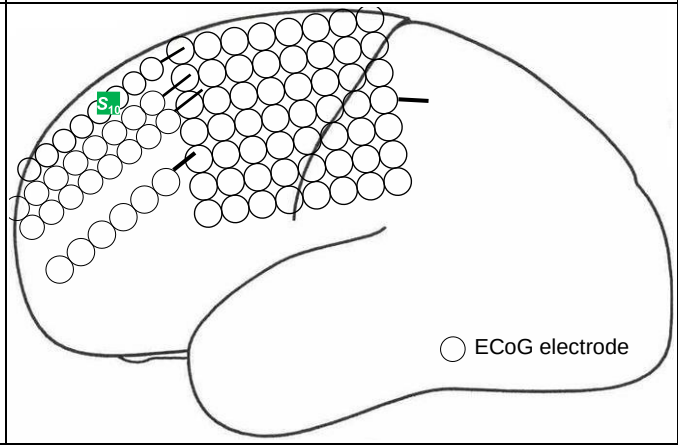	EcoG	LSFG	10	S_{10}

6.2.4 IED parameterisation

First, the EEG was high-pass filtered (low-cut-off at 3 Hz) and segmented into epochs of 600 milliseconds of duration, starting 200 milliseconds before the IED peak marker. For each event, in any given $\boldsymbol{S}_{COI}$, four sharp wave morphological features (**Figure 6-3**) and one sharp wave field extent feature were estimated, as described below. These features were estimated from single-trial IED estimates rather them from raw IED; the reason why is also described below.

The sharp wave amplitude, A, was computed as the voltage value at the peak within a 40 milliseconds - wide window, centred at the maximum of the (COI-specific) averaged IED (**Figure 6-3 A**).

The sharp wave width, W, was computed as the full-width at half maximum (FWHM):

$$W = t_{(V=0.5A)^+} - t_{(V=0.5A)^-} \tag{6-1}$$

where $t_{(V=0.5A)^-}$ and $t_{(V=0.5A)^+}$ represent the points preceding and following, respectively, the IED peak at which the signal is equal to 50% of A (**Figure 6-3 B**)

The sharp wave rising phase slope, S, was computed as the ratio:

$$S = \frac{0.8A - 0.2A}{t_{(V=0.8A)} - t_{(V=0.2A)}} \tag{6-2}$$

where $t_{(V=0.2A)}$ and $t_{(V=0.8A)}$ represent the points preceding the IED peak at which the signal is equal to 20% and 80% of A, respectively (**Figure 6-3 C**).

The sharp wave energy, E, was computed as the area under the curve of the event, over the interval $[t_{(V=0)^-}, t_{(V=0)^+}]$, where $t_{(V=0)^-}$ and $t_{(V=0)^+}$ represent the points preceding and following, respectively, the IED peak at which the signal first crosses 0 (**Figure 6-3 D**).

The sharp wave spatial field extent, SFE, was estimated as the sum of the absolute value of the Pearson correlation coefficients between the epoch time courses from the COI and remaining contacts:

$$SFE = \sum_{c \epsilon C \setminus \{COI\}} |corr(e_{COI}, e_c)| \tag{6-3}$$

where C represents all contacts, e_{COI} is the epoch time course from the COI, e_c is the epoch time course from the contact c, and $corr(\ ,\ )$ stands for the linear Pearson correlation coefficient (computed with the Matlab function *corr*).

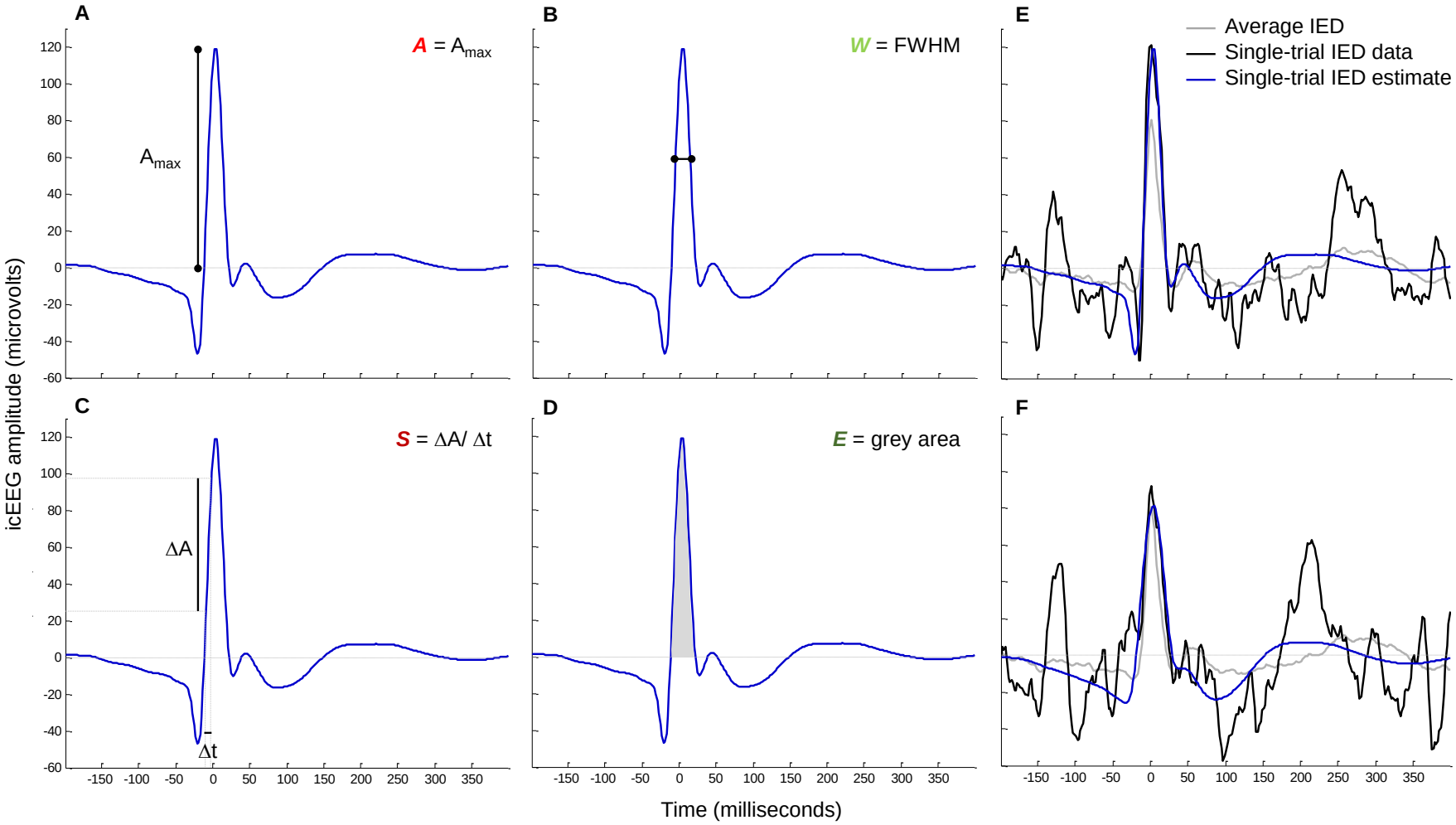

Figure 6-3 **A** - **D** Sharp wave morphology-based features: **A** amplitude, **B** width, **C** rising phase slope, **D** energy, overlaid on an example of a single-trial IED estimate. **E** - **F** Single-trial IED estimates examples. The original IED is displayed in black, the average IED is displayed in grey, and the estimated IED is displayed in blue.

The morphological features were estimated using the EEG analysis toolbox STEP1 (http://iannettilab.webnode.com; Hu et al. (2011)); the spatial field extent was estimated with a Matlab routine developed by me. In brief, the STEP1 processing consists of (1) computing the (COI-specific) average IED; (2) generating a variability matrix that models the variability of the latency and morphology across events (see below for details on how the variability matrix is built); (3) performing a principal component analysis (PCA) on this variability matrix; (4) using the three principal components (PC) that explain the most variance of the variability matrix as the basis set of a linear model, which is then used to obtain the single-trial IED estimate of a raw event. We chose to use a PCA-based method to obtain the single-trial IED estimates to overcome issues concerning the use of the raw signal; most importantly, the strong dependence of the accuracy of the feature estimate on the SNR of the raw signal. Let us, for instance, take the case shown in **Figure 6-3 F**; the energy estimate using the raw signal (black curve) would be contaminated by the artefact peaking 25 milliseconds before the sharp wave peak because the feature energy is computed as the area under the signal curve, over the interval [$t(V{=}0)-$, $t(V{=}0)+$], where $t(V{=}0)-$ and $t(V{=}0)+$ represent the points preceding and following the sharp wave peak, respectively, at which the signal first crosses 0. We chose to use the first three PC to compute the single-trial IED estimates given the way in which the variability matrix is built (by time shifting and changing the width of the (COI-specific) average IED (Hu et al., 2011)). In brief, the variability matrix is an array of multiple plausible synthetic IED, i.e., a basis set, derived from each (COI-specific) average IED and representing every combination of the following manipulations: shifting (by -50 to +50 milliseconds in steps of 5 milliseconds) and changing the width (by a compression factor ranging from 1 to 2, in steps of 0.05) of the (COI-specific) average IED, in relation to each single-trial IED. Therefore, the variability matrix is a set of base functions that differ in their shape, and can be linearly combined to create each single-trial IED estimate. The PCA on the variability matrix is performed to identify the three PC that explain most of the variance of the events shape variability. By linearly combining these PC, we obtain (COI-specific) IED estimates, that are fitted to each raw IED, and from which we can quantity the features of interest. Note that the amplitude variability was not explicitly modelled in the variability matrix but it is captured by the component's weights that result from the PCA. The three PC that explain most variance represent the average event, its temporal derivative, and its temporal dispersion (as shown in Hu et al., 2011) because the construction of the variability matrix is explicitly based on the events shape variability. Note that STEP1 was designed to remove the nefarious effects of noise, and therefore to reduce the proportion of variance which represents noise (i.e. overfitting) by choosing a basis set that captures well the key features of waveforms that most neurophysiologists would recognise as an IED.

The mean and standard deviation of each sharp wave feature are presented in **Table 6-I**.

6.2.5 Models of IED-related BOLD changes

For each $\boldsymbol{S}_{COI}$, a total of six GLM of BOLD changes were estimated: M_O, M_{OA}, M_{OW}, M_{OS}, M_{OE}, and M_{OSFE}, corresponding to the following effects of interest, respectively: IED onsets alone, IED

onsets and amplitude, IED onsets and width, IED onsets and slope, IED onsets and energy, and IED onsets and spatial field extent. See **Table 6-I** for details on which IED classes were modelled for each $\boldsymbol{S}_{COI}$. Let D_O, D_{OA}, D_{OW}, D_{OS}, D_{OE}, and D_{OSFE}, be the respective design matrices of these models. D_O, the design matrix of the basic model, comprised IED onset times convolved with the canonical HRF (regressor O), and the following confounding effects (regressors C): 24 movement related confounds (6 realignment parameters, and their Volterra expansion (Friston et al., 1996)), and 6 fMRI physiological noise related confounds, which include high-frequency noise (Tierney et al., 2015). Each of the design matrices, corresponding to a feature, comprised the respective IED feature, convolved with the canonical HRF, as a modulatory effect of the amplitude of the stick functions placed at the IED onsets, such that D_{OA} = [A O C]; D_{OW} = [W O C]; D_{OS} = [S O C]; D_{OE} = [E O C]; and D_{OSFE} = [SFE O C], and the regressors A, W, S, E and SFE are orthogonalised in relation to the IED onsets regressor O.

6.2.5.1 Variance explained quantification

To quantify the amount of BOLD signal, y, explained by a given model M, the coefficient of determination adjusted for the number of degrees of freedom, R^2adj, was computed as:

$$R^2adj(M) = 1 - \frac{T-1}{\mathrm{T}-P-1}\frac{\sum_{i=1}^{T}(y_i - y_i')^2}{\sum_{i=1}^{T}(y_i - \bar{\mathrm{y}})^2} \qquad (6\text{-}4)$$

Where T is the number of fMRI scans, P is the number of regressors in the model, $\mathrm{y_i}$ and $\mathrm{y_i}'$ are respectively the ith values of y and y' (the estimation of y obtained with M), and $\bar{y}$ is the temporal average of y. R^2adj was chosen because it takes into account the number of degrees of freedom of the model, and expresses the degree to which the additional regressor is capable of explaining more variance than what would be expected by chance (if a random regressor was included).

To quantify the amount of BOLD signal, y, explained by a given regressor or set of regressors R, in addition to a regressor or set of regressors O, we computed the variance explained by R, $VE(R)$, which corresponds to the difference between the R^2adj obtained for the more complete model comprising both the set of regressors O and R, M_{OR}, and the R^2adj obtained for the simpler (and nested in M_{OR}) model comprising only the regressor O, M_O (Bianciardi et al., 2009b; Shmueli et al., 2007), such that:

$$VE(R) = R^2adj(M_{OR}) - R^2adj(M_O) \qquad (6\text{-}5)$$

6.2.5.2 Voxels of interest

All models (M_{OA}, M_{OW}, M_{OS}, M_{OE}, and M_{OSFE}) were estimated using the toolbox SPM12 (http://www.fil.ion.ucl.ac.uk/spm). Let us call the point halfway between the two contacts constituting the COI, the point of interest (POI). The voxels within a distance of 10 millimetres from the POI and showing either BOLD signal increases or decreases in relation to both the IED onset and feature, i.e., a significant correlation ($p < 0.05$, uncorrected) with a positive or negative linear combination of the 2 regressors of interest (O+A, O+W, O+S, O+E, and O+SFE), were

considered of interest. To find them, we used the t-contrasts [1 1 0 …] (pBOLD voxels) and [-1 -1 0 …] (nBOLD voxels), respectively. The variance explained was averaged across the pBOLD and nBOLD voxels, separately.

6.3 Results

Representative examples of voxels of interest are presented in **Figure 6-4**.

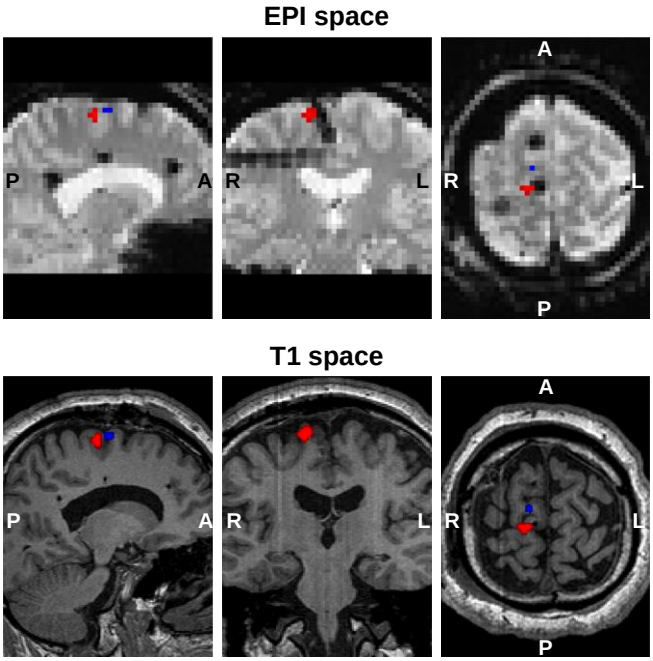

Figure 6-4 Representative example (patient BS, events of interest set: S_2, see

) of IED onset and width related BOLD changes ($p < 0.05$, uncorrected), within a 10mm radius sphere centred at middle distance between the pair of icEEG contacts that shows the largest average IED (COI: PSMA 3 – 4). Positive BOLD changes (pBOLD) are showed in red, and negative BOLD changes (nBOLD) are showed in blue.

Average VE values, for each IED feature, are shown in **Figure 6-5**. The average VE values for the IED feature W were above 0 ($p < 0.05$) in 9/10 sets for the BOLD increases; and 8/10 for the BOLD decreases (**Figure 6-5 A** and **C**). This effect was statistically significant at the group level (**Figure 6-5 B** and **D**). The feature E showed a trend towards explaining more variance (p = 0.092 for the BOLD increases; and p = 0.031 for the BOLD decreases) (**Figure 6-5 B** and **D**).

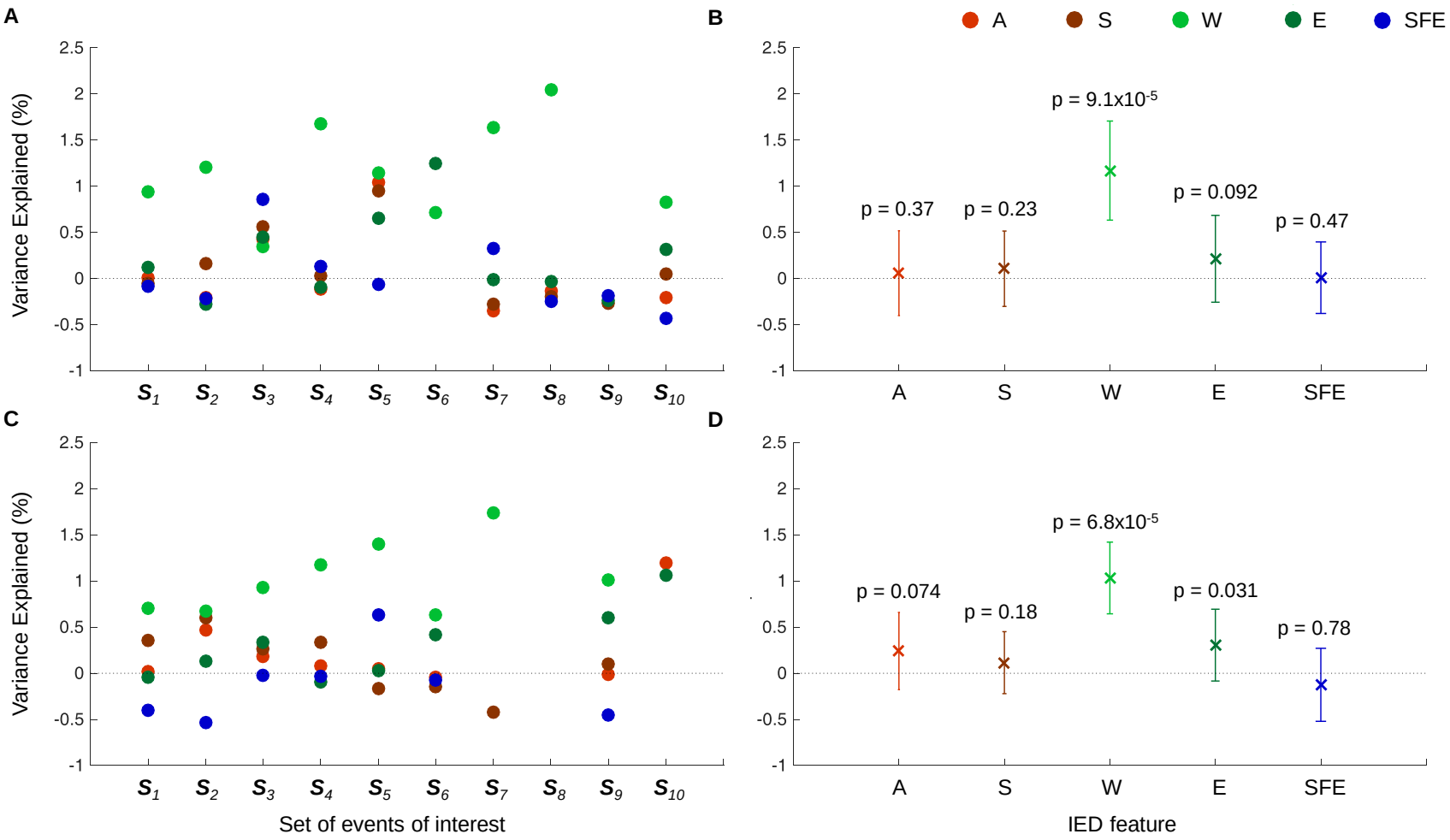

Figure 6-5 Variance explained (VE) results. Experiments level analysis: **A** Average VE values, by modulatory feature; for the set of voxels comprised in pBOLD, and **D** in nBOLD. Group level analysis: **B** Average VE and respective standard deviation values, by modulatory feature; for the set of voxels comprised in pBOLD, and **D** in nBOLD. Undefined values correspond to cases where no voxel had a large enough *t-value* to survive the threshold used ($p < 0.05$, uncorrected).

6.4 Discussion

We investigated the individual capability of four sharp wave morphological (amplitude, width, slope of the rising phase, and energy) and one spatial field extent feature to explain variance of the amplitude of the simultaneous and co-localised BOLD signal that was not explained by the sharp wave onset times. Among these features, the width was the only one found to explain a significant amount of additional variance, suggesting that the amplitude of the BOLD signal depends more on the duration of the underlying field potential (reflected in the sharp wave width) than on the degree of neuronal activity synchrony (reflected in the sharp wave amplitude).

Previous work using a pharmacologic animal model of epilepsy found significant positive correlations between the amplitude and duration of epileptic sharp waves, recorded with LFP, and the amplitude of CBF changes, recorded simultaneously with laser-Doppler flowmetry (Geneslaw et al., 2011). A metabolic-hemodynamic model proposed by Sotero and Trujillo-Barreto (2008, 2007), foresees amplitude, duration, and area under the excitatory curve of the sharp wave to be good predictors of the amplitude of the BOLD signal (Voges et al., 2012). In the standard model of the BOLD effect, an increase in neuronal activity induces an increase in CBF, which provides more oxygen and glucose to the tissues; if the increase in CBF exceeds the simultaneous increase in oxygen consumption, the local concentration of deoxyhaemoglobin decreases and the intensity of the BOLD effect increases (Buxton, 2012). Due to the likely coupling between CBF and BOLD signals (Carmichael et al., 2008), the main finding of this study, i.e., the width of the sharp wave correlates significantly with the amplitude of the co-localised BOLD signal, is in line with both Geneslaw et al. (2011) and Voges et al. (2012). Possible explanations for our findings are discussed in the following subsections.

6.4.1 Sharp wave width neurophysiological correlates and the BOLD signal

Any type of transmembrane current across an excitable membrane contributes to an extracellular field potential that can be measured as LFP or icEEG. This field potential is the superposition of all ionic processes, ranging from fast action potentials to the slowest fluctuations in glia. All currents in the brain superimpose at any given point in space to yield an electrical (differential) potential, at that location. Thus, any transmembrane current, irrespective of its origin, leads to an extracellular voltage deflection, whose characteristics depend on the proportional contribution of the multiple sources and various properties of the brain tissue (Buzsaki et al., 2012). The amplitude and spatiotemporal width of the LFP signal are known to be markedly shaped by the impinging pattern of postsynaptic currents and membrane characteristics (Reimann et al., 2013). Therefore, the width (duration) of icEEG sharp waves is likely to reflect the following aspects: (1) the duration and synchrony of excitatory PSP (EPSP; temporary depolarisation of postsynaptic membrane potential caused by the flow of positively charged ions into the postsynaptic cell, which makes the neuron more likely to fire an action potential), (2) the presence of inhibitory PSP (IPSP; temporary hyperpolarisation of postsynaptic membrane potential, which makes the neuron less likely to fire an action potential), and (3) the time constants of neurons. In particular, the sharp wave width is likely to reflect the distance

travelled by information, i.e., the distance between sources and field potential recording sensors (Gold et al., 2006); a larger distance is likely to be associated with a lower degree of synchrony across multiple EPSP, which can sum and result in a wider (lasting longer) field potential, depending on the cells spatial arrangement. Therefore, our finding suggests that the amplitude of the BOLD signal can be predicted by the duration of the underlying field potential, a likely reflection of the sources geometric arrangement in relation to the recording sensors.

The sharp wave width effect was observed in voxels at which the BOLD signal was either increased or decreased in relation to sharp wave onset times and widths. In other words, we found that the sharp wave width explains additional variance of the amplitude of the BOLD signal in voxels where a linear combination of the sharp wave onset times and widths is positively or negatively correlated with the amplitude of the BOLD signal.

Both IED onset times related BOLD signal increases and decreases have been reported (Benar et al., 2006; Gotman et al., 2006; Grouiller et al., 2010; Jacobs et al., 2014; Lemieux et al., 2008; Moeller et al., 2009; Pittau et al., 2013; Salek-Haddadi et al., 2006); in particular, two studies using icEEG and BOLD fMRI data recorded simultaneously in humans found BOLD signal decreases in the SOZ of a few patients (Cunningham et al., 2012; Vulliemoz et al., 2011). However, the mechanisms underlying a BOLD signal decrease are not completely understood: it may result from (1) a neuronal activity decrease (Shmuel et al., 2006) and associated CBF decrease (Carmichael et al., 2008), or (2) a neuronal activity increase that leads to a tissue oxygen consumption increase that exceeds the simultaneous CBF increase, resulting in a local deoxyhaemoglobin concentration increase (Schridde et al., 2008). Finding that a significant amount of the variance of the amplitude of BOLD signal decreases was explained by the width of the sharp wave suggests that BOLD signal decreases may not be necessarily associated with neuronal activity decreases (hypothesis (1)). Therefore, our main finding and those of Geneslaw et al. (2011), favour hypothesis (2).

6.4.2 Sharp wave amplitude neurophysiological correlates and the BOLD signal

The LFP, icEEG, and scalp EEG signals represent extracellular field potentials primary originated by postsynaptic activity (EPSP and IPSP), integrated over different volumes (Creutzfeldt et al., 1966a, 1966b; Klee et al., 1965; Niedermeyer and Lopes da Silva, 1999). The amplitude of these signals depends on the geometric arrangement of the active neurons, within each element volume, as well as on the degree of synchrony among the multiple element volumes, over larger distances (electrical dipole phase may or may not be locked across element volumes) (Einevoll et al., 2013). Due to the different nature of the EEG and BOLD signals, decoupling between them is to be expected, to some degree (Nunez and Silberstein, 2000). For instance, active pyramidal cells are expected to be associated with a high metabolic demand due to their action potentials firing frequency (Connors and Gutnick, 1990), as well as with large current dipoles that result from the sum of many “open-field generators”. However, the amplitude of the BOLD signal may be independent of the geometric arrangement of active neurons and equally sensitive to synchronous and asynchronous activity (Nunez and Silberstein, 2000). For

instance, BOLD changes may be coupled to neuronal signalling processes rather than to energy demand (Attwell and Iadecola, 2002) or neuronal activity synchronisation. Hence, the sharp wave amplitude may or may not be a good predictor of the amplitude of the BOLD signal.

While Benar et al. (2002) only found a low (not significant), positive correlation between the square root of the of the EEG and BOLD signals in the time range of the interictal event (sharp and slow waves taken together), LeVan et al. (2010) found strong (significant), positive correlations between the amplitude of scalp EEG sharp waves and the amplitude of BOLD changes in the SOZ, but not in distant regions. One of the reasons why we did not find a significant correlation between the amplitude of the icEEG sharp wave and amplitude of the co-localised BOLD response may be related with the spatial scale of our electrophysiological measurements (see § 6.4.4). For instance, Keller et al. (2010) found that sharp waves recorded with microelectrodes in humans could occur with relatively sparse neuronal participation. Furthermore, sharp waves on icEEG can be generated by much smaller neuronal populations than sharp waves on scalp EEG (Cooper et al., 1965; Ebersole, 1997; Nunez and Silberstein, 2000). Therefore, an icEEG sharp wave (recorded with macroelectrodes, placed inside or over the cortex) may be generated by a synchronous, albeit small, population of neurons, whose activity is not necessarily associated with a large increase in metabolic demand.

6.4.3 IED spatial field extent neurophysiological correlates and the BOLD signal

IED generation is thought to reflect a dynamic and complex network phenomenon, not yet completely understood (Keller et al., 2010). However, assuming that IED simultaneously observed at multiple icEEG contacts are comparable to LFP correlated across large distances (> 0.2 millimetres), and noticing that LFP spatial field extent is mainly dependent on the spatial extent of the surrounding, synchronised sources of activity (Einevoll et al., 2013), we may hypothesise that IED are generated by either multiple, synchronous neuronal populations, or by a single population, whose activity (instantaneously) spreads to multiple contacts, through volume conduction. Since the amplitude of the BOLD signal does not seem to strongly reflect the spatial field extent of the sharp wave, it may also not reflect the volume of the surrounding, synchronised sources of activity.

6.4.4 Methodological aspects

This study is based on the comparison of two models, one nested in the other. More specifically, we estimate the amount of variance explained by each feature (sharp wave amplitude, width, slope of the rising phase, energy, and spatial field extent), quantified event-by-event, in addition to the event onset; the latter being the standard way to model interictal epileptic activity. Irrespective of the absolute amount of variance explained by any of these features, this approach allowed us to rank them according to the amount of variance explained in addition to a common reference, the standard model.

We chose to use the simplest possible model for the relationship between the amplitude of the BOLD signal and each sharp wave feature, implying that the former is linearly proportional to

the latter, through convolution with a fixed haemodynamic kernel, in this case, the canonical HRF. This choice was based on three main reasons. Firstly, we had to explicitly and specifically test for BOLD changes related with the EEG-derived features because the primary purpose of this study was to better understand the neurophysiological correlates of the BOLD signal. The canonical HRF simplicity allowed for a limited number of degrees of freedom and, therefore, a more straightforward and unambiguous interpretation of the results. In fact, the number of comparisons would increase dramatically if we had chosen to use a more flexible/complex HRF model, which we think is unwise given the relatively limited amount of data at hand. Moreover, the possibility of using other hemodynamic kernel does not invalidate our main finding: amongst all factors considered, only sharp wave width explained a significant amount of additional variance of the amplitude of the BOLD signal. Secondly, we wanted to be consistent with the previous fundamental studies on the local electrophysiological correlates of the BOLD signal (Goense and Logothetis, 2008; Magri et al., 2012; Nir et al., 2007; Scheeringa et al., 2011a). Thirdly, although some studies of epileptic activity have raised the issue of the choice of the hemodynamic kernel (deviations from the canonical HRF shape have been observed, mostly in relation to generalised discharges or focal discharges in generalised syndromes (Beers et al., 2015; Grouiller et al., 2010; Masterton et al., 2010; Moeller et al., 2008)), others have found this variability to be less significant, particularly in relation to focal discharges, with deviants often remote from the presumed primary generator of epileptic activity (Lemieux et al., 2008; Proulx et al., 2014). This study was focused on BOLD changes in the immediate vicinity of the most active icEEG contacts, i.e., BOLD changes within a small volume of brain tissue not expected to exhibit different haemodynamic responses. Furthermore, reports of HRF shape variability are not limited to studies of epileptic activity; it has also been observed in relation to location in the healthy brain, using a relatively constrained basis set (Aguirre et al., 1998), and in relation to various normal stimuli (Grouiller et al., 2010; Handwerker et al., 2004). Analyses of exceptionally high SNR fMRI data of normal brain activation, using a totally unconstrained hemodynamic kernel basis set, have revealed a wide range of HRF shapes covering almost the entire brain, but with unknown biological meaning (neuronal vs vascular effects) for the deviant ones (Gonzalez-Castillo et al., 2014, 2012).

6.4.5 Technical limitations

As previously discussed in § 5.4.4, partial volume effects together with a diminished SNR in the surroundings of the icEEG contacts are limitations of this study. For instance, not finding a significant correlation between the amplitude of the sharp wave and the amplitude of the co-localised BOLD changes can be a consequence of these limitations because large sharp waves can be the reflection of highly local, synchronised neuronal activity (Einevoll et al., 2013) that is so spatially restricted that it cannot be captured by fMRI. Even so, we found a significant correlation between the width of the sharp wave and the amplitude of the BOLD response because wider sharp waves can be the reflection of widespread, not perfectively synchronised field potentials, that sum, in space, and give rise to a wider field potential.

6.4.6 Relevance to EEG-fMRI studies

Most EEG-fMRI studies of epileptic activity use the IED onset times (O) as the only EEG-derived feature of interest. As a supplementary analysis, we computed the variance explained by O that was not explained by C, i.e. we compared the residuals of the model with the design matrix D_O = [O C] with the model with the design matrix D_C = [C]. We found average VE of 1.17% (pBOLD) and 1.21% (nBOLD). Therefore, the amount of BOLD signal variance explained by the IED onset times in addition to confounds is of the same magnitude as the variance explained by the sharp wave width in addition to the IED onsets and confounds. Furthermore, our VE values are comparable to those reported by studies of physiological noise, Jorge et al. (2013) and Bianciardi et al. (2009), who reported average (within grey matter masks) VE values of the order of 1% and 2%. Therefore, modelling the sharp wave width variability, in addition to their onset times, is likely to improve the BOLD sensitivity related to epileptic activity, and be relevant for scalp EEG-fMRI studies aiming to map the focus and/or propagation networks underlying epileptic activity.

6.4.7 Relevance to Neuroscience

Sharp waves have been observed in both pathological and healthy contexts (Sullivan et al., 2011). In particular, physiological sharp waves have been recorded in the hippocampal CA1 stratum radiatum of healthy rodents having minimal interaction with their environment (during immobility, consummatory behaviours, or slow-wave sleep) (Buzsáki et al., 1983; Suzuki and Smith, 1987), and of healthy macaques at an inactive/drowsy-or-sleeping behavioural state (Skaggs et al., 2007). Since there is no good reason to discard a universal dependence of the amplitude of the BOLD signal on the duration of the underlying field potential, our findings may also be relevant for non-epileptic studies.

6.5 Future Work

It would be interesting to repeat this study using the aforementioned physiological sharp waves; this could potentially result in new insights on whether the electro-haemodynamic coupling function is different for epileptic and non-epileptic brain activities. Furthermore, the morphological and field extent features of slow waves (which often follow sharp waves) can also be investigated; their width may also be a good predictor of the amplitude of the BOLD signal and, together with the sharp wave width, explain variance of the BOLD signal in addition to the IED onset times.

Given the relevance of the EEG signal spectral content on the prediction of the amplitude of the BOLD signal, it would also be interesting to investigate event-by-event time-frequency spectral features such as the “time-frequency extent” (time-frequency amplitude profile area) of broadband (1 - 500 Hz) power increases (in relation to background activity) during IED; or the lower frequency activity (1 - 150 Hz) power decreases that may follow (Jacobs et al., 2011; Kobayashi et al., 2009); or even the ratio between sum of β and γ power bands and the sum of θ and α power bands ($(P_\beta+P_\gamma)/(P_\theta+P_\alpha)$ Bartolomei et al. 2008), in their capability to predict the amplitude of the co-localised BOLD signal.

6.6 Conclusion

We compared a number of epileptic sharp wave features (amplitude, width, energy, slope of the rising phase, and spatial field extent) in terms of their individual capability to explain variance of the co-localised BOLD signal that was not explained by sharp wave onset times alone, and found that the width was the only one explaining a significant amount of additional variance. This suggests that the amplitude of the BOLD signal depends more on the duration of the underlying field potential than on the degree of neuronal activity synchrony, and that modelling the IED duration variability, in addition to their onset times, is likely to improve the BOLD sensitivity related to epileptic activity.

7

General conclusions

This final chapter comprises a few considerations on how data quality could be improved and the principal conclusions of this project.

Our exploratory investigations on how to improve the quality of the icEEG data simultaneously recorded with fMRI showed that we can change the quality of these data by changing the parameters of the artefact template construction. The most interesting result was perhaps the strong dependence of these parameters and related data quality on the location of the icEEG contact. Minimising the temporal variability of any residual MR-related artefacts (by modifying the acquisition set up), developing new or improving the currently available method for MR-related artefacts correction, while also maximising the cut-off frequency of the hardware low-pass filter used, is likely to improve the quality of the icEEG data simultaneously recorded with fMRI, and, potentially, the accuracy of the icEEG-derived features, which would have a positive impact on future studies of the relationship between the two signals.

The magnetic susceptibility effects between the components of the EEG recording system and head tissues, causing localised signal drops and geometric distortions, together with the shielding effects caused by the presence of EEG metallic contacts, leading to SNR losses, are a major technical limitation of this work (Jorge et al., 2015). Using icEEG contacts with better imaging properties (lower magnetic susceptibilities) could potentially improve the quality of the fMRI data, and therefore the impact of including new EEG-derived features in the model of the BOLD signal. The limited spatial resolution of fMRI, which may have led to apparent absences of BOLD changes despite the presence of neuronal activity, is another technical limitation of this work. Using a higher magnetic field strength could allow us to acquired fMRI data with better temporal SNR and spatial sampling rates; however, the corruptive effect of the above mentioned artefacts, together with concerns about safety, increase with the strength of the magnetic field used. Improving the temporal sampling rate of fMRI data could be also valuable, to a limit, given the inherent slow dynamics of the BOLD signal; for instance, we would be able to investigate EEG power fluctuation in the order of a second rather than three.

This work was based on the findings of previous works using LFP, icEEG, or scalp EEG recordings during cognitive, sensory and motor functions, which have systematically revealed significant correlations between the power of the EEG signal and the amplitude of the BOLD signal at the same location, or at regions expected to be involved in the task performed; positive for the higher (>30 Hz) and negative for the lower (α, β, and θ) EEG frequency ranges. Since an identical correlations profile was found by a study of spontaneous brain activity in the visual cortex of anesthetised macaques (Magri et al., 2012), the electro-haemodynamic coupling function may be identical for task and non-epileptic rest conditions. Even though a universal electro-haemodynamic coupling function capable of accounting for a large proportion of the variance of the amplitude of the BOLD signal in different brain states (rest, different tasks, and epileptic states) is still to be found, most studies suggest that such function will be EEG frequency and power dependent.

Fluctuations in the strength of $PAC_{\beta\gamma}$ were found to explain variance of the amplitude of the finger tapping related BOLD changes that was not explained by a combination of the power of the α, β, and γ bands, suggesting that PAC and power fluctuations are associated with different metabolic demands and may therefore result from different neuronal populations or from different behaviours of a particular neuronal population; this is an interesting finding that adds to the literature of the functional correlates of PAC. Furthermore, taking into account the phase of the LF activity by, for instance, including the temporal fluctuations in the strength of PAC, together with the temporal fluctuations in the power of the LF and HF activities, is likely to increase the quality of the fit of the electrophysiology-based model of the BOLD signal, and therefore to increase the sensitivity of future EEG-informed fMRI studies.

Among the five sharp wave morphology (amplitude, width, slope of the rising phase, energy) and spatial field extent related features investigated, the width of the sharp wave, i.e., the duration of the field potential, was the only feature found to explain a significant amount of variance of the amplitude of the co-localised BOLD signal that was not explained by the onset times of the events. Our approach ranked the five features according to the amount of variance explained in addition to a common reference. Therefore, our findings do not prove that the amplitude of the BOLD signal is not related with the amplitude, slope of the rising phase, energy, or spatial field extent of the sharp wave; they simply suggest that the width of the sharp wave relates comparatively better. Therefore, the amplitude of the BOLD signal seems to depend more on the duration of the recorded field potential (likely to be a consequence of the geometric distribution of multiple neuronal populations producing EPSP that sum up and give rise to the recorded field potential), than on the degree of the neuronal activity synchrony, for instance.

Adding to the previous works suggesting that a universal electro-haemodynamic coupling function is likely to depend on the power of multiple EEG frequency bands, this work suggests that such function may depend on the power as well as on the phase of the LF EEG activities and, in particular, on the strength of the coupling between the phase of the lower and the amplitude of the higher frequency activities. While the LF activity is thought to modulate neuronal activity over larger spatial regions, the HF activity is thought to modulate neuronal activity over comparatively smaller spatial regions (von Stein and Sarnthein, 2000). Therefore, the amplitude of the BOLD signal seems to depend not only on highly local, synchronous neuronal activity reflected in the power of γ (> 30 Hz) EEG activity, but also on comparatively more complex interactions across cell populations (network nodes) reflected in the power of α or β EEG activities as well as, perhaps, even more strongly, in the strength of PAC. Furthermore, this work also suggests that the amplitude of the BOLD signal depends on the duration of the simultaneously recorded sharp waves, thought to reflect the distance between the underlying EPSP and the recording sensor, together with the degree of synchrony across EPSP (postsynaptic currents take different times to propagate different distances; from a distant recording sensor point of view, the extracellular field potential may look like it results from a single static current source of longer duration when, in fact, it results from multiple current sources of shorter duration (Gold et al., 2006)). To conclude, this work suggests that the

amplitude of the BOLD signal may reflect both the activity of focal, highly synchronous neuronal populations, and the activity of spatially spread, not necessarily synchronous neuronal populations, which however influence each other. Therefore, a universal electro-haemodynamic coupling function should probably account for the short duration, highly synchronous neuronal activity as well as for the comparatively longer lasting neuronal network activity.

Bibliography

Aghakhani, Y., Beers, C.A., Pittman, D.J., Gaxiola-Valdez, I., Goodyear, B.G., Federico, P., 2015. Co-localization between the BOLD response and epileptiform discharges recorded by simultaneous intracranial EEG-fMRI at 3 T. NeuroImage. Clin. 7, 755–63. doi:10.1016/j.nicl.2015.03.002

Aguirre, G.K., Zarahn, E., D'Esposito, M., 1998. The variability of human, BOLD hemodynamic responses. Neuroimage 8, 360–369. doi:S1053-8119(98)90369-X [pii]10.1006/nimg.1998.0369

Allen, E.A., Liu, J., Kiehl, K.A., Gelernter, J., Pearlson, G.D., Perrone-Bizzozero, N.I., Calhoun, V.D., 2011. Components of cross-frequency modulation in health and disease. Front. Syst. Neurosci. 5, 59. doi:10.3389/fnsys.2011.00059

Allen, P.J., Josephs, O., Turner, R., 2000. A method for removing imaging artifact from continuous EEG recorded during functional MRI. Neuroimage 12, 230–239. doi:10.1006/nimg.2000.0599S1053-8119(00)90599-8 [pii]

Allen, P.J., Polizzi, G., Krakow, K., Fish, D.R., Lemieux, L., 1998. Identification of EEG events in the MR scanner: the problem of pulse artifact and a method for its subtraction. Neuroimage 8, 229–239. doi:10.1006/nimg.1998.0361

Alvarado-Rojas, C., Valderrama, M., Witon, A., Navarro, V., Le Van Quyen, M., 2011. Probing cortical excitability using cross-frequency coupling in intracranial EEG recordings: a new method for seizure prediction. Conf. Proc. IEEE Eng. Med. Biol. Soc. 2011, 1632–5. doi:10.1109/IEMBS.2011.6090471

An, D., Fahoum, F., Hall, J., Olivier, A., Gotman, J., Dubeau, F., 2013. Electroencephalography/functional magnetic resonance imaging responses help predict surgical outcome in focal epilepsy. Epilepsia 54, 2184–2194. doi:10.1111/epi.12434

Andreone, B.J., Lacoste, B., Gu, C., 2015. Neuronal and Vascular Interactions. Annu. Rev. Neurosci. 38, 25–46. doi:10.1146/annurev-neuro-071714-033835

Aru, J., Aru, J., Priesemann, V., Wibral, M., Lana, L., Pipa, G., Singer, W., Vicente, R., 2014. Untangling cross-frequency coupling in neuroscience. Curr. Opin. Neurobiol. 31C, 51–61. doi:10.1016/j.conb.2014.08.002

Attwell, D., Buchan, A., Charpak, S., Lauritzen, M., MacVicar, B., Newman, E., 2010. Glial and neuronal control of brain blood flow. Nature 468, 232–241. doi:10.1038/nature09613

Attwell, D., Iadecola, C., 2002. The neural basis of functional brain imaging signals. Trends Neurosci. 25, 621–625. doi:S0166-2236(02)02264-6 [pii]

Attwell, D., Laughlin, S.B., 2001. An energy budget for signaling in the grey matter of the brain. J Cereb Blood Flow Metab 21, 1133–1145. doi:10.1097/00004647-200110000-00001

Axmacher, N., Henseler, M.M., Jensen, O., Weinreich, I., Elger, C.E., Fell, J., 2010. Cross-frequency coupling supports multi-item working memory in the human hippocampus. Proc Natl Acad Sci U S A 107, 3228–3233. doi:10.1073/pnas.0911531107 0911531107 [pii]

Babajani, A., Nekooei, M.H., Soltanian-Zadeh, H., 2005. Integrated MEG and fMRI model: synthesis and analysis. Brain Topogr 18, 101–113. doi:10.1007/s10548-005-0279-5

Bagshaw, A.P., Hawco, C., Benar, C.G., Kobayashi, E., Aghakhani, Y., Dubeau, F., Pike, G.B., Gotman, J., 2005. Analysis of the EEG-fMRI response to prolonged bursts of interictal epileptiform activity. Neuroimage 24, 1099–1112. doi:S1053-8119(04)00612-3 [pii]10.1016/j.neuroimage.2004.10.010

Bartolo, M.J., Gieselmann, M.A., Vuksanovic, V., Hunter, D., Sun, L., Chen, X., Delicato, L.S., Thiele, A., 2011. Stimulus-induced dissociation of neuronal firing rates and local field potential gamma power and its relationship to the resonance blood oxygen level-dependent signal in macaque primary visual cortex. Eur J Neurosci 34, 1857–1870. doi:10.1111/j.1460-9568.2011.07877.x

Bartolomei, F., Chauvel, P., Wendling, F., 2008. Epileptogenicity of brain structures in human temporal lobe epilepsy: a quantified study from intracerebral EEG. Brain 131, 1818–1830. doi:awn111 [pii]10.1093/brain/awn111

Basar, E., 1980. EEG-brain dynamics: relation between EEG and brain evoked potentials. Elsevier-North-Holland Biomedical Press.

Baumgartner, U., Vogel, H., Ohara, S., Treede, R.D., Lenz, F., 2011. Dipole source analyses of laser evoked potentials obtained from subdural grid recordings from primary somatic sensory cortex. J Neurophysiol 106, 722–730. doi:10.1152/jn.00135.2011jn.00135.2011 [pii]

Becker, R., Reinacher, M., Freyer, F., Villringer, A., Ritter, P., 2011. How ongoing neuronal oscillations account for evoked fMRI variability. J. Neurosci. 31, 11016–27. doi:10.1523/JNEUROSCI.0210-11.2011

Beckmann, C.F., Smith, S.M., 2004. Probabilistic independent component analysis for functional magnetic resonance imaging. IEEE Trans Med Imaging 23, 137–152. doi:10.1109/TMI.2003.822821

Beers, C.A., Williams, R.J., Gaxiola-Valdez, I., Pittman, D.J., Kang, A.T., Aghakhani, Y., Pike, G.B., Goodyear, B.G., Federico, P., 2015. Patient specific hemodynamic response functions associated with interictal discharges recorded via simultaneous intracranial EEG-fMRI. Hum. Brain Mapp. 00, n/a–n/a. doi:10.1002/hbm.23008

Belitski, A., Gretton, A., Magri, C., Murayama, Y., Montemurro, M.A., Logothetis, N.K., Panzeri, S., 2008. Low-frequency local field potentials and spikes in primary visual cortex convey independent visual information. J Neurosci 28, 5696–5709. doi:10.1523/JNEUROSCI.0009-08.200828/22/5696 [pii]

Belluscio, M.A., Mizuseki, K., Schmidt, R., Kempter, R., Buzsaki, G., 2012. Cross-frequency phase-phase coupling between theta and gamma oscillations in the hippocampus. J Neurosci 32, 423–435. doi:10.1523/JNEUROSCI.4122-11.201232/2/423 [pii]

Benar, C.G., Gross, D.W., Wang, Y., Petre, V., Pike, B., Dubeau, F., Gotman, J., 2002. The BOLD response to interictal epileptiform discharges. Neuroimage 17, 1182–1192. doi:S105381190291164X [pii]

Benar, C.G., Grova, C., Kobayashi, E., Bagshaw, A.P., Aghakhani, Y., Dubeau, F., Gotman, J., 2006. EEG-fMRI of epileptic spikes: concordance with EEG source localization and intracranial EEG. Neuroimage 30, 1161–1170. doi:S1053-8119(05)02452-3 [pii]10.1016/j.neuroimage.2005.11.008

Benar, C.G., Schon, D., Grimault, S., Nazarian, B., Burle, B., Roth, M., Badier, J.M., Marquis, P., Liegeois-Chauvel, C., Anton, J.L., 2007. Single-trial analysis of oddball event-related potentials in simultaneous EEG-fMRI. Hum Brain Mapp 28, 602–613. doi:10.1002/hbm.20289

Berman, J.I., McDaniel, J., Liu, S., Cornew, L., Gaetz, W., Roberts, T.P.L., Edgar, J.C., 2012. Variable bandwidth filtering for improved sensitivity of cross-frequency coupling metrics. Brain Connect. 2, 155–63. doi:10.1089/brain.2012.0085

Bianciardi, M., Fukunaga, M., van Gelderen, P., Horovitz, S.G., de Zwart, J.A., Shmueli, K., Duyn, J.H., 2009a. Sources of functional magnetic resonance imaging signal fluctuations in the human brain at rest: a 7 T study. Magn. Reson. Imaging 27, 1019–1029. doi:10.1016/j.mri.2009.02.004

Bianciardi, M., van Gelderen, P., Duyn, J.H., Fukunaga, M., de Zwart, J.A., 2009b. Making the most of fMRI at 7 T by suppressing spontaneous signal fluctuations. Neuroimage 44, 448–54. doi:10.1016/j.neuroimage.2008.08.037

Bishop, G.H., 1949. Potential phenomena in thalamus and cortex. Electroencephalogr. Clin. Neurophysiol. 1, 421–35; discussion 435–6.

Blume, W.T., Luders, H.O., Mizrahi, E., Tassinari, C., van Emde Boas, W., Engel Jr., J., 2001. Glossary of descriptive terminology for ictal semiology: report of the ILAE task force on classification and terminology. Epilepsia 42, 1212–1218. doi:22001 [pii]

Boucousis, S.M., Beers, C.A., Cunningham, C.J., Gaxiola-Valdez, I., Pittman, D.J., Goodyear, B.G., Federico, P., 2012. Feasibility of an intracranial EEG-fMRI protocol at 3T: risk assessment and image quality. Neuroimage 63, 1237–1248. doi:10.1016/j.neuroimage.2012.08.008S1053-8119(12)00801-4 [pii]

Brazier, M.A.B., 1949. The electrical fields at the surface of the head during sleep. Electroencephalogr. Clin. Neurophysiol. 1, 195–204. doi:10.1016/0013-4694(49)90176-5

Bullock, T.H., McClune, M.C., Achimowicz, J.Z., Iragui-Madoz, V.J., Duckrow, R.B., Spencer, S.S., 1995. Temporal fluctuations in coherence of brain waves. Proc Natl Acad Sci U S A 92, 11568–11572.

Bullock, T.H., McClune, M.C., Enright, J.T., 2003. Are the electroencephalograms mainly rhythmic? Assessment of periodicity in wide-band time series. Neuroscience 121, 233–252. doi:S0306452203002082 [pii]

Bushara, K.O., Hanakawa, T., Immisch, I., Toma, K., Kansaku, K., Hallett, M., 2003. Neural correlates of cross-modal binding. Nat Neurosci 6, 190–195. doi:10.1038/nn993nn993 [pii]

Buxton, R.B., 2012. Dynamic models of BOLD contrast. Neuroimage 62, 953–961. doi:S1053-8119(12)00015-8 [pii]10.1016/j.neuroimage.2012.01.012

Buzsaki, G., Anastassiou, C.A., Koch, C., 2012. The origin of extracellular fields and currents - EEG, ECoG, LFP and spikes. Nat. Rev. Neurosci. 13, 407–420. doi:Doi 10.1038/Nrn3241

Buzsáki, G., Anastassiou, C.A., Koch, C., 2012. The origin of extracellular fields and currents--EEG, ECoG, LFP and spikes. Nat. Rev. Neurosci. 13, 407–20. doi:10.1038/nrn3241

Buzsaki, G., Buhl, D.L., Harris, K.D., Csicsvari, J., Czeh, B., Morozov, A., 2003. Hippocampal network patterns of activity in the mouse. Neuroscience 116, 201–211. doi:S0306452202006693 [pii]

Buzsaki, G., Chrobak, J.J., 1995. Temporal structure in spatially organized neuronal ensembles: a role for interneuronal networks. Curr Opin Neurobiol 5, 504–510. doi:0959-4388(95)80012-3 [pii]

Buzsaki, G., Draguhn, A., 2004. Neuronal oscillations in cortical networks. Science (80-.). 304, 1926–1929.

Buzsáki, G., Lai-Wo S., L., Vanderwolf, C.H., 1983. Cellular bases of hippocampal EEG in the behaving rat. Brain Res. Rev. 6, 139–171. doi:10.1016/0165-0173(83)90037-1

Buzsaki, G., Logothetis, N., Singer, W., 2013. Scaling brain size, keeping timing: evolutionary preservation of brain rhythms. Neuron 80, 751–764. doi:10.1016/j.neuron.2013.10.002S0896-6273(13)00904-5 [pii]

Caballero-Gaudes, C., Van de Ville, D., Grouiller, F., Thornton, R., Lemieux, L., Seeck, M., Lazeyras, F., Vulliemoz, S., 2013. Mapping interictal epileptic discharges using mutual information between concurrent EEG and fMRI. Neuroimage 68, 248–262. doi:10.1016/j.neuroimage.2012.12.011

Canolty, R.T., Edwards, E., Dalal, S.S., Soltani, M., Nagarajan, S.S., Kirsch, H.E., Berger, M.S., Barbaro, N.M., Knight, R.T., 2006. High gamma power is phase-locked to theta oscillations in human neocortex. Science 313, 1626–8. doi:10.1126/science.1128115

Canolty, R.T., Knight, R.T., 2010. The functional role of cross-frequency coupling. Trends Cogn. Sci. 14, 506–15. doi:10.1016/j.tics.2010.09.001

Carmichael, D.W., Hamandi, K., Laufs, H., Duncan, J.S., Thomas, D.L., Lemieux, L., 2008. An investigation of the relationship between BOLD and perfusion signal changes during epileptic generalised spike wave activity. Magn Reson Imaging 26, 870–873. doi:S0730-725X(08)00097-0 [pii]10.1016/j.mri.2008.01.041

Carmichael, D.W., Thornton, J.S., Rodionov, R., Thornton, R., McEvoy, A.W., Ordidge, R.J., Allen, P.J., Lemieux, L., 2010. Feasibility of simultaneous intracranial EEG-fMRI in humans: a safety study. Neuroimage 49, 379–390. doi:S1053-8119(09)00854-4 [pii]10.1016/j.neuroimage.2009.07.062

Carmichael, D.W., Vulliemoz, S., Rodionov, R., Thornton, J.S., McEvoy, A.W., Lemieux, L., 2012. Simultaneous intracranial EEG-fMRI in humans: Protocol considerations and data quality. Neuroimage 63, 301–309. doi:S1053-8119(12)00544-7 [pii]10.1016/j.neuroimage.2012.05.056

Cauli, B., 2004. Cortical GABA Interneurons in Neurovascular Coupling: Relays for Subcortical Vasoactive Pathways. J. Neurosci. 24, 8940–8949. doi:10.1523/JNEUROSCI.3065-04.2004

Chatrian, G.E., Shaw, C.M., Leffman, H., 1964. The Significance of Periodic Lateralized Epileptiform Discharges in Eeg: An Electrographic, Clinical and Pathological Study. Electroencephalogr Clin Neurophysiol 17, 177–193.

Chaudhary, U.J., Carmichael, D.W., Rodionov, R., Thornton, R.C., Bartlett, P., Vulliemoz, S., Micallef, C., McEvoy, A.W., Diehl, B., Walker, M.C., Duncan, J.S., Lemieux, L., 2012a. Mapping preictal and ictal haemodynamic networks using video-electroencephalography and functional imaging. Brain 135, 3645–3663. doi:10.1093/brain/aws302aws302 [pii]

Chaudhary, U.J., Duncan, J.S., Lemieux, L., 2013. Mapping hemodynamic correlates of seizures using fMRI: A review. Hum Brain Mapp 34, 447–466. doi:10.1002/hbm.21448

Chaudhary, U.J., Rodionov, R., Carmichael, D.W., Thornton, R.C., Duncan, J.S., Lemieux, L., 2012b. Improving the sensitivity of EEG-fMRI studies of epileptic activity by modelling eye blinks, swallowing and other video-EEG detected physiological confounds. Neuroimage 61, 1383–1393. doi:10.1016/j.neuroimage.2012.03.028S1053-8119(12)00301-1 [pii]

Church, P., Leduc, A., Beique, R.A., 1985. Sensitivity analysis of depth EEG electrodes to dipolar electric sources. IEEE Trans Biomed Eng BME-32, 544–560.

Cohen, M.X., 2008. Assessing transient cross-frequency coupling in EEG data. J. Neurosci. Methods 168, 494–499. doi:10.1016/j.jneumeth.2007.10.012

Cohen, M.X., Axmacher, N., Lenartz, D., Elger, C.E., Sturm, V., Schlaepfer, T.E., 2009a. Good vibrations: cross-frequency coupling in the human nucleus accumbens during reward processing. J Cogn Neurosci 21, 875–889. doi:10.1162/jocn.2009.21062

Cohen, M.X., Elger, C.E., Fell, J., 2009b. Oscillatory activity and phase-amplitude coupling in the human medial frontal cortex during decision making. J Cogn Neurosci 21, 390–402. doi:10.1162/jocn.2008.21020

Colgin, L.L., Denninger, T., Fyhn, M., Hafting, T., Bonnevie, T., Jensen, O., Moser, M.B., Moser, E.I., 2009. Frequency of gamma oscillations routes flow of information in the hippocampus. Nature 462, 353–357. doi:10.1038/nature08573nature08573 [pii]

Colic, S., Lang, M., Wither, R.G., Eubanks, J.H., Liang, Z., Bardakjian, B.L., 2013. Low Frequency-Modulated High Frequency Oscillations in Seizure- Like Events Recorded from in-vivo MeCP2-Deficient Mice, in: 35th Annual International Conference of the IEEE EMBS. pp. 985–988. doi:10.1109/EMBC.2013.6609668

Conner, C.R., Ellmore, T.M., Pieters, T.A., DiSano, M.A., Tandon, N., 2011. Variability of the relationship between electrophysiology and BOLD-fMRI across cortical regions in humans. J Neurosci 31, 12855–12865. doi:31/36/12855 [pii]10.1523/JNEUROSCI.1457-11.2011

Connors, B.W., Gutnick, M.J., 1990. Intrinsic firing patterns of diverse neocortical neurons. Trends Neurosci. 13, 99–104. doi:10.1016/0166-2236(90)90185-D

Cooper, R., Winter, A.., Crow, H.., Walter, W.G., 1965. Comparison of subcortical, cortical and scalp activity using chronically indwelling electrodes in man. Electroencephalogr. Clin. Neurophysiol. 18, 217–228. doi:10.1016/0013-4694(65)90088-X

Creutzfeldt, O.D., Watanabe, S., Lux, H.D., 1966a. Relations between EEG phenomena and potentials of single cortical cells. II. Spontaneous and convulsoid activity. Electroencephalogr Clin Neurophysiol 20, 1–18.

Creutzfeldt, O.D., Watanabe, S., Lux, H.D., 1966b. Relations between EEG phenomena and potentials of single cortical cells. I. Evoked responses after thalamic and erpicortical stimulation. Electroencephalogr. Clin. Neurophysiol. 20, 1–18.

Crone, N.E., Miglioretti, D.L., Gordon, B., Lesser, R.P., 1998. Functional mapping of human sensorimotor cortex with electrocorticographic spectral analysis. II. Event-related synchronization in the gamma band. Brain 121 (Pt 1, 2301–15.

Cunningham, C.B., Goodyear, B.G., Badawy, R., Zaamout, F., Pittman, D.J., Beers, C.A., Federico, P., 2012. Intracranial EEG-fMRI analysis of focal epileptiform discharges in humans. Epilepsia 53, 1636–1648. doi:10.1111/j.1528-1167.2012.03601.x

Dale, A.M., 1999. Optimal experimental design for event-related fMRI. Hum. Brain Mapp. 8, 109–114. doi:10.1002/(SICI)1097-0193(1999)8:2/3<109::AID-HBM7>3.0.CO;2-W

De Curtis, M., Avanzini, G., 2001. Interictal spikes in focal epileptogenesis. Prog Neurobiol 63, 541–567.

doi:S0301-0082(00)00026-5 [pii]

de Hemptinne, C., Ryapolova-Webb, E.S., Air, E.L., Garcia, P.A., Miller, K.J., Ojemann, J.G., Ostrem, J.L., Galifianakis, N.B., Starr, P.A., 2013. Exaggerated phase-amplitude coupling in the primary motor cortex in Parkinson disease. Proc. Natl. Acad. Sci. U. S. A. 110, 4780–5. doi:10.1073/pnas.1214546110

De Luca, M., Beckmann, C.F., De Stefano, N., Matthews, P.M., Smith, S.M., 2006. fMRI resting state networks define distinct modes of long-distance interactions in the human brain. Neuroimage 29, 1359–1367. doi:S1053-8119(05)00625-7 [pii]10.1016/j.neuroimage.2005.08.035

De Munck, J.C., Goncalves, S.I., Huijboom, L., Kuijer, J.P., Pouwels, P.J., Heethaar, R.M., Lopes da Silva, F.H., 2007. The hemodynamic response of the alpha rhythm: an EEG/fMRI study. Neuroimage 35, 1142–1151. doi:S1053-8119(07)00089-4 [pii]10.1016/j.neuroimage.2007.01.022

De Munck, J.C., Goncalves, S.I., Mammoliti, R., Heethaar, R.M., Lopes da Silva, F.H., 2009. Interactions between different EEG frequency bands and their effect on alpha-fMRI correlations. Neuroimage 47, 69–76. doi:S1053-8119(09)00373-5 [pii]10.1016/j.neuroimage.2009.04.029

Debener, S., Mullinger, K.J., Niazy, R.K., Bowtell, R.W., 2008. Properties of the ballistocardiogram artefact as revealed by EEG recordings at 1.5, 3 and 7 T static magnetic field strength. Int. J. Psychophysiol. 67, 189–199. doi:S0167-8760(07)00158-4 [pii]10.1016/j.ijpsycho.2007.05.015

Debener, S., Ullsperger, M., Siegel, M., Fiehler, K., von Cramon, D.Y., Engel, A.K., 2005. Trial-by-trial coupling of concurrent electroencephalogram and functional magnetic resonance imaging identifies the dynamics of performance monitoring. J Neurosci 25, 11730–11737. doi:25/50/11730 [pii]10.1523/JNEUROSCI.3286-05.2005

Demiralp, T., Bayraktaroglu, Z., Lenz, D., Junge, S., Busch, N.A., Maess, B., Ergen, M., Herrmann, C.S., 2007. Gamma amplitudes are coupled to theta phase in human EEG during visual perception. Int. J. Psychophysiol. 64, 24–30. doi:S0167-8760(06)00211-X [pii]10.1016/j.ijpsycho.2006.07.005

Devor, A., Tian, P., Nishimura, N., Teng, I.C., Hillman, E.M.C., Narayanan, S.N., Ulbert, I., Boas, D.A., Kleinfeld, D., Dale, A.M., 2007. Suppressed Neuronal Activity and Concurrent Arteriolar Vasoconstriction May Explain Negative Blood Oxygenation Level-Dependent Signal. J. Neurosci. 27, 4452–4459. doi:10.1523/JNEUROSCI.0134-07.2007

Dickson, C.T., Biella, G., de Curtis, M., 2000. Evidence for Spatial Modules Mediated by Temporal Synchronization of Carbachol-Induced Gamma Rhythm in Medial Entorhinal Cortex. J. Neurosci. 20, 7846–7854.

Difrancesco, M.W., Holland, S.K., Szaflarski, J.P., 2008. Simultaneous EEG/functional magnetic resonance imaging at 4 Tesla: correlates of brain activity to spontaneous alpha rhythm during relaxation. J Clin Neurophysiol 25, 255–264. doi:10.1097/WNP.0b013e3181879d56

Donaire, A., Bargallo, N., Falcon, C., Maestro, I., Carreno, M., Setoain, J., Rumia, J., Fernandez, S., Pintor, L., Boget, T., 2009. Identifying the structures involved in seizure generation using sequential analysis of ictal-fMRI data. Neuroimage 47, 173–183. doi:10.1016/j.neuroimage.2009.03.059S1053-8119(09)00298-5 [pii]

Dreier, J.P., Korner, K., Gorner, A., Lindauer, U., Weih, M., Villringer, A., Dirnagl, U., 1995. Nitric oxide modulates the CBF response to increased extracellular potassium. J Cereb Blood Flow Metab 15, 914–919. doi:10.1038/jcbfm.1995.116

Dürschmid, S., Quandt, F., Krämer, U.M., Hinrichs, H., Heinze, H.-J., Schulz, R., Pannek, H., Chang, E.F., Knight, R.T., 2014. Oscillatory dynamics track motor performance improvement in human cortex. PLoS One 9, e89576. doi:10.1371/journal.pone.0089576

Ebersole, J.S., 1997. Defining epileptogenic foci: past, present, future. J. Clin. Neurophysiol. 14, 470–83.

Eckhorn, R., 1994. Oscillatory and non-oscillatory synchronizations in the visual cortex and their possible roles in associations of visual features. Prog Brain Res 102, 405–426. doi:S0079-6123(08)60556-7 [pii]10.1016/S0079-6123(08)60556-7

Eichele, T., Specht, K., Moosmann, M., Jongsma, M.L., Quiroga, R.Q., Nordby, H., Hugdahl, K., 2005. Assessing the spatiotemporal evolution of neuronal activation with single-trial event-related potentials and functional MRI. Proc Natl Acad Sci U S A 102, 17798–17803. doi:0505508102 [pii]10.1073/pnas.0505508102

Einevoll, G.T., Kayser, C., Logothetis, N.K., Panzeri, S., 2013. Modelling and analysis of local field potentials for studying the function of cortical circuits. Nat. Rev. Neurosci. 14, 770–85. doi:10.1038/nrn3599

Ekstrom, A., 2010. How and when the fMRI BOLD signal relates to underlying neural activity: The danger in dissociation. Brain Res. Rev. 62, 233–244. doi:10.1016/j.brainresrev.2009.12.004

Engel, A.K., Fries, P., Singer, W., 2001. Dynamic predictions: Oscillations and synchrony in top-down processing. Nat. Rev. Neurosci. 2, 704–716. doi:10.1038/35094565

Engel, J., 2013. Seizures and epilepsy, 2nd ed, Contemporary neurology series. Oxford University Press, Philadelphia.

Fender, D.H., 1987. Source localization of brain electrical activity., in: Gevins, A.S., Remond, A. (Eds.), Handbook of Electroencephalography and Clinical Neurophysiology, Vol. 1. Methods of Analysis of Brain Electrical and Magnetic Signals. Elsevier, Amsterdam, pp. 355–99.

Fermaglich, J., 1982. Electric Fields of the Brain: The Neurophysics of EEG, JAMA: The Journal of the American Medical Association. Oxford University Press. doi:10.1001/jama.1982.03320380071046

Ferree, T.C., Clay, M.T., Tucker, D.M., 2001. The spatial resolution of scalp EEG. Neurocomputing 38, 1209–1216.

Fiebelkorn, I.C., Snyder, A.C., Mercier, M.R., Butler, J.S., Molholm, S., Foxe, J.J., 2013. Cortical cross-frequency coupling predicts perceptual outcomes. Neuroimage 69, 126–37. doi:10.1016/j.neuroimage.2012.11.021

Fitzgerald, T.H.B., Valentin, A., Selway, R., Richardson, M.P., 2013. Cross-frequency coupling within and between the human thalamus and neocortex. Front. Hum. Neurosci. 7, 84. doi:10.3389/fnhum.2013.00084

Flanagan, D., Badawy, R.A., Jackson, G.D., 2014. EEG-fMRI in focal epilepsy: Local activation and regional networks. Clin Neurophysiol 125, 21–31. doi:10.1016/j.clinph.2013.06.182S1388-2457(13)00906-1 [pii]

Folbergrova, J., Ingvar, M., Siesjo, B.K., 1981. Metabolic changes in cerebral cortex, hippocampus, and cerebellum during sustained bicuculline-induced seizures. J Neurochem 37, 1228–1238.

Formaggio, E., Storti, S.F., Bertoldo, A., Manganotti, P., Fiaschi, A., Toffolo, G.M., 2011. Integrating EEG and fMRI in epilepsy. Neuroimage 54, 2719–2731. doi:S1053-8119(10)01468-0

[pii]10.1016/j.neuroimage.2010.11.038

Fox, M.D., Snyder, A.Z., Zacks, J.M., Raichle, M.E., 2006. Coherent spontaneous activity accounts for trial-to-trial variability in human evoked brain responses. Nat Neurosci 9, 23–25. doi:nn1616 [pii]10.1038/nn1616

Fox, P.T., Raichle, M.E., 1986. Focal physiological uncoupling of cerebral blood flow and oxidative metabolism during somatosensory stimulation in human subjects. Proc Natl Acad Sci U S A 83, 1140–1144.

Fox, P.T., Raichle, M.E., Mintun, M.A., Dence, C., 1988. Nonoxidative glucose consumption during focal physiologic neural activity. Science (80-.). 241, 462–464.

Freeman, W.J., Zhai, J., 2009. Simulated power spectral density (PSD) of background electrocorticogram (ECoG). Cogn Neurodyn 3, 97–103. doi:10.1007/s11571-008-9064-y

Freyer, F., Becker, R., Anami, K., Curio, G., Villringer, A., Ritter, P., 2009. Ultrahigh-frequency EEG during fMRI: pushing the limits of imaging-artifact correction. Neuroimage 48, 94–108. doi:10.1016/j.neuroimage.2009.06.022S1053-8119(09)00637-5 [pii]

Fried, I., Wilson, C.L., Maidment, N.T., Engel Jr., J., Behnke, E., Fields, T.A., MacDonald, K.A., Morrow, J.W., Ackerson, L., 1999. Cerebral microdialysis combined with single-neuron and electroencephalographic recording in neurosurgical patients. Technical note. J Neurosurg 91, 697–705. doi:10.3171/jns.1999.91.4.0697

Fries, P., 2005. A mechanism for cognitive dynamics: neuronal communication through neuronal coherence. Trends Cogn. Sci. 9, 474–80. doi:10.1016/j.tics.2005.08.011

Fries, P., 2001. Modulation of Oscillatory Neuronal Synchronization by Selective Visual Attention. Science (80-.). 291, 1560–1563. doi:10.1126/science.1055465

Fries, P., Schroder, J.-H., Roelfsema, P.R., Singer, W., Engel, A.K., 2002. Oscillatory Neuronal Synchronization in Primary Visual Cortex as a Correlate of Stimulus Selection. J. Neurosci. 22, 3739–3754.

Friese, U., Köster, M., Hassler, U., Martens, U., Trujillo-Barreto, N., Gruber, T., 2013. Successful memory encoding is associated with increased cross-frequency coupling between frontal theta and posterior gamma oscillations in human scalp-recorded EEG. Neuroimage 66, 642–647. doi:10.1016/j.neuroimage.2012.11.002

Friston, K.J., Williams, S., Howard, R., Frackowiak, R.S.J., Turner, R., 1996. Movement-Related effects in fMRI time-series. Magn. Reson. Med. 35, 346–355. doi:10.1002/mrm.1910350312

Friston, K.J., Zarahn, E., Josephs, O., Henson, R.N., Dale, a M., 1999. Stochastic designs in event-related fMRI. Neuroimage 10, 607–619. doi:10.1006/nimg.1999.0498

Fuglo, D., Pedersen, H., Rostrup, E., Hansen, A.E., Larsson, H.B., 2012. Correlation between single-trial visual evoked potentials and the blood oxygenation level dependent response in simultaneously recorded electroencephalography-functional magnetic resonance imaging. Magn Reson Med 68, 252–260. doi:10.1002/mrm.23227

Geneslaw, A.S., Zhao, M., Ma, H., Schwartz, T.H., 2011. Tissue hypoxia correlates with intensity of interictal spikes. J. Cereb. Blood Flow Metab. 31, 1394–1402. doi:10.1038/jcbfm.2011.16

Gloor, P., 1985. Neuronal generators and the problem of localization in electroencephalography:

application of volume conductor theory to electroencephalography. J. Clin. Neurophysiol. 2, 327–354.

Goense, J.B., Logothetis, N.K., 2008. Neurophysiology of the BOLD fMRI signal in awake monkeys. Curr Biol 18, 631–640. doi:S0960-9822(08)00442-9 [pii]10.1016/j.cub.2008.03.054

Gold, C., Henze, D.A., Koch, C., Buzsáki, G., 2006. On the origin of the extracellular action potential waveform: A modeling study. J. Neurophysiol. 95, 3113–28. doi:10.1152/jn.00979.2005

Goldman, R.I., Stern, J.M., Engel Jr., J., Cohen, M.S., 2002. Simultaneous EEG and fMRI of the alpha rhythm. Neuroreport 13, 2487–2492. doi:10.1097/01.wnr.0000047685.08940.d0

Goncalves, S.I., de Munck, J.C., Pouwels, P.J., Schoonhoven, R., Kuijer, J.P., Maurits, N.M., Hoogduin, J.M., Van Someren, E.J., Heethaar, R.M., Lopes da Silva, F.H., 2006. Correlating the alpha rhythm to BOLD using simultaneous EEG/fMRI: inter-subject variability. Neuroimage 30, 203–213. doi:S1053-8119(05)00707-X [pii]10.1016/j.neuroimage.2005.09.062

Gonzalez-Castillo, J., Hoy, C.W., Handwerker, D.A., Roopchansingh, V., Inati, S.J., Saad, Z.S., Cox, R.W., Bandettini, P.A., 2014. Task Dependence, Tissue Specificity, and Spatial Distribution of Widespread Activations in Large Single-Subject Functional MRI Datasets at 7T. Cereb. Cortex 4667–4677. doi:10.1093/cercor/bhu148

Gonzalez-Castillo, J., Saad, Z.S., Handwerker, D.A., Inati, S.J., Brenowitz, N., Bandettini, P.A., 2012. Whole-brain, time-locked activation with simple tasks revealed using massive averaging and model-free analysis. Proc. Natl. Acad. Sci. U. S. A. 109, 5487–92. doi:10.1073/pnas.1121049109

Gotman, J., Kobayashi, E., Bagshaw, A.P., Benar, C.G., Dubeau, F., 2006. Combining EEG and fMRI: a multimodal tool for epilepsy research. J Magn Reson Imaging 23, 906–920. doi:10.1002/jmri.20577

Grave de Peralta Menendez, R., Gonzalez Andino, S., Lantz, G., Michel, C.M., Landis, T., 2001. Noninvasive localization of electromagnetic epileptic activity. I. Method descriptions and simulations. Brain Topogr 14, 131–137.

Griesmayr, B., Gruber, W.R., Klimesch, W., Sauseng, P., 2010. Human frontal midline theta and its synchronization to gamma during a verbal delayed match to sample task. Neurobiol Learn Mem 93, 208–215. doi:10.1016/j.nlm.2009.09.013S1074-7427(09)00203-2 [pii]

Grisar, T., Lakaye, B., Thomas, E., Bettendorf, L., Minet, A., 1999. The molecular neuron-glia couple and epileptogenesis. Adv Neurol 79, 591–602.

Grouiller, F., Thornton, R.C., Groening, K., Spinelli, L., Duncan, J.S., Schaller, K., Siniatchkin, M., Lemieux, L., Seeck, M., Michel, C.M., Vulliemoz, S., 2011. With or without spikes: localization of focal epileptic activity by simultaneous electroencephalography and functional magnetic resonance imaging. Brain 134, 2867–2886. doi:10.1093/brain/awr156awr156 [pii]

Grouiller, F., Vercueil, L., Krainik, A., Segebarth, C., Kahane, P., David, O., 2010. Characterization of the hemodynamic modes associated with interictal epileptic activity using a deformable model-based analysis of combined EEG and functional MRI recordings. Hum Brain Mapp 31, 1157–1173. doi:10.1002/hbm.20925

Grubb Jr., R.L., Raichle, M.E., Eichling, J.O., Ter-Pogossian, M.M., 1974. The effects of changes in PaCO2 on cerebral blood volume, blood flow, and vascular mean transit time. Stroke 5, 630–639.

Gsell, W., Burke, M., Wiedermann, D., Bonvento, G., Silva, A.C., Dauphin, F., Buhrle, C., Hoehn, M.,

Schwindt, W., 2006. Differential effects of NMDA and AMPA glutamate receptors on functional magnetic resonance imaging signals and evoked neuronal activity during forepaw stimulation of the rat. J Neurosci 26, 8409–8416. doi:26/33/8409 [pii]10.1523/JNEUROSCI.4615-05.2006

Guirgis, M., Chinvarun, Y., Carlen, P.L., Bardakjian, B.L., 2013. The Role of Delta - Modulated High Frequency Oscillations in Seizure State Classification, in: 35th Annual International Conference of the IEEE EMBS. pp. 6595–6598.

Gulrajani, R.M., Roberge, F.A., Savard, P., 1984. Moving dipole inverse ECG and EEG solutions. IEEE Trans Biomed Eng 31, 903–910. doi:10.1109/TBME.1984.325257

Hamandi, K., Powell, H.W., Laufs, H., Symms, M.R., Barker, G.J., Parker, G.J., Lemieux, L., Duncan, J.S., 2008. Combined EEG-fMRI and tractography to visualise propagation of epileptic activity. J Neurol Neurosurg Psychiatry 79, 594–597. doi:jnnp.2007.125401 [pii]10.1136/jnnp.2007.125401

Hamel, E., 2006. Perivascular nerves and the regulation of cerebrovascular tone. J Appl Physiol 100, 1059–1064. doi:100/3/1059 [pii]10.1152/japplphysiol.00954.2005

Händel, B., Haarmeier, T., 2009. Cross-frequency coupling of brain oscillations indicates the success in visual motion discrimination. Neuroimage 45, 1040–6. doi:10.1016/j.neuroimage.2008.12.013

Handwerker, D.A., Ollinger, J.M., D'Esposito, M., 2004. Variation of BOLD hemodynamic responses across subjects and brain regions and their effects on statistical analyses. Neuroimage 21, 1639–1651. doi:10.1016/j.neuroimage.2003.11.029S1053811903007584 [pii]

Hasselmo, M.E., Bodelon, C., Wyble, B.P., 2002. A proposed function for hippocampal theta rhythm: separate phases of encoding and retrieval enhance reversal of prior learning. Neural Comput 14, 793–817. doi:10.1162/089976602317318965

He, B.J., Zempel, J.M., Snyder, A.Z., Raichle, M.E., 2010. The temporal structures and functional significance of scale-free brain activity. Neuron 66, 353–369. doi:S0896-6273(10)00291-6 [pii]10.1016/j.neuron.2010.04.020

Hermes, D., Miller, K.J., Vansteensel, M.J., Aarnoutse, E.J., Leijten, F.S., Ramsey, N.F., 2012. Neurophysiologic correlates of fMRI in human motor cortex. Hum Brain Mapp 33, 1689–1699. doi:10.1002/hbm.21314

Hermes, D., Miller, K.J., Vansteensel, M.J., Edwards, E., Ferrier, C.H., Bleichner, M.G., van Rijen, P.C., Aarnoutse, E.J., Ramsey, N.F., 2013. Cortical theta wanes for language. Neuroimage 85, 738–748. doi:10.1016/j.neuroimage.2013.07.029

Hermes, D., Miller, K.J., Wandell, B.A., Winawer, J., 2015. Stimulus Dependence of Gamma Oscillations in Human Visual Cortex. Cereb. cortex 25, 2951–2959. doi:10.1093/cercor/bhu091

Hewson-Stoate, N., Jones, M., Martindale, J., Berwick, J., Mayhew, J., 2005. Further nonlinearities in neurovascular coupling in rodent barrel cortex. Neuroimage 24, 565–574. doi:S1053-8119(04)00503-8 [pii]10.1016/j.neuroimage.2004.08.040

Hochberg, L.R., Serruya, M.D., Friehs, G.M., Mukand, J.A., Saleh, M., Caplan, A.H., Branner, A., Chen, D., Penn, R.D., Donoghue, J.P., 2006. Neuronal ensemble control of prosthetic devices by a human with tetraplegia. Nature 442, 164–171. doi:nature04970 [pii]10.1038/nature04970

Homma, S., Nakajima, Y., Musha, T., Okamoto, Y., Hagbarth, K.E., Blom, S., Flink, R., 1990. Generator mechanisms of epileptic potentials analyzed by dipole tracing method. Neurosci Lett 113, 181–186.

Hu, L., Liang, M., Mouraux, A., Wise, R.G., Hu, Y., Iannetti, G.D., 2011. Taking into account latency, amplitude, and morphology: improved estimation of single-trial ERPs by wavelet filtering and multiple linear regression. J. Neurophysiol. 106, 3216–29. doi:10.1152/jn.00220.2011

Huttunen, J.K., Grohn, O., Penttonen, M., 2008. Coupling between simultaneously recorded BOLD response and neuronal activity in the rat somatosensory cortex. Neuroimage 39, 775–785. doi:S1053-8119(07)00571-X [pii]10.1016/j.neuroimage.2007.06.042

Hyafil, A., Giraud, A., Fontolan, L., Gutkin, B., 2015. Neural Cross-Frequency Coupling: Connecting Architectures , Mechanisms , and Functions. Trends Neurosci. 38, 725–741. doi:10.1016/j.tins.2015.09.001

Iadecola, C., Nedergaard, M., 2007. Glial regulation of the cerebral microvasculature. Nat Neurosci 10, 1369–1376. doi:nn2003 [pii]10.1038/nn2003

Iannetti, G.D., Di Bonaventura, C., Pantano, P., Giallonardo, A.T., Romanelli, P.L., Bozzao, L., Manfredi, M., Ricci, G.B., 2002. fMRI/EEG in paroxysmal activity elicited by elimination of central vision and fixation. Neurology 58, 976–979.

Ibrahim, G.M., Wong, S.M., Anderson, R.A., Singh-Cadieux, G., Akiyama, T., Ochi, A., Otsubo, H., Okanishi, T., Valiante, T.A., Donner, E., Rutka, J.T., Snead, O.C., Doesburg, S.M., 2014. Dynamic modulation of epileptic high frequency oscillations by the phase of slower cortical rhythms. Exp. Neurol. 251, 30–8. doi:10.1016/j.expneurol.2013.10.019

Isomura, Y., Sirota, A., Ozen, S., Montgomery, S., Mizuseki, K., Henze, D.A., Buzsaki, G., 2006. Integration and segregation of activity in entorhinal-hippocampal subregions by neocortical slow oscillations. Neuron 52, 871–882. doi:S0896-6273(06)00822-1 [pii]10.1016/j.neuron.2006.10.023

Ives, J.R., Warach, S., Schmitt, F., Edelman, R.R., Schomer, D.L., 1993. Monitoring the patient's EEG during echo planar MRI. Electroencephalogr Clin Neurophysiol 87, 417–420.

Jacobs, J., Kahana, M.J., 2010. Direct brain recordings fuel advances in cognitive electrophysiology. Trends Cogn. Sci. 14, 162–71. doi:10.1016/j.tics.2010.01.005

Jacobs, J., Kobayashi, K., Gotman, J., 2011. High-frequency changes during interictal spikes detected by time-frequency analysis. Clin. Neurophysiol. 122, 32–42. doi:10.1016/j.clinph.2010.05.033

Jacobs, J., Levan, P., Moeller, F., Boor, R., Stephani, U., Gotman, J., Siniatchkin, M., 2009. Hemodynamic changes preceding the interictal EEG spike in patients with focal epilepsy investigated using simultaneous EEG-fMRI. Neuroimage 45, 1220–1231. doi:S1053-8119(09)00026-3 [pii]10.1016/j.neuroimage.2009.01.014

Jacobs, J., Menzel, A., Ramantani, G., Körbl, K., Assländer, J., Schulze-Bonhage, A., Hennig, J., LeVan, P., 2014. Negative BOLD in default-mode structures measured with EEG-MREG is larger in temporal than extra-temporal epileptic spikes. Front. Neurosci. 8, 335. doi:10.3389/fnins.2014.00335

Jacobs, J., Rohr, A., Moeller, F., Boor, R., Kobayashi, E., LeVan Meng, P., Stephani, U., Gotman, J., Siniatchkin, M., 2008. Evaluation of epileptogenic networks in children with tuberous sclerosis complex using EEG-fMRI. Epilepsia 49, 816–825. doi:EPI1486 [pii]10.1111/j.1528-1167.2007.01486.x

Jann, K., Dierks, T., Boesch, C., Kottlow, M., Strik, W., Koenig, T., 2009. BOLD correlates of EEG alpha phase-locking and the fMRI default mode network. Neuroimage 45, 903–916.

Jensen, M.S., Yaari, Y., 1997. Role of intrinsic burst firing, potassium accumulation, and electrical coupling in the elevated potassium model of hippocampal epilepsy. J Neurophysiol 77, 1224–1233.

Jones, M.R., Moynihan, H., MacKenzie, N., Puente, J., 2002. Temporal aspects of stimulus-driven attending in dynamic arrays. Psychol. Sci. 13, 313–9.

Jorge, J., Figueiredo, P., van der Zwaag, W., Marques, J.P., 2013. Signal fluctuations in fMRI data acquired with 2D-EPI and 3D-EPI at 7 Tesla. Magn. Reson. Imaging 31, 212–220. doi:10.1016/j.mri.2012.07.001

Jorge, J., Grouiller, F., Ipek, Ö., Stoermer, R., Michel, C.M., Figueiredo, P., van der Zwaag, W., Gruetter, R., 2015. Simultaneous EEG-fMRI at ultra-high field: artifact prevention and safety assessment. Neuroimage 105, 132–44. doi:10.1016/j.neuroimage.2014.10.055

Kajikawa, Y., Schroeder, C.E., 2011. How Local Is the Local Field Potential? Neuron 72, 847–858. doi:http://dx.doi.org/10.1016/j.neuron.2011.09.029

Kandel, A., Buzsaki, G., 1997. Cellular-synaptic generation of sleep spindles, spike-and-wave discharges, and evoked thalamocortical responses in the neocortex of the rat. J Neurosci 17, 6783–6797.

Kavanagh, R.N., Darcey, T.M., Lehmann, D., Fender, D.H., 1978. Evaluation of methods for three-dimensional localization of electrical sources in the human brain. IEEE Trans Biomed Eng 25, 421–429. doi:10.1109/TBME.1978.326339

Kayser, C., Kim, M., Ugurbil, K., Kim, D.S., Konig, P., 2004. A comparison of hemodynamic and neural responses in cat visual cortex using complex stimuli. Cereb Cortex 14, 881–891. doi:10.1093/cercor/bhh047bhh047 [pii]

Keller, C.J., Truccolo, W., Gale, J.T., Eskandar, E., Thesen, T., Carlson, C., Devinsky, O., Kuzniecky, R., Doyle, W.K., Madsen, J.R., Schomer, D.L., Mehta, A.D., Brown, E.N., Hochberg, L.R., Ulbert, I., Halgren, E., Cash, S.S., 2010. Heterogeneous neuronal firing patterns during interictal epileptiform discharges in the human cortex. Brain 133, 1668–1681. doi:10.1093/brain/awq112

Khursheed, F., Tandon, N., Tertel, K., Pieters, T.A., Disano, M.A., Ellmore, T.M., 2011. Frequency-specific electrocorticographic correlates of working memory delay period fMRI activity. Neuroimage 56, 1773–1782. doi:S1053-8119(11)00218-7 [pii]10.1016/j.neuroimage.2011.02.062

Kilner, J.M., Mattout, J., Henson, R., Friston, K.J., 2005. Hemodynamic correlates of EEG: a heuristic. Neuroimage 28, 280–286. doi:S1053-8119(05)00416-7 [pii]10.1016/j.neuroimage.2005.06.008

Kim, D.S., Ronen, I., Olman, C., Kim, S.G., Ugurbil, K., Toth, L.J., 2004. Spatial relationship between neuronal activity and BOLD functional MRI. Neuroimage 21, 876–885. doi:10.1016/j.neuroimage.2003.10.018S1053811903006694 [pii]

Klee, M.R., Offenloch, K., Tigges, J., 1965. Cross-Correlation Analysis of Electroencephalographic Potentials and Slow Membrane Transients. Science (80-.). 147, 519–521.

Kobayashi, K., Jacobs, J., Gotman, J., 2009. Detection of changes of high-frequency activity by statistical time-frequency analysis in epileptic spikes. Clin. Neurophysiol. 120, 1070–1077. doi:10.1016/j.clinph.2009.03.020

Kocsis, B., Bragin, A., Buzsaki, G., 1999. Interdependence of multiple theta generators in the hippocampus: a partial coherence analysis. J Neurosci 19, 6200–6212.

Koehler, R.C., Roman, R.J., Harder, D.R., 2009. Astrocytes and the regulation of cerebral blood flow.

Trends Neurosci. 32, 160–169. doi:10.1016/j.tins.2008.11.005S0166-2236(09)00003-4 [pii]

Koenig, T., Lehmann, D., Saito, N., Kuginuki, T., Kinoshita, T., Koukkou, M., 2001. Decreased functional connectivity of EEG theta-frequency activity in first-episode, neuroleptic-naive patients with schizophrenia: preliminary results. Schizophr Res 50, 55–60. doi:S0920-9964(00)00154-7 [pii]

Koenig, T., Prichep, L., Dierks, T., Hubl, D., Wahlund, L.O., John, E.R., Jelic, V., 2005. Decreased EEG synchronization in Alzheimer's disease and mild cognitive impairment. Neurobiol Aging 26, 165–171. doi:S0197458004001538 [pii]10.1016/j.neurobiolaging.2004.03.008

Köster, M., Friese, U., Schöne, B., Trujillo-Barreto, N., Gruber, T., 2014. Theta-gamma coupling during episodic retrieval in the human EEG. Brain Res. 1577, 57–68. doi:10.1016/j.brainres.2014.06.028

Kottlow, M., Jann, K., Dierks, T., Koenig, T., 2012. Increased phase synchronization during continuous face integration measured simultaneously with EEG and fMRI. Clin Neurophysiol. doi:S1388-2457(12)00005-3 [pii]10.1016/j.clinph.2011.12.019

Krakow, K., Allen, P.J., Symms, M.R., Lemieux, L., Josephs, O., Fish, D.R., 2000. EEG recording during fMRI experiments: image quality. Hum Brain Mapp 10, 10–15. doi:10.1002/(SICI)1097-0193(200005)10:1<10::AID-HBM20>3.0.CO;2-T [pii]

Kramer, M.A., Tort, A.B.L., Kopell, N.J., 2008. Sharp edge artifacts and spurious coupling in EEG frequency comodulation measures. J. Neurosci. Methods 170, 352–357. doi:10.1016/j.jneumeth.2008.01.020

Kunii, N., Kamada, K., Ota, T., Kawai, K., Saito, N., 2013. Characteristic profiles of high gamma activity and blood oxygenation level-dependent responses in various language areas. Neuroimage 65, 242–249. doi:10.1016/j.neuroimage.2012.09.059S1053-8119(12)00976-7 [pii]

Kuschinsky, W., Wahl, M., Bosse, O., Thurau, K., 1972. Perivascular potassium and pH as determinants of local pial arterial diameter in cats. A microapplication study. Circ Res 31, 240–247.

Kwong, K.K., Belliveau, J.W., Chesler, D.A., Goldberg, I.E., Weisskoff, R.M., Poncelet, B.P., Kennedy, D.N., Hoppel, B.E., Cohen, M.S., Turner, R., et al., 1992. Dynamic magnetic resonance imaging of human brain activity during primary sensory stimulation. Proc Natl Acad Sci U S A 89, 5675–5679.

Lachaux, J.P., Fonlupt, P., Kahane, P., Minotti, L., Hoffmann, D., Bertrand, O., Baciu, M., 2007. Relationship between task-related gamma oscillations and BOLD signal: new insights from combined fMRI and intracranial EEG. Hum Brain Mapp 28, 1368–1375. doi:10.1002/hbm.20352

Lakatos, P., Chen, C.-M., O'Connell, M.N., Mills, A., Schroeder, C.E., 2007. Neuronal oscillations and multisensory interaction in primary auditory cortex. Neuron 53, 279–92. doi:10.1016/j.neuron.2006.12.011

Lakatos, P., Karmos, G., Mehta, A.D., Ulbert, I., Schroeder, C.E., 2008. Entrainment of neuronal oscillations as a mechanism of attentional selection. Science (80-.). 320, 110–113. doi:320/5872/110 [pii]10.1126/science.1154735

Lakatos, P., Musacchia, G., O'Connel, M.N., Falchier, A.Y., Javitt, D.C., Schroeder, C.E., 2013. The spectrotemporal filter mechanism of auditory selective attention. Neuron 77, 750–61. doi:10.1016/j.neuron.2012.11.034

Lakatos, P., Shah, A.S., Knuth, K.H., Ulbert, I., Karmos, G., Schroeder, C.E., 2005. An oscillatory hierarchy controlling neuronal excitability and stimulus processing in the auditory cortex. J Neurophysiol 94, 1904–1911. doi:00263.2005 [pii]10.1152/jn.00263.2005

Laufs, H., Kleinschmidt, A., Beyerle, A., Eger, E., Salek-Haddadi, A., Preibisch, C., Krakow, K., 2003a. EEG-correlated fMRI of human alpha activity. Neuroimage 19, 1463–1476. doi:S1053811903002866 [pii]

Laufs, H., Krakow, K., Sterzer, P., Eger, E., Beyerle, A., Salek-Haddadi, A., Kleinschmidt, A., 2003b. Electroencephalographic signatures of attentional and cognitive default modes in spontaneous brain activity fluctuations at rest. Proc Natl Acad Sci U S A 100, 11053–11058. doi:10.1073/pnas.18316381001831638100 [pii]

Lauritzen, M., 2005. Reading vascular changes in brain imaging: is dendritic calcium the key? Nat. Rev. Neurosci. 6, 77–85. doi:10.1038/sj.jcbfm.9591524.0684

Leite, M., Leal, A., Figueiredo, P., 2013. Transfer Function between EEG and BOLD Signals of Epileptic Activity. Front Neurol 4, 1. doi:10.3389/fneur.2013.00001

Lemieux, L., Allen, P.J., Franconi, F., Symms, M.R., Fish, D.R., 1997. Recording of EEG during fMRI experiments: patient safety. Magn Reson Med 38, 943–952.

Lemieux, L., Laufs, H., Carmichael, D., Paul, J.S., Walker, M.C., Duncan, J.S., 2008. Noncanonical spike-related BOLD responses in focal epilepsy. Hum Brain Mapp 29, 329–345. doi:10.1002/hbm.20389

Leopold, D.A., Murayama, Y., Logothetis, N.K., 2003. Very slow activity fluctuations in monkey visual cortex: implications for functional brain imaging. Cereb Cortex 13, 422–433.

LeVan, P., Tyvaert, L., Gotman, J., 2010a. Modulation by EEG features of BOLD responses to interictal epileptiform discharges. Neuroimage 50, 15–26. doi:S1053-8119(09)01333-0 [pii] 10.1016/j.neuroimage.2009.12.044

LeVan, P., Tyvaert, L., Moeller, F., Gotman, J., 2010b. Independent component analysis reveals dynamic ictal BOLD responses in EEG-fMRI data from focal epilepsy patients. Neuroimage 49, 366–378. doi:10.1016/j.neuroimage.2009.07.064 S1053-8119(09)00855-6 [pii]

Lindsley, D.B., Wicke, J.D., 1974. The electroencephalogram: Autonomous electrical activity in man and animals. Bioelectric Rec. Tech. 1, 3–83.

Lippert, M.T., Steudel, T., Ohl, F., Logothetis, N.K., Kayser, C., 2010. Coupling of neural activity and fMRI-BOLD in the motion area MT. Magn Reson Imaging 28, 1087–1094. doi:10.1016/j.mri.2009.12.028S0730-725X(09)00320-8 [pii]

Lisman, J.E., Jensen, O., 2013. The θ-γ neural code. Neuron 77, 1002–16. doi:10.1016/j.neuron.2013.03.007

Lisman, J.E., Jensen, O., 2013. The Theta-Gamma Neural Code. Neuron 77, 1002–1016. doi:10.1016/j.neuron.2013.03.007

Liston, A.D., De Munck, J.C., Hamandi, K., Laufs, H., Ossenblok, P., Duncan, J.S., Lemieux, L., 2006. Analysis of EEG-fMRI data in focal epilepsy based on automated spike classification and Signal Space Projection. Neuroimage 31, 1015–1024. doi:S1053-8119(06)00093-0 [pii]10.1016/j.neuroimage.2006.01.040

Logothetis, N.K., 2010. Neurovascular Uncoupling: Much Ado about Nothing. Front Neuroenergetics 2. doi:10.3389/fnene.2010.000022 [pii]

Logothetis, N.K., 2008. What we can do and what we cannot do with fMRI. Nature 453, 869–878. doi:Doi 10.1038/Nature06976

Logothetis, N.K., 2003. The underpinnings of the BOLD functional magnetic resonance imaging signal. J Neurosci 23, 3963–3971. doi:23/10/3963 [pii]

Logothetis, N.K., Pauls, J., Augath, M., Trinath, T., Oeltermann, A., 2001. Neurophysiological investigation of the basis of the fMRI signal. Nature 412, 150–157. doi:10.1038/3508400535084005 [pii]

Logothetis, N.K., Wandell, B.A., 2004. Interpreting the BOLD signal. Annu Rev Physiol 66, 735–769. doi:10.1146/annurev.physiol.66.082602.092845

Lopes da Silva, F., 2013. EEG and MEG: Relevance to Neuroscience. Neuron 80, 1112–1128. doi:10.1016/j.neuron.2013.10.017 S0896-6273(13)00920-3 [pii]

Lopes da Silva, F., 2010. EEG: Origin and Measurement, in: Mulert, C., Lemieux, L. (Eds.), EEG-fMRI Physiological Basis, Technique, and Applications. Springer, Berlin.

Lopes da Silva, F., 1991. Neural mechanisms underlying brain waves: from neural membranes to networks. Electroencephalogr Clin Neurophysiol 79, 81–93.

Lopes da Silva, F.H., 2011. Computer-Assisted EEG Diagnosis: Pattern Recognition and Brain Mapping, in: Schomer, D., Lopes da Silva, F.H. (Eds.), Niedermeyer's Electroencephalography. Basic Principles, Clinical Applications, and Related Fields. Lippincott Williams & Wilkins.

Lopes da Silva, F.H., van Lierop, T.H., Schrijer, C.F., van Leeuwen, W.S., 1973. Organization of thalamic and cortical alpha rhythms: spectra and coherences. Electroencephalogr Clin Neurophysiol 35, 627–639.

Luo, Q., Glover, G.H., 2012. Influence of dense-array EEG cap on fMRI signal. Magn. Reson. Med. 68, 807–815. doi:10.1002/mrm.23299

Magri, C., Schridde, U., Murayama, Y., Panzeri, S., Logothetis, N.K., 2012. The amplitude and timing of the BOLD signal reflects the relationship between local field potential power at different frequencies. J Neurosci 32, 1395–1407. doi:32/4/1395 [pii]10.1523/JNEUROSCI.3985-11.2012

Maier, A., Wilke, M., Aura, C., Zhu, C., Ye, F.Q., Leopold, D.A., 2008. Divergence of fMRI and neural signals in V1 during perceptual suppression in the awake monkey. Nat Neurosci 11, 1193–1200. doi:10.1038/nn.2173nn.2173 [pii]

Makeig, S., Westerfield, M., Jung, T.P., Enghoff, S., Townsend, J., Courchesne, E., Sejnowski, T.J., 2002. Dynamic brain sources of visual evoked responses. Science (80-.). 295, 690–694. doi:10.1126/science.1066168295/5555/690 [pii]

Malekmohammadi, M., Elias, W.J., Pouratian, N., 2014. Human Thalamus Regulates Cortical Activity via Spatially Specific and Structurally Constrained Phase-Amplitude Coupling. Cereb. Cortex bht358–. doi:10.1093/cercor/bht358

Manning, J.R., Jacobs, J., Fried, I., Kahana, M.J., 2009. Broadband shifts in local field potential power spectra are correlated with single-neuron spiking in humans. J. Neurosci. 29, 13613–20. doi:10.1523/JNEUROSCI.2041-09.2009

Mantini, D., Perrucci, M.G., Del Gratta, C., Romani, G.L., Corbetta, M., 2007. Electrophysiological signatures of resting state networks in the human brain. Proc Natl Acad Sci U S A 104, 13170–13175. doi:0700668104 [pii]10.1073/pnas.0700668104

Maris, E., van Vugt, M., Kahana, M., 2011. Spatially distributed patterns of oscillatory coupling between high-frequency amplitudes and low-frequency phases in human iEEG. Neuroimage 54, 836–850.

doi:S1053-8119(10)01210-3 [pii]10.1016/j.neuroimage.2010.09.029

Marques, J.P., Rebola, J., Figueiredo, P., Pinto, A., Sales, F., Castelo-Branco, M., 2009. ICA decomposition of EEG signal for fMRI processing in epilepsy. Hum Brain Mapp 30, 2986–2996. doi:10.1002/hbm.20723

Marrosu, F., Barberini, L., Puligheddu, M., Bortolato, M., Mascia, M., Tuveri, A., Muroni, A., Mallarini, G., Avanzini, G., 2009. Combined EEG/fMRI recording in musicogenic epilepsy. Epilepsy Res 84, 77–81. doi:10.1016/j.eplepsyres.2008.11.019S0920-1211(08)00363-X [pii]

Martin, C., Martindale, J., Berwick, J., Mayhew, J., 2006. Investigating neural-hemodynamic coupling and the hemodynamic response function in the awake rat. Neuroimage 32, 33–48. doi:S1053-8119(06)00135-2 [pii]10.1016/j.neuroimage.2006.02.021

Martinez-Montes, E., Valdes-Sosa, P.A., Miwakeichi, F., Goldman, R.I., Cohen, M.S., 2004. Concurrent EEG/fMRI analysis by multiway Partial Least Squares. Neuroimage 22, 1023–1034. doi:10.1016/j.neuroimage.2004.03.038S1053811904001946 [pii]

Masamoto, K., Vazquez, A., Wang, P., Kim, S.G., 2008. Trial-by-trial relationship between neural activity, oxygen consumption, and blood flow responses. Neuroimage 40, 442–450. doi:S1053-8119(07)01113-5 [pii]10.1016/j.neuroimage.2007.12.011

Masterton, R.A., Harvey, A.S., Archer, J.S., Lillywhite, L.M., Abbott, D.F., Scheffer, I.E., Jackson, G.D., 2010. Focal epileptiform spikes do not show a canonical BOLD response in patients with benign rolandic epilepsy (BECTS). Neuroimage 51, 252–260. doi:S1053-8119(10)00148-5 [pii]10.1016/j.neuroimage.2010.01.109

Mathiesen, C., Caesar, K., Akgoren, N., Lauritzen, M., 1998. Modification of activity-dependent increases of cerebral blood flow by excitatory synaptic activity and spikes in rat cerebellar cortex. J Physiol 512 (Pt 2, 555–566.

Mathiesen, C., Caesar, K., Lauritzen, M., 2000. Temporal coupling between neuronal activity and blood flow in rat cerebellar cortex as indicated by field potential analysis. J Physiol 523 Pt 1, 235–246. doi:PHY_0136 [pii]

Mazoyer, B., Zago, L., Mellet, E., Bricogne, S., Etard, O., Houde, O., Crivello, F., Joliot, M., Petit, L., Tzourio-Mazoyer, N., 2001. Cortical networks for working memory and executive functions sustain the conscious resting state in man. Brain Res Bull 54, 287–298. doi:S0361-9230(00)00437-8 [pii]

Michel, C.M., Murray, M.M., Lantz, G., Gonzalez, S., Spinelli, L., Grave de Peralta, R., 2004. EEG source imaging. Clin Neurophysiol 115, 2195–2222. doi:10.1016/j.clinph.2004.06.001S1388245704002135 [pii]

Michels, L., Bucher, K., Luchinger, R., Klaver, P., Martin, E., Jeanmonod, D., Brandeis, D., 2010. Simultaneous EEG-fMRI during a working memory task: modulations in low and high frequency bands. PLoS One 5, e10298. doi:10.1371/journal.pone.0010298

Miller, K.J., 2010. Broadband spectral change: evidence for a macroscale correlate of population firing rate? J. Neurosci. 30, 6477–9. doi:10.1523/JNEUROSCI.6401-09.2010

Miller, K.J., Hermes, D., Honey, C.J., Hebb, A.O., Ramsey, N.F., Knight, R.T., Ojemann, J.G., Fetz, E.E., 2012. Human motor cortical activity is selectively phase-entrained on underlying rhythms. PLoS Comput. Biol. 8, e1002655. doi:10.1371/journal.pcbi.1002655

Miller, K.J., Hermes, D., Honey, C.J., Sharma, M., Rao, R.P., den Nijs, M., Fetz, E.E., Sejnowski, T.J., Hebb, A.O., Ojemann, J.G., Makeig, S., Leuthardt, E.C., 2010. Dynamic modulation of local population activity by rhythm phase in human occipital cortex during a visual search task. Front Hum Neurosci 4, 197. doi:10.3389/fnhum.2010.00197

Mitzdorf, U., 1985. Current source-density method and application in cat cerebral cortex: investigation of evoked potentials and EEG phenomena. Physiol Rev 65, 37–100.

Mizuhara, H., Wang, L.Q., Kobayashi, K., Yamaguchi, Y., 2005. Long-range EEG phase synchronization during an arithmetic task indexes a coherent cortical network simultaneously measured by fMRI. Neuroimage 27, 553–563. doi:S1053-8119(05)00278-8 [pii]10.1016/j.neuroimage.2005.04.030

Moeller, F., Moehring, J., Ick, I., Steinmann, E., Wolff, S., Jansen, O., Boor, R., Stephani, U., Siniatchkin, M., 2013. EEG-fMRI in atypical benign partial epilepsy. Epilepsia 54, e103–8. doi:10.1111/epi.12243

Moeller, F., Siebner, H.R., Wolff, S., Muhle, H., Boor, R., Granert, O., Jansen, O., Stephani, U., Siniatchkin, M., 2008. Changes in activity of striato-thalamo-cortical network precede generalized spike wave discharges. Neuroimage 39, 1839–1849. doi:S1053-8119(07)01002-6 [pii]10.1016/j.neuroimage.2007.10.058

Moeller, F., Tyvaert, L., Nguyen, D.K., LeVan, P., Bouthillier, A., Kobayashi, E., Tampieri, D., Dubeau, F., Gotman, J., 2009. EEG-fMRI: adding to standard evaluations of patients with nonlesional frontal lobe epilepsy. Neurology 73, 2023–2030. doi:10.1212/WNL.0b013e3181c55d1773/23/2023 [pii]

Moosmann, M., Ritter, P., Krastel, I., Brink, A., Thees, S., Blankenburg, F., Taskin, B., Obrig, H., Villringer, A., 2003. Correlates of alpha rhythm in functional magnetic resonance imaging and near infrared spectroscopy. Neuroimage 20, 145–158. doi:S1053811903003446 [pii]

Mormann, F., Fell, J., Axmacher, N., Weber, B., Lehnertz, K., Elger, C.E., Fernandez, G., 2005. Phase/amplitude reset and theta-gamma interaction in the human medial temporal lobe during a continuous word recognition memory task. Hippocampus 15, 890–900. doi:10.1002/hipo.20117

Morocz, I.A., Karni, A., Haut, S., Lantos, G., Liu, G., 2003. fMRI of triggerable aurae in musicogenic epilepsy. Neurology 60, 705–709.

Mukamel, R., Gelbard, H., Arieli, A., Hasson, U., Fried, I., Malach, R., 2005. Coupling between neuronal firing, field potentials, and FMRI in human auditory cortex. Science (80-.). 309, 951–954. doi:309/5736/951 [pii]10.1126/science.1110913

Mulert, C., Leicht, G., Hepp, P., Kirsch, V., Karch, S., Pogarell, O., Reiser, M., Hegerl, U., Jager, L., Moller, H.J., McCarley, R.W., 2010. Single-trial coupling of the gamma-band response and the corresponding BOLD signal. Neuroimage 49, 2238–2247. doi:S1053-8119(09)01129-X [pii]10.1016/j.neuroimage.2009.10.058

Mulert, C., Seifert, C., Leicht, G., Kirsch, V., Ertl, M., Karch, S., Moosmann, M., Lutz, J., Moller, H.J., Hegerl, U., Pogarell, O., Jager, L., 2008. Single-trial coupling of EEG and fMRI reveals the involvement of early anterior cingulate cortex activation in effortful decision making. Neuroimage 42, 158–168. doi:S1053-8119(08)00512-0 [pii]10.1016/j.neuroimage.2008.04.236

Mullinger, K., Bowtell, R., 2011. Combining EEG and fMRI, in: Magnetic Resonance Neuroimaging - Methods and Protocols. pp. 303–326. doi:10.1007/978-1-61737-992-5_15

Mullinger, K., Debener, S., Coxon, R., Bowtell, R., 2008. Effects of simultaneous EEG recording on MRI data quality at 1.5, 3 and 7 tesla. Int. J. Psychophysiol. 67, 178–188. doi:S0167-8760(07)00157-2

[pii]10.1016/j.ijpsycho.2007.06.008

Mullinger, K.J., Yan, W.X., Bowtell, R., 2011. Reducing the gradient artefact in simultaneous EEG-fMRI by adjusting the subject's axial position. Neuroimage 54, 1942–1950. doi:10.1016/j.neuroimage.2010.09.079

Murayama, Y., Biessmann, F., Meinecke, F.C., Muller, K.R., Augath, M., Oeltermann, A., Logothetis, N.K., 2010. Relationship between neural and hemodynamic signals during spontaneous activity studied with temporal kernel CCA. Magn Reson Imaging 28, 1095–1103. doi:S0730-725X(09)00308-7 [pii]10.1016/j.mri.2009.12.016

Murta, T., Leal, A., Garrido, M.I., Figueiredo, P., 2012. Dynamic Causal Modelling of epileptic seizure propagation pathways: A combined EEG-fMRI study. Neuroimage 62, 1642–1634.

Murta, T., Leite, M., Carmichael, D.W., Figueiredo, P., Lemieux, L., 2015. Electrophysiological correlates of the BOLD signal for EEG-informed fMRI. Hum. Brain Mapp. 36, 391–414. doi:10.1002/hbm.22623

Neuner, I., Warbrick, T., Arrubla, J., Felder, J., Celik, A., Reske, M., Boers, F., Shah, N.J., 2013. EEG acquisition in ultra-high static magnetic fields up to 9.4 T. Neuroimage 68, 214–220. doi:10.1016/j.neuroimage.2012.11.064S1053-8119(12)01183-4 [pii]

Nguyen, M., Hermes, D., Winawer, J., 2015. Broadband field potentials, but not gamma oscillations, correlate with BOLD fMRI in human visual cortex. J. Vis. 15, 1286. doi:10.1167/15.12.1286

Niazy, R.K., Beckmann, C.F., Iannetti, G.D., Brady, J.M., Smith, S.M., 2005. Removal of FMRI environment artifacts from EEG data using optimal basis sets. Neuroimage 28, 720–737. doi:S1053-8119(05)00472-6 [pii]10.1016/j.neuroimage.2005.06.067

Niedermeyer, E., Lopes da Silva, F.H., 1999. Electroencephalography: basic principles, clinical applications, and related fields. MD: Williams & Wilkins, Baltimore.

Nierhaus, T., Gundlach, C., Goltz, D., Thiel, S.D., Pleger, B., Villringer, A., 2013. Internal ventilation system of MR scanners induces specific EEG artifact during simultaneous EEG-fMRI. Neuroimage 74, 70–76. doi:10.1016/j.neuroimage.2013.02.016S1053-8119(13)00143-2 [pii]

Niessing, J., Ebisch, B., Schmidt, K.E., Niessing, M., Singer, W., Galuske, R.A., 2005. Hemodynamic signals correlate tightly with synchronized gamma oscillations. Science (80-.). 309, 948–951. doi:309/5736/948 [pii]10.1126/science.1110948

Nir, Y., Fisch, L., Mukamel, R., Gelbard-Sagiv, H., Arieli, A., Fried, I., Malach, R., 2007. Coupling between neuronal firing rate, gamma LFP, and BOLD fMRI is related to interneuronal correlations. Curr Biol 17, 1275–1285. doi:S0960-9822(07)01635-1 [pii]10.1016/j.cub.2007.06.066

Nunez, P.L., Silberstein, R.B., 2000. On the relationship of synaptic activity to macroscopic measurements: Does co-registration of EEG with fMRI make sense? Brain Topogr. 13, 79–96. doi:10.1023/A:1026683200895

Ogawa, S., Lee, T.M., Kay, A.R., Tank, D.W., 1990. Brain magnetic resonance imaging with contrast dependent on blood oxygenation. Proc Natl Acad Sci U S A 87, 9868–9872.

Ohl, F.W., Scheich, H., Freeman, W.J., 2001. Change in pattern of ongoing cortical activity with auditory category learning. Nature 412, 733–6. doi:10.1038/35089076

Ojemann, G.A., Corina, D.P., Corrigan, N., Schoenfield-McNeill, J., Poliakov, A., Zamora, L., Zanos, S., 2010. Neuronal correlates of functional magnetic resonance imaging in human temporal cortex. Brain

133, 46–59. doi:10.1093/brain/awp227awp227 [pii]

Osipova, D., Hermes, D., Jensen, O., 2008. Gamma power is phase-locked to posterior alpha activity. PLoS One 3, e3990. doi:10.1371/journal.pone.0003990

Özkurt, T.E., Schnitzler, A., 2011. A critical note on the definition of phase-amplitude cross-frequency coupling. J. Neurosci. Methods 201, 438–43. doi:10.1016/j.jneumeth.2011.08.014

Pachitariu, M., Lyamzin, D.R., Sahani, M., Lesica, N.A., 2015. State-dependent population coding in primary auditory cortex. J. Neurosci. 35, 2058–73. doi:10.1523/JNEUROSCI.3318-14.2015

Palva, J.M., Palva, S., Kaila, K., 2005. Phase synchrony among neuronal oscillations in the human cortex. J Neurosci 25, 3962–3972. doi:25/15/3962 [pii]10.1523/JNEUROSCI.4250-04.2005

Pascual-Marqui, R.D., Michel, C.M., Lehmann, D., 1994. Low resolution electromagnetic tomography: a new method for localizing electrical activity in the brain. Int. J. Psychophysiol. 18, 49–65. doi:0167-8760(84)90014-X [pii]

Peyrache, A., Battaglia, F.P., Destexhe, A., 2011. Inhibition recruitment in prefrontal cortex during sleep spindles and gating of hippocampal inputs. Proc Natl Acad Sci U S A 108, 17207–17212. doi:10.1073/pnas.11036121081103612108 [pii]

Pfurtscheller, G., Lopes da Silva, F.H., 1999. Event-related EEG/MEG synchronization and desynchronization: basic principles. Clin Neurophysiol 110, 1842–1857. doi:S1388245799001418 [pii]

Pittau, F., Fahoum, F., Zelmann, R., Dubeau, F., Gotman, J., 2013. Negative BOLD Response to Interictal Epileptic Discharges in Focal Epilepsy. Brain Topogr. doi:10.1007/s10548-013-0302-1

Praamstra, P., Kourtis, D., Kwok, H.F., Oostenveld, R., 2006. Neurophysiology of implicit timing in serial choice reaction-time performance. J. Neurosci. 26, 5448–55. doi:10.1523/JNEUROSCI.0440-06.2006

Proulx, S., Safi-Harb, M., LeVan, P., An, D., Watanabe, S., Gotman, J., 2014. Increased sensitivity of fast BOLD fMRI with a subject-specific hemodynamic response function and application to epilepsy. Neuroimage 93, 59–73. doi:10.1016/j.neuroimage.2014.02.018

Raichle, M.E., MacLeod, A.M., Snyder, A.Z., Powers, W.J., Gusnard, D.A., Shulman, G.L., 2001. A default mode of brain function. Proc Natl Acad Sci U S A 98, 676–682. doi:10.1073/pnas.98.2.67698/2/676 [pii]

Raichle, M.E., Mintun, M.A., 2006. Brain work and brain imaging. Annu Rev Neurosci 29, 449–476. doi:10.1146/annurev.neuro.29.051605.112819

Ramón y Cajal, S., 1899. Comparative study of the sensory areas of the human cortex.

Reig, R., Zerlaut, Y., Vergara, R., Destexhe, A., Sanchez-Vives, M. V, 2015. Gain modulation of synaptic inputs by network state in auditory cortex in vivo. J. Neurosci. 35, 2689–702. doi:10.1523/JNEUROSCI.2004-14.2015

Reimann, M.W., Anastassiou, C.A., Perin, R., Hill, S.L., Markram, H., Koch, C., 2013. A biophysically detailed model of neocortical local field potentials predicts the critical role of active membrane currents. Neuron 79, 375–90. doi:10.1016/j.neuron.2013.05.023

Riera, J., Aubert, E., Iwata, K., Kawashima, R., Wan, X., Ozaki, T., 2005. Fusing EEG and fMRI based on

a bottom-up model: inferring activation and effective connectivity in neural masses. Philos Trans R Soc L. B Biol Sci 360, 1025–1041. doi:LJDYNHGVDU9X77FL [pii]10.1098/rstb.2005.1646

Riera, J.J., Sumiyoshi, A., 2010. Brain oscillations: ideal scenery to understand the neurovascular coupling. Curr Opin Neurol 23, 374–381. doi:10.1097/WCO.0b013e32833b769f00019052-201008000-00006 [pii]

Riera, J.J., Wan, X., Jimenez, J.C., Kawashima, R., 2006. Nonlinear local electrovascular coupling. I: A theoretical model. Hum Brain Mapp 27, 896–914. doi:10.1002/hbm.20230

Ritter, P., Becker, R., Freyer, F., Villringer, A., 2010. EEG Quality: The Image Acquisiton Artefact, in: Mulert, C., Lemieux, L. (Eds.), EEG-fMRI Physiological Basis, Technique, and Applications. Springer.

Roopun, A.K., Kramer, M.A., Carracedo, L.M., Kaiser, M., Davies, C.H., Traub, R.D., Kopell, N.J., Whittington, M.A., 2008. Temporal Interactions between Cortical Rhythms. Front. Neurosci. 2, 145–54. doi:10.3389/neuro.01.034.2008

Rosa, M.J., Kilner, J., Blankenburg, F., Josephs, O., Penny, W., 2010. Estimating the transfer function from neuronal activity to BOLD using simultaneous EEG-fMRI. Neuroimage 49, 1496–1509. doi:S1053-8119(09)00990-2 [pii]10.1016/j.neuroimage.2009.09.011

Rothlübbers, S., Relvas, V., Leal, A., Murta, T., Lemieux, L., Figueiredo, P., 2015. Characterisation and reduction of the EEG artefact caused by the helium cooling pump in the MR environment: validation in epilepsy patient data. Brain Topogr. 28, 208–20. doi:10.1007/s10548-014-0408-0

Sadaghiani, S., Kleinschmidt, A., 2013. Functional interactions between intrinsic brain activity and behavior. Neuroimage 80, 379–386. doi:10.1016/j.neuroimage.2013.04.100S1053-8119(13)00459-X [pii]

Salek-Haddadi, A., Diehl, B., Hamandi, K., Merschhemke, M., Liston, A., Friston, K., Duncan, J.S., Fish, D.R., Lemieux, L., 2006. Hemodynamic correlates of epileptiform discharges: an EEG-fMRI study of 63 patients with focal epilepsy. Brain Res 1088, 148–166. doi:S0006-8993(06)00524-5 [pii]10.1016/j.brainres.2006.02.098

Salek-Haddadi, A., Lemieux, L., Merschhemke, M., Friston, K.J., Duncan, J.S., Fish, D.R., 2003. Functional magnetic resonance imaging of human absence seizures. Ann Neurol 53, 663–667. doi:10.1002/ana.10586

Salek-Haddadi, A., Mayer, T., Hamandi, K., Symms, M., Josephs, O., Fluegel, D., Woermann, F., Richardson, M.P., Noppeney, U., Wolf, P., Koepp, M.J., 2009. Imaging seizure activity: a combined EEG/EMG-fMRI study in reading epilepsy. Epilepsia 50, 256–264. doi:10.1111/j.1528-1167.2008.01737.xEPI1737 [pii]

Salek-Haddadi, A., Merschhemke, M., Lemieux, L., Fish, D.R., 2002. Simultaneous EEG-Correlated Ictal fMRI. Neuroimage 16, 32–40. doi:10.1006/nimg.2002.1073S1053811902910736 [pii]

Sato, W., Kochiyama, T., Uono, S., Matsuda, K., Usui, K., Inoue, Y., Toichi, M., 2014. Rapid, high-frequency, and theta-coupled gamma oscillations in the inferior occipital gyrus during face processing. Cortex. doi:10.1016/j.cortex.2014.02.024

Scheeringa, R., Bastiaansen, M.C., Petersson, K.M., Oostenveld, R., Norris, D.G., Hagoort, P., 2008. Frontal theta EEG activity correlates negatively with the default mode network in resting state. Int. J. Psychophysiol. 67, 242–251. doi:S0167-8760(07)00163-8 [pii]10.1016/j.ijpsycho.2007.05.017

Scheeringa, R., Fries, P., Petersson, K.M., Oostenveld, R., Grothe, I., Norris, D.G., Hagoort, P., Bastiaansen, M.C., 2011a. Neuronal dynamics underlying high- and low-frequency EEG oscillations contribute independently to the human BOLD signal. Neuron 69, 572–583. doi:S0896-6273(10)01081-0 [pii]10.1016/j.neuron.2010.11.044

Scheeringa, R., Mazaheri, A., Bojak, I., Norris, D.G., Kleinschmidt, A., 2011b. Modulation of visually evoked cortical FMRI responses by phase of ongoing occipital alpha oscillations. J Neurosci 31, 3813–3820. doi:31/10/3813 [pii]10.1523/JNEUROSCI.4697-10.2011

Scherg, M., Von Cramon, D., 1986. Evoked dipole source potentials of the human auditory cortex. Electroencephalogr Clin Neurophysiol 65, 344–360.

Schevon, C.A., Weiss, S.A., McKhann Jr., G., Goodman, R.R., Yuste, R., Emerson, R.G., Trevelyan, A.J., 2012. Evidence of an inhibitory restraint of seizure activity in humans. Nat Commun 3, 1060. doi:10.1038/ncomms2056ncomms2056 [pii]

Schridde, U., Khubchandani, M., Motelow, J.E., Sanganahalli, B.G., Hyder, F., Blumenfeld, H., 2008. Negative BOLD with large increases in neuronal activity. Cereb Cortex 18, 1814–1827. doi:bhm208 [pii]10.1093/cercor/bhm208

Schroeder, C.E., Lakatos, P., 2009. Low-frequency neuronal oscillations as instruments of sensory selection. Trends Neurosci. 32, 9–18. doi:10.1016/j.tins.2008.09.012

Schwartz, T.H., 2007. Neurovascular coupling and epilepsy: hemodynamic markers for localizing and predicting seizure onset. Epilepsy Curr 7, 91–94. doi:10.1111/j.1535-7511.2007.00183.x

Shmuel, A., Augath, M., Oeltermann, A., Logothetis, N.K., 2006. Negative functional MRI response correlates with decreases in neuronal activity in monkey visual area V1. Nat Neurosci 9, 569–577. doi:nn1675 [pii]10.1038/nn1675

Shmueli, K., van Gelderen, P., de Zwart, J.A., Horovitz, S.G., Fukunaga, M., Jansma, J.M., Duyn, J.H., 2007. Low-frequency fluctuations in the cardiac rate as a source of variance in the resting-state fMRI BOLD signal. Neuroimage 38, 306–20. doi:10.1016/j.neuroimage.2007.07.037

Siero, J.C., Hermes, D., Hoogduin, H., Luijten, P.R., Petridou, N., Ramsey, N.F., 2013. BOLD consistently matches electrophysiology in human sensorimotor cortex at increasing movement rates: a combined 7T fMRI and ECoG study on neurovascular coupling. J Cereb Blood Flow Metab. doi:10.1038/jcbfm.2013.97jcbfm201397 [pii]

Sirota, A., Montgomery, S., Fujisawa, S., Isomura, Y., Zugaro, M., Buzsaki, G., 2008. Entrainment of neocortical neurons and gamma oscillations by the hippocampal theta rhythm. Neuron 60, 683–697. doi:S0896-6273(08)00762-9 [pii]10.1016/j.neuron.2008.09.014

Skaggs, W.E., McNaughton, B.L., Permenter, M., Archibeque, M., Vogt, J., Amaral, D.G., Barnes, C.A., 2007. EEG sharp waves and sparse ensemble unit activity in the macaque hippocampus. J. Neurophysiol. 98, 898–910. doi:10.1152/jn.00401.2007

Smith, A.J., Blumenfeld, H., Behar, K.L., Rothman, D.L., Shulman, R.G., Hyder, F., 2002. Cerebral energetics and spiking frequency: the neurophysiological basis of fMRI. Proc Natl Acad Sci U S A 99, 10765–10770. doi:10.1073/pnas.132272199132272199 [pii]

Somers, D., Kopell, N., 1993. Rapid synchronization through fast threshold modulation. Biol Cybern 68, 393–407.

Sotero, R.C., Trujillo-Barreto, N.J., 2008. Biophysical model for integrating neuronal activity, EEG, fMRI and metabolism. Neuroimage 39, 290–309. doi:S1053-8119(07)00704-5 [pii]10.1016/j.neuroimage.2007.08.001

Sotero, R.C., Trujillo-Barreto, N.J., 2007. Modelling the role of excitatory and inhibitory neuronal activity in the generation of the BOLD signal. Neuroimage 35, 149–165. doi:S1053-8119(06)01093-7 [pii]10.1016/j.neuroimage.2006.10.027

Soto, J.L.P., Jerbi, K., 2012. Investigation of cross-frequency phase-amplitude coupling in visuomotor networks using magnetoencephalography. Conf. Proc. IEEE Eng. Med. Biol. Soc. 2012, 1550–3. doi:10.1109/EMBC.2012.6346238

Steriade, M., 2001. Impact of network activities on neuronal properties in corticothalamic systems. J Neurophysiol 86, 1–39.

Steriade, M., Hobson, J., 1976. Neuronal activity during the sleep-waking cycle. Prog Neurobiol 6, 155–376.

Stok, C.J., 1987. The influence of model parameters on EEG/MEG single dipole source estimation. IEEE Trans Biomed Eng 34, 289–296.

Sullivan, D., Csicsvari, J., Mizuseki, K., Montgomery, S., Diba, K., Buzsáki, G., 2011. Relationships between hippocampal sharp waves, ripples, and fast gamma oscillation: influence of dentate and entorhinal cortical activity. J. Neurosci. 31, 8605–16. doi:10.1523/JNEUROSCI.0294-11.2011

Suzuki, S.S., Smith, G.K., 1987. Spontaneous EEG spikes in the normal hippocampus. I. Behavioral correlates, laminar profiles and bilateral synchrony. Electroencephalogr. Clin. Neurophysiol. 67, 348–359. doi:10.1016/0013-4694(87)90123-4

Szczepanski, S.M., Crone, N.E., Kuperman, R.A., Auguste, K.I., Parvizi, J., Knight, R.T., 2014. Dynamic Changes in Phase-Amplitude Coupling Facilitate Spatial Attention Control in Fronto-Parietal Cortex. PLoS Biol. 12, e1001936. doi:10.1371/journal.pbio.1001936

Thivierge, J.P., Cisek, P., 2008. Nonperiodic synchronization in heterogeneous networks of spiking neurons. J Neurosci 28, 7968–7978. doi:28/32/7968 [pii]10.1523/JNEUROSCI.0870-08.2008

Thornton, R., Laufs, H., Rodionov, R., Cannadathu, S., Carmichael, D.W., Vulliemoz, S., Salek-Haddadi, A., McEvoy, A.W., Smith, S.M., Lhatoo, S., Elwes, R.D., Guye, M., Walker, M.C., Lemieux, L., Duncan, J.S., 2010. EEG correlated functional MRI and postoperative outcome in focal epilepsy. J Neurol Neurosurg Psychiatry 81, 922–927. doi:jnnp.2009.196253 [pii]10.1136/jnnp.2009.196253

Thornton, R., Vulliemoz, S., Rodionov, R., Carmichael, D.W., Chaudhary, U.J., Diehl, B., Laufs, H., Vollmar, C., McEvoy, A.W., Walker, M.C., Bartolomei, F., Guye, M., Chauvel, P., Duncan, J.S., Lemieux, L., 2011. Epileptic networks in focal cortical dysplasia revealed using electroencephalography-functional magnetic resonance imaging. Ann Neurol 70, 822–837. doi:10.1002/ana.22535

Thornton, R.C., Rodionov, R., Laufs, H., Vulliemoz, S., Vaudano, A., Carmichael, D., Cannadathu, S., Guye, M., McEvoy, A., Lhatoo, S., Bartolomei, F., Chauvel, P., Diehl, B., De Martino, F., Elwes, R.D., Walker, M.C., Duncan, J.S., Lemieux, L., 2010. Imaging haemodynamic changes related to seizures: comparison of EEG-based general linear model, independent component analysis of fMRI and intracranial EEG. Neuroimage 53, 196–205. doi:S1053-8119(10)00797-4 [pii]10.1016/j.neuroimage.2010.05.064

Tierney, T.M., Croft, L.J., Centeno, M., Shamshiri, E.A., Perani, S., Baldeweg, T., Clark, C.A., Carmichael,

D.W., 2015. FIACH: A biophysical model for automatic retrospective noise control in fMRI. Neuroimage 44, 1–18. doi:10.1016/j.neuroimage.2015.09.034

Tokariev, A., Videman, M., Palva, J.M., Vanhatalo, S., 2015. Functional Brain Connectivity Develops Rapidly Around Term Age and Changes Between Vigilance States in the Human Newborn. Cereb. Cortex bhv219. doi:10.1093/cercor/bhv219

Tort, A.B., Komorowski, R.W., Manns, J.R., Kopell, N.J., Eichenbaum, H., 2009. Theta-gamma coupling increases during the learning of item-context associations. Proc Natl Acad Sci U S A 106, 20942–20947. doi:10.1073/pnas.09113311060911331106 [pii]

Tort, A.B., Kramer, M.A., Thorn, C., Gibson, D.J., Kubota, Y., Graybiel, A.M., Kopell, N.J., 2008. Dynamic cross-frequency couplings of local field potential oscillations in rat striatum and hippocampus during performance of a T-maze task. Proc Natl Acad Sci U S A 105, 20517–20522. doi:0810524105 [pii]10.1073/pnas.0810524105

Tort, A.B.L., Komorowski, R., Eichenbaum, H., Kopell, N., 2010. Measuring Phase-Amplitude Coupling Between Neuronal Oscillations of Different Frequencies. J. Neurophysiol. 104, 1195–1210. doi:10.1152/jn.00106.2010

Traub, R.D., Jefferys, J.G.R., Whittington, M.A., 1999. Fast oscillations in Cortical Circuits. MIT Press, Cambridge, MA.

Tyvaert, L., Hawco, C., Kobayashi, E., LeVan, P., Dubeau, F., Gotman, J., 2008. Different structures involved during ictal and interictal epileptic activity in malformations of cortical development: an EEG-fMRI study. Brain 131, 2042–2060. doi:10.1093/brain/awn145awn145 [pii]

Tyvaert, L., LeVan, P., Dubeau, F., Gotman, J., 2009. Noninvasive dynamic imaging of seizures in epileptic patients. Hum Brain Mapp 30, 3993–4011. doi:10.1002/hbm.20824

Uludag, K., Dubowitz, D.J., Yoder, E.J., Restom, K., Liu, T.T., Buxton, R.B., 2004. Coupling of cerebral blood flow and oxygen consumption during physiological activation and deactivation measured with fMRI. Neuroimage 23, 148–155. doi:10.1016/j.neuroimage.2004.05.013S1053811904002903 [pii]

Uludag, K., Muller-Bierl, B., Ugurbil, K., 2009. An integrative model for neuronal activity-induced signal changes for gradient and spin echo functional imaging. Neuroimage 48, 150–165. doi:10.1016/j.neuroimage.2009.05.051S1053-8119(09)00557-6 [pii]

Ureshi, M., Matsuura, T., Kanno, I., 2004. Stimulus frequency dependence of the linear relationship between local cerebral blood flow and field potential evoked by activation of rat somatosensory cortex. Neurosci Res 48, 147–153. doi:S0168010203003134 [pii]

Valdes-Sosa, P.A., Sanchez-Bornot, J.M., Sotero, R.C., Iturria-Medina, Y., Aleman-Gomez, Y., Bosch-Bayard, J., Carbonell, F., Ozaki, T., 2009. Model Driven EEG/fMRI Fusion of Brain Oscillations. Hum. Brain Mapp. 30, 2701–2721. doi:Doi 10.1002/Hbm.20704

van der Meij, R., Kahana, M., Maris, E., 2012. Phase-Amplitude Coupling in Human Electrocorticography Is Spatially Distributed and Phase Diverse. J. Neurosci. 32, 111–123. doi:10.1523/JNEUROSCI.4816-11.2012

van Houdt, P.J., de Munck, J.C., Leijten, F.S., Huiskamp, G.J., Colon, A.J., Boon, P.A., Ossenblok, P.P., 2013. EEG-fMRI correlation patterns in the presurgical evaluation of focal epilepsy: a comparison with electrocorticographic data and surgical outcome measures. Neuroimage 75, 238–248. doi:10.1016/j.neuroimage.2013.02.033S1053-8119(13)00160-2 [pii]

van Wingerden, M., van der Meij, R., Kalenscher, T., Maris, E., Pennartz, C.M.A., 2014. Phase-amplitude coupling in rat orbitofrontal cortex discriminates between correct and incorrect decisions during associative learning. J. Neurosci. 34, 493–505. doi:10.1523/JNEUROSCI.2098-13.2014

Vanhatalo, S., Palva, J.M., Holmes, M.D., Miller, J.W., Voipio, J., Kaila, K., 2004. Infraslow oscillations modulate excitability and interictal epileptic activity in the human cortex during sleep. Proc. Natl. Acad. Sci. U. S. A. 101, 5053–7. doi:10.1073/pnas.0305375101

VanRullen, R., Koch, C., 2003. Is perception discrete or continuous? Trends Cogn. Sci. 7, 207–213. doi:10.1016/S1364-6613(03)00095-0

Vanzetta, I., Flynn, C., Ivanov, A.I., Bernard, C., Bénar, C.G., 2010. Investigation of linear coupling between single-event blood flow responses and interictal discharges in a model of experimental epilepsy. J. Neurophysiol. 103, 3139–3152. doi:10.1152/jn.01048.2009

Varela, F., Lachaux, J.P., Rodriguez, E., Martinerie, J., 2001. The brainweb: phase synchronization and large-scale integration. Nat. Rev. Neurosci. 2, 229–39. doi:10.1038/35067550

Vaudano, A.E., Di Bonaventura, C., Carni, M., Rodionov, R., Lapenta, L., Casciato, S., Fattouch, J., Egeo, G., Pantano, P., Nucciarelli, V., Maraviglia, B., Prencipe, M., Lemieux, L., Giallonardo, A.T., 2012. Ictal haemodynamic changes in a patient affected by “subtle” Epilepsia Partialis Continua. Seizure 21, 65–69. doi:10.1016/j.seizure.2011.09.003S1059-1311(11)00241-X [pii]

Vaughn, H.G., 1974. The analysis of scalp-recorded potentials., in: Thompson, R.F., Patterson, M.M. (Eds.), Bioelectric Recording Tecniques, Part B. Electroencephalography and Human Brain Potentials. Academic Press, New York, pp. 158–207.

Vaughn, H.G., 1969. The relationship of brain activity to scalp recordinds of event related potentials., in: Donchin, E., Lindsley, D.B. (Eds.), Averaged Evoked Potentials: Methods, Results, Evaluations. NASA, Washington DC, pp. 45–94.

Villringer, A., Mulert, C., Lemieux, L., 2010. Principles of Multimodal Functional Imaging and Data Integration, in: Mulert, C., Lemieux, L. (Eds.), EEG-fMRI Physiological Basis, Technique, and Applications. Springer, Berlin.

Voges, N., Blanchard, S., Wendling, F., David, O., Benali, H., Papadopoulo, T., Clerc, M., Bénar, C., 2012. Modeling of the neurovascular coupling in epileptic discharges. Brain Topogr. 25, 136–156. doi:10.1007/s10548-011-0190-1

von Stein, A., Sarnthein, J., 2000. Different frequencies for different scales of cortical integration: from local gamma to long range alpha/theta synchronization. Int. J. Psychophysiol. 38, 301–313. doi:10.1016/S0167-8760(00)00172-0

Voytek, B., Canolty, R.T., Shestyuk, A., Crone, N.E., Parvizi, J., Knight, R.T., 2010. Shifts in gamma phase-amplitude coupling frequency from theta to alpha over posterior cortex during visual tasks. Front Hum Neurosci 4, 191. doi:10.3389/fnhum.2010.00191

Voytek, B., Kayser, A.S., Badre, D., Fegen, D., Chang, E.F., Crone, N.E., Parvizi, J., Knight, R.T., D’Esposito, M., 2015. Oscillatory dynamics coordinating human frontal networks in support of goal maintenance. Nat. Neurosci. 18, 1318–1324. doi:10.1038/nn.4071

Vulliemoz, S., Carmichael, D.W., Rosenkranz, K., Diehl, B., Rodionov, R., Walker, M.C., McEvoy, A.W., Lemieux, L., 2011. Simultaneous intracranial EEG and fMRI of interictal epileptic discharges in humans. Neuroimage 54, 182–190. doi:S1053-8119(10)01071-2

[pii]10.1016/j.neuroimage.2010.08.004

Vulliemoz, S., Rodionov, R., Carmichael, D.W., Thornton, R., Guye, M., Lhatoo, S.D., Michel, C.M., Duncan, J.S., Lemieux, L., 2010. Continuous EEG source imaging enhances analysis of EEG-fMRI in focal epilepsy. Neuroimage 49, 3219–3229. doi:S1053-8119(09)01241-5 [pii]10.1016/j.neuroimage.2009.11.055

Waziri, A., Schevon, C.A., Cappell, J., Emerson, R.G., McKhann 2nd, G.M., Goodman, R.R., 2009. Initial surgical experience with a dense cortical microarray in epileptic patients undergoing craniotomy for subdural electrode implantation. Neurosurgery 64, 540–5; discussion 545. doi:10.1227/01.NEU.0000337575.63861.1000006123-200903000-00018 [pii]

Weiss, S.A., Banks, G.P., McKhann, G.M., Goodman, R.R., Emerson, R.G., Trevelyan, A.J., Schevon, C.A., 2013. Ictal high frequency oscillations distinguish two types of seizure territories in humans. Brain 136, 3796–808. doi:10.1093/brain/awt276

Whittingstall, K., Logothetis, N.K., 2009. Frequency-band coupling in surface EEG reflects spiking activity in monkey visual cortex. Neuron 64, 281–289. doi:S0896-6273(09)00628-X [pii]10.1016/j.neuron.2009.08.016

Whittington, M.A., Traub, R.D., 2003. Interneuron diversity series: inhibitory interneurons and network oscillations in vitro. Trends Neurosci. 26, 676–682. doi:S0166-2236(03)00336-9 [pii]10.1016/j.tins.2003.09.016

Wieser, H.G., Blume, W.T., Fish, D., Goldensohn, E., Hufnagel, A., King, D., Sperling, M.R., Lüders, H., Pedley, T.A., 2008. Proposal for a New Classification of Outcome with Respect to Epileptic Seizures Following Epilepsy Surgery. Epilepsia 42, 282–286. doi:10.1046/j.1528-1157.2001.35100.x

Winawer, J., Kay, K.N., Foster, B.L., Rauschecker, A.M., Parvizi, J., Wandell, B.A., 2013. Asynchronous broadband signals are the principal source of the BOLD response in human visual cortex. Curr. Biol. 23, 1145–53. doi:10.1016/j.cub.2013.05.001

Womelsdorf, T., Fries, P., Mitra, P.P., Desimone, R., 2006. Gamma-band synchronization in visual cortex predicts speed of change detection. Nature 439, 733–6. doi:10.1038/nature04258

Worsley, K.J., Friston, K.J., 1995. Analysis of fMRI time-series revisited--again. Neuroimage 2, 173–181. doi:S1053-8119(85)71023-3 [pii]10.1006/nimg.1995.1023

Wulff, P., Ponomarenko, A.A., Bartos, M., Korotkova, T.M., Fuchs, E.C., Bahner, F., Both, M., Tort, A.B., Kopell, N.J., Wisden, W., Monyer, H., 2009. Hippocampal theta rhythm and its coupling with gamma oscillations require fast inhibition onto parvalbumin-positive interneurons. Proc Natl Acad Sci U S A 106, 3561–3566. doi:10.1073/pnas.08131761060813176106 [pii]

Yamamoto, Y., Hughson, R.L., 1991. Coarse-graining spectral analysis: new method for studying heart rate variability. J. Appl. Physiol. 71, 1143–1150.

Yan, W.X., Mullinger, K.J., Brookes, M.J., Bowtell, R., 2009. Understanding gradient artefacts in simultaneous EEG/fMRI. Neuroimage 46, 459–471. doi:10.1016/j.neuroimage.2009.01.029

Yanagisawa, T., Yamashita, O., Hirata, M., Kishima, H., Saitoh, Y., Goto, T., Yoshimine, T., Kamitani, Y., 2012. Regulation of motor representation by phase-amplitude coupling in the sensorimotor cortex. J. Neurosci. 32, 15467–75. doi:10.1523/JNEUROSCI.2929-12.2012

Yen, C.C., Fukuda, M., Kim, S.G., 2011. BOLD responses to different temporal frequency stimuli in the

lateral geniculate nucleus and visual cortex: insights into the neural basis of fMRI. Neuroimage 58, 82–90. doi:10.1016/j.neuroimage.2011.06.022S1053-8119(11)00640-9 [pii]

Zijlmans, M., Huiskamp, G., Hersevoort, M., Seppenwoolde, J.H., van Huffelen, A.C., Leijten, F.S., 2007. EEG-fMRI in the preoperative work-up for epilepsy surgery. Brain 130, 2343–2353. doi:awm141 [pii]10.1093/brain/awm141

Appendix A

PAC and the BOLD signal amplitude relationship (experiment 3)

supplementary methods, results, and discussion

In this appendix, we describe the two PAC strength estimation metrics implemented in addition to Canolty's, in A1.1, and discuss the impact of the metric used in the phase-amplitude comodolagram plots and final conclusions, in A2.1. Furthermore, we describe the methods and results regarding the influence of the duration of the epoch of data used to estimate the PAC strength in the final conclusions, in A1.2 and A2.2, respectively.

A1 Methods

A1.1 PAC strength estimation

Tort PAC

Tort's PAC strength estimates were obtained using our own implementation of the methods described in Tort et al. (2008) and He et al. (2010). Tort's metric measures the uniformity of the distribution of $\langle A_{HF}(t)\rangle$ across a number of phase bins, in a particular data epoch and contact.

$\varphi_{LF}(t)$ was segmented into 18 bins and the corresponding $A_{HF}(t)$ values were averaged, yielding 18 mean amplitude values, $\langle A_{HF}\rangle(i = 1, \ldots., 18)$, one for each phase bin (Tort et al., 2008). The normalised $\langle A_{HF}\rangle(i)$ was computed as:

$$P(i) = \frac{\langle A_{HF}\rangle(i)}{\sum_{j=1}^{18}\langle A_{HF}\rangle(j)} \tag{A1-1}$$

and the entropy of P was computed as:

$$H = -\sum_{i=1}^{18} P(i)\ \log P(i) \tag{A1-2}$$

If $A_{HF}(t)$ is not coupled to $\varphi_{LF}(t)$ then $\langle A_{HF}\rangle$ is approximately the same for all the 18 phase bins and P is a roughly uniform distribution.

The raw strength of the coupling between $A_{HF}(t)$ and $\varphi_{LF}(t)$, was then computed as:

$$rPAC_{Tort} = \frac{H_{max} - H}{H_{max}} \tag{A1-3}$$

where $H_{max} = \log(18)$, is the maximum possible entropy, as $P(i) = 1/18$ for any i. Therefore, $rPAC_{Tort}$ quantifies the deviation of P from the uniform distribution.

The z-scored strength of the coupling between $A_{HF}(t)$ and $\varphi_{LF}(t)$ was computed as the difference between $rPAC_{Tort}$ and the mean of a distribution of surrogates of $rPAC_{Tort}$, divided by the standard deviation of the same distribution of surrogates. The distribution of surrogates of $rPAC_{Tort}$ was obtained by: (1) segmenting $\varphi_{LF}(t)$ into five equal-length segments, which were shuffled with no segment staying at its original position (yielding a total of forty-four shuffled $\varphi_{LF}(t)$ time courses), (2) computing a new $rPAC_{Tort}{}'$ value for each new $\varphi_{LF}(t)'$, but keeping the $A_{HF}(t)$ unchanged (He et al., 2010). The shuffling step destroyed any potential coupling between A_{HF} and φ_{LF}, while preserving the temporal structure of the original signal, $x_{composite}(t)$

(Hurtado et al., 2004). The mean and standard deviation of the distribution of surrogates were obtained using the Matlab functions *mean* and *std*.

Özkurt and Schnitzler PAC

Arguing that the previously proposed metrics for PAC strength estimation were designed intuitively and lacked a proper prior definition of PAC itself as a universal phenomenon, Özkurt and Schnitzler (2011) proposed an analytically definition of PAC, and a way to estimate its strength, which they called the direct PAC estimate.

The strength of the coupling between $A_{HF}(t)$ and $\varphi_{LF}(t)$, in a particular epoch comprising T data samples, was computed as:

$$PAC_{\text{Özkurt \& Schnitzler}} = \frac{1}{\sqrt{T}} \frac{\left|\sum_{t=1}^{T} A_{HF}(t) e^{i\varphi_{LF}(t)}\right|}{\sqrt{\sum_{t=1}^{T} A_{HF}(t)^2}} = \frac{rPAC_{\text{Canolty}}}{\sqrt{\frac{1}{T}\sum_{t=1}^{T} A_{HF}(t)^2}} \qquad \text{(A1-4)}$$

Note that $PAC_{\text{Özkurt\&Schnitzler}}$ is equivalent to Canolty's raw PAC estimate, aside from the normalising factor $\sqrt{\frac{1}{T}\sum_{t=1}^{T} A_{HF}(t)^2}$.

A1.2 Data epoch duration for PAC strength estimation

We investigated the influence of the duration of the epoch used to estimate the strength of PAC (to this point, 15 seconds) on the t-values obtained for the $PAC_{\beta\gamma}$, P_{α}, P_{β}, and P_{γ} effects, using six different epoch durations: 3, 5, 7, 9, 11, 13 seconds. We started with 3 seconds because that is the temporal resolution of the BOLD signal.

A2 Results and Discussion

A2.1 PAC strength estimation

A2.1.1 Phase-amplitude comodolagram

Considering each patient individually, the three PAC strength estimation metrics led to qualitatively similar phase-amplitude comodulogram plots (**Figure A-1**), in general. While the frequency pairs showing the higher PAC strengths were roughly in the same frequency range across methods, the exact frequency pairs showing the maximum PAC strength varied across them. For patients LT and IH, the number of frequency pairs that survived the thresholding step was different for Canolty's and Tort's metrics.

By definition, Canolty's metric is not able to detect a bimodal distribution of amplitude modulation (when the HF amplitude has two symmetric local maximums, one at the phase of ϕ and another at $\phi+\pi$), but Tort 's metric is, which may explain the difference between patient IH's Canolty's and Tort's plots. Moreover, Canolty's is equivalent to Özkurt and Schnitzler's, aside from a normalising factor (compare (5-11) with (A1-4)), which may explain the similarity between patient IH's Canolty's and Özkurt and Schnitzler's plots.

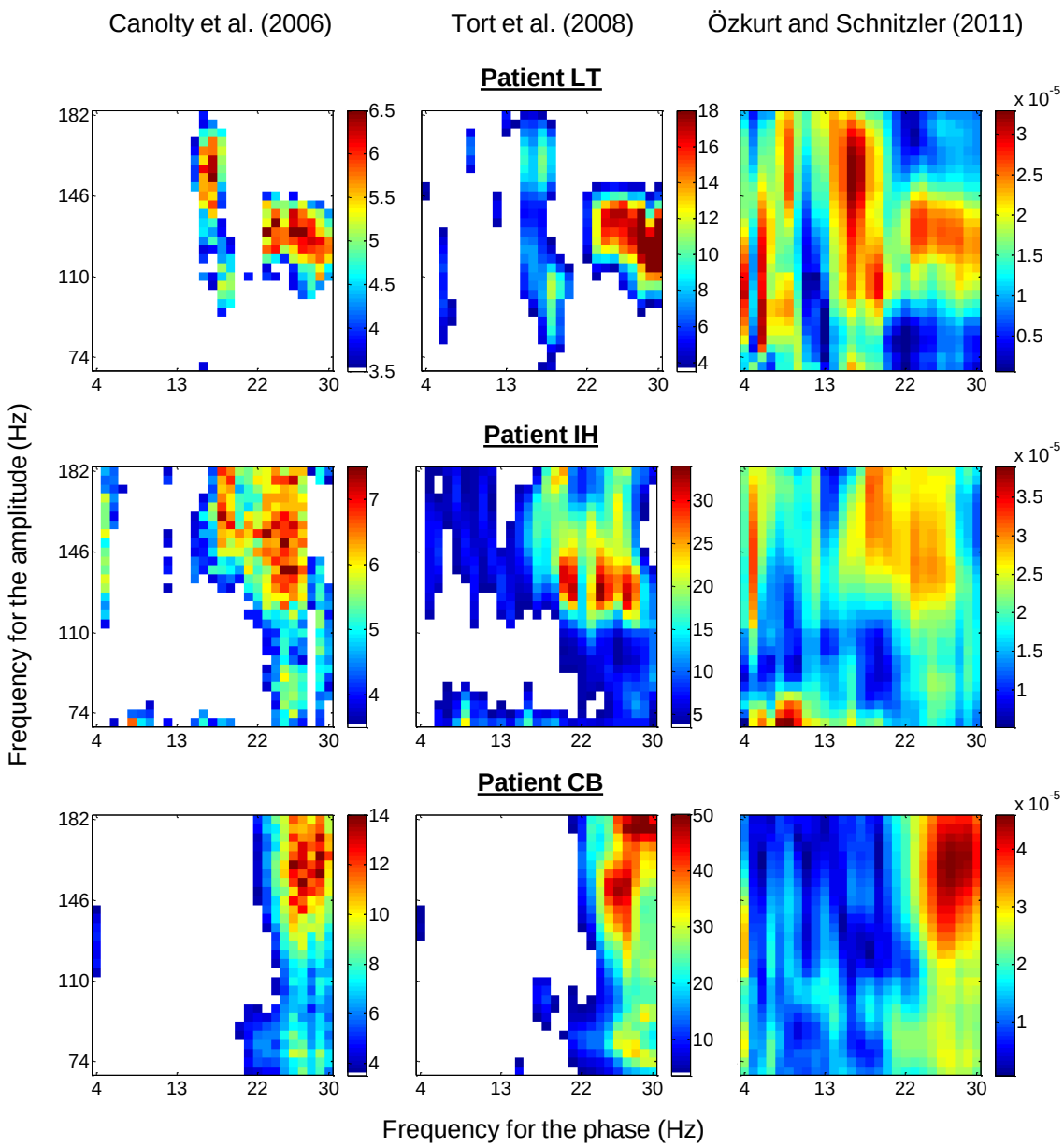

Figure A-1 Phase-amplitude comodulogram plots obtained using three different PAC strength estimation metrics, for each patient-specific COI_{β}. The plots obtained with Canolty's and Tort's metrics are thresholded at $p < 0.05$ and corrected for multiple comparisons using the Bonferroni criterion.

A2.1.2 BOLD signal changes GLM results

The significance of the t-values for the $PAC_{\beta\gamma}$, P_{α}, P_{β}, and P_{γ} effects depends on the PAC strength metric used (**Figure A-2**), however the trend $PAC_{\beta\gamma}$ explains variance in addition to P_{α}, P_{β}, and P_{γ}, while P_{β} does not in addition to $PAC_{\beta\gamma}$, P_{α}, and P_{γ}, is present.

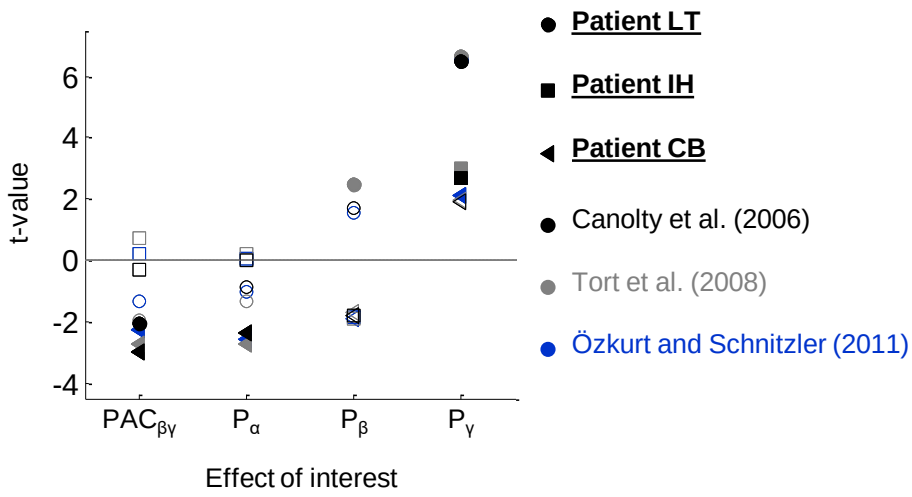

Figure A-2 BOLD signal changes GLM results. t-values for the $PAC_{\beta\gamma}$, P_{α}, P_{β}, and P_{γ} effects. Different colours represent different PAC strength metrics. Different shapes represent different patients. Filled shapes represent t-values with $p < 0.05$.

A2.2 Epoch duration for PAC computation

The significance of the t-values for the $PAC_{\beta\gamma}$, P_{α}, P_{β}, and P_{γ} effects depends on the duration of the data epoch used to estimate the strength of PAC (**Figure A-3**), however the trend $PAC_{\beta\gamma}$ explains variance in addition to P_{α}, P_{β}, and P_{γ}, while P_{β} does not in addition to $PAC_{\beta\gamma}$, P_{α}, and P_{γ}, is present.

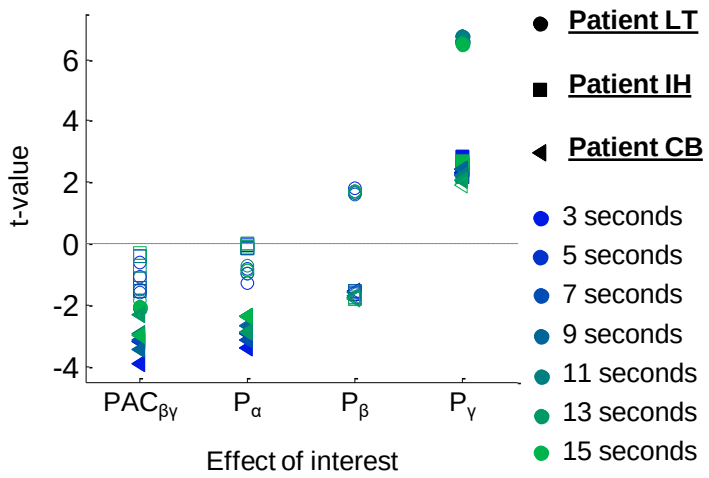

Figure A-3 BOLD signal changes GLM results. t-values for the $PAC_{\beta\gamma}$, P_{α}, P_{β}, and P_{γ} effects. Different colours represent different epoch durations for the estimation of the PAC strength. Different shapes represent different patients. Filled shapes represent t-values with $p < 0.05$.